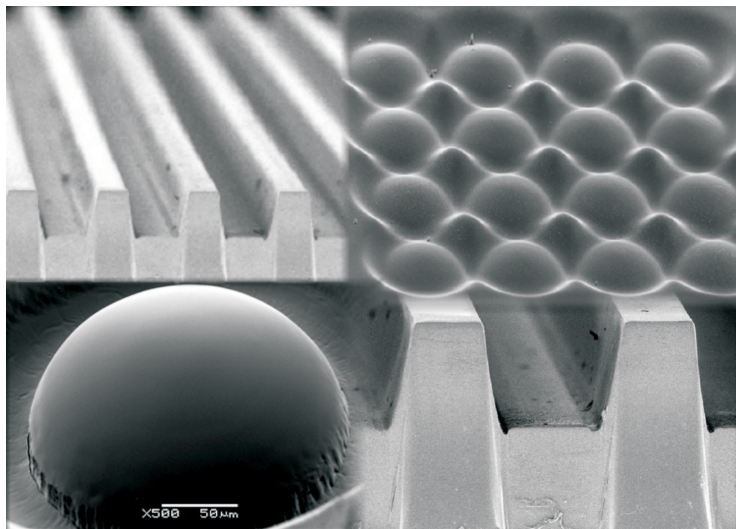UNIVERSITEIT
GENT

Excimeerlaser-ablatie van microstructuren in polymeren voor fotonische toepassingen

Excimer laser ablation of microstructures in polymers for photonic applications

Kris Naessens

INTEC

Promotoren:
Prof. dr. ir. R. Baets   Universiteit Gent, België
Prof. dr. ir. P. Van Daele   Universiteit Gent, België

Examencommissie:
Prof. dr. E. Schacht   Universiteit Gent, België
Prof. dr. ir. H. Thienpont   Vrije Universiteit Brussel, België
Dr. ir. P. Muys   VDM Laser Optics N.V., België
Dr. ir. R. Bockstaele   Universiteit Gent, België
Prof. dr. ir. P. Lagasse   Universiteit Gent, België

Dankwoord

Beste lezer,

Dit werk is tot stand gekomen dankzij de inspanningen van een heleboel mensen. Mag ik hier van de gelegenheid gebruik maken om mijn appreciatie voor hun bijdrage te tonen?

In de allereerste plaats wil ik een woord van dank richten aan mijn promotoren prof. Roel Baets en prof. Peter Van Daele die dit onderzoekswerk hebben mogelijk gemaakt. Voor de steun, deskundigheid en creatieve ideeën die je me toevertrouwde, dankjewel Roel. Mijn oprechte dank gaat eveneens uit naar Prof. Paul Lagasse die de structuur en het kader waarbinnen dit onderzoek werd gevoerd, ter beschikking heeft gesteld.

Verder hebben een heleboel mensen rechtstreeks of onrechtstreeks een handje toegestoken in mijn onderzoeksactiviteiten: Stephan Boons, Steven Van Put, Liesbet Van Landschoot, Steven Verstuyft, Peter Geerinck, Hendrik Sergeant, An Van Hove en Yves Martelé. Mijn bijzondere dank gaat uit naar Prof. Hugo Thienpont voor het ter beschikking stellen van de noodzakelijke lenskarakterisatie-infrastructuur en Heidi Ottevaere voor haar geapprecieerde aanwezigheid, geduld en hulp gedurende de vele dagen die met Mach-Zehnder en Wyko metingen werden gevuld. Finally, I would like to thank Rod Andrew and Yves Canivez from Optec for the many little things concerning Micromaster.

Bedankt Ronny, Peter, Lieven en Dirk voor jullie waardevolle gezelschap en omdat jullie vaak gewillige slachtoffers waren voor een Super Soaker moment. Bedankt beste (ex-)bewoners van de 39, de koffiepauzes met jullie zijn steeds een aangename verpozing geweest. Bedankt ook aan die ene indringer uit het Technicum die telkens een zitje in onze koffiekamer wist te versieren. Nog even volhouden, Thierry!

En aan degene die liever haar naam niet vermeld ziet: bedankt, Els.

Gent, september 2003

Kris Naessens

Inhoudsopgave

Nederlandstalige samenvatting

Chapter 1

Inleiding

1.1 Situering en motivatie van het onderzoekswerk

Onze moderne samenleving is in hoge mate gebaseerd op het verspreiden, verza-
melen en opslaan van informatie. Hierbij is een belangrijke rol weggelegd voor de
data transportmogelijkheden die voor commerciële, sociale, financiële, medische en
wetenschappelijke doeleinden worden gebruikt: telefonie, sensor data, electronische
transacties, Internet verkeer, CATV, etc. Bepalend in dit transport zijn de gigan-
tische hoeveelheden informatie die worden versluisd en naar alle verwachtingen zal
dit volume steeds blijven toenemen. Een belangrijk aspect van het informatie-
transport is het gebruik van licht als informatiedrager in dataverbindingen ('links')
met hoge capaciteit. Zelfs voor afstanden ter grootte van een paar millimeter kun-
nen argumenten worden gevonden om optische links te gebruiken: geen overspraak
tussen naburige signalen, geen warmtedissipatie, efficiënt gebruik van het beschik-
baar fysische volume, een immense beschikbare bandbreedte in vergelijking met
elektrische signalen.
Er is echter ook een belangrijk nadeel: in tegenstelling tot koperdraadjes die heel
eenvoudig aan elkaar kunnen worden gesoldeerd, is optische interconnectie com-
plexer. De lichtbron, detector en eventueel het tussenliggend transportmedium
dienen namelijk nauwkeurig met elkaar te worden gealigneerd. Typische bron-
nen en ontvangers zijn opto-electronische componenten die vervaardigd worden in
halfgeleidermateriaal.

De immer toenemende vraag naar bandbreedte en kostoverwegingen hebben er-
toe geleid dat de afmetingen van opto-electronische componenten en de daarmee
gepaard gaande lichtbundels steeds kleiner worden. Typische bundeldiameters
gegenereerd door oppervlakte-emitterende halfgeleiderlasers (VCSELs) zijn een
tiental micrometer (1 micrometer = 1/1000 van een millimeter), terwijl zijde-
lings emitterende bronnen nog een grootteorde kleiner zijn. Bovendien kan er een
tweede tendens worden waargenomen: enkelvoudige optische paden worden gelei-
delijk vervangen door meerdere kanalen in parallel. Dit is een logisch gevolg van de
commerciële beschikbaarheid van tweedimensionele rijen oppervlakte-emitterende

15

laserbronnen. De typische afstand ('pitch') tussen deze kanalen is 250 μm. Daartegenover staat dat het transportmedium min of meer gelijk is gebleven: single mode vezel voor lange afstanden, multimode glas/plastic vezel of vrije ruimte voor korte afstandscommunicatie.

Het is duidelijk dat de hoge mate aan parallellisme en de kleine optische bundel-groottes van de chips een behoorlijke uitdaging vormen voor een efficiënte in- en uitkoppeling (de interface). Dit geldt zowel op technologisch vlak als vanuit een kosten-baten analyse.

De interface bestaat gewoonlijk uit een drager van glas, keramiek of halfgeleider-materiaal waarin alignatieonderdelen, klemmogelijkheden voor vezel en chip, en eventueel ook micro-optische elementen verwerkt zijn. Deze laatste kunnen helpen bij het afstemmen van de chipmode op het modeprofiel van de vezel (bundelgeome-trie) of het vergemakkelijken van de alignatievereisten.

In tegenstelling tot chipfabricatie-technologie die gebaseerd is op UV lithografie waarbij planaire afmetingen kleiner dan 0.1 μm kunnen worden geconstrueerd, wor-den typische alignatiecomponenten gefabriceerd met andere, minder nauwkeurige technieken die driedimensionele structuren toelaten. Dit kan op een mechanische manier gebeuren zoals bij microfrezen en microboren, of via meer geavanceerde technieken gebaseerd op vonkerosie, laserbewerking en LIGA. Vaak is het vol-doende dat een dergelijke technolgie wordt aangewend om een prototype struc-tuur te maken. Fabricatie in grote aantallen gebeurt vervolgens met bijvoorbeeld spuitgieten of stempelen.

1.2   Excimeerlaser-ablatie

Een alternatief voor hogervermelde fabricatietechnieken is (excimeer)laser-ablatie. Deze microbewerkingstechnologie is gebaseerd op het lokaal wegnemen van ma-teriaal aan een oppervlak met kortstondige maar krachtige laserpulsen en dit op een gecontroleerde manier. Typische pulslengtes bedragen meerdere nanoseconden (1 nanoseoncde = 1/1000.000.000 van een seconde). Een aantal bijzondere eigen-schappen maken van laserablatie een waardevolle techniek: er is geen fysisch con-tact met het te bewerken materiaal en dus ook geen slijtage; patronen worden recht-streeks geschreven in het gewenste materiaal zonder tussenkomst van lithografie en etsstappen; laserablatie kan gebruikt worden bij kamertemperatuur en onder at-mosferische omstandigheden. Deze flexibiliteit en de korte bewerkingstijden maken van excimeerlaser-ablatie dan ook terecht een 'fast prototyping' techniek.

In tegenstelling tot hoogvermogen infrarood lasers zoals Nd:YAG en CO_2 die ook voor laserablatie worden gebruikt, emitteren excimeerlasers in het diepe ultraviolet tussen 157 en 355 nm. Gezien de meeste materialen sterk absorberen in dit gebied en gezien lagere golflengtes een betere optische resolutie geven, is dit type laser heel geschikt om patronen aan te brengen met een nauwkeurigheid in de orde van micrometer en zelfs submicrometer. Dit geldt in het bijzonder voor bewerking van polymeren gezien deze een lage thermische geleidbaarheid bezitten en typisch heel sterk absorberen in het ultraviolet. Bovendien kunnen organische moleculen bij

deze golflengtes via een fotochemisch proces ('koude ablatie') desintegreren.
Excimeerlaser-ablatie biedt naast bovenvermelde eigenschappen nog twee bijzon-
dere voordelen. Ten eerste is het één van de weinige technieken die in staat is
microstructuren voor zowel alignatie- als micro-optische doeleinden aan te maken.
Concreet betekent dit dat excimeerlaser-ablatie kan gebruikt worden voor mono-
litische integratie van beide functionaliteiten in éénzelfde polymeersubstraat. Ten
tweede biedt laserablatie het unieke voordeel dat het kan aangewend worden in
een late fase van een heterogene opto-electronische assemblage. Inderdaad, de con-
tactloze fabricatietechniek oefent geen druk uit op de kwetsbare opto-electronische
module en chemische substanties blijven achterwege. Dit in tegenstelling tot veel
andere fabricatietechnologieën.

Twee belangrijke motieven hebben een rol gespeeld bij het tot stand komen van dit
werk. Een eerste reden betreft de relatief gebrekkige literatuur die de eigenschap-
pen van excimeerlaser-ablatie op het gebied van microfabricatie behandelt. Dit in
tegenstelling tot de vele publicaties die het lasergestuurde erosieproces (proberen
te) modelleren. Bovendien zijn die vaak beperkt tot de relatie tussen ablatiediepte
en pulsenergie. In deze thesis —in het bijzonder hoofdstuk 3— werd een poging
ondernomen om de eigenschappen van excimeerlaser-ablatie met betrekking tot
microfabricatie zorgvuldig te beschrijven en dit voor meerdere commerciële poly-
meren, inclusief uitvoerige experimentele waarnemingen.
Een tweede belangrijke motivering is het potentieel dat excimeerlaser-ablatie bood
op vlak van microlensfabricatie bij de aanvang van ons onderzoekswerk. Hoewel een
aantal onderzoeksgroepen toen reeds op een succesvolle manier lensjes met laser-
ablatie hadden aangemaakt, vereisten deze technieken vaak dure bundelmaskers,
heel geavanceerde opstellingen of lange bewerkingstijden. Met andere woorden,
sleutelaspecten zoals flexibiliteit en fast prototyping gaan hier volledig verloren.
Binnen het kader van dit doctoraat werd een nieuwe techniek ontwikkeld: de
omtrekscan-techniek. Deze past een mouw aan hogervermelde problemen: poly-
mere lenzen en lensrijen met een arbitrair profiel kunnen worden gefabriceerd in
luttele minuten en met een heel eenvoudige, robuuste opstelling. De techniek staat
in detail beschreven in hoofdstuk 4.

1.3 Publicatielijst

Deze kan worden teruggevonden in de Engelstalige versie.

Hoofdstuk 2

UV laserablatie van polymere materialen

2.1 Absorptie- en relaxatieprocessen in organische materialen

Indien een lichtbundel binnentreedt in een materiaal dat niet 100 % transparant is voor de betreffende golflengte, zal de bundelintensiteit afnemen naarmate hij dieper in het materiaal dringt volgens (reflectie buiten beschouwing gelaten)

$$I(x) = I_0 e^{-\alpha x}$$

Dit is de Beer-Lambert wet waarin α de lineaire absorptiecoëfficiënt (cm^{-1}) is. Ter vereenvoudiging is hier enkel een 1-foton absorptieproces in beschouwing genomen. Vaak wordt deze coëfficiënt uitgedrukt in functie van de concentratie absorberende deeltjes N (cm^{-3}) en hun absorptiedoorsnede σ (cm^2): $\alpha = \sigma N$. Hoewel laserablatie betrekking heeft op heel hoge pulsintensiteiten, is de verwaarlozing van multi-fotonprocessen terecht omwille van de hoge waarden voor α bij de excimeergolflengtes, typisch $> 10^4$ cm^{-1}.

Absorptie in organische materialen treedt op ten gevolge van een electronische, vibrationele of rotationele excitatie van de moleculen naargelang de golflengte van de invallende bundel (figuur 2.1). Bij ultravioletstraling worden electronische excitaties in de covalente bindingen van organische media veroorzaakt, waarbij electronen gepromoveerd worden naar een orbitaal met hogere energie. Deze zijn voornamelijk $n \rightarrow \pi^*$ en $\pi \rightarrow \pi^*$ overgangen. Gezien de beperkte overlap van een π orbitaal in vergelijking met de veel sterkere σ binding, kunnen de π electronen veel gemakkelijker door een elektrisch veld worden beïnvloed. De functionele groepen die de absorberende bindingen bevatten, worden chromoforen genoemd.

Een geëxciteerd electron kan terugkeren naar de grondtoestand via een aantal mechanismen, voornamelijk interne conversie en fotochemische reacties (typisch fotodissociatie). In het eerste geval wordt de excitatie-energie opnieuw vrijgegeven

(a)

(b)
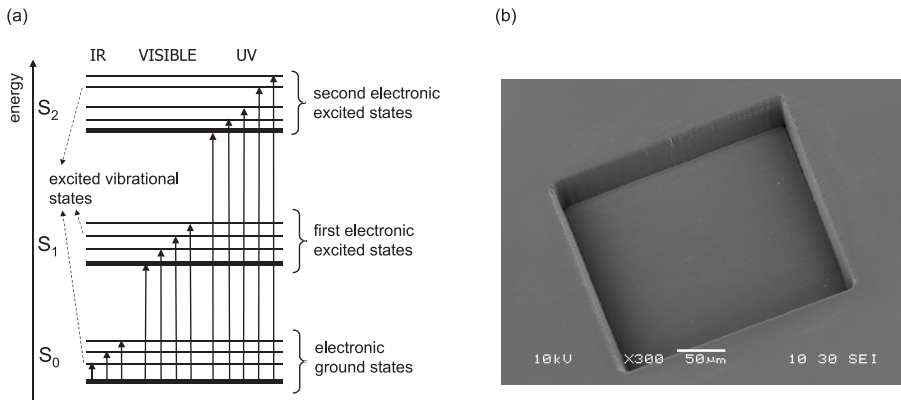
Figuur 2.1: Energieniveaus in een organische molecule en mogelijke transities (a). Lasergeableerde caviteit in polycarbonaat onder atmosferische omstandigheden (b). Laserbron is een KrF laser, energiedichtheid op het polymeeroppervlak is 440 mJ/cm^2.

in de vorm van vibrationele energie (warmte), terwijl men in het tweede geval van een 'koud' proces spreekt. De relaxatieconstante (interne conversie en fotodissociatie) bij polyimide wordt geschat op 35 ps.

2.2 Excimeerlaser-ablatie van polymeren met gepulste lasers

Zoals reeds vermeld zal een laserbundel invallend op een materiaaloppervlak geabsorbeerd worden en zal de intensiteit exponentieel afnemen. Indien de straling voldoende krachtig is, kan de gedeponeerde energie lokaal groter worden dan de dissociatie-energie. Voor excimeerlaserpulsen met een duur van een tiental nanoseconden neemt dit dissociatieproces plaats op een éénzelfde korte tijdsschaal. Doordat het intrinsiek volume van de restproducten vele malen dit van het vaste polymeer overschrijdt, zullen deze deeltjes (gas+macroscopische partikels) op een explosieve wijze het oppervlak verlaten met snelheden tot 10^5 cm/s. Het resultaat is een microscopisch putje dat in het oppervlak achterblijft. Dit proces, inclusief het explosief dissociatiekarakter, wordt laserablatie genoemd. Een voorbeeld is gegeven in figuur 2.1: een plaatje polycarbonaat, geableerd met een KrF laser (248 nm).

2.2.1 Beer model

In de onderstelling dat laserablatie een sequentieel proces is waarbij een invallende puls eerst wordt geabsorbeerd en vervolgens pas aanleiding geeft tot dissociatie,
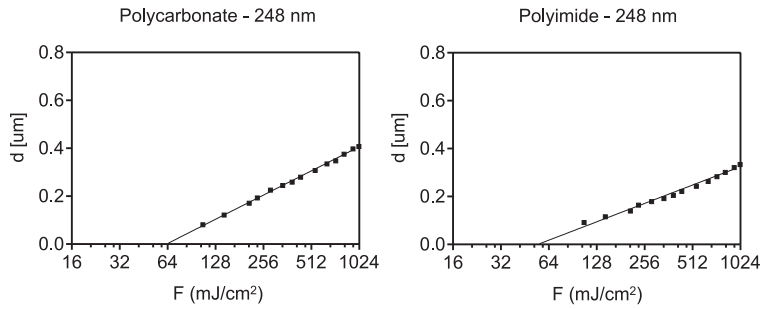
Figuur 2.2: Toepassing van het Beer model op laserablatie van PC en PI bij 248 nm
(16 ns pulsen). De ablatiesnelheden werden bepaald op basis van de etsdiepte voor
20 opeenvolgende pulsen.

kan men uit de wet van Beer-Lambert de etsdiepte afleiden:

$$d = \frac{1}{\alpha} ln((1-R)F/F_{th})$$

waarbij d de ablatiediepte per puls, R de reflectie aan het materiaaloppervlak en F_{th}
de minimale pulsenergiedichtheid[1] (J/cm^2) voor ablatie is. Zodra F deze drempel-
waarde overschrijdt, worden voldoende moleculaire bindingen verbroken gedurende
de laserpuls om relaxatiemechanismen zoals warmtediffusie en herstelprocessen te
overtreffen en het materiaal fyisch te ontbinden.

Het ablatiegedrag van 5 commerciële polymeren werd uitvoerig onderzocht bij
193 nm (ArF laser) en 248 nm (KrF laser): polycarbonaat (PC), polymethylmetha-
crylaat (PMMA), polyethyleen tereftalaat (PET), polyimide (PI) en polystyreen
(PS). De experimentele resultaten staan samengevat in tabel 2.1 en figuur 2.2 geeft
de ablatiecurves voor twee gevallen.
Het model is heel aantrekkelijk omwille van de eenvoud maar lijdt aan een aan-
tal gebreken: gewoonlijk is de lineaire fit (op een log-schaal) slechts geldig in een
beperkt bereik van F en wijken de berekende waarden voor α af van de realiteit.
De oorzaak ligt in het feit dat excimeerlaser-ablatie veel complexer is dan veronder-
steld in het Beer model. In de volgende sectie beschouwen we een aantal aspecten
van het ablatieproces die een meer nauwkeurige modellering vereisen. Deze kunnen
in de Engelstalige tekst in meer detail worden teruggevonden.

Fotochemische versus fotothermische ablatie

Fotochemische ablatie wordt veroorzaakt door electronische relaxatieprocessen die
rechtstreeks tot het verbreken van moleculaire bindingen leiden ('directe dissoci-
atie'). Het dissociatieproces kan gemodelleerd worden als

$$\frac{dn_b(x,t)}{dt}\bigg|_{dd} = k_{dd} \times n(x,t)$$

---

[1] Dit is een Nederlandse term voor het gebruikelijke 'fluence' (Eng.).

	193 nm (ArF)		248 nm (KrF)	
polymeer	F_{th} [mJ/cm^2]	α [μm^{-1}]	F_{th} [mJ/cm^2]	α [μm^{-1}]
PC	21.3	18.9	62.9	6.9
PET	18.4	15.6	36.9	6.6
PI	25.1	18.6	54.6	9.0
PMMA	33.9	6.3	272	1.0
PS	15.3	24.1	135.6	4.4

Tabel 2.1: Absorptiecoëfficiënten en ablatiedrempel berekend volgens het Beer model.

met n_b het aantal gebroken bindingen en n het aantal ongebroken bindingen. k_{dd} is de dissociatieconstante voor directe dissociatie.

Fotothermische ablatie volgt een identieke wet

$$\left.\frac{dn_b(x,t)}{dt}\right|_{th} = k_{th}(T) \times n(x,t)$$

maar ditmaal wordt de dissociatieconstante k_{th} bepaald door de temperatuur (Arrhenius uitdrukking). De vereiste temperatuur voor een snelle dissociatie wordt geleverd door warmteontwikkeling ten gevolge van interne conversie.

Het is niet altijd evident om bij een bepaald polymeer het primaire dissociatieproces te herkennen. Interpretatie van restproducten in de pluim en de snelheidsdistributie van deze deeltjes zal meestal wijzen op een thermisch dissociatiepad. Toch wordt de aanwezigheid van een fotodissociatieve reactie zelden uitgesloten.

Voor het uiteindelijke resultaat maakt het onderliggend dissociatieproces meestal niet veel uit. Zowel voor thermische als fotochemische dissociatie wordt materiaal verwijderd en is er weinig schade aan het rondliggend materiaal door de ontwikkelde temperaturen. In het geval van koude ablatie is deze stelling evident. Voor thermische dissociatie kunnen argumenten aangebracht worden die aantonen dat de warmteontwikkeling in het omliggend materiaal sterk gereduceerd wordt door het ablatieproces zelf.

De pulsduur speelt wel een rol bij thermische ablatie: hoe langer de puls duurt, hoe meer schade wordt berokkend aan het omringend polymeer. Merk op dat bij een te grote pulsduur (vanaf 1/10 van een milliseconde) de explosieve natuur van ablatie verloren gaat. Het erosieproces wordt dan louter een geleidelijke oppervlakteverdamping.

Bewegend ablatiefront en pluimabsorptie

Gezien materiaalejectie reeds plaatsvindt binnen een paar nanoseconden, treden absorptie- en ablatieprocessen bijna gelijktijdig op. Op het ogenblik dat een polymeerlaagje wordt geableerd, gaat het grotendeels over in gastoestand. Op dat moment veranderen de absorptie-eigenschappen. Een nauwkeurige modellering van het ablatieproces dient dan ook deze gewijzigde absorptie in rekening te brengen.

Thermische diffusie

In het Beer model wordt diffusie volledig verwaarloosd. Op een tijdsschaal van luttele nanoseconden heeft dit fenomeen inderdaad weinig invloed op de temperatuursdistributie, maar vanaf een paar tientallen ns wordt de thermische energie uitgespreid over een groter volume. Bij een langere pulsduur is dit proces verantwoordelijk voor de thermische schade aan het omringend materiaal.

Geldigheid van materiaalconstanten

Hoewel typische oppervlaktetemperaturen in de orde van 1600 K werden gemeten gedurende ablatie, maken theoretische modellen vaak gebruik van materiaalconstantes die gedefinieerd zijn bij kamertemperatuur. Meer nauwkeurige modellen maken gebruik van temperatuursafhankelijke materiaalparameters.

Absorptiesaturatie

Absorptie in het polymeer wordt veroorzaakt door een beperkt aantal chromoforen. Indien de fotondensiteit heel hoog wordt in het materiaal, kan de chromofoordensiteit in dergelijke mate dalen dat de absorptie vermindert. Voor excimeerlaserpulsen van meerdere ns, gebeurt dit enkel bij heel hoge pulsenergiedichtheden (in de orde van 10^1-10^2 J/cm^2).

Incubatie-effecten

Bij bepaalde laagabsorberende polymeren worden soms chemische veranderingen vastgesteld bij blootstelling aan excimeerpulsen. Deze veranderingen kunnen van die aard zijn dat de absorptie heel sterk toeneemt. Dit is bijvoorbeeld het geval bij PMMA dat een lage absorptie vertoont voor 248 nm. De eerste pulsen met een voldoende lage pulsenergiedichtheid zullen geen ablatie veroorzaken, maar wel het materiaal zo modifiëren dat het later wel begint te ableren.

2.2.2   Fotofysisch model

Een gesofistificeerd laserablatie-model is voorgesteld door Schmidt en co. in [4]. Het is een model dat alle besproken aspecten van absorptie, relaxatie en decompositie in rekening brengt en via een iteratieproces toelaat het verloop van deze processen te berekenen. Om deze reden wordt het dan ook een fotofysisch model genoemd. Een nadeel is de complexiteit van het model en daaruit volgend het groot aantal materiaal- en laserparameters die moeten gekend zijn om het ablatieproces te voorspellen.

We hebben dit model toegepast op de ablatie van polyimide met een ArF en KrF laser. Een goede overeenkomst tussen experiment en theorie werd vastgesteld bij parameterwaarden uit de literatuur. We verwijzen naar de Engelstalige tekst voor een uitgebreide beschrijving van dit model.

2.2.3 Polymer engineering

De absorptie in een polymeer wordt veroorzaakt door de aanwezigheid van chromo-foren in de molecule. Men kan zich terecht afvragen of het mogelijk is een bepaald polymeertype de gewenste ablatie-eigenschappen te geven door een geschikte func-tionele groep in te planten in de molecule.
Lippert en co. [34, 35] hebben uitgebreid onderzoek gedaan naar het effect van de triazene groep in laser resists. Deze bleek de absorptie van polymeren in het golflengtegebied 310-350 nm sterk te verhogen. Het resultaat is een resist die nauwkeurige ablatie met een XeCl laser (308 nm) toelaat.

In [36] werden gesegmenteerde polyurethanen voorzien van aromatische en alifa-tische groepen. Experimenteel werd vastgesteld dat het inbrengen van een aroma-tische groep in de polymeerketen de UV absorptie sterk verhoogde bij zowel de ArF als KrF golflengte.

Hoofdstuk 3

Microbewerking van polymeren met excimeerlasers

3.1 Excimeerlasers

In een excimeerlaser is het winstmedium een gasmengsel bestaande uit een edelgas (Ar, Kr of Xe) en een halogeen (F of Cl), verdund in een buffergas (Ne of He). Excimeerstraling wordt opgewekt door dissociatie van een geëxciteerde, diatomische molecule bestaande uit een halogeen- en edelgasatoom. De golflengte van het geëmitteerde licht hangt af van het exacte gasmengsel.

De gasexcitatie wordt verkregen via een elektrische ontlading in de lasercaviteit. Om deze reactie in ideale omstandigheden te laten doorgaan, dient heel wat technologie te worden aangewend om electrodespanningen tot tientallen kV te ontwikkelen en de gasontlading zo homogeen mogelijk te laten verlopen (pre-ionisatie).

De excimeerlaser die in deze thesis werd gebruikt voor het experimentele gedeelte, is een Lumonics PulseMaster 848. Deze laser is geschikt om verschillende golflengtes op te wekken naargelang het gasmengsel (tabel 3.1) en de gemiddelde pulsduur bedraagt 16 ns (FWHM). Het bundelprofiel is vrijwel uniform in de horizontale richting ('flat-top') en Gaussiaans in de verticale richting.

3.2 Laserablatie van materialen

3.2.1 Laserbewerking

Het bewerken van materialen met lasers biedt een aantal voordelen ten opzichte van de meer klassieke, vaak mechanische bewerkingstechnieken:

- Heel gelokaliseerde en afgemeten depositie van energie in het materiaal.
- Selectieve verwijdering via doseren van de energie.

	ArF	KrF	XeCl	XeF
golflengte [nm]	193	248	308	351
nominale pulsenergie [mJ]	230	450	300	275
gemiddeld optisch vermogen [W]	30	80	50	45
pulsfrequentie [Hz]	200	200	200	200
FWHM pulsduur [ns]	12-20			
bundelafmetingen [mm × mm]	12 (V) × 25 (H)			
bundeldivergentie [mrad × mrad]	1 (V) × 3 (H)			

Tabel 3.1: PM 848 output specificaties.

- Minimale thermische schade aan omringend materiaal.

- 'Koude' bewerking mogelijk in polymere materialen.

- Heel geschikte techniek voor delicate stukken en ingewikkelde bewerkings-patronen.

- Geen fysisch contact met het te bewerken stuk.

- Geen slijtage zoals bij mechanisch gereedschap.

- Een brede waaier aan materialen is geschikt voor laserbewerking.

- Snelle prototyping is mogelijk.

- Chemische stoffen zijn niet vereist voor de meeste lasertechnieken, in het bijzonder voor laserablatie.

Een bijzondere laserbewerkings-methode die in deze thesis wordt behandeld, is laserablatie. Deze techniek vereist het gebruik van gepulste lasers omwille van de hoge piekintensiteiten die nodig zijn om lokaal een materiaallaagje te verwijderen. Populaire laserbronnen zijn hierbij CO_2, Nd:YAG en excimeerlasers.

Omwille van voorvermelde eigenschappen van laserbewerking worden lasers met succes ingezet in een waaier van toepassingen. Meer concreet wordt ablatie met excimeerlasers commercieel aangewend voor het boren van inkjet printkoppen, fabricatie van microscopische transportbuisjes voor vloeistoffen (lab-on-chip), oog-correcties (LASIK), mantelstrippen van vezels en kabeltjes, boren van microvia's en gepulste laserdepositie. Andere niet-ablatieve toepassingen betreffen het aan-maken van roosterstructuren in optische vezels (Bragg roosters) en uitgloeien van TFT beeldschermen.

3.2.2 Ablatiestrategieën

Om laserablatie te veroorzaken, dient de laserbundel te worden geconcentreerd om voldoende intensiteit te bekomen. Dit kan op twee manieren worden bereikt zoals aangegeven in figuur 3.1.
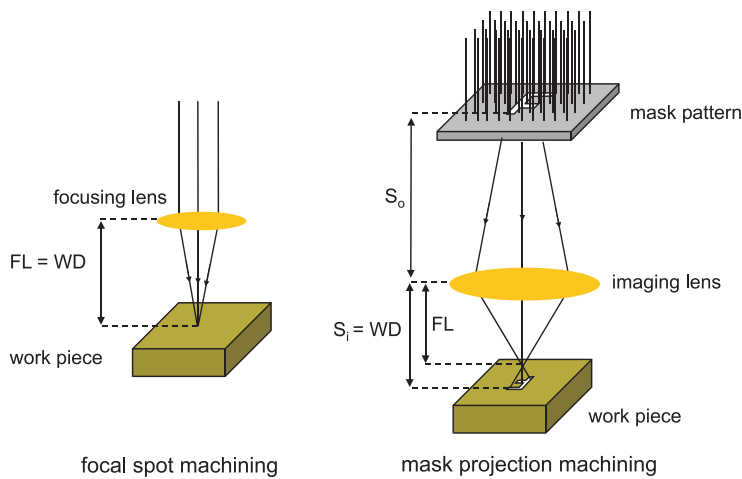
Figuur 3.1: Ableren met een gefocusseerde spot of via maskerprojectie.

Ableren met een gefocusseerde spot (direct-write)

Met een lens wordt de bundel herleid tot een minieme spot in het focale vlak. De kleinste spots worden verkregen voor bundels die een Gaussiaans profiel hebben zoals bij een CO_2, Nd:YAG en Ti:Saffier laser. Hoe kleiner de spot, hoe groter de vermogensdichtheid in het focale vlak.

Bij het ontwerp van het optisch systeem dient een compromis te worden gevonden tussen enerzijds de maximaal aanvaardbare spotgrootte en anderzijds een minimale afstand tussen lens en te bewerken stuk (bescherming optiek).

Ableren via maskerprojectie

Een andere aanpak is gebaseerd op het afbeelden van een maskerpatroon op het te bewerken stuk. Vanaf een bepaalde verkleining zal de intensiteit ter hoogte van het beeldvlak voldoende groot zijn om laserablatie te verkrijgen. Gezien een zo uniform mogelijke bundel is gewenst, worden excimeer en TEA CO_2 lasers vaak in deze situatie gebruikt. Merk op dat maskerprojectie bij sterke verkleining van een eenvoudige circulaire apertuur heel dicht een gefocusseerde spot benadert.

Ter volledigheid vermelden we hier nog dat in sommige systemen gebruik wordt gemaakt van optische vezel in plaats van spiegels en lenzen om de bundel naar de vereiste locatie te transporteren.

3.2.3   Optec Micromaster

Dit toestel bevat de nodige optiek om via projectie een maskerpatroon af te beelden op een materiaaloppervlak. De verkleining kan vrijwel traploos ingesteld worden tussen $4\times$ en $11\times$ door gemotoriseerde verplaatsing van spiegeltjes en projectielens.

polymeer	193 nm			248 nm		
	0.1 J/cm^2	0.3 J/cm^2	1 J/cm^2	0.1 J/cm^2	0.3 J/cm^2	1 J/cm^2
PC	0.078	0.145	0.204	0.073	0.232	0.406
PET	0.104	0.184	0.254	0.168	0.308	0.511
PI	0.075	0.135	0.197	0.086	0.183	0.331
PMMA	0.182	0.342	0.536	-	0.042	1.268
PS	0.074	0.126	0.173	-	0.177	0.438

Tabel 3.2: Ablatiesnelheden (in μm/puls) bij een paar typische waarden voor F, gemeten bij 20 Hz en uitgemiddeld over 20 pulsen.

Deze laatste bestaat uit 3 aparte lenzen in eenzelfde behuizing en verzekert een optische resolutie van $\sim$1.5 μm. Gekoppeld aan een Lumonics PM848 levert dit toestel tot 15 J/cm^2 energiedichtheid in het beeldvlak bij 248 nm. Een attenuator bestaande uit een draaibaar opgesteld kwartsplaatje dient om de energiedichtheid te regelen.

3.3 Laserablatie van polymeren met een excimeerlaser

In deze sectie wordt een reeks eigenschappen van microbewerking met excimeerlaserablatie besproken. Deze werden experimenteel onderzocht voor 5 polymeertypes: polycarbonaat (PC), polyethyleentereftalaat (PET), polyimide (PI), polymethylmetacrylaat (PMMA) en polystyreen (PS) bij 193 nm en 248 nm. Voor een gedetailleerde beschrijving verwijzen we naar de Engelstalige tekst.

3.3.1 Etsdiepte per puls

Zoals reeds in hoofdstuk 2 aangehaald, verloopt de ablatiediepte per puls vrijwel logaritmisch in functie van de pulsenergiedichtheid. Typische ablatiesnelheden bij beide golflengtes staan in tabel 3.2 weergegeven.

3.3.2 Ablatie met meerdere pulsen

Bij het aanmaken van structuren met laserablatie worden meestal meerder pulsen afgevuurd op hetzelfde oppervlakje om een grotere diepte te bekomen. Bij een vaste pulsfrequentie kan dit bekomen worden door dit oppervlakje gedurende een bepaalde tijd bloot te stellen aan de laserbundel. Men kan zich terecht de vraag stellen of de ablatiesnelheid constant blijft gedurende deze tijd. Met andere woorden, is de volle etsdiepte evenredig met het aantal pulsen. In figuur 3.2 worden twee voorbeelden gegeven. In het ene geval is er duidelijk een lineair patroon en kan de etsdiepte afgeleid worden uit het aantal pulsen bij eenzelfde pulsenergiedichtheid
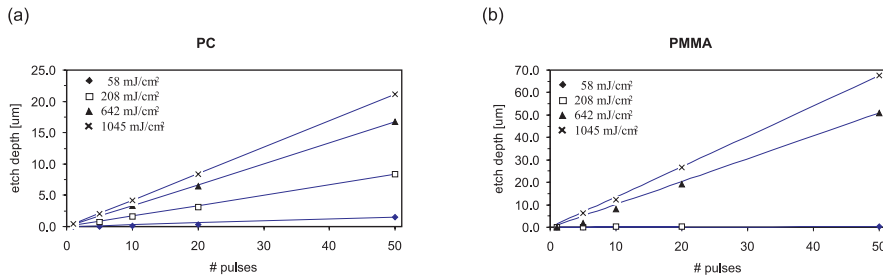
Figuur 3.2: Verloop van de ablatiediepte met het aantal pulsen bij 248 nm voor PC (a) en PMMA (b).

(geval a, PC). Bij PMMA (geval b) is er voor de hoogste energiedichtheid weliswaar ook een lineair verloop, maar voor lagere F spelen incubatie-effecten een belangrijke rol. Deze zorgen ervoor dat de ablatiediepte niet eenduidig bepaald is door het aantal pulsen.

3.3.3 Repetitiesnelheid

Deze parameter is vooral belangrijk om de verwerkingscapaciteit van laserablatie in een productieomgeving te bepalen. Hogere pulssnelheden leiden immers tot snellere fabricatie.

Experimenteel werd de ablatiesnelheid gemeten bij verschillende pulsfrequenties. Bij alle polymeren behalve PMMA bleek de ablatiesnelheid vrijwel onafhankelijk van de pulsfrequentie. De toenemende etssnelheid van PMMA bij hogere pulsfrequenties in KrF regime kan worden toegeschreven aan een cumulatieve opwarming van het materiaal. De hogere temperatuur geeft vervolgens aanleiding tot een grotere thermische dissociatie en dus snellere ablatie.

3.3.4 Opwarming van het substraat

In de literatuur zijn schattingen gegeven voor de oppervlaktetemperaturen van polymeren tijdens ablatie. Deze zijn voor PI en PMMA respectievelijk 1500 K en 600 K. Dergelijke temperaturen kunnen ertoe leiden dat omringend materiaal thermisch wordt beschadigd gedurende ablatie.

Na ablatie van een materiaallaagje blijft er een zone achter die een onvoldoende gedeelte van de puls heeft geabsorbeerd om te worden geëjecteerd. De thermische energie die in deze laag werd gedeponeerd, is evenredig met F_{th}. Dit betekent dat polymeren met een hoge ablatiedrempel behoorlijk kunnen opwarmen door deze restfractie van de pulsenergie. In de praktijk blijken dit polymeren te zijn die eveneens een lage absorptiecoëfficiënt vertonen zoals PMMA en teflon.
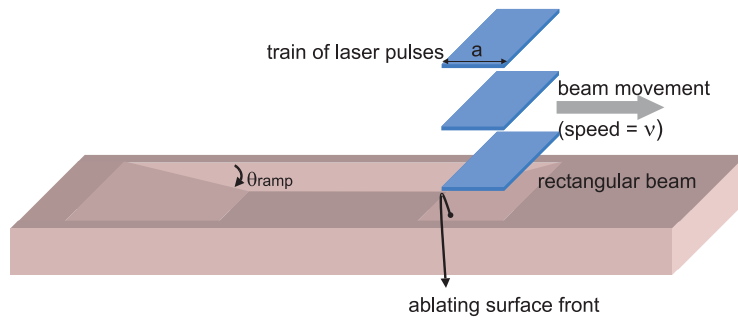
Figuur 3.3: Aanmaken van een groef via translatie van de laserbundel gedurende het afvuren van een pulstrein.

3.3.5 Caviteitsprofiel

Lasergeableerde caviteiten in polymeren vertonen wanden die gewoonlijk een 5 tot 20 graden afwijken van de verticale voor pulsenergiedichtheden tussen 0.1 en 1.5 J/cm^2. Hoe hoger de laserintensiteit, hoe kleiner deze wandhoek.

3.3.6 Dynamische ablatie

In de meeste toepassingen van laserablatie dient de laserbundel te worden bewogen over het materiaaloppervlak om de volledige structuur te kunnen aanmaken. De lokale ablatiediepte wordt dan bepaald door de translatiesnelheid en de bundel-grootte. Voor een rechthoekige laserspot met een lengte a (langsheen de translatie-as) die beweegt met een constante snelheid v, kan men de lokale ablatiediepte schatten op

$$depth = d\frac{fa}{v}$$

met d de etsdiepte per puls en f de pulsfrequentie.

Een dergelijke beweging van de laserbundel ableert een groef met een helling aan de start- en stopplaats van de bundel. In werkelijkheid vertonen deze helling een trapjesprofiel met stapbreedte v/f door het discreet karakter van gepulste laser-ablatie. Indien deze stapbreedte kleiner is dan de resolutie van het ablatieproces, kunnen de opeenvolgende pulsen niet meer van elkaar worden onderscheiden en verkrijgt men een glooiend oppervlak.

Gedurende de beweging van de gepulste laserbundel maakt het onderliggend op-pervlakje een hoek θ met de horizontale (figuur 3.3). Naarmate diepere groeven worden geableerd, zal deze hoek steeds groter worden. Experimenteel werd vast-gesteld dat een goede bodemkwaliteit van de geableerde strook een kleine θ vereist, typisch lager dan 10 graden.

3.3.7 Diepte en resolutie van de laserbewerking

Door de aanwezigheid van de niet-verticale wanden is de ablatiediepte beperkt. Zo kan men stellen dat voor geableerde gaten met een opening van 100 μm en een wandhoek van 5 graden, de maximale ablatiediepte 600 μm is. Merk op dat in de praktijk dergelijke afstanden de focusdiepte vele malen overschrijden.

De resolutie van het laserablatie-proces geeft vaak aanleiding tot verwarring, meestal gevoed door onrealistische verwachtingen betreffende de minimale feature sizes. In tegenstelling tot diepe UV lithografie die geometrische patronen ter grootte van 0.1 μm kan genereren, is excimeerlaser-ablatie een veel 'ruwer' proces waarbij de kleinste features gewoonlijk nog steeds laterale afmetingen ter grootte van 1 μm of meer hebben. De oorzaak is tweeërlei: enerzijds dient de optiek een voldoende ruime werkafstand te respecteren en wenst men een zo groot mogelijke focusdiepte. Daardoor wordt vaak gekozen voor een kleine numerieke apertuur die echter ook tot een lagere resolutie leidt. Anderzijds gebeurt ablatie vaak (gedeeltelijk) via thermische dissociatie. De onvermijdelijke diffusie van thermische energie kan de resolutie van het ablatieproces eveneens verminderen.

3.3.8 Oppervlakteruwheid van de geableerde caviteit

De bodem van een geableerd putje is niet perfect vlak maar vertoont een zekere oppervlakteruwheid. Experimenteel werd vastgesteld dat de bodemkwaliteit bij PC, PI en PS vergelijkbare resultaten oplevert (typisch een 200 nm rms ruwheid voor een caviteit van 40 μm diep of 0.5 % van de totale diepte), terwijl PET en vooral PMMA een grotere ruwheid vertonen bij KrF.

3.3.9 Debris

Bij laserablatie wordt het vaste materiaal niet steeds volledig omgezet naar gasvormige toestand vooraleer het geëjecteerd wordt. Dit betekent dat er zich in de pluim macroscopische partikels kunnen bevinden die veel zwaarder zijn dan hun gasvormige soortgenoten. Het resultaat is dan ook dat deze deeltjes snel terugvallen op en rond het geableerde oppervlak. Deze neerslag wordt debris genoemd. Hoewel debris vrijwel onvermijdelijk is, kunnen een aantal maatregelen genomen worden om de neerslag te minimaliseren: het gebruik van een vacuümkamer blijkt heel efficiënt. Een kwartsvenster wordt gebruikt om de bundel toegang te verschaffen tot het substraat in de kamer. Een laterale gasstroom (bij voorkeur helium) wordt gebruikt om te voorkomen dat de pluim neerslaat op dit kwartsvenster.

3.4 Prototypefabricatie van microstructuren met excimeerlaser-ablatie

In de onderzoeksgroep Fotonica werd excimeerlaser-ablatie met succes aangewend voor prototypefabricatie van een aantal structuren waarvan sommige in figuur 3.4 worden gegeven:
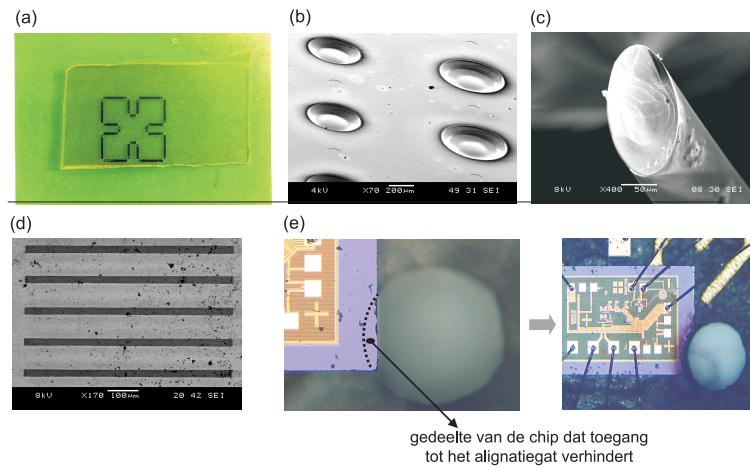
Figuur 3.4: Prototype microstructuren aangemaakt in de vakgroep Informatietech-nologie.

- Microscopisch klaverblad in GaN op een saffiersubstraat voor Hall-metingen.

- Mastertool voor chipalignatie [22] (zie hoofdstuk 5).

- 2D-connector voor plastic optische vezel [23, 25, 24] (zie hoofdstuk 5).

- Microlenzen [26, 27, 28] (zie hoofdstuk 6).

- Definitie van structuren in dunne lagen polymeren met bioanalyse- en sen-sortoepassingen [29, 31, 30].

- Klieven van optische vezels [32].

- Op maat (uit)snijden van patronen [33].

De toepassingen met betrekking tot klaverbladsnijden en mastertoolfabricatie gebeur-den in samenwerking met de Opto-Electronische Technologiegroep van INTEC.

Hoofdstuk 4

Laserablatie van refractieve microlenzen in plastic

4.1 Inleiding

Er bestaan verscheidene technieken om microlenzen aan te maken in halfgeleidermaterialen, plastics en glastypes. Deze zijn gewoonlijk gebaseerd op fotothermische zwelling, thermische reflow van resistlagen, schrijven met een laserstraal in een resist, microjet printing, diepe lithografie met protonen, laserablatie of een combinatie van voorgaande. In de Engelstalige tekst kan een vrij volledig overzicht van deze technieken worden gevonden, samen met een beknopte beschrijving van de optische eigenschappen die microlenzen bezitten.

4.2 Lenskarakterisatie

Karakterisatie en evaluatie van microlenzen vereisen een aantal criteria om de kwaliteit van microlenzen te bepalen. Enerzijds hebben deze betrekking op de transparantie van het substraatmateriaal en de afwerking van het lensoppervlak (ruwheid geeft aanleiding tot verstrooiing). Anderzijds bestaan er ook maatstaven voor de afbeeldende eigenschappen van de microlens. Een bijzondere regel is Maréchal's criterium dat stelt dat de lens als diffractie-gelimiteerd kan beschouwd worden indien de rms (root-mean-square) waarde van de aberraties kleiner is dan $\lambda/14$ (λ is de golflengte). Deze aberraties geven de fasefouten weer die in het golffront aan de exit pupil van de lens aanwezig zijn.

De meetinstrumenten die werden gebruikt voor de lenskarakterisatie zijn een electronenmicroscoop (SEM), een contactloze oppervlakteprofilometer (Wyko) en een optische microscoop voor oppervlaktemetingen, en een Mach-Zehnder interferometer voor de aberraties. De aberratie- en Wyko metingen werden uitgevoerd in de laboratoria van het departement Toegepaste Natuurkunde en Fotonica, Vrije Universiteit Brussel.
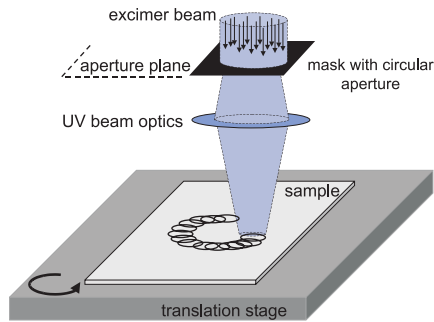
Figuur 4.1: Laserablatie van groeven in een polymeer met de omtrekscan-techniek.

4.3   Omtrekscan-techniek

De fabricatietechniek voor lenzen die in deze thesis wordt beschreven, is ontwikkeld in onze vakgroep. Er wordt gebruik gemaakt van excimeerlaser-ablatie met een eenvoudige circulaire apertuur in het maskervlak, typisch een 100 μm in diameter. Terwijl de laser met een constante repetitiefrequentie pulsen afvuurt op een polymeersubstraat, maakt deze laatste opeenvolgende cirkelvormige bewegingen met verschillende diameters (figuur 4.1). Gedurende deze beweging is de contoursnelheid van de translatietafel constant. Op deze manier wordt in het polymeer een reeks cirkelvormige groeven geableerd die met elkaar kunnen overlappen. Merk op dat tussen twee cirkelvormige bewegingen de tafel zich moet verplaatsen naar een nieuwe startpositie voor de volgende contour. De pulstrein van de laser wordt gedurende deze tijd dan ook telkens even onderbroken.

Elke contourbeweging is bepaald door een contoursnelheid v en diameter D. Een algoritme gebaseerd op 'simulated annealing' werd ontwikkeld om een set van dergelijke contouren te zoeken die bij superpositie een gewenste, cirkelsymmetrische lensvorm in het polymeer ableren.

Na ablatie van deze contourset vertoont het polymeer een oppervlak dat dicht aanleunt tegen de gewenste vorm, maar waarin de afzonderlijke ablatieputjes nog steeds kunnen worden onderscheiden. Dit is een natuurlijk gevolg van het discrete karakter van gepulste ablatie. Om de oppervlaktekwaliteit te verbeteren, wordt gebruik gemaakt van een grote bundelapertuur die de lens volledig bedekt. Vervolgens wordt de lens dieper in het polymeer geableerd. Gezien bij het ablatieproces in zekere mate thermische effecten optreden, kan op die manier een glooiend lensoppervlak verkregen worden.

Een theoretische analyse van de omtrekscan-techniek is gegeven in de Engelstalige tekst.
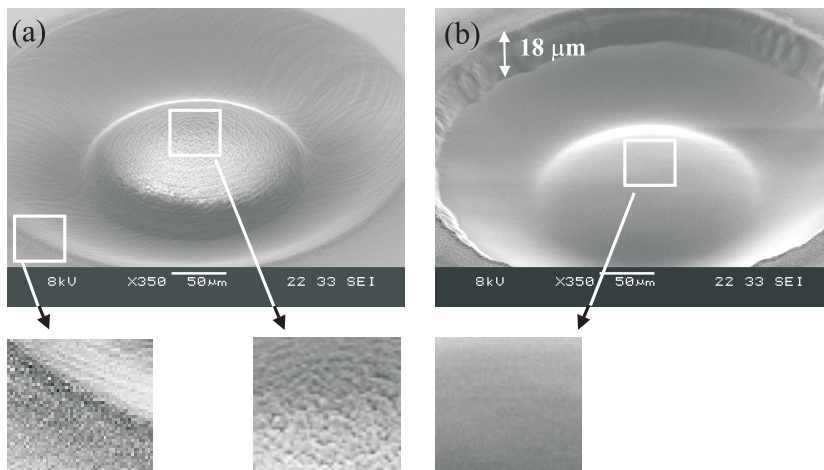
Figuur 4.2: Microlens met R=800 μm in polycarbonaat na het omtrekscannen (a) en na het glooien van het oppervlak (b).

4.4 Fabricatie van sferische microlenzen

Bovenstaande techniek werd met succes gebruikt om sferische microlenzen aan te maken met de ArF excimeerlaser in polycarbonaat. Daartoe werd het polymeer-plaatje gemonteerd in de vacuümkamer die zich op de translatietafel bevindt.

Via simulated annealing werd een contourset berekend voor een reeks sferische lenzen met eenzelfde diameter (200 μm), maar met een verschillende kromtestraal. Telkens werd dezelfde apertuur gebruikt (100 μm diameter spotgrootte). Vervolgens werden de lenzen geableerd en glooiend gemaakt zoals beschreven in de vorige sectie. Het resultaat is een microlens zoals afgebeeld in figuur 4.2. De typische fabricatietijd is 1 tot 10 minuten naargelang de kromtestraal.

Een uitgebreide bespreking van de fabricatietoleranties op basis van aberratie-metingen valt buiten het kader van deze samenvatting. We geven hier dan ook slechts de conclusies van de lenskarakterisatie:

- Hogere pulsenergiedichtheden leiden niet alleen tot een kortere fabricatietijd, maar geven ook aanleiding tot meer aberraties (inclusief een grotere sprei-ding) bij lenzen met een grote $F/\#$. Bij lenzen met een hoge numerieke apertuur is dit effect niet zo meetbaar.

- De repetitiesnelheid van de laser tijdens fabricatie speelt weinig rol voor de lensaberraties. Voor een bereik van 20 tot 80 Hz werden er geen meetbare verschillen in lenskwaliteit vastgesteld.

- Op theoretische wijze werd aangetoond dat er een optimaal bereik voor omtreksnelheden van de tafel bestaat ($v_{max} < 150$ μm) op basis van een een-voudig ablatiemodel. Experimenteel werd vastgesteld dat verdere verhoging

35

van de omtreksnelheid inderdaad aanleiding geeft tot een hogere spreiding van de rms aberraties.

Tenslotte hebben metingen van het lensoppervlak met de profilometer aangetoond dat de rms waarden voor de oppervlakteruwheden typisch tussen 21 en 105 nm bedragen. Lenzen met $R > 400$ μm vertoonden ruwheden beneden 30 nm. De gemeten profielen hadden een kromtestraal die gemiddeld slechts 3 % afweek van de gewenste waarde.

4.5   Niet-sferische lenzen en lensrijen

De omtrekscan-techniek biedt twee belangrijke voordelen. Ten eerste zijn de mogelijke lensvormen niet beperkt tot sferische profielen. Experimenteel werd aangetoond dat parabolische en kegelvormige structuren eveneens tot de mogelijkheden behoren. Ten tweede kan de enkelvoudige apertuur in het maskervlak vervangen worden door een (tweedimensionele) rij van aperturen. Op die manier wordt een (tweedimensionele) rij van lenzen aangemaakt binnen dezelfde tijdspanne die nodig is om een enkele lens te ableren. In figuur 4.3 zijn een aantal voorbeelden gegeven.
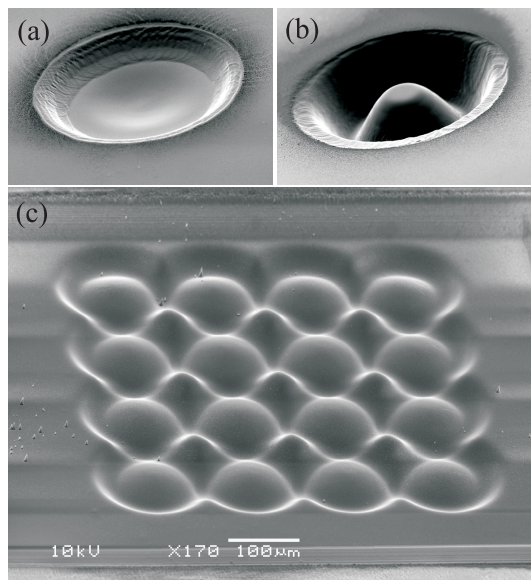
Figuur 4.3: Niet-sferische en niet-convexe lensvormen die met de omtrekscan-techniek werden aangemaakt: concave lens (a), parabolische lens met een vlakke top (b) en een 4×4 lensrij (c).

Hoofdstuk 5

Excimeerlaser-ablatie van structuren voor fotonische toepassingen

5.1 Inleiding

Excimeerlaser-ablatie is binnen de onderzoeksgroep Fotonica aangewend om alignatiestructuren aan te maken die gebruikt werden voor optische doeleinden. Laserablatie is niet de enige techniek die in staat is dergelijke componenten te realiseren op micrometerschaal, doch het gebruik van deze geavanceerde technologie biedt een aantal inherente voordelen. Zo treedt er geen fysisch contact op met het te bewerken materiaal en komen er geen chemische substanties aan te pas. Bovendien laat laserablatie toe om in een heel laat stadium in te grijpen in de montage van een heterogene opto-electronische module om bijvoorbeeld microlensjes op een vrij oppervlak aan te brengen. Weinig andere fabricatietechnieken kunnen deze voordelen aanbieden. Een lijst van concurrerende technieken kan worden teruggevonden in de Engelstalige versie.

In dit hoofdstuk worden 2 componenten besproken: een ferrule voor tweedimensionele rijen van plastic optische vezels en een mastertool.

5.2 Prototypefabricatie van een ferrule voor 2D rijen van plastic optische vezel

We hebben reeds in hoofdstuk 1 het belang onderstreept van parallelle optische interconnecties. Daarbij wordt de voorkeur gegeven aan 2D rijen van optische verbindingen gezien typische bronnen zoals VCSELs en MCLEDs ook in deze configuratie voorkomen. Om dergelijke links te voorzien van lichtgeleidende structuren
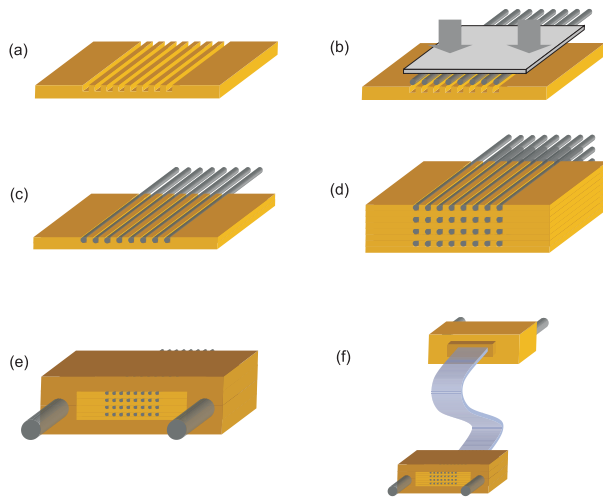
Figuur 5.1: Montageproces van de ferrule (a)→(d). Integratie van de ferrule in een connectorbehuizing met alignatie-elementen (e)→(f).

("guided wave approach") is er nood aan een geschikt golfgeleidertype en aan connectoren voor rijen van golfgeleiders. Voor korte afstanden (tot enkele meters) is plastic optische vezel een heel bruikbare en goedkope commerciële golfgeleider voor dergelijke doeleinden. De connector is een andere zaak: momenteel bestaan er geen commercieel beschikbare types die 2D rijen van vezels kunnen huizen. In deze sectie bespreken we de prototypefabricatie van een dergelijke 2D connector, geschikt om 4×8 vezels te connecteren.

5.2.1 Montage

De basisstructuur van de ferrule is een polymeerplaatje waarin een rij van 8 groeven is aangebracht, welke is gefabriceerd met excimeerlaser-ablatie. In deze groeven worden plastic optische vezels ingebracht langs de bovenzijde en vervolgens met een UV-hardende lijm vastgekleefd. Aan één zijde van het plaatje met de vezelrij wordt een vlak facet verkregen door snijden met een mesje op 100 °C.

Tenslotte worden verschillende plaatjes gestapeld boven elkaar met een 'virtuele alignatietechniek' die beschreven staat in de Engelstalige versie. Na verlijming bekomt men een 2D ferrule die enkel nog een finale polijststap vereist om een facet van optische kwaliteit te bekomen. Figuur 5.1 illustreert deze montagestappen.

5.2.2 Fabricatie van de groevenrij in polymeerplaatjes

Als substraatmateriaal voor de plaatjes werd PC en PMMA gekozen. Beide materialen genieten de voorkeur omwille van hun ablatie-eigenschappen. De groefstructuur die in deze plaatjes wordt aangemaakt, bestaat uit een rij van 8 groeven,
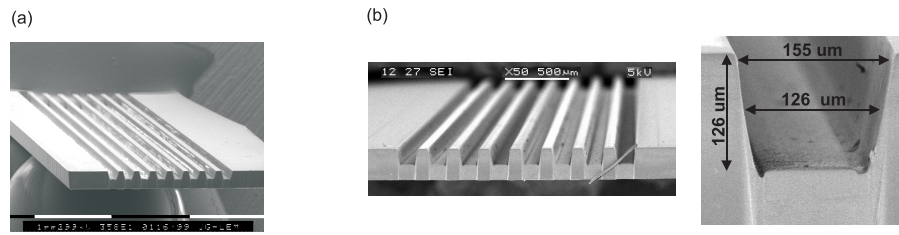
Figuur 5.2: Groevenrij aangemaakt met apertuurscannen (a) en hybride masker-projectie (b).

	F [mJ/cm^2]	d [μm/puls]	materiaal	fabricatietijd
apertuurscannen	180	0.150	pc	12 uur
hyb. maskerprojectie	270	0.215	pmma	20 min.

Tabel 5.1: Apertuurscantechniek en hybride maskermethode.

elk 125 μm diep en op een onderlinge afstand van 250 μm. De openingsbreedte is zo gekozen dat deze groeven op halve diepte even breed zijn als de vezels (op een kleine extra ruimte voor lijm na). Deze structuur werd op verschillende manieren aangemaakt.

- Scannen met vierkante bundelapertuur of laserspot

Deze techniek vereist geen specifiek maskerontwerp; een eenvoudige vierkante apertuur volstaat om de groeven aan te maken. De breedte van de apertuur stemt overeen met de groefbreedte en door het bewegen van het substraat gedurende de opeenvolgende ablatiepulsen wordt een groef getrokken in het polymeer. Elke groef wordt tot 125 μm diep geableerd door meerdere passages. Als een groef klaar is, transleert de tafel 250 μm opzij en een nieuwe groef wordt begonnen. De fabricatie van de gehele groevenrij neemt heel veel tijd in beslag, in de orde van meerdere uren.

- Hybride maskerprojectiemethode

Om de fabricatietijd te reduceren, werd een masker ontworpen waarop zich 4 rechthoekige aperturen bevinden. De lengte en het aantal van deze aperturen is gelimiteerd door de beperkte apertuur van de projectielens. Het masker bestaat uit Suprasil 1 (kwarts) met een lithografisch gedefinieerd metaalpatroon.
Beide methodes zijn gebruikt om groefrijen te verkrijgen in respectievelijk PC en PMMA: tabel 5.1 geeft een overzicht en figuur 5.2 illustreert de resultaten.

Experimenteel werden een aantal vaststellingen gemaakt: PMMA ableert heel snel bij 248 nm door zijn lage absorptie, maar dit gaat gepaard met een verhoogde

(a)   (b)
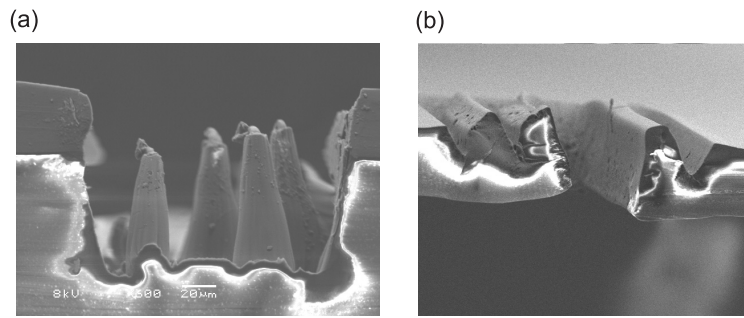
Figuur 5.3: ArF ablatie van PC met apertuurscannen (a): redepositie van macroscopische partikels die het onderliggend oppervlak maskeren voor de laserbundel. Het gevolg is vorming van kegelvormige structuren op de bodem. KrF ablatie van PMMA met hybride maskertechniek (b) bij 690 mJ/cm^2 met 100 Hz repetitiesnelheid.

ruwheid van het oppervlak; tijdens ArF ablatie blijkt de bodemkwaliteit dan weer uitstekend. Bij polycarbonaat zien we net het omgekeerde: bij 193 nm wordt heel veel debris geproduceerd die verdere ablatie vaak hindert (figuur 5.3); KrF ablatie vertoont deze moeilijkheden niet.

De keuze van de laserintensiteit (of equivalent: de ablatiesnelheid) en repetitiesnelheid is niet zo belangrijk. Zolang beide parameters niet te groot worden gekozen (figuur 5.3) stellen zich geen problemen en wordt de fabricatietijd verder ingekort. Om deze reden werd steeds gewerkt bij energiedichtheden kleiner dan 300 mJ/cm^2 en pulsfrequenties tot 50 Hz, hoewel de exacte grenzen voor nauwkeurige fabricatie niet werden onderzocht.

Tenslotte werd experimenteel vastgesteld hoeveel passages nodig waren om de beste groeven te produceren in termen van bodemruwheid. Bij de apertuurscantechniek bleek een minimum van 3 bewegingen vereist terwijl in het geval van de hybride maskermethode weinig verschil werd gemerkt tussen het aantal passages. De oorzaken van deze vaststellingen kunnen worden teruggevonden in de Engelstalige versie.

5.2.3   Experimentele resultaten

Na stapeling van de plaatjes werden de posities van de vezels in de matrix experimenteel geverifieerd. Zoals kan worden vastgesteld in de tabel, werden twee soorten plastic optische vezels gebruikt: Toray vezels met een 116 μm kern en Asashi met een 63 μm kern. Beide hebben een nominale manteldiameter van 125 μm.

Uit tabel 5.2 volgt dat de standaardafwijking op de vezelkernposities in een rij behoorlijk groot is. Daarbij dient men rekening te houden met het feit dat Asashi een prototype vezel is met een grote standaardafwijking op de vezeldiameter. De betere resultaten in geval van de commerciële Toray bevestigen dit probleem.

POF	stapel	pitch in X richting		pitch in Y richting	
		streefwaarde	gemeten	streefwaarde	gemeten
125/63	4×8	250	249 ± 10	250	246 ± 11
125/116	2×8	250	248 ± 6	280	279.5

Tabel 5.2: Gemeten positionele nauwkeurigheden van de vezelkernen in een stapel plaatjes, uitgedrukt in μm. Merk op dat de doelwaarde voor de Y pitch bij de tweede stapel 280 μm was door een afwijking op de dikte van de plaatjes. Figuur 5.4 geeft de betekenis van de tabelwaarden weer.
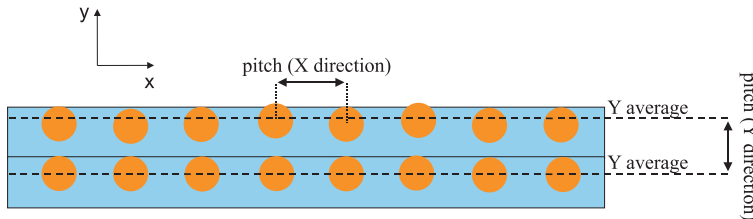
Figuur 5.4: Definitie van de parameters in tabel 5.2.

5.3 Fabricatie van een mastertool voor alignatie van een VCSEL-chip

Met excimeerlaser-ablatie werd een microcomponent gefabriceerd om alignatie van een VCSEL-chip met een MT connectorhouder mogelijk te maken.

5.3.1 Opbouw van de module

Een MT connector met een 1×8 rij van plastic fibers (Toray 125/116) kan in en uit een heterogene optoelectronische assembly geplugd worden. Deze laatste bestaat uit een keramische drager waarop een VCSEL chip is gemonteerd. Vervolgens wordt rondom de chip een spacer aangebracht die voorzien is van twee alignatie-gaten waarin de pinnen van de MT connector passen. Voor een goede werking van de module dient de spacer nauwkeurig gealigneerd te worden met de VCSEL chip. Daartoe werd een mastertool gefabriceerd in polycarbonaat. Deze bevat alignatiefeatures die de chippositie ten opzichte van de spacer vastleggen.

5.3.2 Fabricatie van de mastertool met laserablatie

De mastertool staat afgebeeld in figuur 5.5. Twee gaten met een diameter van 700 μm en met een spatiëring van 4.6 mm dienen om met behulp van MT con-nectorpinnen de spacer vast te houden. Via een bijkomend gat in het midden van de mastertool, wordt de chip vastgehouden met een vacuümaanzuiging eenmaal de
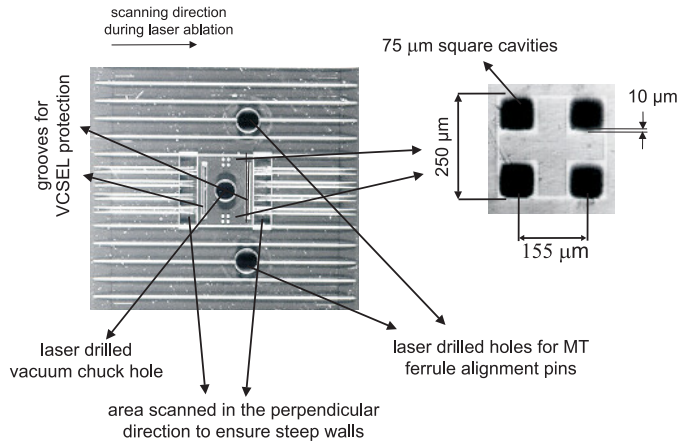
Figuur 5.5: Lasergeableerde mastertool in een PC plaatje met een dikte van 250 μm. De fabricatie gebeurde met een KrF excimeerlaser bij 10 Hz.

spacer en chip gealigneerd zijn. Twee patronen die elk bestaan uit 4 ondiepe gaatjes met een vierkante geometrie worden gebruikt om nauwkeurige alignatie met de chip te verkrijgen. Doordat de bovenzijde van de spacer 50 μm uitsteekt boven de chip (bescherming van de fragiele opto-electronica), werd een eiland geableerd in de mastertool. Op deze manier kunnen de aligneringspatronen vlak op de alignatiekruisen van de chip vergeleken worden. Zoniet zou het diepteverschil de alignatie via de camera bemoeilijken (beperkte scherptediepte bij een vergroting van 300×). Additionele groeven in dit eiland voorkomen dat de VCSELs worden beschadigd bij contact tussen chip en mastertool.

5.3.3   Experimentele resultaten

Bij montage van de spacer rond de chip werd een alignatienauwkeurigheid bekomen tussen 5 en 10 μm naargelang de vergroting op de camera. De assembly werd met twee verschillende mastertools uitgevoerd. Het ene type is, zoals hierboven besproken, met laserablatie gefabriceerd. Het andere met een mechanische techniek (microdrilling) waarbij er geen centraal eiland is voorzien. Experimenteel werd vastgesteld dat de tolerantie en de randkwaliteit van de alignatiestructuurtjes op het lasergeableerde stuk veel beter waren dan bij de niet-geableerde mastertool. De reden is tweeërlei: enerzijds kan de camera niet focusseren op de alignatiestructuren van de chip en de mechanisch geboorde mastertool tegelijkertijd. Aan de andere kant waren de geboorde features gevoelig voor afkruimelen van het materiaal.

De koppelverliezen van VCSEL naar plastic vezel werden geraamd op 1 tot 1.4 dB. Indien de facetreflecties, NA mismatch en plastic vezelverliezen in rekening worden gebracht, kan men stellen dat verliezen door misalignatie verwaarloosbaar zijn.

Hoofdstuk 6

Fabricatie van microlenzen voor vezel-naar-vezel koppelingen

6.1 Inleiding

Reeds in het eerste hoofdstuk werd het belang van rendabele optische interconnecties met lage verliezen tussen chips en/of vezels beklemtoond. In dit hoofdstuk gaan we dieper in op de koppeling tussen twee single-mode vezels.

Voor enkelvoudige semi-permanente vezelverbindingen bestaan op dit ogenblik heel geschikte commerciële oplossingen: ST, SC en FC connectoren. Gezien optische interconnects een steeds hogere datahoeveelheid dienen te verwerken en gezien deze stromen vaak in parallel gebeuren, is er een groeiende nood aan connectoren die meerdere vezels tegelijkertijd huizen. Hier wringt het schoentje wel eens: MT ferrules kunnen weliswaar rijen van vezels met elkaar verbinden, doch deze componenten zijn beperkt tot 1-dimensionele vezelrijen, moeten voldoen aan heel strenge fabricatietoleranties en zijn heel gevoelig voor stofdeeltjes. Echte 2-dimensionele connectoren zijn commercieel niet beschikbaar.

In dit hoofdstuk zullen we het gebruik van microlenzen in de connectordelen onderzoeken en bekijken hoe deze componenten de alignatietoleranties kunnen vergroten en dus de betrouwbaarheid verbeteren. De betreffende koppelefficiënties en bijhorende toleranties worden met Gaussiaanse optica berekend.

Daarvoor zijn twee goede redenen. Ten eerst benadert het modeprofiel van een single mode vezel heel sterk een Gaussiaanse distributie. Concreet betekent dit voor een Corning SMF-28 vezel[1] dat de mode vrijwel overeenstemt met een Gaussiaanse bundel met halve breedte $w_0 = 5.1$ μm. Ten tweede laten Gaussiaanse bundels een analytische berekening van de koppelefficiënties toe.

---

[1] Dit type vezel wordt als een standaard type single-mode vezel beschouwd.
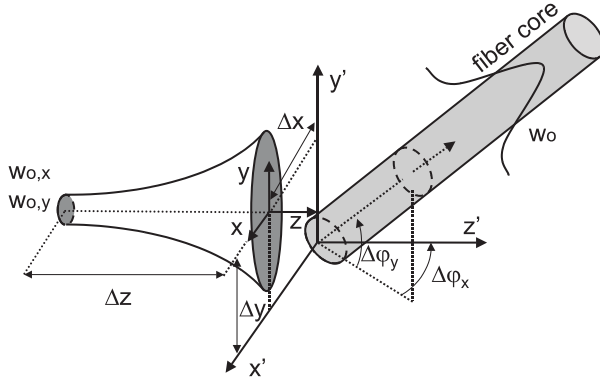
Figuur 6.1: Koppeling van een Gaussiaanse bundel naar een vezelmode.

6.2 Koppelefficiëntie van een arbitraire Gaussiaanse bundel naar een vezelmode

In de volgende secties zullen regelmatig koppelefficiënties (KE's) worden berekend om de alignatietoleranties te bepalen van connectoren. Deze geven weer in welke mate het vermogen van een mode ψ_1 wordt gekoppeld naar een andere mode ψ_2. De KE wordt berekend door evaluatie van de overlapintegraal

$$\eta = \left| \int \int_S \psi_1 \psi_2^* dS \right|^2$$

in een vlak waar beide modes aanwezig zijn.

Alvorens micro-optische elementen te betrekken in de analyse, is het aangewezen eerst de koppeling van een Gaussiaanse bundel in een optische vezel zonder microlenzen te beschouwen (figuur 6.1). Hoewel de analyse verder zal beperkt worden tot vezel-naar-vezel koppelingen, kan onderstaande uitdrukking ook gebruikt worden voor een Gaussiaanse bundel die niet afkomstig is van een andere vezel, maar van bijvoorbeeld een geïntegreerde golfgeleider of een zijwaarts emitterende halfgeleiderlaser op een chip.

$$\eta(\Delta x, \Delta y, \Delta z, \Delta\varphi_x, \Delta\varphi_y) = \eta_0(\Delta z)\eta_x(\Delta x, \Delta z, \Delta\varphi_x)\eta_y(\Delta y, \Delta z, \Delta\varphi_y) \qquad (6.1)$$

met

$$\eta_0 = \frac{4}{\sqrt{(\frac{w_x}{w_0}+\frac{w_0}{w_x})^2+\left(\frac{nkw_xw_0}{2R_x}\right)^2}\sqrt{(\frac{w_y}{w_0}+\frac{w_0}{w_y})^2+\left(\frac{nkw_yw_0}{2R_y}\right)^2}}$$

$$\eta_x = e^{-\left[\frac{2\Delta x^2}{w_0^2}-\frac{2\left(\frac{\Delta x^2}{w_0^4}-(\frac{k\Delta\varphi_x}{2})^2\right)\left(\frac{1}{w_x^2}+\frac{1}{w_0^2}\right)+\frac{n^2k^2\Delta x\Delta\varphi_x}{R_xw_0^2}}{(\frac{1}{w_0}+\frac{1}{w_x})^2+\left(\frac{nk}{2R_x}\right)^2}\right]}$$

$$\eta_y = e^{-\left[\frac{2\Delta y^2}{w_0^2}-\frac{2\left(\frac{\Delta y^2}{w_0^4}-(\frac{k\Delta\varphi_y}{2})^2\right)\left(\frac{1}{w_y^2}+\frac{1}{w_0^2}\right)+\frac{n^2k^2\Delta y\Delta\varphi_y}{R_yw_0^2}}{(\frac{1}{w_0}+\frac{1}{w_y})^2+\left(\frac{nk}{2R_y}\right)^2}\right]}$$

Koppelverliezen geven aanleiding tot een KE die verschillend is van 1. Gezien optische verliezen typisch in dB worden uitgedrukt, zullen we gebruik maken van de grootheid

$$L = -10\log(\eta)$$

Een voordeel van deze logaritmische uitdrukking is dat het totale verlies van een optische link kan worden uitgedrukt als de som van de opeenvolgende subcomponenten en transmissiemedia.

6.3 Single-mode vezel-naar-vezel koppeling

Gezien we connectoren met en zonder micro-optiek willen vergelijken, moeten we een aantal criteria definiëren die kunnen gebruikt worden om een bepaald ontwerp te evalueren. Deze maatstaven kunnen van allerlei aard zijn: mechanische robuustheid, temperatuursgedrag, vochtbestendigheid, optische koppelefficiëntie, reflectie, etc. De eenvoudige analyse die nu volgt zal enkel het optische aspect in rekening brengen, met name

- de minimale koppelverliezen L_{min}

- de 0.2 dB tolerantie voor transversale, longitudinale en angulaire misalignatie (= 96 % KE)

- de 0.3 dB tolerantie voor transversale, longitudinale en angulaire misalignatie (= 93 % KE)

Deze tolerantiewaarden zijn gekozen op basis van typische specificaties voor enkelvoudige vezelconnectoren die 0.2 dB als typisch en 0.3 dB als maximaal verlies vermelden.
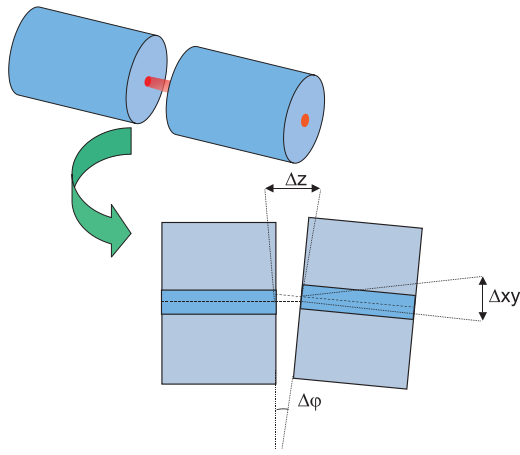
Figuur 6.2: Geometrie van directe vezel-naar-vezel koppeling.

loss tolerance	air		index-matching	
	0.2 dB	0.3 dB	0.2 dB	0.3 dB
Δxy [μm]	± 1.1	± 1.4	± 1.1	± 1.4
Δz [μm]	± 23.8	± 29.3	± 35	± 43
$\Delta \varphi$ [deg]	± 1.2	± 1.4	± 0.8	± 1.0

Tabel 6.1: Alignatietoleranties voor vezel-naar-vezel koppeling.

6.3.1 Directe vezel-naar-vezel koppeling

MT is een commercieel type connector dat op het principe van directe koppeling is gebaseerd. Deze connectoren zijn beperkt tot 1-dimensionele vezelrijen. De individuele vezels die worden samengebracht maken fysisch contact met elkaar en op die manier worden facetreflecties onderdrukt. In het onderstaande zullen dergelijke verliezen steeds worden verwaarloosd omdat een geschikte AR coating deze toch willekeurig klein kan maken.

Gebruik makend van vergelijking (6.1) kunnen de toleranties berekend worden voor de individuele alignatiefouten. Figuur 6.2 licht deze fouten toe. Gezien er geen mode-mismatch optreedt bij vezel-naar-vezel koppeling is de maximale KE in geval van perfecte alignatie 100 % ($L_{min} = 0$ dB).
Tabel 6.1 geeft de toleranties op alignatiefouten tussen de connectorblokken. Hierbij kan men stellen dat longitudinale uitlijnfouten weinig belang hebben, maar dat de toleranties op transversale misalignering wel heel streng zijn: slechts 1.1 μm.

De fabricatietoleranties voor beide connectordelen die worden gepaard, zijn nog strikter (tabel 6.2). Deze werden afgeleid uit voorgaande tabel in de veronderstelling dat fabricatiefouten in de twee connectorblokken even groot zijn en dat de verliezen mogen worden opgeteld. We zullen van nu af aan dan ook een onderscheid maken tussen beide oorzaken van misalignering:

tolerantie	lucht		index-matching	
	0.2 dB	0.3 dB	0.2 dB	0.3 dB
δxy [μm]	±0.6	±0.7	±0.6	±0.7
δz [μm]	±11.9	±14.7	±17.3	±21.3
$\delta\varphi$ [μm]	±0.6	±0.7	±0.4	±0.5

Tabel 6.2: Toleranties op de vezelposities in elk van beide connectordelen. Als intermediair medium werd lucht en een index-matching gel gekozen.

1. Fabricatiefouten: dit zijn fouten die optreden in elke component afzonderlijk en die verschillend kunnen zijn voor de individuele vezels. Deze geometrische afwijkingen worden bepaald door het fabricatieproces, inclusief het inbrengen van de vezels. Doordat massafabricatietechnieken welgekende toleranties bezitten, zijn deze fouten doorgaans dan ook welbepaald. De toleranties op dergelijke fouten zullen voortaan door δ worden weergegeven.

2. Gebruiksfouten: dit zijn uitlijnfouten tengevolge van het sluiten en openmaken van de connectordelen en hebben met andere woorden betrekking op het geheel van alle vezels in elk blok. De eventuele misaligneringen hangen af van het aantal keer dat de connector wordt geopend en gesloten, en op welke manier dit gebeurt. Gezien dit moeilijk voorspelbaar is, zijn deze fouten moeilijk in te schatten. De toleranties op dergelijke fouten zullen voortaan door Δ worden weergegeven.

Voor elk type uitlijnfout kunnen toleranties worden berekend die een minimale KE verzekeren in afwezigheid van andere misaligneringen. Het spreekt voor zich dat een doordacht connectorontwerp de invloed van gebruiksfouten verkleint (dus grotere Δ) en dus de duurzaamheid en betrouwbaarheid van de connector vergroot. Zelfs als dit gebeurt ten koste van strengere maar nog steeds haalbare fabricatietoleranties.

6.3.2 Koppeling met micro-optiek

Microlenzen die worden geplaatst in de optische paden tussen vezels, dienen om het golffront dat vertrekt van de ene vezel te reconstrueren op het facet van de andere. Gezien het koppelprobleem volledig symmetrisch is en de connector uit twee verwijderbare delen moet bestaan, moet hij opgebouwd zijn uit twee symmetrische delen. Om reflectieverliezen te minimaliseren, dient het aantal grensvlakken in de optische paden te worden beperkt. Het minimum aantal is 2 per connectorblok: één aan de vezelzijde en een tweede gericht naar het ander blok. Een uitvoering van een dergelijke connector is gegeven in figuur 6.3 waarbij elk optisch pad tussen twee vezels voorzien is van individuele microlenzen. Merk op dat symmetrie vereist dat er zich in het centrum een 'beam waist' bevindt.
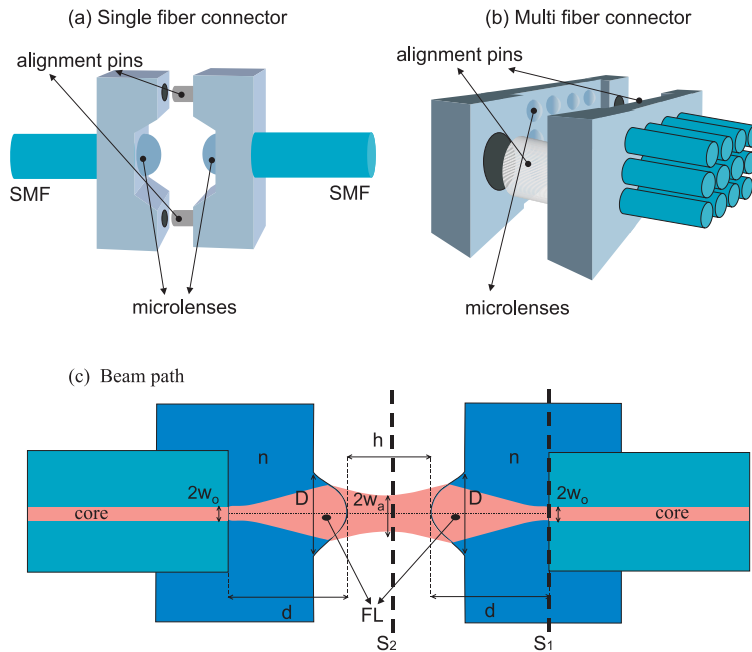
Figuur 6.3: Vezel-naar-vezel koppeling met microlenzen.

6.3.3 Design van het lenzensysteem

Vertrekkend van een ontwerp zoals in figuur 6.3 kunnen we de lenzen en de relevante afstanden dimensioneren. De lensdiameter D_{lens} wordt bepaald door het 99 % transmissiecriterium dat vereist dat deze anderhalve keer de bundelbreedte bedraagt. De afstand h kan worden gevonden door het berekenen van de locatie van de beam waist die zich centraal tussen de lenzen bevindt. We kunnen deze uitdrukkingen als volgt samenvatten:

general system

$$h = 2\frac{\alpha_n d\left(\frac{\alpha_n d}{FL} - \alpha_n n\right) + \frac{1}{FL}}{\left(\frac{\alpha_n d}{FL} - \alpha_n n\right)^2 + \frac{1}{FL^2}}$$

$$D_{lens} = 3w_0\sqrt{1 + (\alpha_n d)^2}$$

$$w_a = \frac{FL}{kw_0}\sqrt{\frac{4}{1 + \alpha_n^2(d - nFL)^2}}$$

waarbij de keuze van 2 parameters uit de set (FL, d, h) het volledige systeem bepaalt.

Er bestaan twee speciale gevallen naargelang de werkafstand d:

a) 4-F systeem

In geval $d = nFL$ wordt het lenzensysteem als volgt bepaald:

$$4 - \text{F system}$$

$$
\begin{array}{rcl}
d & = & nFL \\
h & = & 2FL \\
D_{lens} & = & 3w_0\sqrt{1 + (\alpha_n d)^2} \\
w_a & = & \frac{2FL}{kw_0}
\end{array}
$$

Deze configuratie wordt een 4-F systeem genoemd gezien de afstand tussen het voorwerps- en beeldvlak $4FL$ bedraagt indien de lenzen zich in lucht bevinden.

b) 8-F systeem

Een ander bijzonder geval doet zich voor als $w_a/w_o = 1$. Indien we FL groot veronderstellen ten opzichte van de Rayleigh lengte, dan kunnen we het systeem als volgt dimensioneren:

$$8 - \text{F system}$$

$$
\begin{array}{rcl}
d & = & 2nFL \\
h & = & 4FL \\
D_{lens} & = & 3w_0\sqrt{1 + (\alpha_n d)^2} \\
w_a & = & w_0
\end{array}
$$

Tabel 6.1 toont dat de tolerantie voor angulaire uitlijnfouten $1.2°$ bedraagt. In de veronderstelling dat het ferrulefacet uiterst vlak is, kan men stellen dat deze tolerantie heel gemakkelijk haalbaar is voor de typische afmetingen van bijvoorbeeld een 8×8 vezelmatrix. De tolerantie voor transversale misalignaties is daarentegen wel heel streng ($\Delta xy_{0.2B} = 1.1$ μm): stofdeeltjes in de optische paden of speling tussen de connectorblokken kunnen reeds de optische koppeling behoorlijk verstoren. Versoepelen van deze tolerantie kan worden bereikt door een grotere bundel (grotere w_a) tussen de lenzen na te streven. Een gedetailleerde beschrijving van de toleranties die we kunnen verwachten voor zowel de alignatie als voor de parameters FL, d en h wordt gegeven in de Engelstalige versie.

6.3.4 Berekening van de lensvorm

In het voorafgaande werden optimale focale lengtes berekend, maar die zijn niet ondubbelzinnig met een welbepaalde 3-dimensionele lensvorm geassocieerd. Gezien optische vezels een rotationeel-symmetrische bundel emitteren, spreekt het voor zich dat de lenzen alvast een circulair ondervlak bezitten. De exacte vorm kan berekend worden op basis van fase-afstemming van de bundels respectievelijk komende van het vezelfacet en van de 'waist' w_a. Op deze manier bekomen we

$$l(x,y) = \frac{x^2 + y^2}{2(n-1)}\left[\frac{n}{d(1 + (\frac{nkw_0^2}{2d})^2)} + \frac{1}{\frac{h}{2}(1 + (\frac{kw_a^2}{h})^2)}\right]$$

49

Deze vergelijking definieert een parabool van de vorm $l(r) = cr^2$ met $r = \sqrt{x^2 + y^2}$ en c een constante. De kromtestraal ter hoogte van de vertex is gegeven door $\frac{(1+l'(r))\sqrt{1+l'(r)}}{l''(r)}$ en bedraagt dus $1/2c$. De overeenkomstige focale lengte is $R/(n - 1)$.

6.4 Fabricatie van microlenzen met excimeerlaser-ablatie

Microlensjes met een geschikte vorm voor 4-F afbeelding werden gerealiseerd met excimeerlaser-ablatie. Deze lensjes werden aangewend om vezel-naar-vezel koppeling te evalueren. Hoewel de experimenten om praktische redenen beperkt werden tot enkelvoudige vezels (dus geen vezelrijen), geven de resultaten toch een heel goede indicatie van wat microlenzen kunnen bieden op het gebied van alignatie-toleranties.

6.4.1 Lensontwerp en beschrijving van het fabricatieproces

Op elk van de vezelfacetten is een polymeerplaatje aangebracht met een UV-hardende lijm. Dit plaatje dient als substraat voor het microlensje dat achter-af wordt geableerd vlak boven de vezelkern. Het loodrecht aanbrengen van het polymeerplaatje op de as van de vezel wordt vergemakkelijkt door een geconnec-toriseerde SM vezel te gebruiken. Het FC/PC ferrule facet is bovendien groot genoeg voor een goede verlijming. De plaatjes zijn polycarbonaat, verkrijgbaar in een dikte van 250 μm bij Goodfellow Inc.

Indien 15 μm moet verwijderd worden om een glooiend lensoppervlak te verkrijgen en rekening houdend met een 5 μm diepte van de lens na het ableren van de omtrek-groeven, betekent dit een werkafstand van 230 μm. Voor een 4-F lenzensysteem is dit in overeenstemming met een bundelbreedte $w_a = 14.2$ μm tussen de lenzen en dus een transversale alignatietolerantie $\Delta xy_{0.2dB} = 3.1$ μm. De overige lenspara-meters zijn weergegeven in tabel 6.3. De lenzen werden gefabriceerd door gebruik te maken van de omtrekscan-techniek zoals beschreven in hoofdstuk 4. Slechts 13 contouren waren nodig om de lensvorm te benaderen en de gekozen ablatiesnelheid bedroeg 105 nm per puls. Door inkoppelen van een laserbundel (laserdiode) in de vezel en de vezelspot onder het PC plaatje te lokaliseren met de TTL ("Through The Lens") camera, werd alignatie van de lens met de onderliggende vezelkern verkregen. Figuur 6.4 geeft een voorbeeld van een geconnectoriseerde SM vezel met een microlensje.

6.4.2 Lenskwaliteit

De geableerde lenzen werden uitvoerig bestudeerd. Aberratiemetingen met de Mach-Zehnder interferometer toonden aan dat de lenzen vrijwel diffractiegelimi-teerd zijn met een Strehl Ratio van 0.96 en een rms waarde voor de aberraties

d [μm]	FL [μm]	h [μm]	w_a [μm]	D_{lens} (D_{min}) [μm]
230	149.7	299.3	14.2	70 (45.4)

Tabel 6.3: Lensparameters voor vezel-naar-vezel koppeling met een 4-F lenssysteem dat gebruik maakt van 250 μm plaatjes in polycarbonaat. De kromtestraal aan de vertex is 81 μm.

Figuur 6.4: FC/PC geconnectoriseerde SM vezel met microlens.

beneden 0.04λ. Merk op dat deze metingen bij 633 nm gebeuren en niet bij 1.55 μm. Een verre veldmeting bevestigde de grootte van de bundel tussen de lenzen: een divergentiehoek van 4.5 graden is in overeenstemming met een beam waist ter grootte van 13 μm, of heel dicht tegen de gewenste 14 μm.

Tenslotte werden koppelexperimenten uitgevoerd zoals weergegeven in figuur 6.5: twee vezels worden met elkaar gealigneerd op een afstand van ongeveer 300 μm. Vervolgens werden de transmissieverliezen gemeten van de gehele structuur bestaande uit 2 patchcords met het 4-F lenssysteem ertussen. De resultaten zijn weergegeven in tabel 6.4.

Hoewel de gemiddelde transmissie van 88 % nog steeds behoorlijk afwijkt van de theoretische 100 % (reflecties werden reeds in rekening gebracht), is dit reeds een beloftevol resultaat. Een verdere verbetering van de koppeling mag verwacht worden indien de lenzen nauwkeuriger kunnen worden gepositioneerd boven de vezels. In figuur 6.6 wordt de koppelefficiëntie in functie van de transversale misalignatie weergegeven. Uit deze resultaten volgt dat de experimentele $\Delta xy_{0.2dB}$ 3.3 μm bedraagt, welke heel dicht de gewenste 3.1 μm benadert.
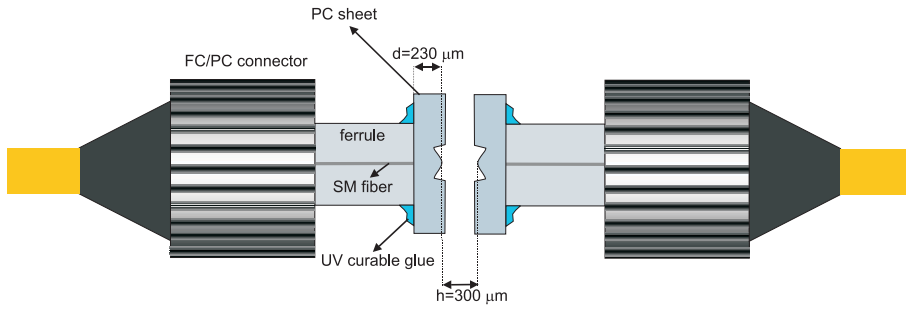
Figuur 6.5: Vezel-naar-vezel koppeling met een 4-F lenssysteem.

end-to-end verlies [dB]	geschat 4-F verlies* [dB]	4-F transmissie [%]
1.199	0.459	90.0
1.157	0.417	90.8
1.540	0.800	83.2
1.383	0.643	86.2
1.320±0.177	**0.580±0.177**	**87.6±3.5**

*Door de verliezen in elk van de patchcords (0.17 dB) en Fresnelverliezen (0.2 dB per facet) in rekening te brengen.

Tabel 6.4: Experimentele koppelverliezen voor het 4-F lenssysteem.
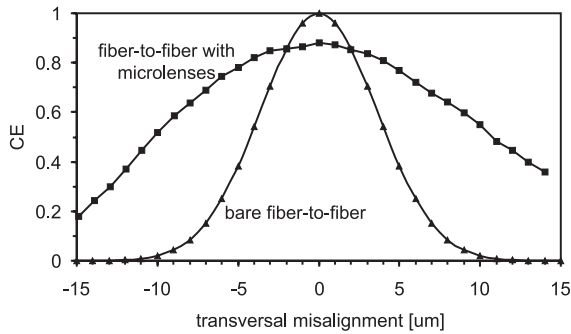
Figuur 6.6: Koppelefficiëntie in functie van de transversale misalignering tussen de vezels.

Hoofdstuk 7

Besluiten en toekomstperspectieven

Deze thesis had drie belangrijke doelstellingen: wat is excimeerlaser-ablatie, hoe kan het gebruikt worden voor microbewerking en voor welke welke toepassingen is deze techniek heel geschikt.

In dit werk hebben we uitgebreid de fysische processen besproken die plaatsvinden tijdens laserablatie en beschreven hoe korte maar krachtige laserpulsen lokaal een materiaallaagje kunnen verwijderen. In het bijzonder hebben we de modellering van thermische en niet-thermische dissociatie besproken en aangetoond dat beide tot goed afgelijnde caviteiten kunnen leiden.

Op basis van deze kennis hebben we de kwaliteiten van excimeerlaser-ablatie als microbewerkingstechniek bestudeerd. De belangrijkste bijdrage van deze thesis op dit vlak is tweeërlei. Enerzijds is er het systematisch onderzoek naar de ablatieve eigenschappen van 5 belangrijke, commerciële polymeren (PC, PMMA, PI, PS en PET) en dit bij zowel 193 nm als 248 nm. Daarbij werden alle bevindingen met uitgebreide experimentele data gestaafd. Ten tweede hebben we hier voornamelijk de ablatie-eigenschappen met betrekking tot microbewerking onderzocht. Dit in tegenstelling tot de vele artikels die zich beperken tot modellering van het ablatieproces bij 1 of 2 polymeren en die vaak irrelevant zijn in typische laserbewerkingsomstandigheden zoals pulstreinen, diepe structuren, bewegende laserbundel, etc.

Een tweede gedeelte van de thesis behandelt een aantal toepassingen: excimeerlaser-ablatie werd gebruikt om microalignatie en micro-optische componentjes aan te maken in polymeren. Vooral deze laatste toepassing, de fabricatie van microlenzen, was een grote uitdaging door de hoge vereisten met betrekking tot de finale oppervlaktekwaliteit.

In hoofdstuk 4 wordt een nieuwe manier voor microlensfabricatie voorgesteld: de omtrekscan-techniek. Deze werd ontwikkeld binnen het kader van dit doctoraat en laat toe lenzen te maken met een vrijwel arbitrair profiel binnen een aanvaardbare tijd van luttele minuten (voor lenzen met 200 μm diameter). In combinatie met

de voordelen van contactloze en direct-write fabricatie, is de techniek uitermate geschikt om zelfs in een late fase van een heterogene opto-electronische assembly lenzen en lensrijen te definiëren in een polymeer oppervlak. Deze unieke eigenschap maakt van excimeerlaser-ablatie een waardevolle prototyping techniek voor microlensfabricatie. Wel moet nog steeds een beperking worden gerespecteerd: de omtrekscan-techniek kan voorlopig geen diffractie-gelimiteerde lenzen met hoge $f/\#$ aanmaken. De beperkte nauwkeurigheid van de translatietafel en pulsenergie-variaties spelen hier een niet onbelangrijke rol.

Het experimentele werk werd op vlak van microlensfabricatie beperkt tot lenzen met een rotationele symmetrie. Toch werd reeds in hoofdstuk 4 gesuggereerd dat de scantechniek kan worden uitgebreid naar lenzen met een niet-cirkelvormige, meer bepaald elliptische basis. Dergelijke lenzen bieden heel wat potentieel voor de optische koppeling van zijwaarts emitterende halfgeleiderlasers naar optische vezel. Een ander type lens dat niet aan bod kwam in deze thesis zijn diffractieve lenzen. Hoewel deze maskerpatronen op maat vereisen, hebben ze toch reeds de aandacht getrokken van een aantal onderzoeksgroepen. Beide pistes kunnen een logische uitbreiding vormen op het onderzoekswerk dat reeds werd verricht.

In een meer algemene context kan men stellen dat een recent type laser zijn opmars maakt op vlak van microfabricatie: de Ti:Saffier laser die pulsen met een lengte van slechts een paar tientallen fs (1 femtoseconde = $1/1.000.000.000.000.000$) kan emitteren. Door de extreem korte pulsduur vermijdt deze 'ultrafast' technologie elke vorm van thermische schade die kan optreden bij laserablatie. Bovendien bieden deze lasers nog heel wat potentieel naast laserablatie: driedimensionele microfabricatie van structuren met nanometer features door fotopolymerisatie en golfgeleiderfabricatie in bepaalde glastypes door geïnduceerde brekingsindex-variaties. De verwachting is dat deze lasers in de toekomst meer en meer de aandacht zullen trekken naarmate de technologie zich verder ontwikkelt.

English text

Foreword

Within the research group Photonics —formerly known as OCS— of Ghent University it has been a tradition that PhD topics are strongly related to the field of optical communication, with emphasis on photonic components and systems. This also applied to the research that I started in 1998. At that time, a brand new state-of-the-art excimer laser workstation had just been installed. The system basically consisted of a powerful UV laser source and some optics to focus the beam onto a sample. This was sufficient to serve its main purpose: drilling of microvias in PCB layers and microstructuring. The controllable and contactless removal of matter that occurs when the beam focus is directed onto a material surface, was the key process to fabricate structures with micron accuracy. The link with photonics was rather obvious: the workstation would be an ideal tool for fabrication of fiber and chip alignment structures, although these would be limited to multimode devices due to the lack of submicron accuracy in the lateral dimensions. Since its installment, the laser ablation workstation has been used for many purposes: not only definition of optical fiber alignment structures and microvias in polymers, but also microlens sculpting, fiber cleaving, ablation of waveguides in ORMOCER, fabrication of micromechanical components for a variety of purposes and micropatterning of biomolecules on solid surfaces to name a few. In other words, the range of applications for excimer laser ablation is certainly not limited to the field of optical communications only. This statement is confirmed by a look at the worldwide commercial and scientific employment of excimer laser ablation today: nozzle drilling, microchannel ablation for fluid transport on a microscale, Pulsed Laser Deposition, photorefractive Keratectomy and LASIK, contactless fiber stripping, etc. It is therefore important to realize that the applications considered in this work —alignment structures and microlenses— reveal only a small part of the potential of laser ablation. Due to this multi-disciplinary nature of the technique, we chose to keep this thesis accessible to people with various scientific backgrounds as much as possible. Every chapter of interest can be read as a stand-alone part, almost requiring no knowledge of previous chapters.

Chapter 1

Introduction

1.1 Research context and motivation

It is beyond doubt that one of the main hallmarks of our modern society is its large dependency on collection, storage, transfer and exchange of information. Data transportation occurs over a broad range of distances and serves commercial, social, financial, medical and scientific purposes as voice telecommunication, sensor networks, Internet data traffic, electronic transactions, CATV, etc. A key aspect is the massive amount of information involved, and this volume is still increasing rapidly. This has been made possible thanks to the introduction of light beams for data transmission rather than electrical signals in high bandwidth communication links. Indeed, photons can transfer much larger amounts of data over very long distances at negligible loss without suffering from interference with neighboring fibers. Even for short distance communication involving beam paths as short as a few mm, the advantages of optical links are numerous: no cross-talk, full three-dimensional employment of the available space (free space propagation), no heat dissipation and large bandwidth. However, there is also a drawback: contrary to copper, optical interconnection requires accurate alignment of source, detector and in case of guided-wave propagation the intermediate transmission medium.

As a result of cost considerations and the ever-increasing demand for higher bandwidths, photonic components are gradually shrinking in size —including the beam spots— and tremendous efforts are made for monolithic integration of various photonic functionalities in next-generation opto-electronic components. In addition single optical paths are being gradually replaced by many optical channels in parallel: instead of one detector and emittor interconnected by a single optical pathway, one-dimensional arrays and even two-dimensional arrays are being introduced to handle the increasing data traffic. In the meantime the transmission medium has remained more or less the same: single mode fiber for long distance communication and multimode glass/plastic fiber or free space for short distance interconnects. It is obvious that the high degree of parallellism and small optical field sizes in the opto-electronic chips turn efficient in-and-out coupling of light into quite a chal-
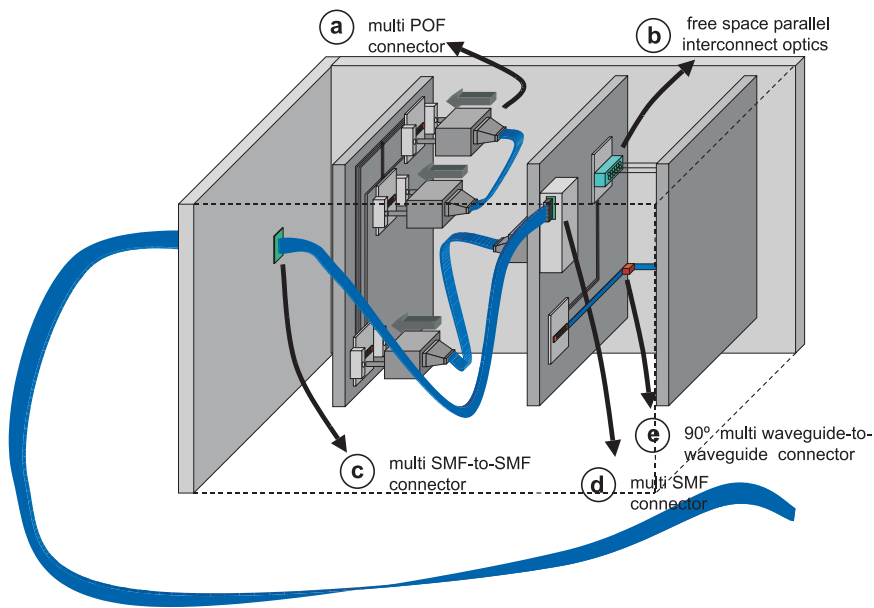
Figure 1.1: Fiber and fiber array alignment structures in opto-electronic modules.

lenge, both from a technological and cost-efficiency point of view. Even in the case of ultimate cost reduction by fully monolithic integration of all functionality into one single chip, there still needs to be communication with the outside world via a fiber (array) or any other transmission medium. The interface between the chip and this fiber consists of a carrier material (plastic, ceramic or semiconductor) equipped with alignment features, fiber and chip clamping parts, and possibly microoptics. The latter can help in matching the modal field sizes or serve to relax the alignment tolerances. In figure 1.1 an example is given of a multi-board electronic processing system with high-speed optical interconnects between chips on the same board or on neigboring boards. These can be based on either free-space or through-waveguide propagation. A long-distance optical communication path starts from a board and passes through the closure (which can serve as a hermetic sealing) to the outside world. All these connections need some interface between the receiver and transmitter chips or between two fiber or waveguide arrays. In figure 1.1 the different optical interconnect technologies are shown on the same boards. In reality, they will be rarely used together.

Contrary to chip fabrication techniques which are based on lithography and are able to produce features smaller than 0.1 μm (in 2003), alignment components are usually fabricated with less accuracy. These structures are created using mechanical means as micro milling and micro turning, and more advanced techniques as micro-EDM (Electrode Discharge Machine), laser machining and LIGA. Often only one prototype device needs to be fabricated and subsequent mass replication in plastics is obtained with injection molding and casting.

1.2 Excimer laser ablation

An interesting alternative for the prototype fabrication techniques mentioned in
the previous section, is excimer laser ablation. This micromachining technology is
based on the controlled removal of material with short and intense excimer laser
pulses. The direct-write and contactless nature of the process and the fact that
it can be employed under atmospheric conditions and at room temperature, make
laser ablation very attractive as micromachining technology.
Contrary to high-power infrared Nd:YAG and CO_2 lasers that are also used for
laser ablation, excimer lasers typically emit in the UV range 157-355 nm. As most
materials absorb very well in the UV and as shorter wavelengths correspond to a
better optical resolution of the beam delivery system, this type of laser is very suit-
able for patterning with micron and even submicron accuracy. This is in particular
the case when the machined substrate is a polymer since this material features a
low thermal conductivity, extremely high UV absorption and the ability to photo-
chemically decompose under excimer irradiation.
Next to direct-write and contactless patterning, excimer laser ablation has two very
important advantages that make it a rather unique prototyping technology. Firstly,
it is one of the few techniques that is capable of fabricating both microalignment
and microoptical structures, making monolithic integration of both functionalities
onto the same polymer substrate possible. Indeed, prototyping technologies for
lenses such as thermal reflow of resist layers or microjet printing are not able to
produce microalignment features on the same substrate as the lenses. Monolithic
integration of both structures thus requires a combination of one or more tech-
niques, making the assembly far more complex and thus less feasible. Secondly,
excimer laser ablation offers the unique advantage that it can be employed for struc-
turing a top surface of a heterogeneous opto-electronic module in a late phase of the
assembly process. Contrary to most other microfabrication technologies, the ma-
chined part is not put under mechanical stress neither are any chemically reactive
substances or high temperatures necessary that can damage (other) components in
the heterogeneous assembly.

Excimer laser ablation is commercially employed in a variety of applications: via-
drilling, inkjet nozzle drilling, ablation of fluid capillaries for lab-on-chip purposes,
refractive surgery, fiber and wire stripping and Pulsed Laser Deposition to name
the most important ones. In addition excimer lasers are also used for non-ablative
material processing: TFT annealing, Fiber Bragg Grating writing and UV litho-
graphy.

At the start of our research work in 1998 excimer laser ablation was considered
a feasible technique for surface structuring with micron accuracy [1, 2]. It should
be noted that literature on practical employment of the technique was scarce at
that time as modeling of the ablation process captured most of the attention.
This modeling has mainly focused on single pulse ablation rather than typical
micromachining situations where multiple pulses are fired onto moving substrates.
This observation has been one motive for our research work.
Another rationale has been the potential of excimer laser ablation for fabrication
of microlenses. The required optical surface finish (RMS roughness $< \lambda/10$ or

0.1 μm) is a considerable challenge for a technique that is developed to realize structures with typical feature sizes of microns in the lateral dimensions. In 1998 the employment of laser ablation for microoptics fabrication has been rather limited and usually involved complex mask patterns or time-consuming reflow processes [3, 4, 5, 6]. More recent techniques suffer from the same problems: fabrication times of several hours, requirement of very sophisticated optical set-ups and severe limitations on the range of microlenses that can be made [7, 8, 9]. In other words, the benefits of a rapid and flexible prototyping technique that laser ablation offers in micromachining applications, are totally lost when refractive surfaces need to be fabricated. The contour ablation technique developed in the framework of our doctoral research work, meets most of the demands of rapid prototyping: it is very flexible in terms of lens shape, lenses are fabricated on a time scale of minutes and only a very basic set-up is required.

1.3 Chapter overview

This work consists of four main parts. In chapter 2 the physical processes governing excimer laser ablation of polymers are discussed. Emphasis is put on understanding the influence of several laser and material aspects on the ablation behavior, in casu the etch depth per laser pulse. Chapter 3 deals with the ablation process in the much broader sense of a micromachining technique: excimer laser and beam delivery technology, key properties of ablated cavities in commercial polymers and applications of excimer laser ablation. The chapter finishes with some prototype components that have been developed at Intec, Ghent University. The third part (chapter 4, 5 and 6) will focus on two dedicated micromachining applications where excimer laser ablation was applied successfully. Chapter 4 and 6 concentrate on laser ablated microlenses and the potential of these microoptical components for single mode fiber coupling, while chapter 4 discusses a specific fiber alignment structure that has been used for constructing a 2-D plastic optical fiber connector. General conclusions are proposed in chapter 7.

1.4 List of publications

The following journal papers have been published or are accepted for publication:

K. Naessens, H. Ottevaere, P. Van Daele and R. Baets, "Flexible fabrication of microlenses in polymer layers with excimer laser ablation", Appl. Surf. Sc. **208**, 159 (2002).

Y. Martele, K. Callewaert, I. Swennen, K. Naessens, R. Baets, V. Van Speybroeck, M. Waroquier, H. Van Aert, P. Dierickx and E. Schacht, "Micropatterning of polyurethanes with lasers", Polym. Int. **51**, 1172 (2002).

K. Callewaert, Y. Martele, L. Breban, K. Naessens, P. Van Daele, R. Baets, H. Geuskens and E. Schacht, "Excimer laser induced patterning of polymeric surfaces", Appl. Surf. Sc. **208**, 218 (2002).

Y. Martele, K. Callewaert, K. Naessens, P. Van Daele, R. Baets and E. Schacht, "Controlled patterning of biomolecules on solid surfaces", Mat. Sc. & Eng. C **23**, 341 (2003).

K. Naessens, H. Ottevaere, R. Baets, P. Van Daele and H. Thienpont, "Direct-writing of microlenses in polycarbonate with excimer laser ablation", Appl. Opt. **42**, 6349 (2003).

The following papers have been presented at international conferences:

K. Naessens, S. Boons, A. Van Hove, T. Coosemans, S. Verstuyft, H. Ottevaere, L. Vanwassenhove, P. Van Daele and R. Baets, "Excimer laser ablated U-groove alignment structure for optical fibre arrays", LEOS Benelux Symposium, Mons, Belgium, Proc. ISBN 2-9600226-0-2 , 187 (1999).

K. Naessens, A. Van Hove, T. Coosemans, S. Verstuyft, H, Ottevaere, L. Vanwassenhove, R. Baets and P. Van Daele, "Fabrication of microgrooves with excimer laser ablation techniques for optical fibre array alignment purposes", in Laser Applications in Microelectronic and Optoelectronic Manufacturing V, San Jose, USA, Proc. SPIE **3933**, 309 (2000).

A. Van Hove, J. Haes, K. Naessens, B. Dhoedt, R. Baets and P. Van Daele, "MT compatible red VCSEL module for parallel optical interconnections", in Optoelectronic Interconnects VII; Photonics Packaging and Integration II, San Jose, USA, Proc. SPIE **3952**, 134 (2000).

T. Coosemans, R. Bockstaele, A. Van Hove, K. Naessens, J. Derluyn, L. Vanwassenhove, P. Van Daele, I. Moerman, and R. Baets, "Substrate removed 850nm RCLED's and small core (63/125mm) plastic optical fibers for optical data communication", in Light-Emitting Diodes: Research, Manufacturing and Applications IV, San Jose, USA, Proc. SPIE **3939**, 160 (2000).

T. Coosemans, A. Van Hove, K. Naessens, L. Vanwassenhove, P. Van Daele and R. Baets, "Fabrication of a 2D connector for coupling a 4x8 array of small diameter plastic optical fiber (117/125 um) to MCLED or VCSEL arrays", in 50th Electronic Components & Technology Conference, Las Vegas, USA, Proc., 1236 (2000).

K. Naessens, A. Van Hove, T. Coosemans, S. Verstuyft, P. Van Daele and R. Baets, "Microgroove fabrication with excimer laser ablation techniques for optical fiber array alignment purposes", in First International Symposium on Laser Precision Microfabrication, Omiya, Japan, Proc. SPIE **4088**, 327 (2000).

K. Naessens, P. Van Daele and R. Baets, "Microlens fabrication in PMMA with scanning excimer laser ablation techniques", in LEOS Benelux Symposium, Delft, Netherlands, Proc. ISBN 9090142606, 99 (2000).

T. Coosemans, K. Naessens and R. Baets, "Connectors for parallel optical datalinks using 2x8 arrays of embedded small diameter (125um) plastic optical fibres", in Plastic Optical Fiber World 2001, Amsterdam, Netherlands, Proc. ISBN 3-905084-67-8, 147 (2001).

K. Naessens, P. Van Daele and R. Baets, "Laser-ablation-based technique for flexible fabrication of microlenses in polymer materials", in Second International Symposium on Laser Precision Microfabrication, Singapore, Proc. SPIE **4426**, 124 (2001).

H. Ottevaere, P Tuteleers, B. Volckaerts, V. Baukens, J. Lamprecht, J. Schwider, A. Hermanne, K. Naessens, I. Veretennicoff and H. Thienpont, "Microlens arrays fabricated by deep lithography with protons and their characterization", in Micro- and Nano-optics for Optical Interconnection and Information Processing, San diego, USA, Proc. SPIE **4455**, 272 (2001).

K. Naessens, P. Van Daele and R. Baets, "Excimer laser ablation based microlens fabrication for optical fiber coupling purposes", in Laser Micromachining for Optoelectronic Device Fabrication, Brugge, Belgium, Proc. SPIE **4941**, 133 (2002).

K. Naessens, P. Van Daele and R. Baets, "Excimer laser ablation based microlens fabrication in polymer materials", LEOS Annual Meeting, Glasgow, Scotland, Proc. ISSN 1092-8081 , 655 (2002).

The following paper was presented at a symposium without proceedings:

K. Naessens, P. Van Daele and R. Baets, "Flexible fabrication of microlenses in polymers with excimer laser ablation", 2nd PhD Symposium, Gent, Belgium, 2001

This presentation was awarded the price "laureaat presentatieprijs".

In the context of this work, the following patent application has been filed:

J. Watte, K. Naessens, R.Baets and P. Van Daele, "Optical fibre cleaving", PCT-GB2003-002671.

Bibliography

[1] E. Harvey and P. Rumsby, "Fabrication techniques and their application to produce novel micromachined structures and devices using excimer laser projection" in Micromachining and Microfabrication Process Technology III, Austin, USA, Proc. SPIE **3223** (1997).

[2] P. Rumsby, E. Harvey, D. Thomas and N. Rizvi, "Excimer laser patterning of thick and thin films for high density packaging", in Microelectronic Packaging and Laser Processing, Singapore, Proc. SPIE **3184** (1997).

[3] X. Wang, J. Leger and R. Rediker, "Rapid fabrication of diffractive optical elements by use of image-based excimer laser ablation", Appl. Opt. **36**, 4660 (1997).

[4] R. Matz, H. Weber and G. Weimann, "Laser-induced dry etching of integrated InP microlenses", Appl. Phys. A **65**, 349 (1997).

[5] S. Mihailov and S. Lazare, "Fabrication of refractive microlens arrays by excimer laser ablation of amorphous teflon", Appl. Opt. **32**, 6211 (1993).

[6] S. Lazare, J. Lopez, J.-M. Turlet, M. Kufner, S. Kufner and P. Chavel, "Microlenses fabricated by ultraviolet excimer laser irradiation of poly(methyl methacrylate) followed by styrene diffusion, Appl. Opt. **35**, 4471 (1996).

[7] M. Wakaki, Y. Komachi and G. Kanai, "Microlenses and microlens arrays formed on a glass plate by use of a CO_2 laser", Appl. Opt. **37**, 627 (1998).

[8] T. Jitsuno, K. Tokumura, N. Nakashima and M. Nakatsuka, "Laser ablative shaping of plastic optical components for phase control", Appl Opt. **38**, 3338 (1999).

[9] F. Beinhorn, J. Ihlemann, K. Luther and J. Troe, "Microlens arrays generated by UV laser irradiation of doped PMMA", Appl. Phys. A **68**, 709 (1999).

11

Chapter 2

UV laser ablation of polymer materials

In this chapter the physical nature of the laser ablation process, in particular for polymer materials, will be discussed. In order to expound the underlying processes, a few basic principles concerning photon absorption in condensed media will be introduced. Based on these processes, models can be derived which predict the ablative behavior of polymers exposed to strong UV laser pulses. Model predictions are compared to experimental results for some commercial polymers.

2.1 Light absorption in solids

2.1.1 Macroscopic description of absorption

When a light beam with intensity I_0 hits a material surface (figure 2.1), the part of the beam which is not reflected will be subject to attenuation inside the matter due to absorption[1]. The attenuation per unit of length depends on the intensity of the beam and will be proportional to I^n for a n-photon absorption process. Mathematically, the decrease of intensity through the medium can be written as

$$\frac{dI(x)}{dx} = -(\alpha^{(1)}I(x) + \alpha^{(2)}I^2(x) + \alpha^{(3)}I^3(x) + ...)$$

in which we assumed that several absorption mechanisms are present. For low values of I, higher order terms can be neglected and it is sufficient to consider 1-photon absorption only: $\alpha^{(1)} = \alpha$. In this case the local amount of absorbed light equals $\alpha I(x)$ and the beam intensity decreases exponentially according to

$$I(x) = I_0 e^{-\alpha x}$$

---

[1]Losses due to scattering will not be taken into account.
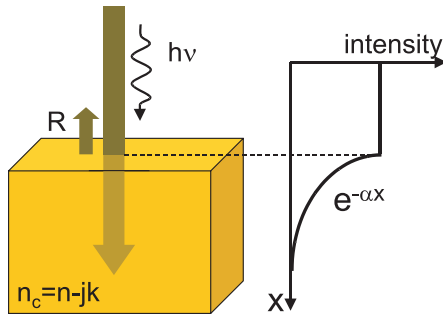
Figure 2.1: Propagation of a light beam through matter.

material	λ [μm]	$\alpha^{(1)}$ or $\alpha^{(2)}$	remarks
PI	0.193	$\alpha^{(1)} = 4.5 \times 10^5$ cm^{-1}	from [2, 3]
PMMA	0.193	$\alpha^{(1)} = 4.5 \times 10^3$ cm^{-1}	from [4]
	0.248	$\alpha^{(1)} = 5 \times 10^2$ cm^{-1}	from [4]
SiO$_2$	0.264	$\alpha^{(1)} < 0.02$ cm^{-1}	Heraeus suprasil
		$\alpha^{(2)} = 1.7 \times 10^{-11}$ W^{-1}cm	quartz [5]
Cu	0.248	$\alpha^{(1)} = 9 \times 10^5$ cm^{-1}	calculated via $\alpha = 4\pi k/\lambda$
GaAs	0.248	$\alpha^{(1)} = 1.9 \times 10^6$ cm^{-1}	calculated via $\alpha = 4\pi k/\lambda$

Table 2.1: absorption coefficients for various materials at some important wavelengths, measured at 300 K.

what is known as the Beer-Lambert law. α is called the absorption coefficient (cm^{-1}) while α^{-1} is identified with the characteristic penetration depth. α can be related to the complex refractive index of the material $n_c = n - jk$ via $\alpha = 4\pi k/\lambda$. In case the absorbing species (impurities in a non-absorbing crystalline structure, dopants in low-absorbing PMMA, etc.) can be identified in the medium, α is often replaced by $\alpha = \sigma N$ where σ is the absorption cross-section per absorber (cm^2) and N the absorber concentration (cm^{-3}). E.g. Kapton features an absorption $\alpha = 4.2 \times 10^5$ cm^{-1} at 193 nm [1] corresponding to a penetration depth of 23 nm and $k = 0.645$. UV absorption in Kapton is caused by well-defined molecular bonds called chromophores. Their absorption cross-section σ and density N can be estimated at 4.8×10^{-17} cm^2 and 8.7×10^{21} cm^{-3}. The absorption coefficients of various materials at some UV wavelengths are given in table 2.1.
In the argumentation above, α is assumed to be independent of intensity. Strictly speaking this is only valid within a limited range of values for I. E.g. absorption in metals is usually accompanied by local heating for considerable values of I, leading

to changes in the volume density and phonon population. In turn these processes influence α. Another example can be found in organic materials: an effect often referred to as 'bleaching' can occur due to a substantial decrease of the available non-excited absorbers at high I.

It might seem odd that we only discussed the simplified case of 1-photon absorption, whereas laser ablation is typically the result of the interaction between high-intensity laser pulses and a material surface. The reason for this seeming contradiction is that laser ablation is usually only employed for materials with very large values of the single-photon α ($>10^4$ cm^{-1}) at the laser wavelength. In this case $\alpha^{(1)}I >> \alpha^{(2)}I^2$. At the excimer wavelengths (λ between 157 and 355 nm) an exception should be made for crystalline insulators such as SiO_2 and CaF_2 that are highly transmissive at these wavelengths. Absorption in these materials only occurs when the intensity is sufficient to initiate two-photon processes. Another example of multiphoton absorption is polytetrafluroethylene (PTFE), a polymer that absorbs very little at $\lambda > 200$ nm and only ablates smoothly via a 2-photon process using ultrashort laser pulses [6].

Although α is an important parameter in determining how strongly a material absorbs laser irradiation, another related issue is the absorbance. From figure 2.1 it can be seen that part of the incident radiation is reflected on the air-solid interface and will never be available for absorption. If a slab of material is considered, the absorbance is defined as

$$A = 1 - R - T$$

with R and T respectively the reflected and transmitted portion of the beam. For sufficiently high absorption T can be neglected.

Figure 2.2 illustrates the typical absorbance for some material types. Note the low absorbance of metals and insulators in the visible to IR due to respectively high reflection at metal interfaces and high transmission of crystalline insulators.

2.1.2 Absorption processes in organic media

The absorption coefficient is used for macroscopic modeling of the absorbing properties of a material. The exact mechanisms involved in the light absorbing behavior of the solid are determined by the nature of the incident light and the material. In the following sections we will focus on organic media as this class of solids includes polymer materials. Other types as metals, semiconductors and insulators are briefly covered in 2.3.

The response of organic compounds to radiation can be understood by the following molecular model. Atoms and molecules can absorb electromagnetic radiation, but only at certain discrete wavelengths. As the discussion will involve transitions between energy levels of a molecule, it is beneficial to associate the wavelength of the incident light with a discrete photon energy (figure 2.3). The different energy levels that occur within a molecule are illustrated in figure 2.4. The three groups of lines correspond to different electronic configurations or states. The most stable configuration is called the ground state electron configuration (S_0) and has
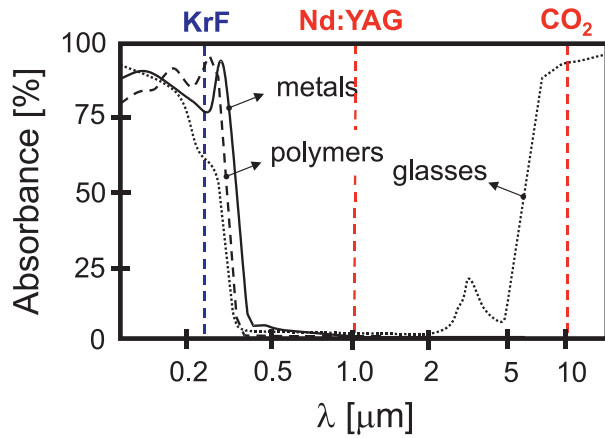
Figure 2.2: Typical absorbance values (source: H. Huegel, "Strahlwerkzeug laser", B.G. Teubner Stuttgart). A polymer absorbance curve has been added to complete the overview.
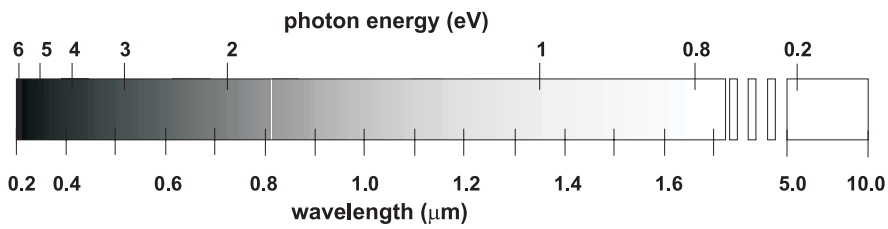
Figure 2.3: Wavelength versus photon energy.

the lowest energy. Certain photons can cause molecules to become vibrationally and/or electronically excited depending on the photon energy:

- Photons corresponding to deep UV and X-ray wavelengths can excite valence electrons to levels that are energetic enough to become ejected from the molecule.

- Visible and UV photons can cause electrons to populate higher energy orbitals with conservation of their spin multiplicity. This means that only singlet-singlet or triplet-triplet excitations are possible when a photon is absorbed. The transition from the ground to an excited electronic state occurs nearly instantaneously, without the atomic nuclei being able to respond yet (Franck-Condon transition).

- Infrared photons can merely excite molecules[2] to one of the many vibrational levels within the same electronic state. The low photon energy is not sufficient for electronic excitation.

- Radiation in the microwave region is even less energetic than infrared radiation. Although it cannot excite vibrations anymore, it can cause molecules to be rotationally excited. These excitations are not represented in figure 2.4 but should be pictured as additional levels between the vibrational excited states.

Note that electronic transitions are usually accompanied by additional vibrational and rotational excitation. A brief overview of some vibrational excitations is given in figure 2.5. Excitations with IR waves are outside the scope of this work and will not be discussed here.

The UV excitations of organic molecules can be identified with some particular electronic transitions in the covalent bonds. Of the many possible excitations ($\sigma \rightarrow \sigma^*$, $\pi \rightarrow \sigma^*$, $n \rightarrow \sigma^*$, $\sigma \rightarrow \pi^*$, $\pi \rightarrow \pi^*$, $n \rightarrow \pi^*$), only the transitions $n \rightarrow \pi^*$ and $\pi \rightarrow \pi^*$ can be triggered with UV and visible light. This is illustrated in figure 2.6 for formaldehyde. The other excitations (involving a σ or σ^* orbital) need photon energies beyond UV. π-bonding is weaker than σ-bonding and generally occurs as a component in a double or triple bond since only 1 σ-bonding is allowed per covalent bond. The weaker nature is a direct consequence of the limited lateral overlap of the original atomic orbitals forming the molecular orbital. This contrary to σ bonds which strongly overlap in the longitudinal direction. Due to the reduced overlap π electrons are less localized and can be more easily triggered by an external electric field.

The functional groups in an organic molecule which exhibit the characteristic absorbing behavior in the UV and visible spectrum, are called chromophores. They contain electrons which can be easily moved by the incident EM wave. Some typical chromophores and their corresponding UV absorption peaks and molar extinction coefficients ε ($lmol^{-1}cm^{-1}$) are given in table 2.2. The extinction coefficient is

---

[2]IR excitation assumes that the molecule has a net dipole moment, otherwise no interaction will take place.
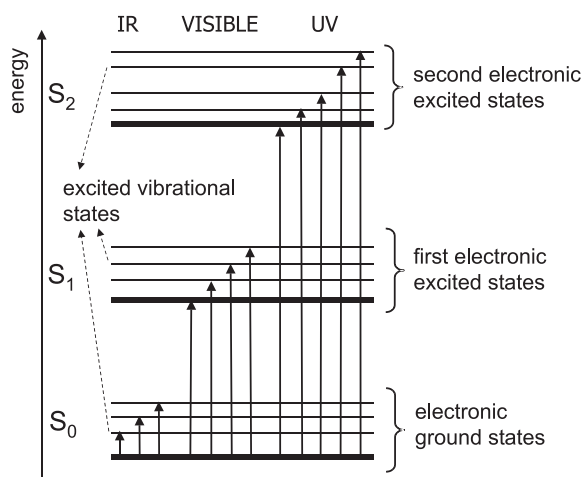
Figure 2.4: Energy levels of a molecule.

related to the absorption coefficient via $\varepsilon = 0.434\alpha/M$ with M the molarity of the chromophore in a solvent (mol/l) and α expressed in cm^{-1}. When the density ρ $(\mathrm{g/cm}^3)$ and molecular weight m (g/mol) of the monomer carrying the chromophore is known, the molarity can be calculated as ρ/m.

The peaks in the table should not be interpreted as discrete wavelengths but rather as absorption bands with a certain width due to the many superimposed vibrational and rotational levels concentrated around the ground and excited electronic states. Note that these peaks generally shift to larger wavelengths as the π-system is extended in the chromophore over several double (or triple) bonds in parallel planes, alternated by single bonds. This behavior is called conjugation and is responsible for delocalizing the electrons even more in the π orbitals. Another observation is that the $n \rightarrow \pi^*$ transition occurs with a smaller probability (lower absorption) than $\pi \rightarrow \pi^*$. The factors that influence this probability are quite complex and outside the scope of this work. However, one obvious factor is the overlap between the orbitals involved in the transition. n and π^* nearly show no overlap, contrary to π and π^*. As a consequence the $\pi \rightarrow \pi^*$ transition is much more likely than the one involving a n orbital.

2.2 Relaxation processes in organic media

In the previous sections it was shown how electrons can be promoted to excited states due to absorption of UV photons. In general the excited electronic state will be accompanied by an additional vibrational excitation. From this state the electron will rapidly relax to the vibronic ground level within the same electronic state as illustrated in figure 2.7. Organic molecules consisting of many atoms (such as polymers) show a high density of vibrational and rotational levels, facilitating
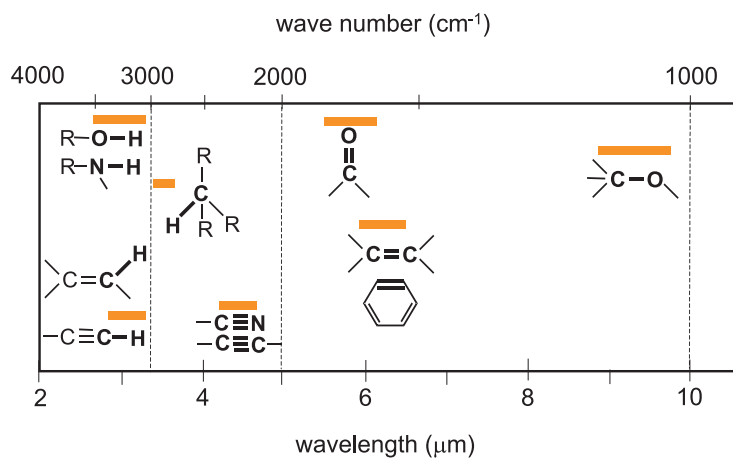
Figure 2.5: IR spectra of some important molecular bond excitations (stretching of the molecule).
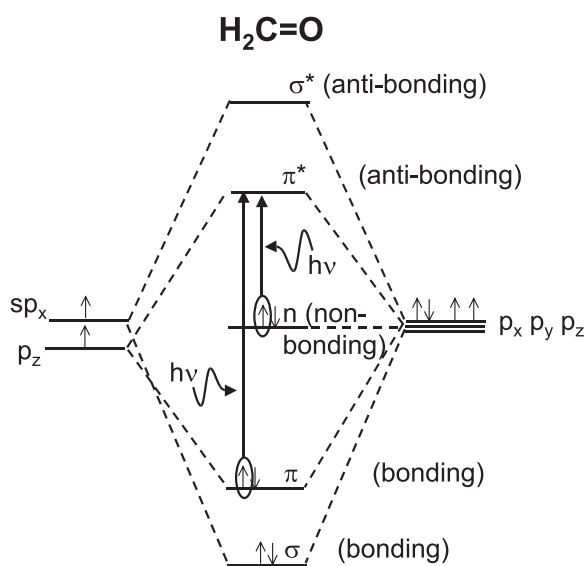
Figure 2.6: Molecular orbital diagram for formaldehyde.
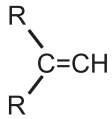
chromophore	λ_{max} (nm)	transition	ε (l/mole cm)
CH_3-CH_3	135	$\sigma \rightarrow \sigma^*$	-
$R-O-H$	185	$n \rightarrow \sigma^*$	500
$R-S-H$	225	$n \rightarrow \sigma^*$	125
$H_2C=CH_2$	165	$\pi \rightarrow \pi^*$	10000
$HC \equiv CH$	173	$\pi \rightarrow \pi^*$	6000
$C=C-C=C$	217	$\pi \rightarrow \pi^*$	21000
⬡	180	$\pi \rightarrow \pi^*$	60000
	200	$\pi \rightarrow \pi^*$	8000
	255	$\pi \rightarrow \pi^*$	215
$\begin{smallmatrix} R \\ \quad C=CH \\ R \end{smallmatrix}$	150	$\pi \rightarrow \pi^*$	-
	190	$n \rightarrow \sigma^*$	1900
	280	$n \rightarrow \pi^*$	20

Table 2.2: Transition types and corresponding λ peaks in the UV for some chromophores. ε is the molar absorptivity or extinction coefficient.

rapid relaxation on a time scale of tens of fs to ps. In addition, interactions with the neighboring molecules (phonons, collective vibrations) can enhance the vibrational relaxation rate.

In a second phase the electronic state will relax to the ground state. A brief overview of some important relaxation mechanisms is given below.

Fluorescence

This relaxation process is accompanied by the emission of a photon. As the ground electronic state features many vibrational levels, the emission can have several peaks at different wavelengths. The lifetime associated with this radiative decay can be estimated at the order of ns.

Phosphorescence

When relaxation takes place between a triplet and a singlet state, the radiative decay is called phosphorescence. It is a forbidden transition as there is a change in electron spin multiplicity involved. Therefore, the transition has a low probability and will thus feature a long lifetime of the order of ms and longer.

Internal conversion

Via this non-radiative decay mechanism the excited electronic state can relax to the ground state with the same spin multiplicity, but with a much higher vibrational excitation level. After internal conversion there is rapid relaxation to the ground vibrational state.

Intersystem crossing

This process has generally a low probability as it involves a formally forbidden change of spin multiplicity. Still, it can be present when a vibronic energy level of the singlet is nearly degenerate with the energy of a triplet vibronic state. After intersystem crossing there will be a rapid relaxation to the ground vibrational state of the excited triplet. From there, either phosphorescence or external conversion can take place.

Photochemical reaction

This relaxation mechanism will chemically change the organic molecule. Typical reactions are photodissociation, photosynthesis and photo-induced electron-transfer. In case of photodissociation the molecule will disintegrate in two parts and the reaction can be written as:

$$AB + h\upsilon \rightarrow A + B$$
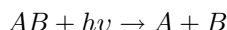
External conversion

In this case the excited molecules transfer their energy to other species while they relax to the ground state. This type of conversion can take place when the spectrum of a substance is measured: the chromophores are diluted in a solution and energy transfer to the solvent is possible.

The electronic relaxation pathway with the shortest lifetime will dominate the decay process. During ablation polymers will not likely relax via fluorescence or phosphorescence [7, 8], but rather via a photochemical reaction and internal conversion. In the first case photodissociation [8, 9] will take place, leading to the so-called 'cold ablation' process. The other possibility is internal conversion [1, 8, 9, 10, 11, 12, 13]. This means that the electronic energy is released as vibrational energy and thus results in heat generation. In [8] lifetimes for photodecomposition and internal conversion are estimated respectively $\tau_{DC} = 1$ ns and $\tau_{IC} = 38$ ps for polyimide. An overall radiationless decay time of 35 ps was measured for the excited states in polyimide in [14] . Schmidt *et al.* [8] claims for PMMA $\tau_{DC} = 0.25$ ns and $\tau_{IC} = 0.05$ ns. For both polymers internal conversion can be considered the main relaxation mechanism.

2.3 Absorption and relaxation in other materials

For completeness we discuss here briefly excitation and relaxation processes in non-organic materials.

Metals

Metals have a valence band which is partially filled with electrons (figure 2.8). The latter behave as a pool of free electrons and will instantly respond to an incident EM wave by strong oscillation, thus enabling high reflection. E.g. Ag reflects 98.4 % at 550 nm. The photon absorption mechanism differs according to the
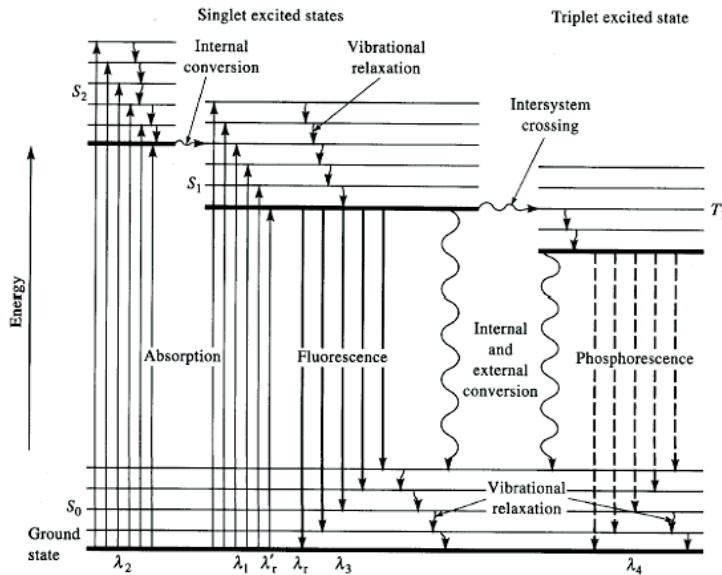
Figure 2.7: Relaxation processes from electronic excited states.

wavelength of the incident radiation: intraband transitions account for the strong absorption down to deep UV and interband electronic transitions start playing a role when the photon energy exceeds the bandgap, typically at UV wavelengths. Intraband transitions can only occur towards vacant states, therefore the energy of the incident photons will determine the range of electrons that can participate: IR wavelengths only affect electrons very close to the Fermi energy at low temperatures. E.g. at the CO_2 laser wavelength of 10.6 μm, the photon energy is 0.12 eV and thus much smaller than the Fermi energy of a metal, typically several electron volts. At elevated temperatures the electrons will occupy states according to a Fermi-Dirac distribution. Consequently, a larger range of electron energy levels can interact with IR photons. The low photon energy however, will merely be able to redistribute those energy levels close to the Fermi energy.

At UV wavelengths electrons can be ejected from the metal since UV photons can have energies comparable to the work function of the metal, typically 4 to 5 eV. Electrons that do not leave the surface become highly excited and will dissipate their excess energy by electron-electron and electron-phonon scattering. As the electrons get mutually faster in thermal equilibrium than with the lattice, it is possible that short intense UV pulses decouple the electron temperature from the lattice temperature. This decoupling can lead to superheating of the electrons and can be achieved with ultrashort laser pulses. Typical values for α in the UV region are of the order of 10^6 cm^{-1}.

The increased kinetic energy of the electrons is transferred to the lattice on time scales of ps via electron-phonon scattering, resulting in considerable elevation of
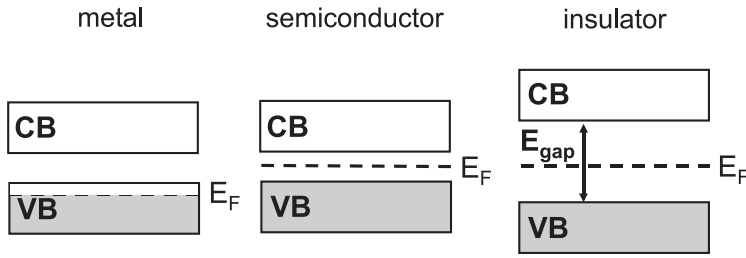
Figure 2.8: Band structure for metals, semiconductors and insulators.

the temperature. For long pulses (longer than a few ps) heating occurs during the pulse and one can treat absorption and heating as simultaneous processes.

Insulators and semiconductors

Insulators show a wide electronic bandgap, typically above 5-6 eV. Absorption can occur at IR due to excitation of ionic vibrations in the crystal. At UV wavelengths mainly interband transitions (non-localized absorption), excitonic resonances (close to $E_{bandgap}$) and the presence of impurities and defects (localized absorption) are responsible for absorption. The defect and impurity concentration is determined by the preparation process and radiation history.
In general the bandgap is higher than the photon energy, with typical bandgap values between 7 and 11 eV. This means that multi-photon absorption is required for interband transitions. One of the main insulator materials is SiO_2, commonly referred to as fused quartz. The bandgap of this material is 9.1 eV, requiring a photon wavelength of 136 nm. Some very moderate absorption peaks can be detected between 4 and 7 eV due to contaminants and defects. Typical 1-photon absorption values are 0.001-0.02 cm^{-1} at 264 nm, while 2-photon absorptions can be estimated at 1.7×10^{-11} cmW^{-1} [5]. Strong UV irradiation can introduce additional defects and absorption centra in the crystal matrix, leading to enhanced absorption.

Semiconductors have a bandstructure similar to that of an insulator but feature a much smaller bandgap: typically of the order of 1 eV. IR photons ($\lambda > 3$ μm) are generally not energetic enough to cause interband transitions, but UV photons are able to strongly trigger 1-photon interband absorption. High absorption coefficients ($\sim 10^6$ cm^{-1}) are possible in the visible and UV region.

Compared to metals, the electronic energy tends to be more localized in these materials. Still, one can argue that most of the energy is again quickly transformed into thermal energy.

23

2.4 Pulsed excimer laser ablation of polymers

In this section we will limit the discussion to the case of polymer ablation with pulsed excimer lasers. This phenomenon is by far one of the most popular subjects in literature related to laser ablation. Even more so since it has been extensively proven that excimer lasers are capable of machining commercial polymers with high accuracy and with little damage to the remaining material.

Next to excimers, quite some other laser sources are used for material removal: in industrial environments IR lasers as CO_2 and Nd:YAG are commonly employed for processing metals and ceramics. On research level, emerging technologies as femtosecond laser ablation are being explored. As an elaborate treatment of these techniques is out of the scope of this work, we refer the interested reader to literature on this topic.

2.4.1 Phenomenological description of laser ablation

When an EM wave enters opaque material, part of the radiation will be absorbed via vibrational or electronic excitations as described in the previous paragraph. Assuming a 1-photon absorption process, the beam intensity will drop exponentially along the propagation axis according to the Beer-Lambert law (see 2.1). The absorbed energy per unit volume in the material locally equals $\alpha I(x)$. For sufficiently high values of α, this energy is spatially confined in a very thin layer beneath the surface. When the beam fluence is increased, it is possible that the deposited energy will equal or surpass the amount required for decomposition. Assuming that α remains constant throughout the full range of intensities, the highest amount of energy is absorbed at the material interface where the intensity is maximal. As a consequence, the decomposition will start there. For a laser emitting short and intense pulses, this dissociation process will occur on a very small time scale in the order of ns. As the intrinsic volume of the degradation products −containing mainly gaseous components− is a multiple of the original solid, the decomposed material will be forcefully ejected ('phase explosion') from the surface. The species travel with a speed ranging from 10^4 to 10^5 cm/s and are preceded by a shockwave front due to compression of the ambient medium. These observations are illustrated in figure 2.9. The ejected plume consists of vapor −driving gas− and fragments of which some will be redeposited in the neighborhood of the ablated area. These particles are called debris and are often undesired. Deposition of debris can be minimized by replacing the ambient medium by He or H_2 at low pressures. These gases allow the plume to expand much faster and thus limit the interaction time between the ejected fragments, leading to much less particle formation and recondensation. The ambient medium, either vacuum or air at atmospheric pressure, has no noticeable influence on the etch rate [10].

After evaporation a clean and well-defined cavity with the same lateral dimensions as the laser beam cross-section can be seen in the polymer surface. An example of an ablated crater is given in figure 2.10. The removal of 28 μm polycarbonate required 100 pulses at a fluence of 440 mJ/cm^2, corresponding to an ablation rate of 0.28 μm per pulse. If we assume a square pulse shape of 16 ns, the applied laser
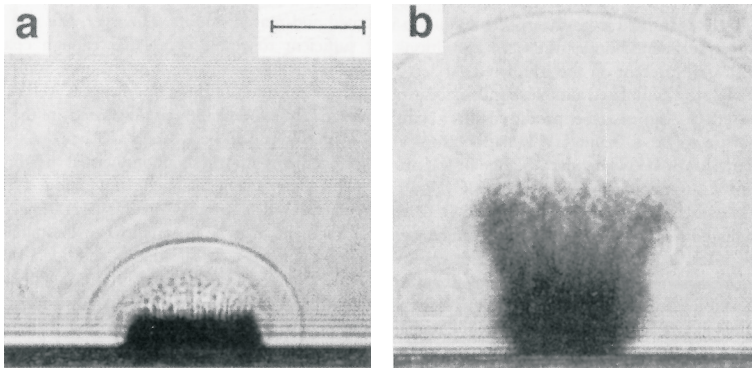
Figure 2.9: Photographs of the blast wave and material ejected from a PMMA surface on the impact of a single UV laser pulse from an ArF excimer laser. The time intervals after the start of the laser pulse are (a) 500 ns and (b) 2.9 μs [4]. The scale bar length is 0.5 mm.
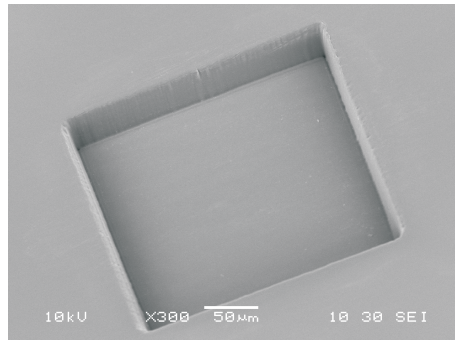
Figure 2.10: Laser ablated cavity (250×250 μm) in polycarbonate under atmospheric pressure. Laser source: pulsed KrF excimer laser operating at 248 nm. 100 pulses of 440 mJ/cm^2 were applied to drill 28 μm deep.

intensity can be estimated at 2.75×10^7 W/cm^2.

This phenomenon, the removal of material due to interaction with strong laser irradiation, is called laser ablation (Latin: *ablatio* − removal, taking away). In order to avoid confusion with related laser processes, this definition should be completed with some additional requirements:

The ambient medium is inert or vacuum

This excludes any process that involves a chemically reactive medium. In this case the laser light would not be solely responsible for the material removal (cfr. laser-assisted chemical etching).

Ablation is due to the absorbed laser energy in the material

From experiments it is known that mechanical failure of a transparent material can be caused by generation of a shock wave in the ambient medium (a gas or liquid).

A vapor plume of ablation products is produced during ablation

Through formation of microcracks, surface crumbling can be introduced by laser irradiation. Although it complies with the former two requirements, this mechanism is not considered a laser ablation process.

2.4.2   Literature review

The first detailed phenomenological descriptions of ablation in polymers due to pulsed ultraviolet lasers are reported by Srinivasan *et al.* [15, 16] in 1982, although laser-induced etching of organic matter was already observed by others before they started their research. A range of polymers including polymethyl methacrylate (PMMA), polyethylene terephthalate (PET) and polyimide (PI) have been ablated and investigated since, mostly using UV excimer lasers emitting nanosecond pulses. For all polymers the conclusion was that for sufficiently high laser fluences above a threshold value F_{th}, ablation of the polymer takes place. The removal process was accompanied by a loud audible report as a result of the shock wave propagating at supersonic velocities due to the explosive nature of ablation. Another observation was the generation of a bright plume above the sample [15]. Inside the material stress waves were measured that nearly coincided with the moment of pulse penetration. For subthreshold fluences the stress wave was attributed to local volumetric expansion of the material, leading to a compressive front that is sometimes followed by a rarefaction wave[3]. For fluences above F_{th}, recoil pressure of the ejected material is held responsible for stresses up to 2×10^6 Pa (20 atm!). An excellent review on early work on laser ablation can be found in [9].

In later years important contributions to a better understanding of the excimer laser ablation process of polymers have been made. Initial focus was on the photothermal or photochemical nature of the process [1, 11, 12, 2, 18] and related

---

[3]The origin of the material expansion is not unambiguous: according to [9] thermal expansion is responsible for the stress wave, while Zweig *et al.* [17] claim —many years later— that gas formation inside the material and subsequent out-diffusion is likely to be the primary cause. Their experiments also revealed a different stress behavior for fluences considerably higher than F_{th} (above ∼1 J/cm^2), where plasma plume expansion plays a major role. As it partially decouples the beam from the laser irradiation, the increase in stress becomes less distinct.

mechanisms as thermal diffusion and the dynamics of a moving ablation front [19]. More recently the aspect of plume shielding [8, 20], incubation effects [8, 18] and bleaching [1, 8, 18, 20] has been introduced. The description of these mechanisms has not always led to a successful correlation between experimental ablation rates and model predictions. The most prominent cause is the lack of models that incorporate *all* of these mechanisms with process parameters obtained from calculations based on solid arguments and measurements rather than from fitting. An exception can be made for models developed by Arnold *et al.* [21] and Schmidt *et al.* [8]. Although exclusion of photochemical effects in the theory of Arnold *et al.* obviously limits the number of polymers where it can be used successfully.

In the following discussion on modeling excimer laser ablation of polymers, we have chosen to use a very simple model (Beer model) as starting point. In a second step we comment on the shortcomings of this model, gradually clarifying the complexity of the ablation phenomenon. Finally we discuss how the model suggested by Schmidt *et al.* can be implemented numerically to predict etch rates. The results will be compared to our experimental data on several commercially available polymers.

2.4.3 Beer model for ablation depth prediction in polymers

In this approach that was widely adopted in early literature [9], it is assumed that absorption and ablation are two processes that occur *sequentially* and do not overlap in time. Taking Beer's absorption law into account, we can write for the beam fluence $F_m(x)$ (J/cm^2) inside the material (integrated beam intensity over the pulse length)

$$F_m(x) = (1-R)Fe^{-\alpha x}$$

with R the reflectivity at the surface and F the fluence incident on the solid. For a square pulse shape, the pulse intensity I equals F/τ with τ the pulse length. It has been experimentally observed that laser ablation only occurs if a minimum pulse fluence F_{th} is employed. In general the pulse length should be sufficiently short for ablation and will influence the threshold F_{th}. If we denote the etch depth with d, then we can write for fluences $F > F_{th}$

$$d = \frac{1}{\alpha} ln((1-R)F/F_{th}) \tag{2.1}$$

as etching will automatically stop at the depth where the local fluence has dropped below F_{th}. This equation describes the etching depth versus pulse fluence independently of the underlying processes causing the material removal. The physical interpretation of a threshold level is rather straightforward for multi-photon absorption, but not evident for a single-photon process. One can argue that ablation only occurs if a minimum amount of bonds have been broken per unit volume and the internal stresses in the exposed volume have become sufficient to eject the fragments. This will take a certain F_{th} to obtain a sufficient density of absorbed photons per time unit $(\alpha F_{th}/\tau)/h\nu$ in order to surpass various relaxation paths as

27
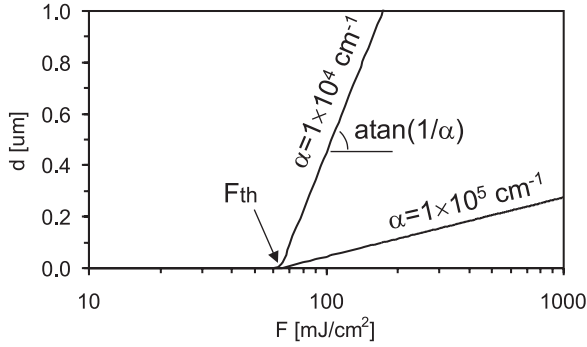
Figure 2.11: Calculated ablation rate versus pulse fluence according to the Beer model for $F_{th} = 60$ mJ/cm^2 and $R = 6\%$.

heat diffusion and bond healing.

The surface reflectivity is often ignored as it generally accounts for only a mere 6-10 % of the total fluence. A graphical representation of (2.1) is given in figure 2.11 for $F_{th} = 60$ mJ/cm^2.

The intersection of the graph with the ordinate equals F_{th} and the slope is $1/\alpha$. This means that higher values of α result in slower ablation rates as the laser energy remains confined in a thinner region. The absorption coefficient is highly dependent on the laser wavelength and the material characteristics. In general higher UV absorption and a lower F_{th} is observed at shorter wavelengths. This is in agreement with the theory that a minimum amount of energy αF_{th} needs to be deposited in the ablating layer. High ablation rates can be achieved for polymers with low α at sufficiently high fluences ($F >> F_{th}$). In practice a minimum value of 10^4 cm^{-1} is desired for α to initiate ablation.

We have experimentally verified the ablation behavior of 5 commercial polymers at the ArF and KrF excimer wavelengths. These polymers are Polycarbonate (PC), Polyethylene terephthalate (PET), Polyimide (PI), Polymethylmethacrylate (PMMA) and Polystyrene (PS). The maximum pulse fluence has been limited to 1 J/cm^2 as high-accuracy polymer lasermachining typically require fluences in this range.

The etch rates versus log fluence and their linear fits are shown in figure 2.12 for PC and PI. The other polymers show a similar behavior. As can be seen from both graphs, the ablation rates can be adequately approximated by a linear fit. Although a small deviation can be observed between experiment and model for higher fluences (0.9 J/cm^2 and above). The absorption coefficients and fluence thresholds of all the polymers are derived from fitting experimental data to expression (2.1) and are given in table 2.3.
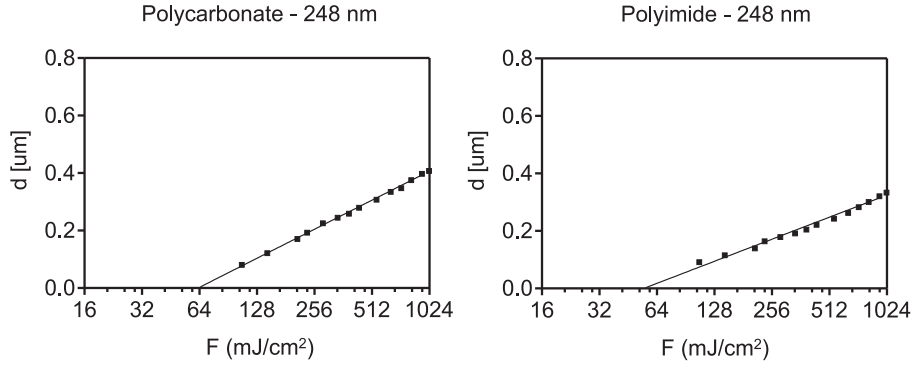
Figure 2.12: Beer model applied to laser ablation of PC and PI at 248 nm (16 ns pulse duration). The etch rates are calculated via the measured cavity depth for 20 successive pulses.

	193 nm (ArF)		248 nm (KrF)	
polymer	F_{th} [mJ/cm^2]	α [μm^{-1}]	F_{th} [mJ/cm^2]	α [μm^{-1}]
PC	21.3	18.9	62.9	6.9
PET	18.4	15.6	36.9	6.6
PI	25.1	18.6	54.6	9.0
PMMA	33.9	6.3	272	1.0
PS	15.3	24.1	135.6	4.4

Table 2.3: Calculated absorption coefficients and threshold fluences according to the Beer model. Reflection losses have been ignored.

wavelength	α_{lin} [μm^{-1}]	α_{Beer} [μm^{-1}]	remarks
193	45	18	from [2, 3]
248	22-26	10-16	from [10, 22]
308	10-11	9-9.4	from [10, 2, 23]

α_{lin} is the absorption coefficient measured with UV spectroscopy at fluences below ablation threshold.
α_{Beer} is the absorption coefficient that follows from fitting measurement data to (2.1).

Table 2.4: Absorption coefficients of polyimide for different fluence levels and wavelengths.

2.4.4 Validity of the model

There are two main objections against the Beer model. Firstly, it usually only fits the data within a very limited range. It is not valid for very low fluences as ablation rates seem to be a non-linear function of log fluence close the threshold [19] (the so-called Arrhenius tails [13]) and neither applies to substantial fluences of several J/cm^2. Secondly, the calculated absorption coefficients generally do not correspond to the true values as illustrated by table 2.4 with spectroscopic data.
In addition the model assumes that F_{th} is unambiguously determined by the material properties and laser characteristics. In practice, accurate measurement of the threshold is quite difficult due to the Arrhenius tail and is also hindered by incubation and precursor effects. The latter means that the threshold can depend on the number of pulses fired onto the substrate: ablation will start at lower fluences for a train of pulses than for a single pulse. This is typically the case for low absorption polymers as PMMA (400-1000 cm^{-1} at 248 nm) and PTFE (158 cm^{-1} at 248 nm [6]).

The limited validity of the model is the result of some false assumptions. It assumes that absorption and etching are separated in time, while several reported experiments have revealed that decomposition and ejection of degraded material starts within a few nanoseconds and thus during the pulse [4, 24]. Another shortcoming of the Beer model is that the duration of the pulse is irrelevant since only the time-integrated intensity appears in the equation. It has been shown that the exact pulse length has little influence on F_{th} [25] and the nominal etch rate of some polymers with XeCl ($\lambda = 308$ nm) pulses in the range 7-300 ns. Although evidence can be found that this is not the case for PMMA [26] due to incubation effects. The use of fluence as a parameter is a natural consequence of the fact that it can be measured far more easily than the time-dependent intensity of a pulsed laser. As excimer lasers typically emit pulses of 10 to 40 ns (well within the range 7 to 300 ns), fluence can be considered the relevant quantity for determining the ablation depth for these lasers. One should keep in mind that for some polymers heat diffusion during the pulse cannot always be disregarded. Although polymers have a very small heat diffusivity (a typical diffusion length $\sqrt{Dt}$ of 0.1 μm during a 20 ns laser pulse), it is obvious that heat diffusion cannot be ignored for polymers with

strong absorption[4]. Note that when ultrashort fs or ps pulses are compared to the ns regime, the effect of pulse length becomes substantial: etch rates seem to change dramatically due to the occurrence of non-linear effects and plasma shielding.

A final remark concerning the Beer model is related to precursor or incubation effects: low absorption polymers as PMMA need several pulses before any physical ablation occurs, even at fluences far above threshold. This effect is not incorporated in equation (2.1). As it occurs both at long and short pulse-to-pulse intervals, thermal effects can be ruled out to a large extent. It is believed that during these initial pulses, the polymer is chemically modified into a highly absorbing material [27].

In the following section we will discuss several physical mechanisms that occur during ablation and indicate how these aspects can be modeled mathematically. Note that although the Beer model does not take into account most of these phenomena, it remains quite popular in literature due to its simplicity and the fact that the ablation-fluence curve of a polymer can be characterized by only two parameters.

2.4.5 Physical processes and observations during ablation

Photochemical versus photothermal ablation

The Beer model assumes a minimum fluence for ablation, irrespective of the underlying physical mechanism. It is generally accepted that there are two pathways for material removal. In case of photothermal ablation, ablation is obtained by laser heating the material locally until it vaporizes. The photochemical pathway assumes that electronic excitation of the chromophores leads to direct dissociation without any intermediate heat dissipation. It is instructive to comment on both mechanisms for material removal in a more detailed way.

In the photothermal case [12] the electronically excited chromophore relaxes back to the ground state via internal conversion with the absorbed photon energy $h\upsilon$ being fully converted into vibrational energy. This means that the energy will be dissipated in the material via heating. If n_0 and n_1 denote the population of the chromophores in respectively the ground and excited electronic states S_0 and S_1 ($n_0 + n_1 = n_c$ is the total chromophore density), then we can write

$$\frac{dT(x,t)}{dt}\bigg|_{ic} = -\frac{dn_1(x,t)}{dt}\bigg|_{ic} \times \frac{h\nu}{c_p}$$

for the increase of temperature due to internal conversion. c_p is the heat capacity or specific heat (J/Kcm^3). The rate of electronic excitation to S_1 is determined by the absorption dynamics taking the Beer-Lambert law into account:

$$\frac{dn_1(x,t)}{dt}\bigg|_{abs} = -\frac{dn_0(x,t)}{dt}\bigg|_{abs} = \alpha \frac{I(x,t)}{h\nu}$$

---

[4] For strong absorption, the pulse energy is largely confined in a thin layer with thickness $1/\alpha$. For PI this means a layer smaller than 0.1 μm, which becomes comparable with the heat diffusion length.
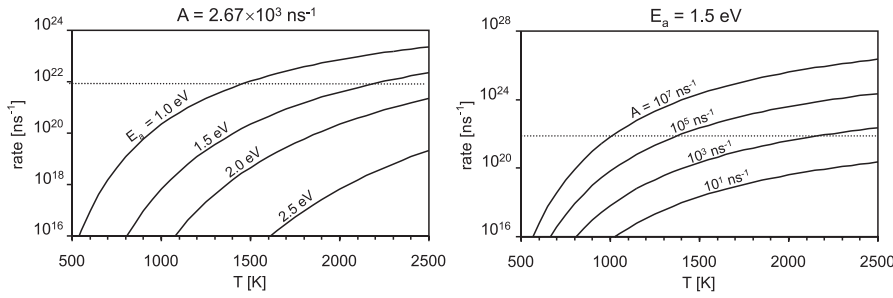
Figure 2.13: Thermal dissociation rate versus material temperature. For polyimide, $A_{therm} = 2.67 \times 10^3$ ns^{-1} and $E_a = 1.5$ eV [13]. The dotted line indicates the required amount of broken bonds for ablation (90 % of the present bonds).

with $I(x,t)$ the local beam intensity.
The heating will trigger thermal bond breaking and the dissocation rate can be described by

$$\left.\frac{dn_b(x,t)}{dt}\right|_{therm} = k_{therm}(T) \times n(x,t)$$

with n the amount of available bonds for cleavage (cm^{-3}) and n_b the amount of broken bonds. The rate constant can be described by an Arrhenius expression [1, 8, 12, 21, 28, 2] $k_{therm} = A_{therm}e^{-E_a/k_bT}$ with A_{therm} a frequency factor (s^{-1}), E_a an activation energy (eV) and k Boltzmann's constant. For $n = 8.95 \times 10^{21}$ cm^{-3} —which equals the density of the weakest bonds for Kapton [1, 13, 20]— the calculated thermal dissociation rates for several values of A_{th} and E_a are given in figure 2.13. From the graph we can derive that on the scale of a typical excimer laser pulse length (10-20 ns), a surface temperature of around 1600 K is needed. This value agrees well with [29, 30]. The thermal dissociation process consumes a reaction enthalpy ΔH, leading to a decrease in temperature:

$$\left.\frac{dT(x,t)}{dt}\right|_{therm} = -\left.\frac{dn_b(x,t)}{dt}\right|_{therm} \times \frac{\Delta H}{c_p}$$

with $\Delta H > 0$ for a reaction requiring supply of energy. Material dissociation is assumed when n_b reaches a threshold value which is determined by the composition of the polymer.

When a photochemical process is considered, deactivation of the excited chromophore takes place via a dissociation of the bond instead of internal conversion. Note that vibrational relaxation within the excited state might preceed the photochemical process, leading to partial heating of the substrate. If we assume that this dissocation is defined by a simple rate constant k_{dd}, we can express the direct dissociation as

$$\left.\frac{dn_b(x,t)}{dt}\right|_{dd} = k_{dd} \times n(x,t)$$

In [8] the rate constant k_{dd} is estimated at 1 ns^{-1} for PI at 248 nm. Similar to the case of thermal ablation, material decomposition is assumed when n_b reaches a threshold value.

In practice it is not easy to determine whether degradation takes place via a primarily thermal or photochemical process. Experimental verification of k_{dd} and k_{th} can be tricky in typical ablation situations that are marked by pulse delivery and material removal on nanosecond scale, and a large uncertainty on temperature and effective material parameter values as C_p.
One approach involves inspection of the ejecta. Interpretation of the plume composition and velocity distribution has favored the photothermal theory in many cases, still it has seldomly ruled out a photochemical contribution. In some cases the ejected fragments even differ significantly from what would be expected in case of pyrolysis. For example it is known that PMMA degrades via an unzipping mechanism during thermal decomposition, resulting in a high yield of monomer in the vapor. But inspection of the plume during KrF or ArF ablation evidences that little or no monomer is present in the plume generated by ablation. We can conclude that PMMA does not ablate via the usual thermal degradation, suggesting that there is a photochemical mechanism active. In turn, this contradicts the presence of a resolidified layer and melt splashes around the edges which clearly indicates that high temperatures accompany ablation.

From a processing point of view it is of little importance if the underlying mechanism is either a thermal or photochemical process as both decomposition pathways make it possible to achieve well-defined ablation cavities with little thermal damage. For photochemical dissociation this claim is straightforward. For the thermal process it requires some insight in the dynamics of material removal: once a layer of material is heated to the proper temperature and dissociates, the decomposed layer will be ejected together with the excess of thermal energy stored in its volume. In other words, heating of surrounding material will primarily occur *before* full decomposition. The time scale for dissociation is of the same order as the pulse length of excimer lasers, meaning that the time for heating the surrounding material via conduction is very short. We can clarify this statement with a numerical example. It is known that polyimide degrades thermally during excimer laser ablation [10, 2, 31]. Using a numerical model we can calculate the temperature at the time ablation ends inside that material exposed to KrF laser pulses of 0.5 J/cm^2. From the temperature profiles in figure 2.14, we can clearly conclude that the material removal process results in a much cooler surface than when ablation would be ignored[5]. Without ablation the temperature is elevated to more than 32000 K, while only 3700 K is calculated in case of ablation. The thermal energy stored in the remaining material is only 8 % of the total pulse energy, meaning that the major part is ejected with the dissociated fragments. It should be noted that the high temperature in case of inhibited ablation does not reflect any physical meaning, it simply points out that ablation cools down the material substantially. The numerical model we used for these calculations is based on a simplified thermal ablation scheme that has been proposed by Cain *et al.* [1]. We extended the

---

[5]Inhibition of ablation is accomplished by setting E_a to an immense 10^5 J/mol instead of the more realistic value of 502 J/mol.

chromophore density	8.7×10^{21} cm^{-3}
thermal diffusivity	4.0×10^{-4} cm^{2}s^{-1}
absorption coefficient	2.6×10^5 cm^{-1}
absorption cross-section	3.0×10^{-17} cm^{-1}
electronic relaxation constant	35 ps
broken bonds threshold for ablation	50 %
specific heat	1.55 Jcm^{-3}K^{-1}
activation energy (Eyring model)	502 kJ/mol
wavelength	248 nm
pulse length (FWHM)	16 ns

Table 2.5: Material and laser parameters for the calculation of temperature in polymide.

model to take heat diffusion and material decomposition during pulse heating into account. The equations governing thermal ablation according to Cain *et al.* are described in the appendix. The material and laser parameters are given in table 2.5.

Via a discretization of the pulse in short time slices of length dt, the energy and temperature distributions inside the material are calculated. Diffusion will spread the thermal energy in time and thermal dissociation will selectively remove material. A layer of material is considered ablated when 50 % of the bonds are broken. Note that an evaporation enthalpy ΔH is not taken into account in the calculations and would even further decrease the surface temperature.

Another interesting feature is the effect of pulse length on the thermal load. In case of a purely thermal process, the pulse length will have a large impact on the heat dissipation in the material. From table 2.6 it can be seen that the fraction of thermal energy left in the material after ablation with 245 ns pulses is about twice as large as for the shorter pulses (2.5 and 16 ns). At the same time, the total ablation depth seems to be little effected by the pulse duration in the ns regime. In figure 2.15 the temporal behavior of etch depth is depicted. As expected, the lower intensity of the long pulses considerably delays the start and the end of ablation. When very long pulses are considered ($\tau > 0.1$ ms), the explosive nature of the process will be lost and material removal will turn into a gradual surface evaporation process.

In a following section a more accurate model will be presented. Although [1] over-estimates the activation energy and thus the temperatures at the material surface (roughly by a factor of 2), it is still very suitable for qualitatively demonstrating surface cooling by ablation and the influence of pulse length on the thermal load.

Moving ablation interface and plume absorption

It has been repeatedly reported that the decomposition and removal process starts during the laser pulse for nanosecond laser pulses [4]. This implies that calculation
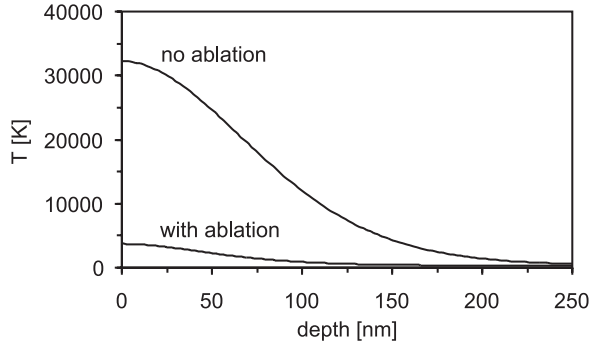
Figure 2.14: Effect of material removal on temperature in polyimide resist, irradiated with 16 ns pulse of 0.5 J/cm^2 from a KrF laser. In one case ablation was inhibited by substantially increasing the activation energy for thermal degradation. The temperature profile is taken at the end of the ablation process (for the nominal activation energy), 56 ns after the pulse started. $d = 0$ is the true material surface after the pulse.

pulse length (FWHM)	2.5 ns	16 ns	73 ns	245 ns
end time [ns]	16	57	160	425
ablation depth [μm]	0.22	0.22	0.22	0.21
energy left in material [%]	6.9	8.0	11.1	16.3

Table 2.6: Impact of pulse length in a thermal ablation process (KrF $-$ 0.5 J/cm^2).
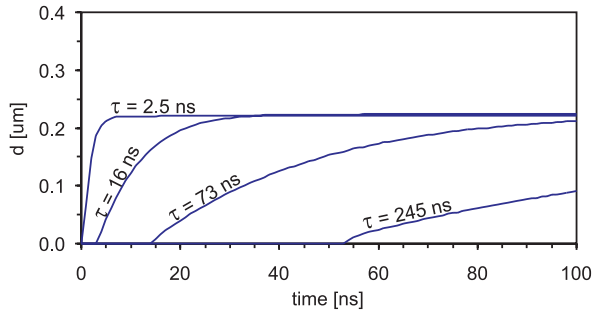
Figure 2.15: Ablation depth as function of time (KrF $-$ 0.5 J/cm^2).

of pulse absorption at a time t_i should incorporate a modified absorption coefficient for the degraded material layer due to decomposition at $t < t_i$. A kinetic model [19, 24] has been developed to take the moving interface into account by postulating that its velocity is given by

$$v(t) = k(I_s(t) - I_{th})$$

with I_{th} a threshold value for ablation and k a rate constant expressed in $cmW^{-1}s^{-1}$ (figure 2.16). The etch depth after the laser pulse is then given by

$$\int_0^\tau k(I_s(t) - I_{th})dt$$

In this formula I_s is the intensity of the beam that reaches the solid material surface and should thus incorporate plume absorption. The plume consists primarily of non-absorbing gaseous products as CO, CO_2 and H_2. Still there is a considerable amount of substances with a more complex composition. These can be the monomer, polymer and other fragments and may absorb the laser beam. A number of techniques are employed for analysis of the plume composition: IR spectroscopy, optical spectroscopy, GC/MS (Gas Chromatography and Mass Spectroscopy), LIF (Laser Induced Fluorescence) spectroscopy and TOF-MS (Time-Of-Flight Mass Spectroscopy). More details on plume composition can be found in [31, 32].

Usually, the absorption of the decomposed or plume material is modeled by a single-photon absorption coefficient β and the fraction of absorbed light at a time t is given by $1 - e^{-\beta d(t)}$ with $d(t)$ the instant ablated depth. We can then write for the beam intensity on the moving material surface

$$I_s(t) = I_0 e^{-\beta d(t)}$$

with I_0 the laser beam intensity. In other words, the plume acts as an attenuating layer of material that grows in time due to ablation.
A more accurate model takes plume expansion into account. As the plume leaves the surface, it expands slowly with a semi-angle of $\theta_{plume} = 20 - 30°$. It remains peaked in the direction perpendicular to the surface [32]. The expansion will obviously reduce the local beam attenuation as the concentration of absorbing species decreases away from the surface. If we neglect the forward peaking and assume a homogeneous expansion within an angle θ_{plume} of the plume particles with all the same constant velocity v_x along the surface normal (figure 2.16), then we can write for the instant beam fluence [8]

$$I_s = I_0 \int_{-d(t)}^{pf} e^{-\beta(x)x}dx$$

where we integrate from the time-dependent cavity bottom to the upper plume front.
The variable absorption coefficient is given by

$$\begin{aligned}
\beta(x) &= \frac{1}{\left(1 + \frac{2x}{\phi} \times tan(\theta_{plume})\right)^2}\beta_0 & x > 0 \\
&= \beta_0 & x < 0
\end{aligned} \tag{2.2}$$

36
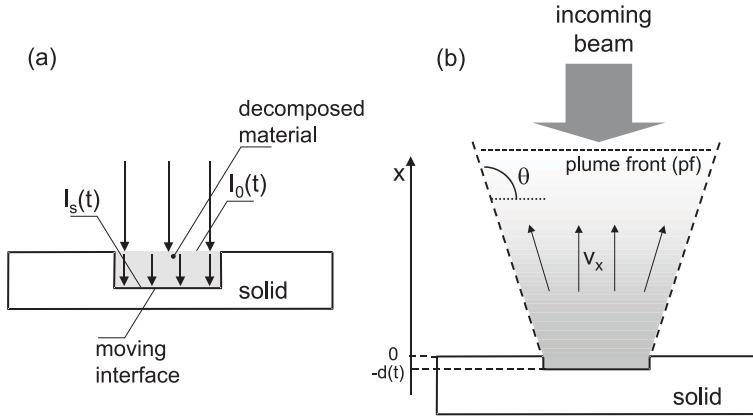
Figure 2.16: Moving interface during pulse absorption (a) and absorption by the decomposed layer and plume (b).

with ϕ the beam diameter and β_0 the plume absorption coefficient before expansion. The plane $x = 0$ is the initial material surface. Equation (2.2) expresses that as long as the plume propagates within the crater, no expansion can take place and the absorption remains constant. As soon as the ablated layer reaches the material surface, it can freely expand with an angle θ_{plume}.

The effect of plume attenuation and moving ablation front on the ablation rate will become more pronounced as the pulse length increases and will depend on the exact pulse shape. A square pulse approximation is usually a rather crude estimate of the true pulse. In figure 2.17 the pulse shape of a Lumonics PM 848 excimer laser is depicted, together with a more sophisticated approximation given by

$$I_0(t) = \frac{F}{t_a}\frac{t}{t_a}e^{-\frac{t}{t_a}} \tag{2.3}$$

with F the laser fluence and $t_a = 6$ ns. The FWHM τ of the laser pulse is approximately equal to $2.7t_a$.

The influence of plume absorption on the etch rate can be observed in figure 2.18. The material parameter values are taken from table 2.5 and the numerical simulations were performed for 4 arbitrary values of the plume absorption β, which was assumed constant for reasons of simplicity. The effect of the plume is a more pronounced saturation of the etching at elevated fluences because its transparancy decreases exponentially with the amount of ablated material. The etch rate has a practically linear fluence dependence in the absence of plume absorption, which is in accordance with [19]. As soon as β approaches 0.1α, a substantial decrease in etch rate occurs. In the limit of $\beta \rightarrow \alpha$ the plume will behave identically to the solid and the ablation process can be described by the Beer approach (2.1).

37
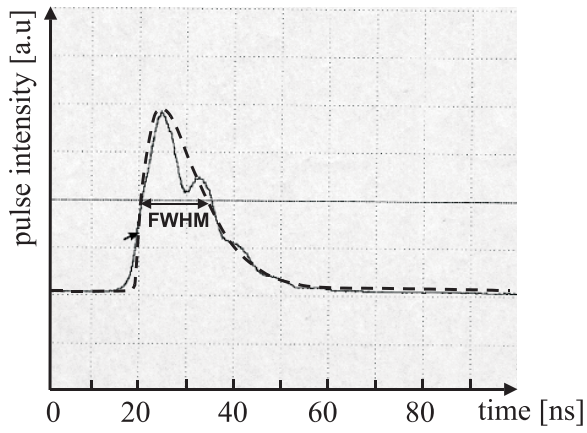
Figure 2.17: Pulse shape of Lumonics PM848. The dotted line indicates the approximation according to equation (2.3). The FWHM of the pulse is 16 ns.
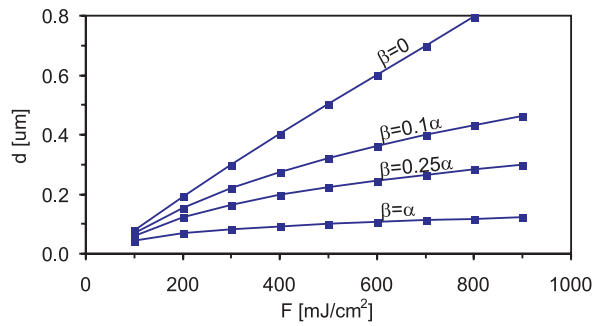
Figure 2.18: Effect of plume absorption on ablation of a polyimide resist.
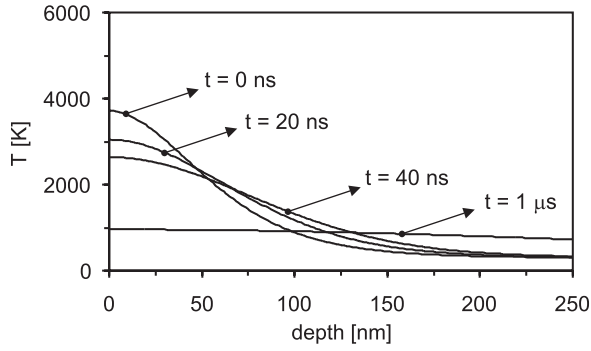
Figure 2.19: Thermal diffusion redistributes the temperature inside the polymer.

Thermal diffusion

In the Beer model the energy distribution inside the polymer is solely determined by the photon absorption, leading to an exponential decay of the energy away from the surface. This assumption is probably valid at the beginning of the pulse. But on a time scale of tens of nanoseconds, heat conduction will certainly start spreading the thermal energy away from the irradiated zone. The effect of this phenomenon can be modeled by

$$\frac{\partial T(x,t)}{\partial t} = D\frac{\partial^2 T(x,t)}{\partial x^2}$$

with D the thermal diffusivity (cm^2s^{-1}). This material constant is related to the thermal conductivity K ($\text{WK}^{-1}\text{cm}^{-1}$) and specific heat c_p ($\text{JK}^{-1}\text{cm}^{-3}$) via $D = K/c_p$. In figure 2.19 the temperature distribution inside the material is depicted for several delays after ablation finished. Material and laser parameters are given in table 2.5. The surface cools in time and the remaining thermal energy is gradually spread over an area exceeding the absorption zone.

Validity of material constants

The majority of polymer ablation models assumes that the material properties remain constant during material removal. The relevant material parameters concern mainly the specific heat c_p and thermal conductivity K. Usually they are specified at room temperature. This seems to be in contrast with observed surface temperatures exceeding 1600 K during laser ablation [30], quite beyond 300 K.

Exact information on these material properties is scarce, all the more since the material is quickly evaporated at the temperatures of interest. In [30] data for Kapton ca be found up to 400°C. Linear fits to the reported measurement results are

$$\begin{aligned} C_p &= 0.371 + 0.00344 \times T \\ K &= 0.0017 \end{aligned} \tag{2.4}$$
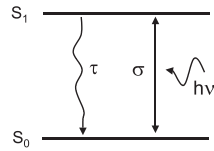
Figure 2.20: Two energy level for absorption in a polymer.

and have been used by [8]. Estimations for higher temperatures can be obtained via extrapolation.

Absorption saturation: bleaching of the polymer

Laser ablation typically involves fluences above 0.1 J/cm^2 penetrating the polymer surface. The corresponding density of absorbed photons in the material right below the surface equals $\alpha I_s / h\upsilon$ or 10^{21}-10^{22} photons/cm^{-3} for the lowest fluences! This quantity is of the same order as the chromophore concentration and it is therefore possible that the number of non-excited chromophores decreases considerably. The consequence of this effect is that $\alpha = \sigma n_0$ decreases with photon flux and the beam will penetrate deeper into the material. Characterizing the material by a two energy level system[6] and modeling the absorption by the corresponding rate equations is usually employed to calculate the energy distribution in the polymer (figure 2.20):

$$
\begin{aligned}
\frac{dn_0}{dt} &= \sigma(n_1 - n_0)\frac{I}{h\upsilon} + \frac{n_1}{\tau_1} \\
\frac{dn_1}{dt} &= \sigma(n_0 - n_1)\frac{I}{h\upsilon} - \frac{n_1}{\tau_1}
\end{aligned}
$$

The ground state chromophores n_0 decrease proportionally to the photon flux $I/h\upsilon$ ($s^{-1}cm^{-2}$) and their cross-section for absorption (cm^2). A radiationless relaxation mechanism is taken into account with a lifetime $\tau_1 \approx 35$ ps [14]. Fluorescence has been neglected as this is generally considered an inefficient relaxation mechanism compared to radiationless decay. In figure 2.21 the relative populations for the excited and ground state are given for two fluences. At a typical micromachining fluence of 1 J/cm^2 with 17 ns excimer laser pulses, the excited species hardly reach 2 % of the ground state population. Therefore saturation effects can be neglected for pulses of tens of nanoseconds. Only at extremely high fluences, depletion of the ground state can be observed as indicated in the figure for 100 J/cm^2. When shorter pulses are employed, saturation will occur at lower fluence levels: for 1.5 ns pulses considerable saturation already appears at 5 J/cm^2.

Incubation and precursor effects

There is a broad consensus on the absorption behavior of PMMA at the ArF (193 nm) and KrF (248 nm) wavelengths[7]. At 193 nm the absorption coefficient is

---

[6]Sometimes a three level energy systems is considered.

[7]As PMMA is virtually transparent for the longer excimer wavelengths, mostly ArF and KrF excimer wavelengths are used.
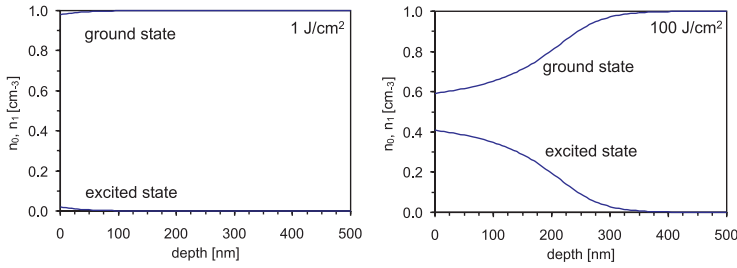
Figure 2.21: Evidence of saturation effects at 1 ns after a KrF excimer laser pulse (τ=16 ns) strikes a polyimide film.

about 4.5×10^3 cm^{-1}, sufficient to allow direct ablation. At KrF another ablation mechanism is observed: the initial absorption coefficient at low fluences can be estimated at 400-1000 cm^{-1} or a pulse penetration depth of up to 25 μm. This absorption seems to increase dramatically during exposure to sub-threshold pulses at KrF due to chemical modifications (precursor effects) that take place in the irradiated area [27, 33]. The modification seems irreversible as the higher absorption remains unchanged after exposure.

The consequence is that material removal does not occur immediately when pulses with a fluence above threshold are fired. Instead ablation will only start after a sufficient number of pulses depending on the fluence. This delayed ablation is called 'incubation'. During the precursor pulses, a moderate swelling of PMMA has been observed. From IR and UV spectroscopy and identification of the gas products from PMMA ablation, it is assumed that the formation of unsaturated species in the PMMA matrix is responsible for increased absorption and reduction of mechanical stability. As a result, the density of absorbed photons rises and ablation can start occurring. Simultaneously, the remaining material under the bottom of the etch cavity will undergo the same photochemical modifications and will ablate with the next pulses. In this way the removal process will reach a steady state regime.

Figure 2.22 illustrates the effects of delayed ablation and depicts the experimentally measured ablation depth for different pulse counts. Without incubation one expects the etch depths to lie on a single straight line which intersects the pulse axis at the origin. Instead, no or little ablation is observed for a limited number of pulses and this effect is more pronounced at low fluences. Sometimes the exposed area even exihibits a bump due to gas formation (methyl formate) inside the material. This explains the 'negative' depth for the case of single pulse ablation at 1 J/cm^2. A formally similar absorption mechanism is observed for ablation of polyethylene.

Strongly absorbing polymers do not exhibit this incubation behavior. Still, one can argue that the absorption depth of a pulse is always larger than the depth of the ablated cavity. In other words, the remaining material has probably degraded to some extent. Due to strong confinement of the pulse in the material, this zone
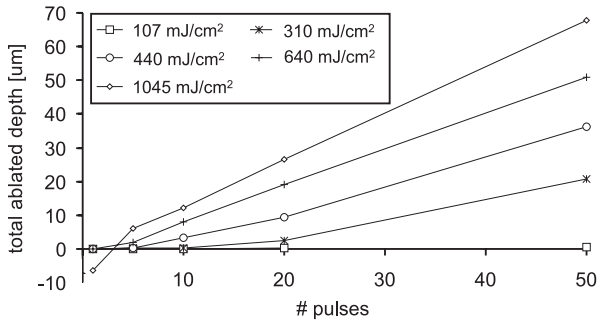
Figure 2.22: KrF ablation of PMMA: experimental etch rate versus pulse count for several fluences.

is rather limited and can be estimated at some tens of nm. The amount of energy (per cm^2) that remains in the polymer for $F > F_{th}$ is limited by F_{th} according to the Beer model[8]. Measurement of the thermal energy left in the substrate after ablation also shows a nearly constant value for $F > F_{th}$. It is therefore likely that the major part of the energy is dissipated through thermal diffusion, though photochemical changes cannot be excluded.

2.4.6 Photophysical model for excimer laser ablation of polymers (Schmidt *et al.*)

In this section a so-called photophysical model is proposed, i.e. a model that takes both thermal and non-thermal features of the ablation process into account. An early attempt for constructing such a model is given in [28]. However, it fails to predict any incubation effects or plume absorption. A more sophisticated model has been introduced by Schmidt, Ihlemann *et al.* [8] to examine the effects of spot size and pulse duration. It takes all of the mechanisms explained in 2.4.5 into account. In this section we will focus on this model that we implemented numerically. Simulation results will be presented, indicating the influence of the several laser and material parameters on the etch rate. Since the PM848 excimer laser does not feature an adjustable pulse length, verification of the plume expansion parameters was not possible. In our implementation we chose these parameters identical to [8]. One disadvantage of the model is the large number of parameters involved, although this can be expected for a process as complex as ablation. As it is practically impossible to obtain accurate data on all the parameters for most polymers, fitting the predicted etch rates to the measured values is rather speculative. PI can be considered an exception as most parameter values can be found in literature.
We will now describe the different aspects of the model: the absorption mechanism, decomposition pathways, temperature considerations and plume expansion.

---

[8]The photochemical ablation model in [18] confirms this statement.

1. Rate equations for absorption and decomposition

The photon flux of the laser pulse is absorbed with a distribution according to the Beer-Lambert absorption law. A two energy level system with a ground and excited singlet state is assumed for the absorbing chromophores. Ground state chromophores (population n_0 and cross-section σ_{init}) can reach the excited state (population denoted by n_1) when they absorb a photon. Relaxation from that state can happen in two ways: either the electronic energy is converted into vibrational energy and the chromophore populates the ground state again (internal conversion with rate constant k_{ic}), or photochemical dissociation occurs (direct decomposition with rate constant k_{dd}). In the latter case the chromophore will modify to another type (population denoted by n_{mod} and absorption cross-section $\sigma_{mod} \neq \sigma_{init}$). These processes can be described via

$$\frac{dn_1}{dt}\Big|_{abs} = -\frac{dn_0}{dt}\Big|_{abs} = \sigma n_0 \frac{I}{h\nu}$$

$$\frac{dn_1}{dt}\Big|_{ic} = -\frac{dn_0}{dt}\Big|_{ic} = -k_{ic} \times n_1$$

$$\frac{dn_1}{dt}\Big|_{dd} = -\frac{dn_{mod}}{dt}\Big|_{dd} = -k_{dd} \times \left(\frac{n_c - n_{mod}}{n_c}\right) n_1$$

Note that direct decomposition needs an umodified chromophore in the state S_1 and the density of this chromophore type is $\left(\frac{n_c - n_{mod}}{n_c}\right) \times n_1$.

A modified chromophore can still be promoted to the excited state S_1 and relax back to S_0 (internal conversion) but cannot regain its original properties. Physically this means that the non-exposed polymer has chromophore sites with cross-section σ_{init} and initial density n_c. Once the laser pulse penetrates the polymer, the total amount of chromophores is distributed among the ground and excited states. From time to time the relaxation path will involve cleavage of a nearby bond in the molecule and this will lead to a locally modified chemical structure with other chromophore characteristics. The total density of chromophores n_c equals $n_0 + n_1$ throughout the whole process, but the effective cross-section of the chromophores will change with n_{mod} according to

$$\sigma = \sigma_{init} + (\sigma_{mod} - \sigma_{init})\frac{n_{mod}}{n_{thres}} \qquad n_{mod} < n_{thres}$$
$$\sigma = \sigma_{mod} \qquad n_{mod} \geq n_{thres}$$

with n_{thres} the threshold value for the density of broken bonds. This σ reflects the change in density of ground state chromophores with modified characteristics. In case the density of broken bonds exceeds n_{thres}, the polymer layer decomposes and becomes plume material.

In the rate equations it is assumed that no thermal energy is released in the case of direct dissociation. Multi-photon absorption is ignored as single-photon absorption of a polymer is usually very large and nanosecond pulses are generally not sufficiently intense to initiate a competing two-photon absorption process. Other relaxation mechanisms as fluorescence −including spontaneous and stimulated emission− can be safely ignored [14].

Next to photochemical modifications, there is another competing dissociation mechanism which is based on thermal degradation. The mathemathical formulation of
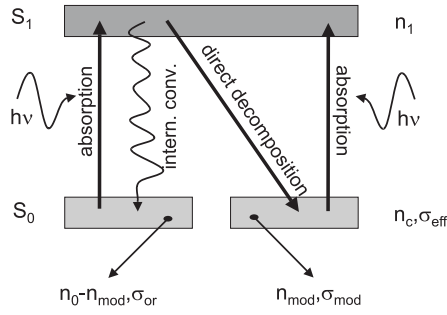
Figure 2.23: Absorption system in the polymer.

this process is

$$\frac{dn_{mod}}{dt}\bigg|_{therm} = k_{therm}\frac{n_c - n_{mod}}{n_c}n_0$$

with the thermal rate constant defined by

$$k_{therm} = A_{therm}e^{-Ea/kT}$$

2. Temperature calculations

Several mechanisms influence the local temperature in the polymer: internal conversion releases thermal energy, thermal decomposition needs a reaction enthalpy dH and diffusion will flatten thermal gradients. This means that the rate equations from the previous paragraph have to be completed with

$$
\begin{array}{ccccc}
\frac{dT}{dt}\big|_{ic} & = & -\frac{dn_1}{dt}\big|_{ic} & \times & \frac{h\nu}{c_p} \\
\frac{dT}{dt}\big|_{therm} & = & -\frac{dn_{mod}}{dt}\big|_{therm} & \times & \frac{dH}{c_p} \\
\frac{dT}{dt}\big|_{diff} & = & \frac{K}{c_p} & \times & \frac{d^2T}{dx^2}
\end{array}
$$

Note that $dH > 0$ for a reaction requiring supply of energy in order to take place. The thermal conductivity and heat capacity are calculated via equation (2.4).

3. Plume expansion modeling

Plume absorption strongly influences the etch rates at higher fluences as previously shown in figure 2.18. During ablation the plume content leaves the ablation surface at high speeds up to 10^4- 10^5 cm/s[9]. For a pulse duration of 10 ns these particles can travel up 10 μm. The plume absorption will show little change during that time if we take the small angular spread and typical beam size into account. However,

---

[9]For comparison: the speed of sound under atmospheric conditions is 3.4×10^4 cm/s.

plume expansion can play a role for longer pulses. This is certainly the case when the beam diameter becomes smaller.

A layer that is ablated at t_0 will start moving upwards with a velocity v_x. As long as it propagates inside the cavity, it is laterally surrounded by walls and it will remain confined. Once it reaches the top surface (at $t_1 = t_0 + d(t_0)/v_x$), it will freely expand with an angle θ_{plume}. This layer will thus feature an absorption cross-section given by

$$
\begin{array}{rcll}
\sigma_{plume} & = & \sigma_{mod} & x < 0 \\
\sigma_{plume} & = & \sigma_{mod} \times \dfrac{1}{\left(1 + \frac{2v_x(t - t_1)}{\phi} \times tan(\theta_{plume})\right)^2} & x > 0
\end{array}
$$

These expressions are formally identical to (2.2).

Results

We implemented the Schmidt model and solved the coupled equation numerically. The material is divided in layers of thickness dx and a time discretization in slices of dt is used for this purpose. At every moment $i \times dt$, all quantities are evaluated for every layer in the following order:

1. Temperature distribution with boundary values $\frac{\partial T}{\partial x}\big|_{x=0} = 0$ and $T\big|_{x=\infty} = T_{ambient}$

2. Material variables c_p, K, σ and σ_{plume}

3. Rate constant k_{therm}

4. Distribution of I through the material according to the Beer-Lambert law

5. The resulting n_0, n_1 and n_{mod} due to absorption and relaxation processes

The model was applied to polyimide for ablation at 193 nm and 248 nm. As it is difficult to obtain accurate data on the several model variables, we limited our simulations to this polymer as the most relevant parameters are readily available from literature. These material parameters are summarized in table 2.7 and a comparison between experimental data and model predictions is given in figure 2.24. Note that a fitting $\alpha_{mod} = 2.2 \times 10^5$ cm^{-1} deviates significantly from the value proposed by Schmidt (6.5×10^4 cm^{-1}).

Although Schmidt's approach corresponds much better with the physical nature of ablation than any other (more simplified) model, there are a few weaknesses. A first shortcoming is the fact that the modified absorption coefficient of the solid α_{mod} equals the plume absorption. For PI the fragments in the plume have a much smaller molecular weight than the monomer (one fast wave with amu ≤ 36 and a slower wave with amu ≤ 100 according to [31, 32]). This is in agreement with our choice for the dissociation threshold for broken bonds ($N_{thres} = 4$ per monomer) since the monomer has a weight of 382 amu. Still, it leaves room for a secondary decomposition mechanism in the plume. The latter can lead to plume

parameter	193 nm	248 nm	remarks
dH [kJ/mol]	170 (equals 1.76 eV per molecule)		Value chosen between 145 and 181 kJ/mol from [21, 8].
α_{init} [cm^{-1}]	4.5×10^5	3.2×10^5	For KrF identical to [21]. For ArF according to [1, 2].
α_{mod} [cm^{-1}]	3.5×10^5	2.2×10^5	Fitting parameter. Much higher than indicated by [8]. Less than twice the value suggested by [13].
n_{mon}[cm^{-3}]	2.24×10^{21}		Monomer density.
N_{thres} (broken bonds/monomer)	4		This is the number of broken bonds per monomer required for ablation. Together with $Z = 10$ this means that 40% of the bonds need to be broken. This value lies between 10% and 90% as indicated by respectively [8] and [21].
chromophores per monomer Z	10		Of the same order as in [20]. Nearly twice as assumed by [21] (compensates difference in n_{thres}).
A_{th} [s^{-1}]	1.0×10^{13}		Nearly the same as in [21].
E_a [kJ/mol]	180 (=1.87 eV per molecule)		Value chosen between 175 and 250 kJ/mol from [21, 8].
k_{ic} [s^{-1}]	2.0×10^{10}		Order of magnitude is given by [14].
k_{dd} [s^{-1}]	0.8×10^{10}		Order of magnitude given by [14].
plume velocity [cm/s]	9.0×10^5		Calculated by [8].
θ_{plume} [deg]	20.0		Calculated by [8].
refractive index	1.66		Estimated value.
$T_{ambient}$ [K]	300		
τ [ns]	16		Measured value.
pulse shape	as in (2.3)		Derived from curve-fitting to the measured pulse shape (source: GSI Lumonics).

Table 2.7: Material and laser parameters for PI ablation at 193 and 248 nm.
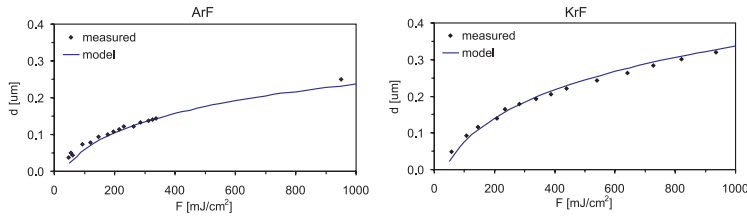
Figure 2.24: Comparison Schmidt model and experimental ablation depth.

absorption which differs from α_{mod}. An appropriate extension of the model would thus incorporate an additional absorption coefficient $\beta \neq \alpha_{mod}$ for the plume. The deviation between our fitting value for the modified absorption coefficient and reported data is presumably caused by this shortcoming.

A second remark concerns the fate of the broken bonds in the material: there is no relaxation mechanism provided and thus the broken bonds remain in the material until the next pulse occurs, independently of the time in between the pulses. Note that these broken bonds can be interpreted as an incubation effect: the formation of a chemically modified substance with a different absorption coefficient. It is obvious that in some cases bond healing or radical combination might occur, leading to a decrease of broken bonds in time. This effect can be taken into account by adding a decay term n_{mod}/τ_{mod} to the rate equation for n_{mod}. Estimation of the lifetime τ_{mod} is not an obvious task as it will highly depend on the polymer type. PMMA is known to show incubation effects which are independent of the repetition rate of the laser, indicating that τ_{mod} is probably very large. On the other side incubation plays a minor role in PI, suggesting that the lifetime is very small in this case.

Influence of the laser and material parameters

Based on the Schmidt model it can be verified how the ablation curve (etch depth versus pulse fluence) varies with some laser and material parameters, in particular the rate constants for relaxation and dissociation. Unfortunately there is no experimental confirmation of this behavior available.

In case of PI the degradation is mainly thermal. The influence of a single parameter change on the etch curves is given in figure 2.25. We can conclude that

- A higher thermal dissociation rate (larger A_{therm} and/or smaller E_a) increases the etch rate substantially and decreases the threshold fluence for ablation as expected.

- A larger α_{mod} results in faster saturation of the etch curve, but has little effect on the threshold fluence. The parameter α_{init} does not influence the etch rates noticeably.

- The number of chromophores Z does not influence the etch rate, except when it (almost) equals the threshold value for bondbreaking N_{thres}. Depletion of unmodified chromophores will then lower the probability of additional excitation when n_{mod} approximates n_{thres}.

- A higher threshold value N_{thres} for broken bonds per monomer results in slower ablation and higher ablation threshold fluences. When n_{thres} equals the chromophore density, substantial decrease in etch depth is observed (due to depletion of the unmodified chromophores as stated above).

- A larger reaction enthalpy surpresses the ablation process as every broken bond decreases the local temperature more and thus slows down thermal dissociation. Since little ablation takes place at low fluences, the effect of a higher reaction enthalpy on the threshold fluence is negligble.

47

- When photochemical modification becomes the dominant relaxation process from the excited state S_1, ablation starts at lower fluences. Since there is no minimal temperature required anymore for ablation, practically every photon is used to increase the density of modified chromophores and little energy is lost to the bulk. However, the overall etch rate drops (at fluences above 100 mJ/cm^2). For a photothermal driven ablation process, a more pronounced threshold is observed as the slope of the ablation curve becomes steeper. This behavior can be explained by the thermal dissociation constant k_{therm}, which is very temperature sensitive.

The model values for k_{DD} and k_{IC} were chosen to keep $k_{DD} + k_{IC}$ constant in order to respect the overall relaxation time of 35 ps.

2.5   Polymer engineering

From the considerations in this chapter, one can conclude that absorption centra in organic molecules can be identified with specific groups and bonds called chromophores. With this knowledge it is possible to engineer polymer chains to incorporate certain functional groups in order to achieve desired ablative properties as strong absorption and efficient decomposition into gaseous constituents. The latter property is important as it decreases the amount of particles dropping back on the sample after ejection from the surface. Lippert *et al.* [34, 35] have thoroughly investigated the insertion of a triazene group (-N=N-N<) in laser resists. This engineered polymer features a very high absorption in the 310-350 nm region, resulting in linear absorption coefficients as high as 1.0×10^5 cm^{-1} and 6.6×10^4 cm^{-1} at respectively 308 nm (XeCl) and 248 nm (KrF). The main decomposition products are volatile N$_2$ and phenyl radicals. They act as a driving gas, carrying away the larger fragments. The etching of the triazene polymer was found to start *and* end with the laser pulse, clearly indicating photochemical etching [35]. As the monomer decomposition is essentially an exothermic reaction, thermal processes cannot be entirely ignored as observed in [34].

In [36] the ablation properties of segmented polyurethanes (soft segment was polycarbonate) were investigated at ArF and KrF. It was observed that polymers based on aromatic compounds could be given absorption coefficients as high as 9.8×10^4 cm^{-1}. They proved to be far more sensitive to laser irradiation than the aliphatic compounds, which featured absorption coefficients down to 1.9×10^4 cm^{-1}. The result is that the use of an aromatic diisocynate in the polymer leads to much better defined ablation cavities than in case of the aliphatic type. A detailed description can be found in [36] and an application for these polymers is given in [37].

2.6   Conclusions

Polymer materials are very good absorbers in the UV, including the wavelengths produced by excimer lasers. Absorption coefficients as large as 1.0×10^5 cm^{-1} are
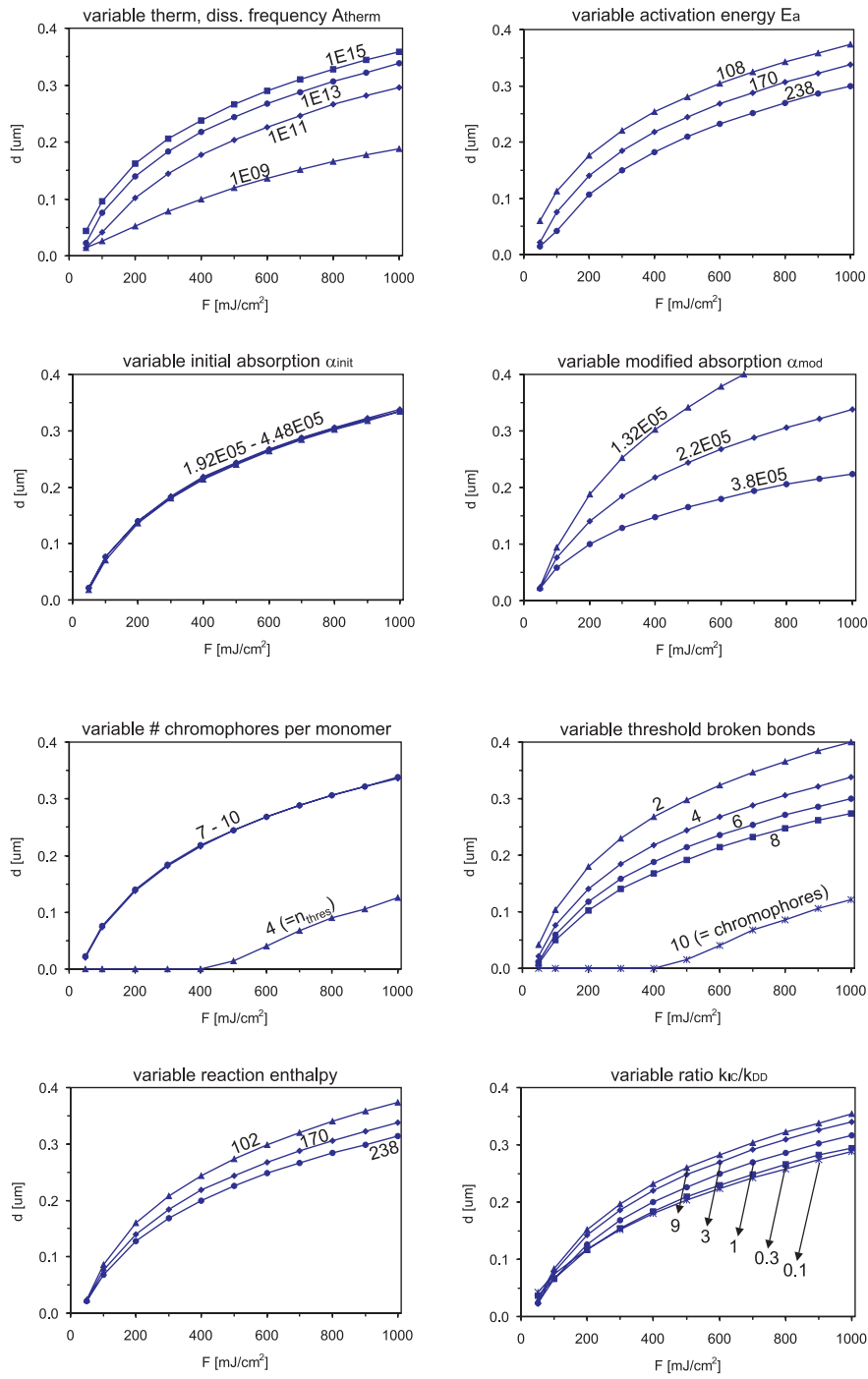
Figure 2.25: Influence of material parameters on the etch rate.

no exception. These are caused by the high density of chromophores that can be excited to higher electronic states.

Excimer laser induced dissociation of these materials occurs via both a photothermal and photochemical relaxation process. Due to the short pulse duration (order of ns) and the high absorption, the dissociation occurs on a very limited time scale and leads to explosive removal of the decomposed material. Independently of the particular dissociation pathway, the injected thermal energy in the material is efficiently removed by the evaporating decomposition fragments.

A simple model based on the Beer-Lambert absorption law has been proposed to predict the ablation rate of polymers. Several mechanisms as plume absorption, a moving interface during ablation, thermal diffusion and precursor effects are not incorporated in this simple Beer model. Therefore, we implemented a more sophisticated scheme taken from Schmidt *et al.* and compared it to experimental results. More insight in the relevance of some material parameters is achieved in this way.

Appendix A Extended thermal ablation model derived from Cain *et al.*

Cain models the absorption of a laser pulse in a material via a 2-energy system for the chromophores. The chromophores in the ground state can absorb photons and spontaneous relaxation from the excited state takes place with a time constant τ_{relax}. All absorbed photon energy is released inside the material as thermal energy via internal conversion.

The material is considered to feature a certain bond density. Via thermal degradation this bond density drops according to an Arrhenius law and when a certain critical level is obtained, the material is considered decomposed. Heat diffusion can take place throughout the unablated material during and after the laser pulse.
The relevant quantities are:

- Instant laser intensity $I(x,t)$ inside the material.

- Chromophore density in the ground and excited state, respectively $n_0(x,t)$ and $n_1(x,t)$. At any time $n_0(x,t) + n_1(x,t) = n_{chrom}$, the total number of chromophores.

- Temperature distribution $T(x,t)$ inside the material.

- Chromophore absorption cross-section $\sigma(x,t)$, equaling σ_{solid} or σ_{plume} depending on the state of the material: solid or decomposed. The plume absorption was added in our extended model as the original scheme according to Cain neglects σ_{plume}.

- Local bond density $n_{bonds}(x,t)$. The material is considered decomposed when $n_{bonds}(x,t) < n_{thres}$.

Consider a slab of material that is exposed to a laser pulse during the time interval

$t = [0, \tau]$. Before the pulse hits the surface, we can write down for all quantities:

$$
\begin{aligned}
I(x) &= 0 \\
n_1(x) &= 0 \\
n_0(x) &= n_{chrom} \\
T(x) &= T_{ambient} \\
\sigma &= \sigma_{solid}
\end{aligned}
$$

As soon as the pulse penetrates the material, the governing equations describing the dynamics inside the material become:

$$
\begin{aligned}
\frac{dI}{dx} &= \sigma(n_0 - n_1)I \\[2mm]
\frac{dn_1}{dt} &= \sigma(n_0 - n_1)\frac{I}{h\nu} - \frac{n_1}{\tau_{relax}} \\[2mm]
n_0 &= n_{chrom} - n_1 \\[2mm]
\frac{dT}{dt} &= \frac{(n_0 - n_1)\sigma I}{c_p} + D\frac{dT^2}{dx^2} \\[2mm]
\frac{dn_{bonds}}{dt} &= -\left(\frac{kT}{h}\right)e^{-E_a/kT}
\end{aligned}
$$

with h Planck's constant, $h\nu$ the photon energy, D the thermal diffusivity and E_a the thermal activation energy for bond breaking. Note that heat diffusion is included in our model during the pulse, while Cain only considered diffusion *after* the laser pulse. The rate equations for the chromophore densities (excited and ground state) do not incorporate a loss of chromophores due to bond-breaking, which is in accordance with Cain's assumptions.

The pre-exponential term in the Arrhenius equation ($\frac{kT}{h}$) is derived from Eyring dissociation theory [1]. The lifetime of the excited state can be estimated at 35 ps [14].

After the pulse is finished, the excited chromophores relax very fast to the ground state. The temperature and bond density change according to:

$$
\begin{aligned}
\frac{\partial T}{\partial t} &= D\frac{\partial^2 T}{\partial x^2} \\[2mm]
\frac{dn_{bonds}}{dt} &= -\left(\frac{kT}{h}\right)e^{-E_a/kT}
\end{aligned}
$$

The equations have been solved numerically: the material has been divided into several thin slabs of 1 nm thickness and the time variable has been discretized into time slices of 1 ps. The temperature boundary condition at the material surface has been taken $\frac{dT}{dx}\big|_{surf} = 0$, reflecting the absence of thermal conduction from the solid material into air or plume. The pulse shape was modeled according to figure 2.3 with a FWHM length of 16 ns.

Bibliography

[1] S. Cain, F. Burns, C. Otis and B. Braren, "Photothermal description of polymer ablation: Absorption behavior and degradation time scales", J. Appl. Phys **72**, 5172 (1992).

[2] S. Babu and G. D'Couto, "Excimer laser induced ablation of polyetheretherketone, polyimide and polytetrafluoroethylene", J. Appl. Phys. **72**, 692 (1992).

[3] G. Gorodetsky, T. Kazyaka, R. Melcher and R. Srinivasan, "Calorimetric and acoustic study of ultraviolet laser ablation of polymers", Appl. Phys. Lett. **46**, 828 (1985).

[4] R. Srinivasan, "Ablation of polymethyl methacrylate films by pulsed (ns) ultraviolet and infrared (9.17 μm) lasers - a comparitive study by ultrafast imaging", J. Appl. Phys. **73**, 2743 (1993).

[5] A. Dragomir, j. McInerney, D. Nikogosyan and P. Kazansky, "Two-photon absorption properties of commercial fused silica and germanosilicate glass at 264 nm", Appl. Phys. Lett. **80**, 1114 (2002).

[6] S. Kuper and M. Stuke, "Ablation of polytetrafluoroethylene (Teflon) with femtosecond UV excimer laser pulses", Appl. Phys. Lett. **54**, 4 (1989).

[7] G. Arjavalingam, G. Hougham and J. Lafemina, "Emission mechanism in Polyimide", Polymer **31**, 840 (1990).

[8] H. Schmidt, J. Ihlemann, B. Wolff-Rottke, K. Luther and J. Troe, "Ultraviolet laser ablation of polymers: spot size, pulse duration and pulse attenuation effects explained", J. Appl. Phys. **83**, 5458 (1998).

[9] R. Srinivasan and B. Braren, "Ultraviolet laser ablation of organic polymers", Chem. Rev. **89**, 1303 (1989).

[10] J. Brannon, J. Lankard, A. Baise, F. Burns and J. Kaufman, "Excimer laser etching of polyimide", J. Appl. Phys. **58**, 2036 (1985).

[11] G. D'Couto and S. Babu, "Heat transfer and material removal in pulsed excimer-laser-induced ablation: pulsewidth dependence", J. Appl. Phys. **76**, 3052 (1994).

[12] S. Cain and F. Burns, "On single-photon ultraviolet ablation of polymeric materials", J. Appl. Phys. **71**, 4107 (1992).

[13] N. Arnold, N. Bityurin and D. Baurle, "Laser-induced thermal degradation and ablation of polymers: bulk model", Appl. Surf. Sc. **138**, 212 (1999).

[14] J. Frisoli, Y. Hefetz, T. Deutsch, "Time-resolved UV absorption of polyimide - implications for laser ablation", Appl. Phys. B **52**, 168 (1991).

[15] R. Srinivasan and W. Leigh, "Ablative photodecomposition: action of far-ultraviolet (193 nm) laser radiation on poly(ethyleneterephthalate) films ", J. Am. Chem. Soc. **104**, 6784 (1982).

[16] R. Srinivasan and V. Mayne-Banton, "Self-developing photoetching of poly(ethyleneterephthalate) films by far-ultraviolet excimer laser radiation", App. Phys. Lett. **41**, 576 (1982).

[17] A. Zweig, V. Venugopalan and T. Deutsch, "Stress generated in polyimide by excimer-laser irradiation", J. Appl. Phys. **74**, 4181 (1993).

[18] G. Mahan, "Theory of polymer ablation", Appl. Phys. Lett. **53**, 2377 (1988).

[19] S. Lazare and V. Granier, "Empirical photoablation rate model exemplified with the etching of polyphenylquinoxaline", Appl. Phys. Lett. **54**, 862 (1989).

[20] R. Sauerbrey and G. Pettit, "Theory for the etching of organic materials by ultraviolet laser pulses", Appl. Phys. Lett. **55**, 421 (1989).

[21] N. Arnold and N. Bityurin, "Model for laser-induced thermal degradation and ablation of polymers", Appl. Phys. A **68**, 615 (1999).

[22] G. Koren and J. Yeh, "Emission-spectra, surface quality and mechanism of excimer laser etching of polyimide films", Appl. Phys. Lett. **44**, 1112 (1984).

[23] E. Arakawa, M. Williams, J. Ashley and L. Painter, "The optical properties of Kapton - measurement and applications", J. Appl. Phys. **52**, 3579 (1981).

[24] P. Simon, "Time-resolved ablation-site photography of XeCl-laser irradiated polyimide", Appl. Phys. B **48**, 253 (1989).

[25] R. Taylor, D. Singleton and G. Paraskevopoulos, "Effect of optical pulse duration on the XeCl laser ablation of polymers and biological tissue", Appl. Phys. Lett. **50**, 1779 (1987).

[26] R. Srinivasan and B. Braren, "Influence of pulse width on ultraviolet laser ablation of poly(methyl methacrylate), Appl. Phys. Lett. **53**, 1233 (1988).

[27] R. Srinivasan, B. Braren and K. Casey, "Nature of 'incubation pulses' in the ultraviolet laser ablation of polymethyl methacrylate", J. Appl. Phys. **68**, 1842 (1990).

[28] R. Srinivasan, M. Smrtic and S. Babu, "Excimer laser etching of polymers", J. Appl. Phys. **59**, 3861 (1986).

54

[29] P. Dyer and J. Sidhu, "Excimer laser ablation and thermal coupling efficiency to polymer films", J. Appl. Phys. **57**, 1420 (1985).

[30] D. Brunco and M. Thompson, "Temperature measurements of polyimide during KrF excimer laser ablation", J. Appl. Phys. **72**, 4344 (1992).

[31] S. Hansen, "Study of ultraviolet-laser ablation products of several polymers using time-of-flight mass spectroscopy", J. Appl. Phys. **66**, 1411 (1989).

[32] D. Krajnovich, "Near-threshold photoablation characteristics of polyimide and poly(ethylene terephthalate)", J. Appl. Phys. **82**, 427 (1997).

[33] S. Kuper and M. Stuke, "UV-excimer-laser ablation of polymethylmethacrylate at 248 nm: characterization of incubation effects with fourier transform IR- and UV-spectroscopy", Appl. Phys. A **49**, 211 (1989).

[34] T. Lippert, S. Langford, A. Wokaun, G. Savas and J. Dickinson, "Analysis of neutral fragments from ultraviolet laser irradiation of a photolabile triazeno polymer", J. Appl. Phys. **86**, 7116 (1999).

[35] T. Lippert, M. Hauer, C. Phipps and A. Wokaun, "Polymers designed for laser applications - Fundamentals and applications", in Symposium on High-Power Laser Ablation, Taos, USA, Proc. SPIE **4760** , 63 (2002) .

[36] Y. Martele, K. Callewaert, I. Swennen, K. Naessens, R. Baets, V. Van Speybroeck, M. Waroquier, H. Van Aert, P. Dierickx and E. Schacht, "Micropatterning of polyurethanes with lasers", Pol. Int. **51**, 1172 (2002).

[37] Y. Martele, K. Callewaert, K. Naessens, P. Van Daele, R. Baets and E. Schacht, "Controlled patterning of biomolecules on solid surfaces", Mat. Sc. & Eng. C **23**, 341 (2003).

Chapter 3

Micromachining polymers with an excimer laser

This chapter deals with the feasibility of high-power lasers for structuring polymer surfaces. A brief description of the laser operation principle explains the nature of important machining parameters as beam shape, fluence, coherence and wavelength. In a next section two ablation strategies that are suitable for laser machining are examined: focal point and mask imaging operation. Although several commercial lasers can be used for micromachining, primary focus is on excimer lasers. Some major commercial applications illustrate the potential of these lasers.
In a second part, a detailed description of polymer micromachining with excimer laser sources follows. Important aspects as resolution, ablation speed, aspect ratio, surface roughness and laser parameters will be discussed. Finally, an overview is given of prototype components that have been fabricated within the context of our research work.

3.1 Lasers for micromachining

3.1.1 Laser operation principle

Gain medium

When molecules or atoms in a medium make a transition from one energy state to another, it is possible that a photon is emitted or absorbed during this transition. The photon energy $h\upsilon$ will correspond to the difference in atomic or molecular energy ($\Delta E = E_2 - E_1$). Three different processes can be distinguished (figure 3.1):

- Transition from a higher energy state to a lower one, accompanied by *spontaneous emission* of a photon. The probability of this transition is proportional to the population of E_2 (denoted by N_2).
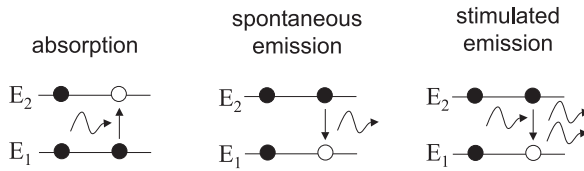
Figure 3.1: Absorption, spontaneous and stimulated emission.
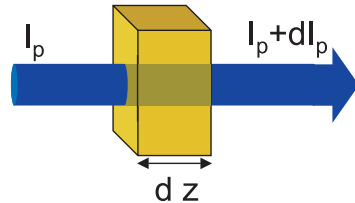
Figure 3.2: Light amplification.

- Transition from a lower energy state to a higher one, accompanied by the *absorption* of a single photon. The probability of this transition is proportional to the population of E_1 (denoted by N_1) and the photon density.

- Transition from a lower energy state to a higher one due to interaction with an incident photon. This is accompanied by emission of another photon in phase with the triggering one and is called *stimulated emission*. The probability of this transition is proportional to the population N_2 and photon density.

When a light beam (photon flux denoted by I_p) propagates through a medium with thickness dz and with an atomic or molecular ΔE matching the photon energy (figure 3.2), the flux at the exit plane in the same direction can be calculated as

$$I_p + dI_p = I_p - \underbrace{C_1 N_1 I_P dz}_{absorption} + \underbrace{C_2 N_2 I_p dz}_{stim.\,emission} + \underbrace{C_3 N_2 dz}_{spont.\,emission}$$

where C_i are constants that can be expressed in terms of the Einstein coefficients and the propagation speed of the beam in the material. Spontaneous emission is an isotropic process since the photons are emitted in all directions. Consequently, its contribution to the beam that leaves the elementary volume in the same direction as the incident beam, can be neglected. Based on the Boltzmann theory for energy state populations in thermal equilibrium, the coefficients C_1 and C_2 can be considered identical for equal degeneration factors[1]. The flux profile inside a slab

---

[1] It can be shown that for non-equilibrium conditions the assumption $C_1 = C_2$ is still valid.
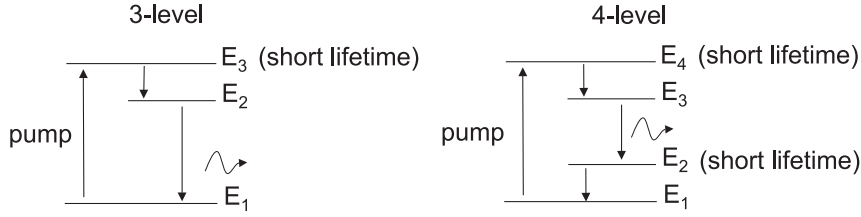
Figure 3.3: 3-level and 4-level pumping.

of this medium can now be written as:

$$I = I_0 e^{C_1(N_2 - N_1)z} = I_0 e^{gz}$$

I_0 is the beam flux as it enters the slab and g denotes the gain (expressed in cm^{-1}). The slab is called the gain medium or active medium.

From this expression it can be seen that amplification of the beam requires N_2 to exceed N_1, a situation which is referred to as population inversion. Reaching this state requires an external 'pumping' process which populates E_2. This can be accomplished by using a 3-level or 4-level system (figure 3.3). In case of a 3-level scheme, a pumping mechanism populates E_3. From there, the excited atoms quickly relax to E_2. N_2 will surpass N_1 for sufficient pumping and light amplification will occur for low I. As I increases, the higher rate of stimulated emission will start depopulating E_2 and will lead to gain saturation. A similar situation occurs for a 4-level system, although the required pumping for population inversion is lower in this case due to the depleted energy level E_2 (state with a short lifetime).
One might have the impression that the involved energy states are discrete and well-defined energy levels. However, this is not true. Due to atomic and molecular collisions, finite lifetimes of excited particles and other mechanisms, the gain curve will feature a certain spectral width.

Laser cavity

Next to a gain medium, a laser oscillator needs a feedback mechanism which redirects the light multiple times through the amplifiying medium. It is this system which is responsible for the narrow spectral width of the laser beam. The feedback is realized by positioning the gain medium between 2 mirrors which can be either fully or partially reflecting (figure 3.4). Note that at least one mirror requires to be partially reflective in order to let the laser beam escape from the cavity.
Considering the simplified case of a plane wave propagating inside the cavity, feedback is only possible when the phase of the wave after one back and forth propagation is a multiple of 2π (constructive interference). Assuming a refractive index n for the gain medium, this phase condition means

$$\phi_{roundtrip} = 2nkL = 2m\pi \implies L = \frac{m\lambda}{2n} \tag{3.1}$$

59
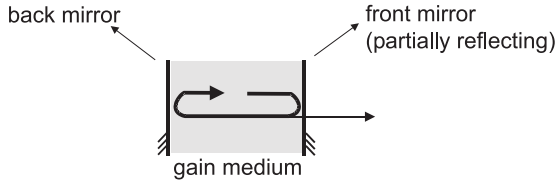
Figure 3.4: Laser cavity.

Lasing in the stationary regime is accomplished in the following way: initially, spontaneous emission is amplified due to population inversion and light propagates randomly through the gain medium. Only the wave propagating back and forth between the mirrors and satisfying the phase condition will be maximally amplified (highest number of roundtrips through the cavity). As soon as the the photon density reaches a certain level, the roundtrip gain will drop to unity and the populations of E_1 and E_2 will reach an equilibrium. In this regime the following condition is satisfied:

$$r_1 r_2 e^{2Lg/2} e^{-j\phi_{roundtrip}} = 1 \tag{3.2}$$

in which the left-hand term is the amplification for the field amplitude after a roundtrip in the cavity. Note that this is an amplitude-related condition, while the gain g refers to intensity amplification.

Equation (3.1) is satisfied by a number of wavelengths spaced by $\Delta\lambda = \lambda^2/(2nL)$. The fields related to these wavelengths are called the longitudinal modi of the cavity. The one with the highest gain will be the lasing mode[2].

Transversal laser modes

In the previous cavity analysis we assumed a plane wave propagation between the mirrors. In reality the cavity modes will show a finite transversal pattern which is not uniform over its cross-section. Condition (3.2) remains valid and expresses that a lasing mode should end up having the same transversal pattern after one roundtrip. Some transversal modes are depicted in figure 3.5. Note that for every transversal mode, a set of longitudinal modes exists. Due to slight differences in propagation constants for the different transversal modes with the same longitudinal mode number, these modes will be lasing at different frequencies.

---

[2]Usually the gain will be slightly different for neighboring modi near the gain maximum. This means that only the longitudinal mode with the highest gain can reach a unity roundtrip amplification under stationary conditions. However, other modi with a slightly lower gain can also oscillate due to a power contribution of the spontaneous emission.
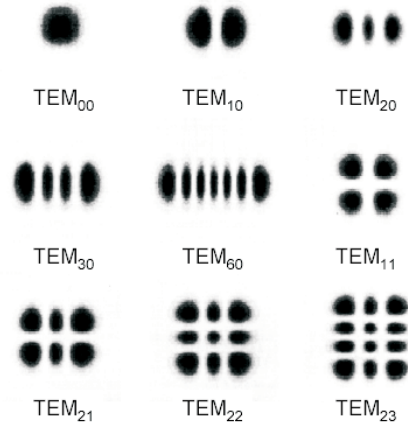
Figure 3.5: Transversal mode profiles.

Beam coherence

One of the interesting properties of a laser beam is its high degree of coherence. Coherence is associated with the correlation between the phases of an EM-wave in two different points in space and/or time: either there is a well-defined time-independent relationship between the two phases (coherent light) or there is not (incoherent light). If these two points are located on the same wavefront of the EM-wave, the phase correlation is called spatial coherence; if the two locations coincide and the phases are related to two different points in time, then the correlation is called temporal coherence. Often a laser will only be coherent to a certain extent.

For the temporal coherence one defines τ_c as the period during which the phase correlation disappears. The associated coherence length L_c is given by $L_c = c\tau_c$ (c is the travel speed of light in vacuum and equals 3×10^8 m/s). The temporal coherence of a laser source is determined by its spectral width or line width $\Delta\nu$: $\tau \simeq 1/\Delta\nu$.

The other type of coherence, spatial coherence, is often expressed by the beam parameter M^2. A perfectly coherent beam will propagate through a homogeneous medium with minimum expansion or broadening governed by diffraction effects. A beam which is not considered fully coherent, will diffract with a larger divergence angle. M^2 is defined as

$$M^2 = \frac{\pi n \theta D}{4\lambda}$$

with θ the full far field divergence angle, D the beam diameter at the waist and n the refractive index of the propagation medium.

61

The minimum spot size D_{spot} that can be achieved with a laser beam using a lens with focal length FL is given by:

$$D_{spot} = M^2 \frac{4\lambda FL}{\pi n D}$$

For a diffraction-limited beam M^2 equals 1 and the minimum spot size is given by $4\lambda FL/\pi n D$. A non diffraction-limited beam will thus result in a larger spot size.

In the neighborhood of the spot, the beam diameter will deviate only slightly from the spot size. In this context the Rayleigh length is defined as the spot diameter divided by the full divergence angle:

$$z_R = \frac{D_{spot}}{\theta}$$

For a diffraction-limited beam the Rayleigh length is $\pi D_{spot}^2/4\lambda$ and can be considered the distance over which the beam broadens by a factor $\sqrt{2}$ with respect to the spot size. The full distance over which the beam size stays within $\sqrt{2}D_{spot}$ is called Depth Of Focus (DOF) and thus equals $2z_R$. Note that a smaller spot size will accordingly decrease the DOF. For a non-diffraction limited beam the DOF is given by $2z_R/M^2$.

3.1.2 Excimer lasers

Pulsed excimer lasing

In this laser a gas of excimer molecules serves as active medium. Excimer is an abbreviation of excited dimer, which is a diatomic excited molecule of a noble (rare) gas atom R and a halide atom H[3]. The diatomic molecule is bound in excited states only, while its electronic ground states are purely repulsive or very weakly bound. The energy diagram of the relevant molecules is given in figure 3.6.
Consider for example the KrF transition. The following processes are involved in creating an excimer :

$$\begin{array}{rcl} e^- + Kr & \rightarrow & 2e^- + Kr^+ \\ e^- + F_2 & \rightarrow & F^- + F \\ Kr^+ + F^- + B & \rightarrow & (KrF)^* + B \end{array} \quad (3.3)$$
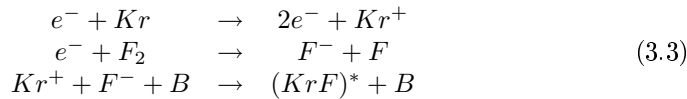
The electrons are made available via an electrical discharge. The buffer gas, denoted B in the reaction equations, acts as collision partner and ensures conservation of energy and momentum. Suitable buffer gases are helium and neon. Due to the discrete nature of the discharge pumping, the laser operates in pulsed mode.

As the lasing transition occurs between two electronic states, the emitted light typically has a wavelength situated in the ultraviolet (UV). The lower energy level of

---

[3]A more correct nomenclature is exciplex since an excimer refers strictly speaking to a diatomic excited molecule of the same atom, e.g. F_2. However, in literature the term 'excimer' often replaces 'exciplex'. We will therefore use the conventional terminology.
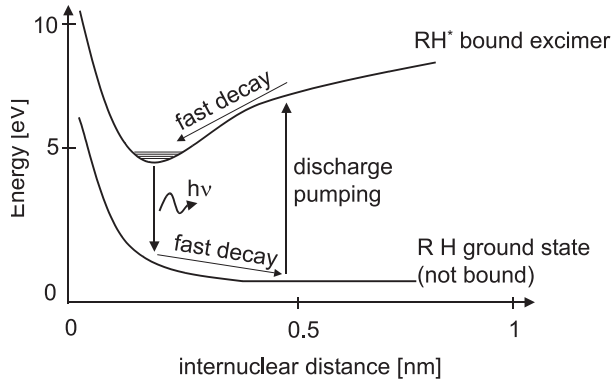
Figure 3.6: Electronic transitions during excimer lasing.

the lasing transition is almost empty due to rapid decay of the non-excited molecule (order of ps) and facilitates pumping towards population inversion as expected in a 4-level system. The light amplification is of the order of 0.1-0.2 cm^{-1} and leads to saturation after only a few roundtrips. As the cavity length is typically several tens of cm, the excimer laser beam will contain a multitude of longitudinal modes. In addition, the flat cavity mirrors and the absence of any mode-selective element inside the cavity are responsible for the excitation of many transversal modes in a laser pulse. The large, highly multimodal beam inevitably limits the spatial coherence down to the order of 100-200 μm. The temporal coherence length is determined by the rather broad linewidth −typically 0.5 nm− and can be estimated at 100-200 μm. Contrary to other gas laser types as HeNe, the cavity mirrors are not both high-reflecting: the back mirror typically reflects 100 %, but the front mirror's power reflection is seldomly chosen above 30 % due to the high amplification in the gain medium. Fresnel reflection at the bare air-quartz interface is often satisfactory. Finally, it should be noted that a typical excimer laser will emit an unpolarized beam as there is no polarization selective element inside the cavity.

Excimer wavelengths

A suitable combination of a halogen (Cl or F) and a noble atom (Ar, Kr, Xe) makes lasing possible at different wavelengths. Table 3.1 gives an overview of wavelengths that are commercially available. For reasons of completeness, we added F_2 which does not contain a rare (noble) gas atom. Note that radiation of F_2 −and to a lesser extent also ArF− is absorbed by air. In this case nitrogen gas is commonly employed for beam path purging in order to avoid absorption by O_2 and water molecules. This is not a strict requirement for ArF since the air absorption is only 0.1-0.2 per meter. However the absorption is accompanied by ozone formation, which is a hazardous gas.

RH molecule	λ [nm]	$h\nu$ [eV]	remarks
F_2	157	7.9	Highest photon energy for an excimer laser and therefore suitable for machining of high-bandgap materials as quartz.
ArF	193	6.43	Energy transfer from discharge to optical power is less efficient than for KrF. The short wavelength is responsible for the very short absorption lengths in common polymers.
KrF	248	5.00	Optimum combination of power and lasing efficiency. Ideal for micromachining purposes.
XeCl	308	4.03	Long lifetime of gas fill, longer absorption lengths in polymers.
XeF	351	3.54	Very low photon energy, less attractive for machining purposes.

Table 3.1: Commercial excimer wavelengths.

Technology

Creating the ideal circumstances for the reactions in (3.3) can be quite a technological challenge. In order to let the three collisions occur with a high probability, a vessel pressure of several atmospheres is needed. Pumping to population inversion is realized by discharge excitation of the gas. To obtain a typical population of the excited state necessary for lasing ($10^{15}/cm^3$), current densities of the order of 10^3 A/cm^2 are required over the entire electrode area. Since the lifetime of the excited state can be estimated at around 5 ns, the discharge time should be chosen sufficiently small for high efficiency (10 to 30 ns). Peak powers up to 10^9 W are delivered by the electrodes. As the excimer gas impedance is pretty low ($\sim 0.1~\Omega$), impedance-matching requires a high-voltage circuitry with low-inductance. The electrode in the vessel is typically a copper bar with a length of about 1 meter. Since the discharge needs to take place in a very homogeneous way over the entire cross-section of the electrode, the gas needs a preparatory excited state density of 10^7-10^8/cm^3 before discharge takes place. This pre-ionization is realized by pre-ionization gaps (figure 3.8) in series with the peaking capacitors. A full discharge cycle consists of the following steps (figure 3.7):

1. Charging of the main discharge capacitor by a high-voltage source through a charging resistor.

2. Switching of the thyratron, charge transfer to the peaking capacitors through
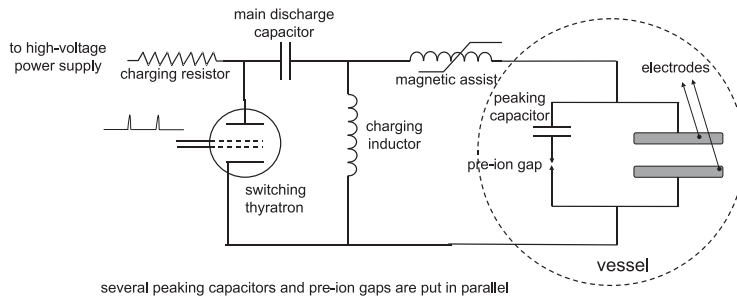
Figure 3.7: Pulsed power section and laser discharge system.

the small pre-ion gaps. The sparks form the necessary UV source for ionizing the gas between the electrodes.

3. Once the peaking capacitors reach a sufficiently high voltage, breakdown of the gas occurs and discharge takes place.

4. During the discharge the material is driven into population inversion and light amplification occurs.

After discharge the active gas volume between the electrodes needs full replacement to avoid discharge instabilities. High flow gas circulation systems are used for this purpose.

Due to pre-ionization techniques the pulse-to-pulse energy variations are very limited and feature a standard deviation of 2 %.

Another important technological issue is passivation of the laser cavity: the gas mix requires a certain halogen content for proper laser operation. Unfortunately these molecules react easily with impurities inside the vessel leading to a depletion of the halogen content below the optimum concentration. In order to limit the presence of suitable bonding partners for the halogen, organic materials should be avoided as much as possible (e.g. sealing rings). With time, contaminants end up in the vessel due to impurities in the gas cylinder, electrode erosion, etc. Therefore it is appropriate to eliminate these active contaminants by a passivation procedure from time to time. In essence the particles are 'deactivated' by accumulating a non-reactive layer on their surface. In this way the particles can no longer deplete the halogen.

There are two ways to passivate the laser vessel: one approach is to fill the vessel with helium and a considerable amount of halogen (10 times the partial pressure required for lasing) for 10 to 15 hours without operating the laser. During this time, the halogen can react with and thus passivate the contaminants inside the vessel. Another technique uses a much lower halogen content inside the vessel while the laser is operated with a low excitation discharge for half an hour. The ionized halogen will again react with contaminating particles. The degree of passivation
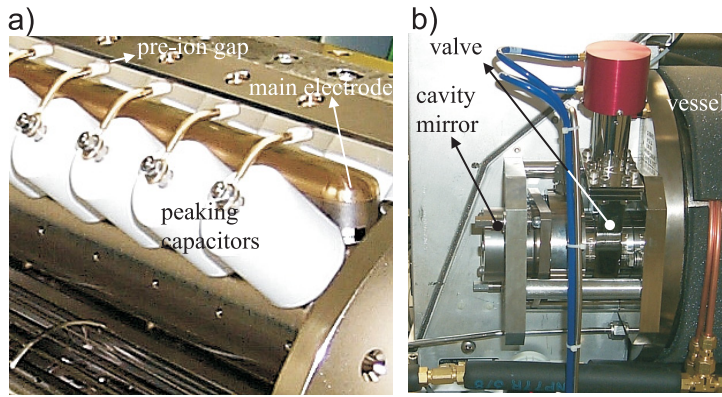
Figure 3.8: Detail of the pre-ionization pins and peaking capacitors (a). The optics valve at the ends of the vessel (b).

	F_2	ArF	KrF	XeCl	XeF
pulse energy [mJ]	30	275	450	250	200
max. rep. rate [Hz]	200	200	200	200	200
average power[1] [W]	6	45	80	45	35
beam size [mm×mm]	10×20				
pulse length [ns]	10 to 30				
[1] Measured at maximum repetition rate.					

Table 3.2: Typical characteristics of commercial excimer lasers.

can be observed by the color of the discharge: a red tone indicates that an amount of halogen species is still present in the discharge volume, blue proves that these particles have disappeared.

The vessel usually consists of a stainless steel structure with polyvinyl and teflon components used for optics clamping. Commercial excimer lasers usually feature valves between the main vessel and the optics ports to facilitate optics cleaning and replacement (figure 3.8).

Excimers lasers vary according to beam size, repetition rate, pulse fluence and wavelength. Typical specifications for a high-power excimer laser are given in table 3.2. Smaller types might have beam fluences down to 10 mJ. Table 3.3 gives an idea of the maintenance schedule and operation costs for an excimer laser installed in a production environment. Note that XeCl is the 'cheapest' wavelength and ArF is more expensive than KrF operation.

	pulses	down time	cost [%]
halogen injection	10^6	-	
gas replacement	10^7	<15'	10
optics replacement	10^8	<15'	10
laser tube exchange	10^9	<4h	65
HV components replacement	2-3 10^9	n.a.	
cost per hour	$\pm$\$15 for continuous KrF operation @140 Hz		

Table 3.3: Maintenance schedule for a typical excimer laser and operating costs (source: GSI Lumonics).

	ArF	KrF	XeCl	XeF
wavelength [nm]	193	248	308	351
nominal pulse energy [mJ]	230	450	300	275
average power [W]	30	80	50	45
repetition rate [Hz]	200	200	200	200
FWHM pulse length [ns]	12-20			
beam dimensions [mm $\times$ mm]	12 (V) $\times$ 25 (H)			
beam divergence [mrad $\times$ mrad]	1 (V) $\times$ 3 (H)			

Table 3.4: PM 848 output specifications.

Lumonics PulseMaster 848

The PM 848 laser is used for the experimental part in this thesis. It features optics gate valves, soft pre-ionization, cavity with co-axial geometry, external water cooling and an internal feedback system for stabilizing the output beam power. By insertion of suitable resonator optics, the laser can operate at different wavelengths (table. 3.4). Maximum optical power is achieved for KrF operation. In this case 450 mJ pulse energy is concentrated into a beam of 3 cm^2, equaling an irradiance of 150 mJ/cm^2. At ArF this value drops to 75 mJ/cm^2. The pulse energy can be controlled by the discharge voltage. The range for permitted voltages depends on the chosen gas fill (table 3.5). The Stabilase feedback system in the PM 848 exploits the voltage dependence of the pulse energy for stabilising the laser output in time: higher voltages can offset the effects of halogen depletion and temperature. For every wavelength there exists an optimum gas mix of the halogen, noble and buffer gas and optimum vessel pressure. Table 3.6 gives the detailed gas fill descriptions.

From table 3.4 we learn that the pulse length τ (FWHM) is between 12 and 20 ns, depending on the accumulated number of pulses after the last gas fill ($\pm$1 ns variation) and depending on the operating voltage ($\pm$1 ns for KrF within the full voltage range and right after a new gas fill, $\pm$2 ns for an non-fresh fill). The exact pulse shape (figure 3.9) is asymmetric: the rise time is quite small (6 ns), but the

laser transition	min. voltage	max. voltage
ArF	26	35
KrF	28	37
XeCl	26	35
XeF	25	34

Table 3.5: Typical discharge voltages of PM 848.

gas mix	type	fill [%]	cylinder bottle %	individual pressure [mBar]	total fill pressure [mbar]
ArF	F_2	0.08	5	135	
	Ar	2.00	100	150	4500
	Ne	balance	100	balance	
KrF	F_2	0.07	5	100	
	Kr	1.20	100	100	5000
	Ne	balance	100	balance	
XeCl	HCl	0.06	5	54	
	Xe	1.00	10	675	5400
	Ne	balance	100	balance	
XeF	F_2	0.10	5	150	
	Xe	0.20	10	240	5000
	Ne	balance	100	balance	

Table 3.6: Required gas mix in the vessel for PM 848.
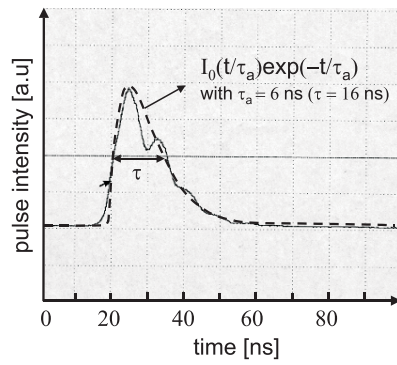
Figure 3.9: Pulse shape for PM 848.
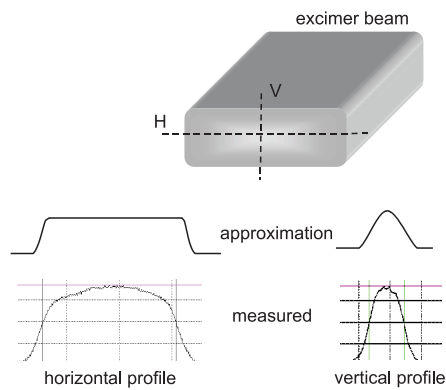
Figure 3.10: Typical excimer beam profile.

tail of the pulse is rather extended. The shape can be approximated by

$$I(t) = I_0 \frac{t}{t_a} e^{-\frac{t}{t_a}}$$

Fitting this curve to the pulse shape yields $t_a = 6$ ns, corresponding to a FWHM τ of 16 ns.

The typical beam intensity profile for a well-aligned PM 848 is given in figure 3.10. The profile is flat-topped in the horizontal direction and Gaussian-like in the vertical direction. For pattern projection, homogenous exposure of the mask is desired. Unless homogenizing optics are used in the beam path, the Gaussian beam profile limits the vertical size of the mask pattern down to a few mm.

STABLE RESONATOR

UNSTABLE RESONATOR
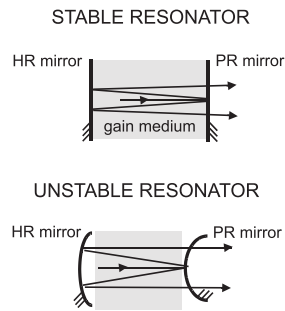
Figure 3.11: Stable and unstable resonator for excimer laser.

Stable and unstable operation

As mentioned above, an excimer laser will typically emit a beam with a rather large divergence of 1 to 3 mrad and containing several hundreds of transversal modes. Although this can be an appreciated property in mask projection systems, it is usually not desired for focusing purposes since the large divergence implies a high M^2 and thus a large focal spot size. Reducing the number of modes and the beam divergence angle can be accomplished by choosing an unstable resonator (figure 3.11). Higher order modes will show much higher diffraction losses at the mirrors and their content in the output beam will thus largely reduce. The beam divergence is of the order of 300 μrad and is more suitable for large distance propagation. The higher spatial coherence for this resonator set-up can run up to the mm-range and makes the laser more appropriate for applications where diffractive optics are used: e.g. writing of Bragg gratings in SM fiber with a phase mask.

Spectral narrowing of the excimer output

An important non-ablative application of excimer lasers is microlithography. Current commercial chip fabrication technologies depend on lithography processes capable of producing 0.09-0.25 μm feature sizes that use deep UV sources as KrF, ArF and F_2 lasers (figure 3.12). The refractive lens systems used to tranfer the mask to a resist exposure pattern are quite complex and mainly feature quartz lenses[4]. These lenses are not color corrected and should only be used with monochromatic light. As the natural emission of the KrF laser shows a spectral width of up to 0.5 nm, the resolution of the resist pattern is limited by the chromatic aberrations. Dispersive elements (e.g. a grating or etalon) inside the cavity are used to narrow the spectral width down to 0.4 pm and below [1]. The temporal coherence length increases up to the order of cm.

---

[4]Large lenses in high-quality CaF_2 have been introduced recently and can be used in combination with fused silica for chromatic correction of the optics.
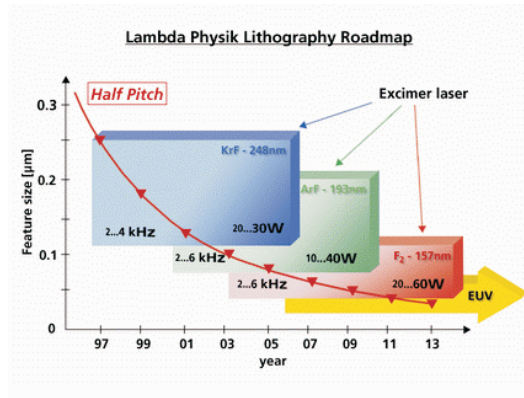
Figure 3.12: Roadmap for microlithography (courtesy of Lambda Physik).

3.2 Laser ablation based micromachining

There can be quite some confusion about the meaning of 'laser micromachining'. Therefore it is a good idea to clearly define the concept. In general laser micromachining refers to laser-induced fabrication of surface patterns or 3-D structures with typical feature sizes of the order of μm rather than mm. Strictly speaking it does not necessarily mean that solely laser-matter interaction should be responsible for the pattern definition: laser etching in a chemical active medium can also be considered a laser machining technique. Another typical misconception assumes that micromachining only covers erosive processes, while techniques as Pulsed Laser Deposition have an essentially additive nature.

This broad definition of laser micromachining includes applications as laser drilling of vias in PCBs, laser-assisted chemical etching, laser-LIGA, writing of Fiber Bragg gratings, photopolymerization, waveguide writing in glasses with ultrafast lasers, UV lithography, etc. This concept is depicted in figure 3.13.

The following sections of this chapter deal with one particular laser micromachining technique: laser ablation. As the physics behind this laser-matter phenomenon have already been discussed elaborately in the previous chapter, we will in this part focus on the feasibility of the technique for microstructuring.

An extensive description of suitable laser sources for processing of materials and their applications is beyond the scope of this thesis and will therefore not be treated. A brief overview of the most important material processing techniques is given in the Appendix, including some words on emerging applications for ultrafast lasers.

71
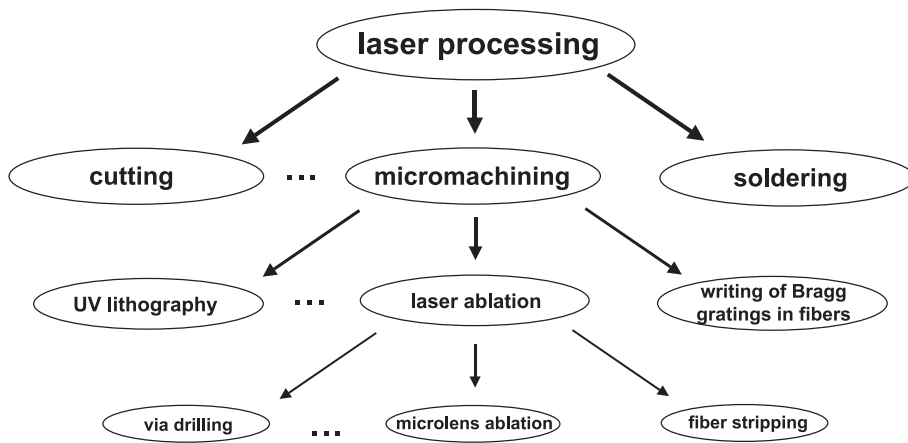
Figure 3.13: Laser processing tree.

3.2.1 Motivation for the deployment of lasers for material processing

The introduction of lasers for material processing purposes already took place some decades ago. Ever since, the range of machining applications where lasers can be used advantageously has been expanding rapidly. In the past laser micromachining gradually replaced the more traditional techniques using mechanical means or chemical substances. Today, market growth for laser microfabrication is realized by emerging technologies in the field of semiconductor manufacturing, microelectronics packaging, data storage, communications, medical and diagnostic equipment. The impact of lasers in material processing and other disciplines is illustrated in figure 3.14, taken from the Laser Focus World issue of January 2003.

With respect to the traditional micromachining techniques, laser processing offers quite a few advantages:

- Very localized and well-controlled energy deposition due to the high laser irradiance, excellent focusability and control of power-on-target.

- Selective removal via control of power-on-target.

- Minimized heat affected zone.

- 'Cold ablation' in dedicated materials, in particular polymers.

- Excellent tool for delicate objects and difficult geometries.

- No mechanical contact with the machined part.

- No tool wear as with mechanical machining.

- Broad range of suitable materials.
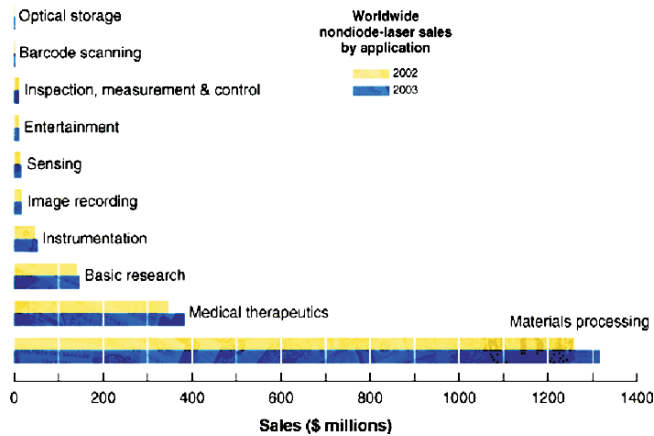
Figure 3.14: Worldwide laser sales by application.

- Excellent technique for fast-prototyping.

- No chemicals involved except for some dedicated techniques as laser-assisted chemical etching.

In most applications these benefits offset the main drawback of investment cost and reflect the true potential of laser processing as a valuable microfabrication technique.

3.2.2 Common lasers for ablation-based micromachining

The patterning capabilities of laser ablation highly depend on the properties of the employed laser and material: wavelength, pulse duration, intensity, absorption, thermal conductivity, molecular composition, etc. Although some materials can be very challenging for laser machining, it is quite fair to state that for every solid a suitable laser exists that permits accurate machining under the appropriate conditions. In general pulsed lasers are preferred to continuous wave (cw) sources for micromachining purposes:

- Pulsed lasers can easily obtain peak irradiances that are sufficient for ablation and the pulsed energy is more efficiently employed for material vaporization.

- Energy transfer to the material and ablation depth are accurately controlled via pulse count and repetition rate.

- Pulsed operation limits the interaction time between photons and material, leading to a better management of undesired damage to the surrounding area.

73

CONTINUOUS WAVE	PULSED
output power P [W]	pulse energy E [J]
irradiance $I = P/S_{spot}$ [W/cm^2]	fluence $F = E/S_{spot}$ [J/cm^2]
	pulse length τ [ns]
	peak irradiance I_{peak} [W]
	repetition rate f [Hz]
	output power $P = fE$ [W]
wavelength λ [μm]	
efficiency [%]	
beam quality (M^2)	
cost & reliability	

Table 3.7: Important laser characteristics for laser ablation purposes. S_{spot} is the spot area.

  In other words: better control over melting, deformation and composition changes of the neighboring material.

- When scanning ablation is employed, the scan velocity does not need to be continuous. This is in particular important when the sample or beam needs to abruptly change scan direction as in the corner of a rectangular cut.

The relevant laser properties for (micro)machining materials are given in table 3.7. As the driving force behind laser ablation is the energy transfer from the laser towards the ablated part, these properties are all related to laser power and pulse energy for respectively cw and pulsed operation.

In table 3.8 an overview is given of the most popular pulsed laser sources for micro-machining purposes. Note that some of these lasers (Ti:Sapphire, F$_2$ excimer and to a lesser extent Copper Vapor) are practically solely used for research purposes and did not enter the industrial market yet.
One remarkable aspect of the lasers in the table concerns the shape of their output beam. In general, two types of laser beams are commercially available: either the laser is operating in the fundamental mode, emitting a Gaussian or nearly Gaussian beam. The beam quality of these lasers is usually specified by M^2 and should be close to 1.0. Another type of laser beam can be found in TEA CO$_2$ and excimer lasers. The large beam typically features a high number of transversal modes, making these lasers suitable for large area fabrication rather than focal point writing.

laser	λ [μm]	τ	E_{max}	f	beam
CO_2 TEA[1]	9 to 11	1 μs	10^3 mJ	< 0.5 kHz	multimode
CO_2 sealed, Q-switched	9 to 11	100 ns	10^1 mJ	kHz range	Gaussian
Nd:YAG	1.06	20 ns	10^1 mJ	kHz range[2]	Gaussian
Nd:YAG (2ω, 3ω and 4ω)	0.532 0.355 0.266	20 ns	10^1 mJ	kHz range	Gaussian
diode bars	$\sim$0.9	150 μs	10^1 mJ	kHz range	multi-beam elliptical
excimer	0.157 0.193 0.248 0.308 0.351	20 ns	10^2 mJ	< 0.5 kHz	multimode
copper vapor	0.510 0.578	20 ns	10^0 mJ	kHz range	Gaussian
ultrafast Ti:Sapphire	0.780 to 0.820	150 fs	10^0 mJ	kHz range	Gaussian
[1] TEA = Transverse Electric Atmospheric. [2] These high repetition rates are only possible with diode pumping.					

Table 3.8: Pulsed lasers for micromachining. Values for pulse length and energy are indicative.
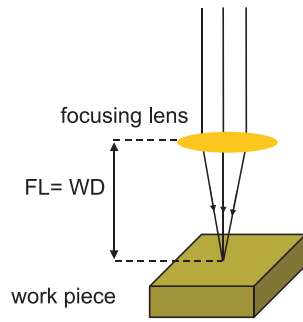
Figure 3.15: Focal point writing technique for micromachining.

3.2.3 Ablation strategy

Focused spot or direct-write operation

This optical set-up in figure 3.15 is used for maximally concentrating the beam irradiance into a single focal spot. In 3.1.1 it was shown that a beam with a high spatial coherence can be focused to a very small spot. For this reason only CO_2 (excluding TEA CO_2), Copper vapor, Ti:Sapphire and Nd:YAG lasers emitting a nearly Gaussian beam will be used for this purpose. The laser is specified by its optical output power P (pulse energy E for a pulsed laser), wavelength λ and beam diameter D_{beam}.

In direct-write operation the laser beam is focused onto the work piece through a lens with focal length FL and the separation between that part and the lens is called the working distance WD. When a single, thin lens is considered, the working distance equals the focal length.

The minimum focal spot size, depth of focus and corresponding spot intensity (cw laser output power divided by spot area) is given by

$$WD = FL$$

$$D_{spot} = \frac{M^2 4\lambda FL}{\pi D_{beam}}$$

$$DOF = \frac{\pi D_{spot}^2}{2\lambda M^2}$$

$$I_{spot} = \frac{4P}{\pi D_{spot}^2}$$

If a pulsed laser is considered, the last expression should be replaced by

$$F_{spot} = \frac{4E_{beam}}{\pi D_{spot}^2}$$

As an example, consider a pulsed CO_2 laser ($\lambda = 10.6\ \mu$m) with beam parameter $M^2 = 1.1$, emitting 10 W of optical power at 1 kHz. The beam diameter is 5 mm

FL [mm]	spot size [mm]	F_{spot} [J/cm^2]	I_{peak} [W/cm^2]	I [W/cm^2]	DOF [mm]
		pulsed		cw	
400	1.187	0.9	$9.0{\times}10^5$	$9.0{\times}10^2$	190.0
200	0.594	3.6	$3.6{\times}10^6$	$3.6{\times}10^3$	47.5
50	0.148	57.8	$5.8{\times}10^7$	$5.8{\times}10^4$	3.0

Table 3.9: Typical values for focal spot size, intensity, WD and DOF for a CO_2 laser ($D_{beam} = 5$ mm, $P = 10$ W, $M^2 = 1.1$) with raw beam intensity 51 W/cm^2 in cw operation or pulse fluence 0.051 J/cm^2 in pulsed operation at 1 kHz (square pulse shape).

and the pulse length 1 μs. It can be verified that the pulse energy is 10 mJ and the raw beam fluence 51 mJ/cm^2. The spot sizes and fluences achieved for different lenses are given in table 3.9. With pulse fluences of the order of 1-10 J/cm^2 (for 1 μs pulses), holes can be drilled in polymer and glass materials. For comparison we also added the irradiance in the focal plane if the laser would have been operated in cw. The peak irradiance in pulsed mode is a multiple of the one obtained in cw operation. Since ablation needs a minimum intensity level, this example clearly illustrates the benefits of pulsed laser sources.
In general the optical system will also feature a variable beam attenuator for choosing a desired spot fluence ($0 \leq F_{spot} \leq F_{max}$). The repetition rate can also be used to control the amount of power dissipated in the material.

Higher intensities can only be achieved by decreasing the spot size and thus the focal length for a given laser. However, in practical situations a sufficiently long working distance is appreciated as this prevents the lens of becoming damaged by fumes due to evaporating material. In addition, certain applications as cutting thick sheets or processing non-flat material require a long depth of focus. Higher DOF and WD can be achieved by increasing the focal length. These conflicting requirements for the focal length illustrate the compromise that has to be made when designing a laser machining system.

Focused spot operation is obviously capable of producing the high spot intensities needed for material removal. However, it is essentially a 'serial' writing technique as it can only machine one single spot at the time. On the other side this serial nature also offers a very large flexibility in terms of the ablated pattern geometry.

It should be noted that D_{spot} and F_{spot} in the equations above are optimum values, without considering aberrations of the optics and reflection/transmission losses along the beam path.

Mask projection operation

The focused spot machining approach suffers from some important disadvantages: due to its serial nature the processing of large areas can be quite time-consuming.
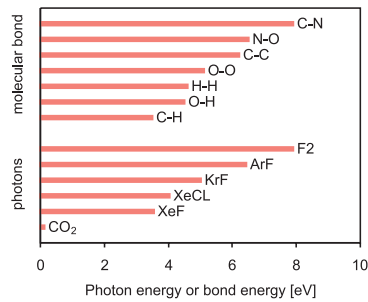
Figure 3.16: Molecular bond energies found in polymer materials and typical excimer laser photon energies. By comparison, the energy of CO_2 photons is given as well.
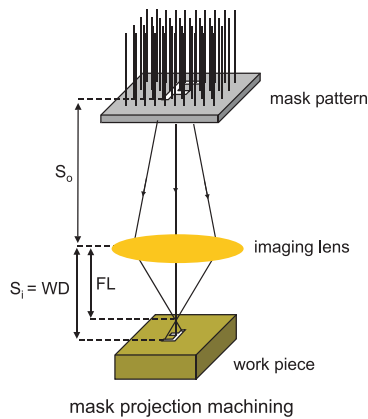
Figure 3.17: mask projection technique for micromachining.

On the other side, some lasers have quite some potential for micromachining due to their wavelength, large beam area and/or high pulse energy. This is in particular the case for TEA CO_2 and excimer lasers. Figure 3.16 illustrates the importance of the excimer wavelengths for micromachining polymer materials: many dissociation energies associated with molecular bonds that are found in organic materials, match the photon energies from excimer lasers. The material removal process due to direct bond-breaking with laser irradiation, is called photochemical ablation.

As the beam of TEA CO_2 and excimer lasers is highly multimodal, it does not focus very well. However, its large transversal dimensions make these lasers very suitable for mask imaging or projection purposes. A generic lay-out for a material machining workstation based on mask projection is given in figure 3.17. A laser beam is used to illuminate a mask consisting of opaque and transparent areas. The incident rays on the transpart parts will be transmitted through the mask, collected by the imaging lens and directed onto the part surface. If the latter is lying in the

	demag. 4×		demag. 10×		demag. 15×	
beam fluence [J/cm^2]	F_{part} [J/cm^2]	area [mm^2]	F_{part} [J/cm^2]	area [mm^2]	F_{part} [J/cm^2]	area [mm^2]
0.100	1.60	6.25	10.00	1.0	22.50	0.36
0.200	3.20	6.25	20.00	1.0	45.00	0.36

Table 3.10: Typical pulse fluences and corresponding machining areas obtained at the image plane with a mask projection system. The maximum mask area was chosen at 100 mm^2.

image plane, the irradiated geometry on the part will be identical to the pattern of the mask except for a constant factor called the demagnification of the system. The positions of the mask, part and lens plane are related by

$$\frac{1}{S_o} + \frac{1}{S_i} = \frac{1}{FL}$$

and the ratio S_o/S_i equals the demagnication DM. Using this parameter in the equation above, the part location can be calculated as

$$S_i = (1 + \frac{1}{DM})FL$$

For large demagnifications the image plane nearly coincides with the focal plane. In other words: mask projection systems can mimic focused-spot operation by imaging a circular aperture at the mask plane with a large demagnification.
Since the image dimensions are scaled with a factor $(DM)^{-1}$ with respect to the mask geometry, the intensity (or fluence) on the work piece will increase with $(DM)^2$ except for transmission losses that might occur in the optical path. As the raw beam will usually not be powerful enough for ablation, DM can be used for enhancing the beam fluence to an appropriate level. However, the demagnification will limit the part area that can be processed for a given mask. Table 3.10 illustrates this behavior for some typical demagnifications and raw beam fluence values. An area of 10×10 mm^2 was considered as a feasible mask size.

An important aspect of mask imaging systems is telecentricity. A single lens is perfectly capable of imaging a mask pattern on the part surface. As the pattern is drilled into the material, the rays' angle of incidence determines the drilling direction. Figure 3.18 shows that using a single lens for imaging will result in non-perpendicular incidence of the rays on the substrate for mask features which are not on the optical axis of the system. This behavior is generally not desired and can be solved by inserting a lens that focuses the beam in the focal plane of the projection lens.

Obviously, the incident beam on the mask should be as homogeneous as possible over the relevant mask area. In this context the parameter M^2 is irrelevant as criterion for beam quality in mask projection systems. A more appropriate measure should indicate to what extent the laser beam approximates a 'top hat' function:
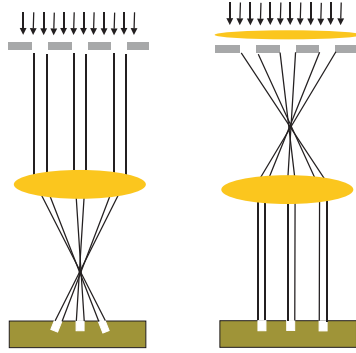
Figure 3.18: Telecentricity in a mask imaging system.

the homogeneous beam area, the average intensity and its standard deviation over the beam area. The beam from an excimer laser is essentially top hat in one direction and more or less Gaussian in the other. The homogeneous part is in this case limited to a few mm in the vertical direction. Beam homogenizing devices are usually based on splitting up the beam in several parts and then superimpose them in the mask plane by using (micro)optics. The roof prism and fly's eye beam homogenizer are based on this superposition technique. The maximum mask area that can be imaged onto the part is determined by the flat top area and the field of the lens.

For a mask projection system the Beam Utilization Factor (BUF) is defined as the relative area of the mask with respect to the homogeneous beam area. High values for this parameter indicate an efficient use of the optical power of the laser. In case the useable beam area does not match the mask size, one can insert a beam concentrator/expander in front of the mask as depicted in figure 3.19. Using a positive and a negative lens separated by the sum of their focal lengths, the output beam diameter scales proportionally to (FL_2/FL_1) and the pulse fluence with a factor $(FL_2/FL_1)^2$.

An important challenge in the design of a micromachining system based on mask projection is dimensioning the imaging lens. Quite some boundary conditions should be taken into account when choosing such a lens: working distance, de-magnification, machining resolution, aberrations, manufacturing cost, etc. It is obvious that compromises have to be made. Usually a low NA lens with a focal length of several cm is chosen. As the working distance equals the focal length for a single lens (or is at least of the same order for a multiple lens system), this order of magnitude is sufficient for preventing debris and fumes to reach the lens surface. The low NA −usually around 0.1− determines the machining resolution and depth of focus, with typical values respectively of the order of 1 μm and several tens of μm.

If the mask projection technique is used for machining or ablating a pattern in the part while mask and part stand still, it is called *static ablation*. If mask and/or
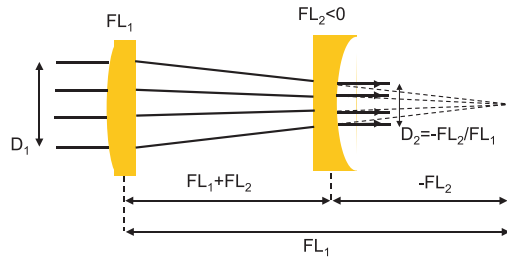
Figure 3.19: Beam concentrator for adjusting beam size to mask area.

part are moved, the technique is called *scanning ablation*. Scanning can be extremely useful if the ablation pattern is invariable in one direction. E.g. scanning ablation of U-shaped grooves with a length that surpasses the maximum pattern size for static ablation. In this case the mask pattern can be chosen to contain a number of rectangular apertures —one for each trench— with a certain length. While the mask is kept fixed, the part is translated along the axis of the grooves with a constant velocity.

Another scanning technique offers the opportunity to transfer an arbitrary mask pattern larger than the laser beam onto the part. By a coordinated translation of both mask and part in opposite directions, the full mask pattern can be continuously scanned and copied into the part surface (figure 3.20).

Yet another approach is homogeneous exposure of the part. The precise geometry of the ablated structure can then be controlled by covering the part with a patterned opaque layer or sheet, called the contact mask. As this sheet is exposed to a much higher fluence than the projection mask, the range of materials and mask thicknesses is more limited. An example of the contact mask technique can be found in via drilling in Printed Circuit Board (PCB). These boards typically consist of layers of FR4 sandwiched between copper layers. Via formation with laser machining can be accomplished by drilling a hole in the copper layer with a YAG laser and subsequent ablation of the FR4 down to the next copper layer with a CO_2 laser. The large CO_2 laser beam is typically quite larger than the hole and does not need accurate alignment as the high reflectivity and thermal conductivity of the metal prevents ablation of the remaining copper layer. For a sufficient number of laser pulses, the depth of the via is determined by the underlying copper layer.

3.2.4 Optec MicroMaster workstation

The commercial MicroMaster micromachining workstation is used for the experimental work in this thesis and is depicted in figure 3.21. It basically consists of a computer-controlled excimer beam manipulation section and a high-accuracy motorized sample stage, mounted on a highly stable granite frame. In combination with the PM 848, it is suitable for machining polymers, glasses, ceramics and metals. Figure 3.22 illustrates the beam path inside the Micromaster. The excimer beam is guided through an attenuator consisting of a rotatable quartz plate which
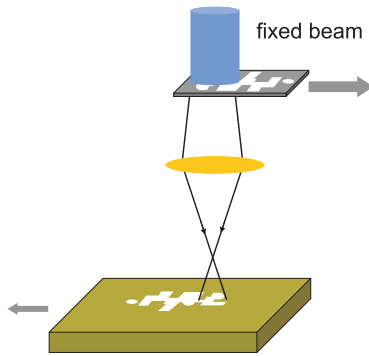
fixed beam

Figure 3.20: Coordinated translation of mask and part for large mask area imaging.

has an anti-reflection (AR) coating on one side. The non-coated interface attenuates the beam via fresnel reflection and the transmitted power can be adjusted according to the angle of the plate with respect to the beam. High-reflection mirrors direct the beam through the mask. The mask pattern is imaged onto the sample surface using a 3-element projection lens (optical resolution $\sim$1.5 μm). The lack of telecentricity is not critical since the lens' field of view is a mere 2 mm and the working distance quite large ($\pm$10 cm).

Two illumination systems and cameras incorporated in the workstation make it possible to track the beam and the sample on-axis and off-axis. The Micromaster offers continuously variable demagnification $-$between $4\times$ to $11\times-$ by motorized movement of the projection lens and two mirrors in the beam path. This feature can be extremely useful when the mask pattern size deviates from the desired value by a scaling factor. Through well-considered lens design the image planes of the mask at the excimer wavelength and visible (red) light coincide. In this way the machined surface is in focus for the excimer beam and for the camera system at the same time. The maximum achievable fluence on target depends on the laser source and is of the order of 15 J/cm^2 for KrF and 7 J/cm^2 for ArF operation.

The sample is positioned on a rotation stage, which in turn is mounted on a 200 mm$\times$200 mm X-Y translation stage (respectively 0.01° rotation and 1 μm motion resolution).

Sample motion and beam handling is fully computer-controlled in a Windows environment. Compatibility with industry file formats as Excellon, Gerber, HPGL and DXF offers the opportunity to define complex patterns with a CAD tool.

During laser machining a plume will be generated at the ablated surface. The plume consists of evaporated material which can propagate towards the beam optics, and of non-evaporated particles which can drop back on the sample near the ablated area. In order to avoid optics contamination, fume extraction is provided right above the sample.
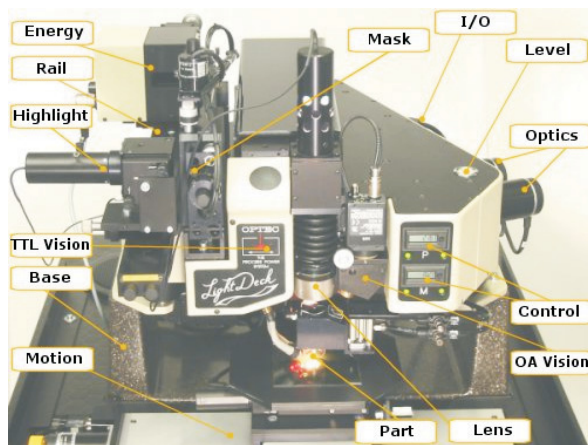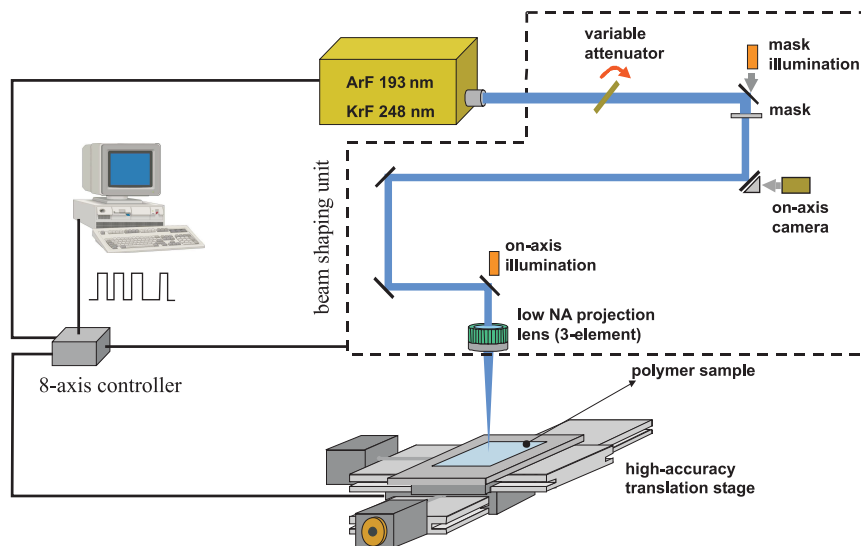
Figure 3.21: Optec Micromaster.

Figure 3.22: Scheme of the micromachining workstation consisting of PM 848 and Micromaster.

material	transmission limit [nm]	solubility in H_2O	thermal conduct. [W/mK]	radiation resistance
SiO_2	160	low	6-10	good
CaF_2	130	low	10	good
MgF_2	110	very low	21	good
BaF_2	140	high	12	good

Table 3.11: Typical substrate materials for excimer beam handling optics.

material	refractive index	wavelength limit [nm]
MgF_2	1.40-1.45	<200
AlF_3	1.40-1.45	200
CaF_2	1.45-1.50	<200
SiO_2	1.45-1.55	200
LaF_3	1.6-1.65	250
CeF_3	1.65-1.75	250
Al_2O_3	1.70-1.80	200
Sc_2O_3	1.90-2.05	300
Y_2O_3	2.0-2.1	250
HfO_2	2.3-2.4	250
ZrO_2	2.3-2.4	300

Table 3.12: Suitable dielectric coating materials for deep UV applications.

3.2.5 Optics for excimer lasers

Lenses and beam mirrors

There are only a few choices for highly transmissive optical materials at the excimer wavelengths, certainly when considering wavelengths below 250 nm. The primary requirements for these materials are low absorption and high transmission at the laser wavelength, adequate radiation resistance, suitable for coating deposition and non-hygroscopic. Materials that satisfy these criteria are wide bandgap oxides and fluorides such as SiO_2, CaF_2 and MgF_2. Table 3.11 gives an overview of the relevant properties of these materials for deep UV beam handling.

In order to reduce transmission losses in the optics and avoid damage due to back reflections, the optical elements in the beam guiding system are coated. Anti-reflection (AR) coatings are deposited on the transmissive optics and high-reflection (HR) coatings are used for beam mirrors. Only dielectric stacks are employed for these coatings as even slight absorption of the high-power laser pulse inevitably heats up the coating and substrate, eventually damaging the optical component. Suitable dielectrics for use in the UV are given in table 3.12. Some examples are Sc_2O_3/SiO_2 stacks for HR and Al_2O_3/SiO_2 stacks for AR coatings with damage thresholds of respectively 16 and 6 J/cm^2.

Mask substrates for excimer ablation

There are several ways to make suitable masks depending on the beam fluence, required accuracy and quality of the edge-definition. The easiest approach uses a metal sheet as base material and the desired mask pattern is simply cut out with mechanical tools via drilling, sawing and milling. Although such masks can be fabricated rather rapidly, the edge-definition of the apertures is generally very poor due to burring and might be unsuitable for high-precision machining. Another approach is based on using a UV transparent material as Suprasil (a SiO_2 derivative suitable for deep UV) and applying the desired pattern via lithographic techniques. The opaque areas are created by a thin metal film (order of a few hundred nm) on the substrate, typically chrome. This technique permits high-accuracy pattern definition with excellent edge-quality, but is not feasible for high-energy applications as fluences above 100 mJ/cm^2 will simply ablate the metal layer. More sophisticated techniques replace the metal layer by a HR dielectric stack: the opaque regions are now based on reflection of the laser fluence without any absorption, making the mask also suitable for exposure to high fluences.

A less conventional technique uses a polymer as mask substrate. Although polymers generally have low ablation thresholds and thus strongly limit the mask lifetime, they can be machined very accurately with an excimer laser. In this work several structures were ablated using a mask of polyimide as thin as 50 μm. As the film is not self-supporting, it was glued onto a metal frame with a suitable aperture. Next the pattern definition was realized with KrF laser ablation through the film using a simple but well-defined beam aperture. Obviously, the range of feasible patterns is limited to connected structures. It was experimentally verified that this technique offers a valuable alternative for prototyping purposes involving small beam fluences at the mask. Moderate to high intensities can still be realized on the part by selecting a high demagnification.

3.3 Suitable materials for excimer laser ablation

3.3.1 Overview

The range of materials that can be ablated with excimer lasers is extremely broad: ceramics, glasses, organic materials, metals and semiconductors. The ablation efficiency and quality of a certain material depends on properties as reflectivity, absorption depth at the laser wavelength, thermal conductivity, enthalpy of evaporation, bond energy, defect density, etc. Quality is in this context related to smoothness of the ablated crater, extent of damage to the surrounding material, depth of ablation and definition of the crater edges. Without going into detail, we give here some rules of thumb for ablation of different material types.

metals, semiconductors

These materials have very high absorption coefficients, leading to optical absorption depths down to the nm range. Despite this very confined photon penetration, the

affected area increases considerably due to thermal diffusion of the incident pulse energy. The high surface reflectivity and thermal conductivity are responsible for the high fluences needed for ablation: typically several Joules/cm^2 and more. During ablation −which is essentially a transition of solid to melt and vapor phase for these materials− melting will affect the bottom and edge quality of the ablated cavity. Melt droplets are splashed around during ablation and a recast layer is formed afterwards.

ceramics and glasses

These materials also show high absorption, but contrary to metals the thermal conductivity is much lower. The overall result is a lower ablation threshold and a better edge definition. Ablation is accompanied by the introduction of additional stresses into the material leading to cracks in the vicinity of the crater.

low-absorption crystalline oxides

The most important material in this category is quartz. Its low UV absorption makes it very suitable as base material for excimer optics, provided that it is used in a very pure, crystalline form. For the same reason excimer lasers are of little use in ablation of quartz: the low absorption spreads the pulse energy over a large depth and is responsible for the very high ablation thresholds. At sufficiently high laser fluences, ablation will occur due to the presence of impurities in the crystal and multi-photon processes that bridge the bandgap energy. The result is a crater of poor edge and bottom quality, and sensitive to crack formation. An exception should be made for the F_2 laser: its photon energy (7.9 eV) practically matches the bandgap of SiO_2. As a consequence, ablation occurs as a clean material removal process.

polymer materials

The typical bonds in their molecular chains feature bond energies which are in the same range as the excimer photon energies. This property is responsible for their high absorption coefficients at UV wavelengths and the 'cold ablation' phenomenon: the absorbed photons excite electronic states in certain organic bonds and relaxation from the excited state can occur via direct dissociation. In practice the ablation process always features thermal and non-thermal material dissociation and evaporation.

The importance of the UV wavelength for polymer ablation is illustrated in figure 3.23. Polyimide is ablated with 3 different laser types: a fast axial-flow pulsed CO_2, a Q-switched Nd:YAG and a KrF excimer laser. The high precision and the absence of any damage (burring and swelling) to the surrounding area in case of excimer laser ablation is evident from this picture.

Polymers offer low ablation thresholds (0.01-0.5 J/cm^2), high-quality edge definition and surface finish, and there is little or no evidence of thermal damage to the
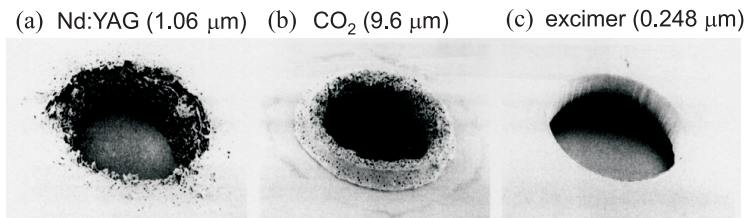
(a) Nd:YAG (1.06 μm)   (b) CO$_2$ (9.6 μm)   (c) excimer (0.248 μm)

Figure 3.23: 300 μm holes in a polyimide film of 75 μm thickness. The holes were drilled using three common laser types for ablation.

surrounding material.

Figure 3.24 compares cavities ablated with a KrF excimer laser in different materials: alumina, polycarbonate, GaAs and steel. A closer look at these craters allows to conclude that polymers show indeed an excellent surface finish compared to the burred edges, recast deposition and fracture that often occurs with other materials.

3.3.2   Polymers

From the analysis in the former section we can conclude that polymers are an excellent base material for micromachining with excimer lasers. The range of commercial polymers is extremely large and even today new types are developed or 'engineered'. Usually they feature one or more specific properties that can be used with advantage in a particular application.

In this thesis five polymers have been selected for experimental verification of their ablative properties. They have been chosen based on their mechanical and optical qualities as required for the applications in the following chapters. The polymers are polymethylmethacrylate (PMMA), polycarbonate (PC), polystyrene (PS) and polyethylene terephthalate (PET). The yellow colored polyimide (PI, brand name Kapton) was added to this list because of the many applications (flex circuits in portable electronics nozzle plates of inkjet printers) and its appreciated laser processing qualities: IR and UV lasers are commercially employed for via drilling, cutting and skiving of Kapton layers.

Table 3.13 briefly indicates the most important properties of these commercial optical polymers. For reasons of completeness, COC and COP materials are also shown in the list as these rather new polymers feature some appreciated advantages. The ablative properties of these polymers have not been investigated experimentally in this work, but it has been reported in [2] that COC can be ablated smoothly with an ArF laser.

Each polymer has one or more key advantages with respect to the others on thermal, mechanical or optical behavior. But there is no single material that can be considered superior in every field. PMMA is appreciated for its generally good scratch resistance and chemical inertness, low wavelength dispersion and high transmission; PC features a high temperature resistance and impact strength. PS is the low-cost solution among optical polymers. It shows high clarity but cannot be used at ele-

87
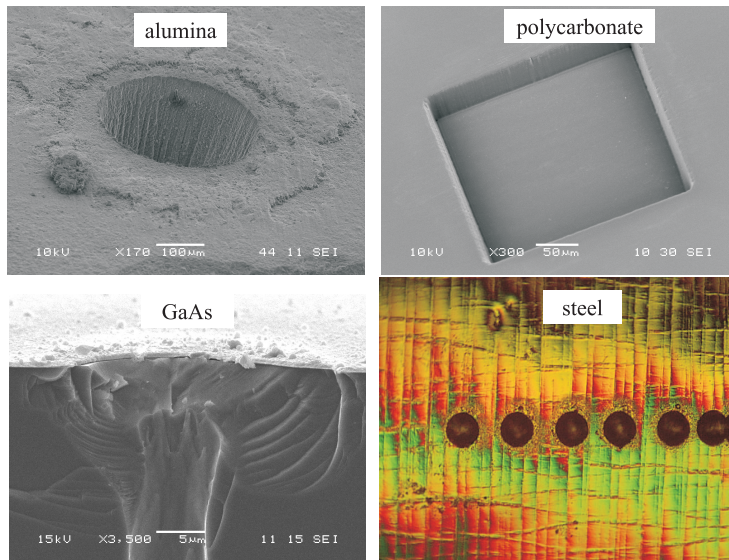
Figure 3.24: Excimer ablation of different material types. For GaAs, a cross-section of the cavity instead of a top view is shown.

vated temperatures. The COC and COP materials are appreciated for their high temperature resistance, low water absorption, low weight and high transmission.

3.4 Commercial applications of excimer laser processing

3.4.1 Applications based on laser ablation

Inkjet nozzle drilling

The key component in an inkjet printing device is the inkjet head that forms ink droplets and ejects them towards the paper. Two distinct technologies are used to accomplish droplet ejection. The first approach is based on rapid heating of ink with a thin-film resistor [4] and is depicted in figure 3.25. A small current is applied to the resistor, leading to heating of a very thin 100 nm ink layer right above the resistor surface (typically up to 300 °C within 3 μs). On the resistor surface bubble nucleation evolves towards a single bubble expansion within 10 μs and leads to ejection of an ink droplet through the upper orifice. In a next step the vapor bubble collapses and draws in fresh ink. The refill of the ink chamber is typically accomplished within 80 μs. The other technology is called piezoelectric printing and is based on creating a mechanical force for droplet ejection by a piezoelectric

	acrylic (PMMA)	polycarbonate (PC)	polystyrene (PS)	cyclic olefin copolymer (COC)	cyclic olefin polymer (COP)
n					
@ 486 nm	1.497	1.593	1.604	1.540	1.537
@ 589 nm	1.491	1.586	1.590	1.530	1.530
@ 651 nm	1.489	1.576	1.584	1.526	1.527
abbe value	57.2	34	30.8	38	55.8
T[1] [%]	92	85-91	87-92	92	92
haze[2] [%]	1-2	1-2	2-3	1-2	1-2
max. temp. [$^\circ$C]	92	124	82	130	123
water absorption[3] [%]	0.3	0.15	0.2	<0.01	<0.01
density [g/cm^3]	1.190	1.20	1.06	1.03	1.01
therm. exp. [x10^{-5}/$^\circ C$]	6.74	6.6 to 7.0	6.0 to 8.0	6.0 to 7.0	6.0 to 7.0
dn/dT [x10^{-5}/$^\circ C$]	-8.5	-13.0	-12.0	-10.1	-8.0
brand names	perspex	lexan	styron	topas	zeonex

[1] Visible light transmission for a sample with a thickness of 3.174 mm. This includes Fresnel reflections at the back and front side of the slab.

[2] Forward scattering.

[3] In water for 24 hrs. at room temperature.

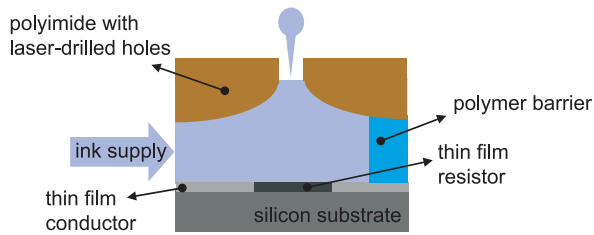Table 3.13: Optical polymers properties. Data taken from [3].

Figure 3.25: Thermal inkjet operation.

cell instead of the heating resistor.

Proper operation of the droplet squirting assumes smooth, tapered holes or orifices in the upper sealing layer called the nozzle plate. Currently the market is dominated by three fabrication processes for the orifices: silicon etching, electroforming and excimer laser machining. The material choice for the plate typically depends on this fabrication process and will be either silicon or polyimide (Kapton). Excimer laser drilling is now by far the most popular and best all-round technique for inkjet hole drilling, making the highly UV absorbing polyimide an excellent base material. The excimer beam is converted to a line source using cylindrical optics and an array of holes is drilled simultaneously using mask projection. Typical ablation rates are around 0.2 μm/pulse using some 600 mJ/cm^2. As the polyimide sheet features a thickness of 50 μm, it takes about 200-300 pulses to create a single nozzle plate. For 600 dpi printers, arrays as large as 300 holes with a pitch of 42 μm and a hole size (exit diameter) of 28 μm are required. Uniformity of the droplets limits diameter tolerances down to 0.5 μm.

As in any other ablation process debris (see 3.5.10) is formed on the beam entrance side during hole drilling and is hardly removable from the surface afterwards. Since it will likely contaminate the ink chambers with carbon particles and block the orifices, debris should be avoided. A sacrificial, water-soluble coating is applied to the polyimide before the hole drilling. Afterwards the coating is removed by rinsing in a water solution. Finally it should be noted that applying a proper backside substrate to the polyimide ensures well-defined exit holes. In figure 3.26 the polyimide drilling process and the resulting orifice array are depicted.

In the near future growth of the inkjet technology is expected from emerging applications in textile printing and medical diagnostics.

Ablation of fluid capillaries

Excimer lasers experience quite some competition from other pulsed UV laser types (frequency tripled and quadrupled Nd:YAG) for micromachining polymers. Still, excimer lasers offer the unequaled advantage of processing large areas at once by using mask projection. For this reason excimer lasers are quite attractive for fabricating arrays of microscopic fluid channels and reservoirs in polymer substrates (figure 3.27). These structures, with their ability to generate electro-osmotic flow,
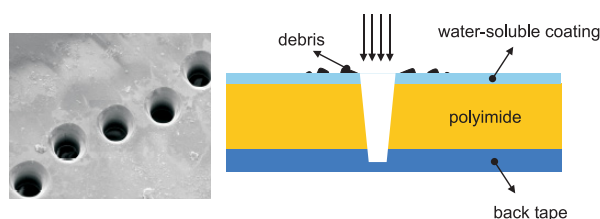
Figure 3.26: Ablated orifice array and cross-section of the material sandwich for hole drilling through the polyimide.

find applications in conventional and miniaturized capillary electrophoresis[5] instrumentation and liquid-handling platforms. Note that miniaturization of mechanical pumps and valves for liquid flow control can be techniqually very problematic, whereas electro-osmotic flow control can be easily realized as it basically requires only the insertion of two electrodes. As polymers are inexpensive and mask projection allows fast patterning of complex devices, the technique offers quite some potential for development of disposable diagnostic lab-on-chip devices. Suitable polymers for these chips are polyethylene terephthalate and cellulose acetate due to their high electro-osmotic flow velocity [5].

Trenches are typically ablated by scanning the polymer substrates with a mask consisting of several rectangular apertures. In a next step large holes are drilled through the substrate at the far ends of the grooves, which will act as reservoirs for the fluid. Finally a sealing layer (usually polyethylene terephthalate) is applied onto the groove substrate using thermal lamination (at 135 °C). Compared to the original substrate, the ablated areas are usually less charged due to a reduced carbon/oxygen ratio and thus more hydrophobic. On the other side, oxygen incorporation and increased charge have been noted for the ejected fragments during ablation. These heated particles are usually redeposited onto the surrounding area and make the surface more hydrophylic. The result is that the ablated capillaries will prove to be more hydrophobic than the original substrate for static ablation. In case of scanning ablation the trenches will be rather hydrophylic since debris is now also redeposited in the groove. An optimum flow velocity can be obtained by a well-chosen mask pattern and scan velocity [6]. When adsorption of reagents during electrophoresis should be avoided, the ablated channels can be coated with a protective layer.

Laser shaping of the eye's cornea: PRK and LASIK

Until the mid-90s, correction of myopia (near-sightedness) was surgically performed with refractive keratectomy. Radial incisions were made in the eye's surface and these weakened the outer cornea. As a result, the cornea bulged slightly forward and flattened in the middle. The first FDA approvement for vision correction

---

[5]An electrochemical process in which macromolecules or colloidal particles with a net electric charge migrate in a solution under the influence of an electric field.
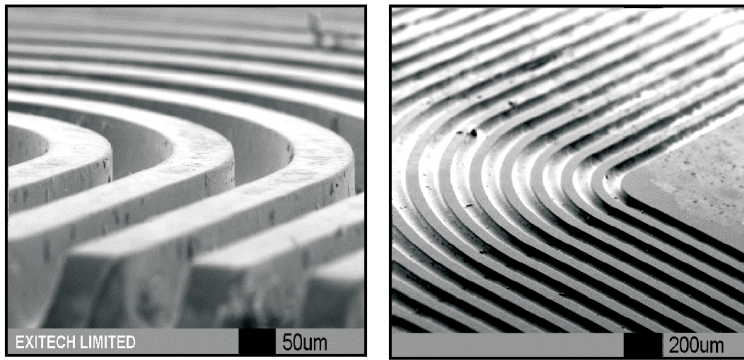
Figure 3.27: Arrays of fluid cappilaries ablated with excimer laser ablation (courtesy of Excitech).

with laser treatment was obtained in 1995 by Summit, a US company. From then, doctors used ArF excimer lasers for sculpting the cornea surface in a way as depicted in figure 3.28. This technique is referred to as PRK or Photorefractive Keratectomy. The surface treatment creates a great deal of pain and discomfort for the patient. A more subtle technique was introduced in 1998: LASIK or Laser in SItu Keratomileusis. The ablated area is now buried into the corneal layer as a flap of surface is cut and rolled aside before the laser is used to remove material in the cleared area. Afterwards the flap is put back in its place so the ablated part (which can be considered a wounded area) is protected from foreign influences. With this technique patient discomfort is reduced to merely a few hours.

Although it is clear from literature that an ArF laser is used to remove corneal material at a nominal etch rate of around 0.27 μm per pulse (160 mJ/cm^2), the exact sculpting process for flattening or bulging of the cornea is not always precisely described. Generally, commercial systems are based on one of the following techniques:

- **Static ablation** – In this case a large beam with adjustable fluence distribution (presumably realized by an aperture of variable size) is centered on the cornea. The desired ablation pattern —with deepest ablation in the center for myopia— can be realized by varying the aperture diameter from small to large while the laser fires at a constant pulse frequency.

- **Scanning slit ablation** – A slit is used for beam shaping and scans the central part of the cornea in multiple directions. The scanning directions are perpendicular to the slit axis. The final result is again a spatially controllable ablation depth.

- **Flying spot ablation** – A small beam (diameter of the order of 1 mm or smaller) scans the surface of the eye at elevated speeds while the laser is operated at high pulse frequencies, typically 100 Hz. This technique offers a lot more flexibility in terms of the exact ablation profile.
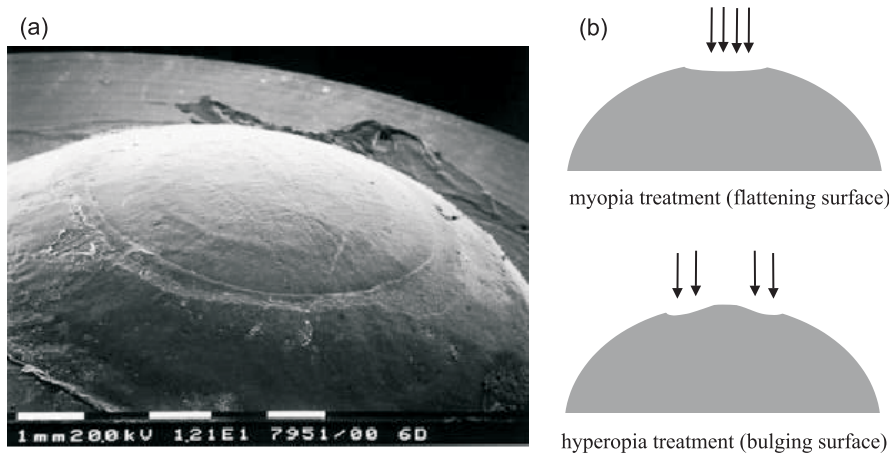
92

(a)

(b)

myopia treatment (flattening surface)

hyperopia treatment (bulging surface)

Figure 3.28: SEM image of an ablated corneal surface (a). Required surface correction for myopia and hyperopia (b).

Fiber and wire stripping

The protective coating of electrical wires can be efficiently removed in a contactless by using UV and infrared lasers. As the threshold for laser damage of metals is an order of magnitude larger than for polymers, it is possible to selectively remove the coating by choosing a suitable laser fluence. Selective removal without mechanical tooling is essential for contacting wires on miniaturized devices as hard disk heads or small sensors for electronic measurement systems. Usually a rectangular beam is employed for stripping the wire. The part of the beam that does not hit the wire surface directly is reflected back by a concave mirror (figure 3.29).

Stripping of optical fiber is necessary for interfacing with opto-electronic components and can be achieved in a similar way as the wire case. At every optical interface a certain length of the protective fiber coating needs to be removed (end-stripping) and the fiber requires cleaving, often at a specific angle to avoid back-reflection. Another situation occurs when a FBG (Fiber Bragg Grating) needs to be 'written' in the fiber core or when the fiber cladding needs to be exposed to the ambient medium for sensor applications. In both situations the acrylic or polyimide coating needs to be removed locally along the fiber ('mid-span' stripping) and this can be a challenging task with mechanical means.

Manual stripping can be very time-consuming, certainly when arrays of fibers are processed. In the latter case the yield of the fiber preparation process can become very low as breakage of a single fiber during stripping means that the process needs to be repeated for the full array. Commercial stripping equipment is based on either mechanical, thermal-mechanical or chemical processes. Each technique suffers from either reproducibility problems, lack of flexibility (in terms of fiber diameter and strip length range) and/or environmental issues. Stripping the plastic coating with a UV or IR laser at sufficiently low fluences allows exposure of the glass fiber
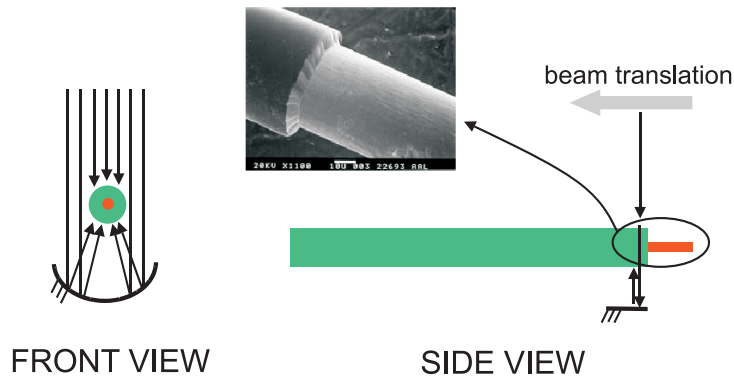
FRONT VIEW   SIDE VIEW

Figure 3.29: Laser stripping of optical fibers and electrical wires.

to air in a contactless way. Obviously the stripping length can be chosen arbitrarily as the laser beam can be scanned along the fiber axis and both mid-span and fiber-end stripping can be easily obtained. Suitable lasers are CO_2, excimer and Nd:YAG, although the UV wavelengths should be excluded when dealing with photosensitive fibers (e.g. prior to Fiber Bragg Grating writing). Typical stripping speeds are of the order of several hundreds of microns per second.
A commercial CO_2-based fiber stripping device developed by Resonetics (Nashua, USA) is described in [7].

Pulsed Laser Deposition

In PLD or ablative sputtering, material is ablated from a solid target in vacuum and the plasma plume consisting of evaporated material is redeposited on another substrate (figure 3.30). Due to rapid heating, the stoichiometry of the material can be maintained during transfer from target to substrate. Since the plume has a narrow angular distribution, uniform deposition can be problematic. For this reason the sample is usually mounted on a rotation stage and the laser beam is capable of raster scanning the target. Both conceptually and experimentally, PLD is very straightforward. The fact that the evaporating laser source is not present inside the sealed area makes PLD very flexible in operation: reactive gases can be injected in the chamber, additional optical components can be easily put in the beam path without being limited by the vacuum chamber, etc. The technique is extremely suitable for depositing materials with a very high melting point or with a composition which is difficult to deposit by other processes. Epitaxial growth of II-VI compound semiconductors by PLD is reported in [8].
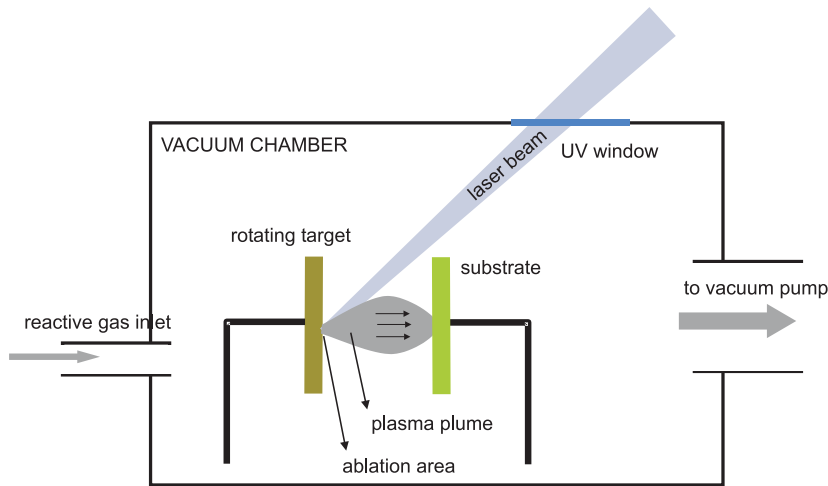
Figure 3.30: PLD set-up.

Microvia drilling

The fabrication of a microvia[6] in multilayer flex or PCB involves two distinct steps: first a hole is created in the dielectric between two copper layers and in a second step an electrical path is realized in the hole via copper plating.

In the late 80s, volume production of microvia formation with excimer lasers was first introduced by Siemens: 80 μm vias were drilled into polyimide Multi Chip Modules [9]. As excimer laser-drilling involves fewer process steps than other methods, it has been the preferred technique for drilling vias in thin film packages. Using masks containing large arrays of holes, many vias (order of thousands) can be drilled at once.
Development of reliable, high repetition rate 3ω Nd:YAG and CO_2 lasers in terms of stability and power (replacement of flashlamp by diode pumping for YAG, introduction of RF slab-discharge for CO_2) have pushed aside the more expensive excimer lasers running at a mere 200 Hz and requiring frequent toxic gas refills.
Vias can be drilled in several ways: if the laser beam matches the via diameter, percussing drilling is used. When the beam is smaller than the via, the beam scans the substrate along one or more concentric circles in order to fully remove the material inside the required via diameter. This technique is called trepanning. Yet another method is helical drilling: contrary to trepanning the beam can contour more than once along the same circular path, gradually ablating the via. All these techniques are illustrated in figure 3.31.

Traditional techniques for via formation in PCBs and flex as mechanical drilling, chemical etching and punching are not suited any more for creating low-cost vias below 100-150 μm. Instead RF CO_2 lasers are employed for fast percussion drilling

---

[6]The term 'micro' is used when the dimensions of the via are below a certain diameter, typically around 100-200 μm.
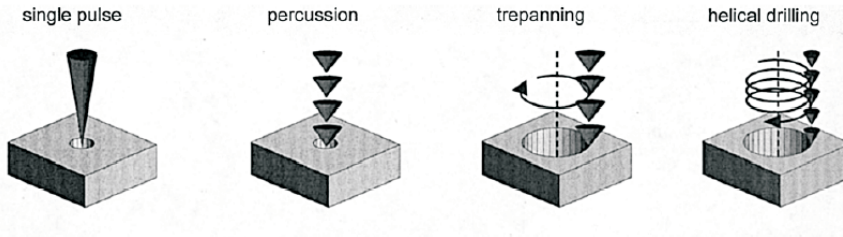
Figure 3.31: Via drilling strategies.

of dielectric material and UV DPSS[7] for ablating copper via trepanning. The UV wavelength of a 3ω Nd:YAG is needed as the high reflectivity in the far IR prevents ablation with RF CO_2[8]. Direct-write systems with CO_2 lasers are limited to spot sizes with a diameter above 100 μm due to the large wavelength while frequency-tripled Nd:YAG lasers can achieve spot sizes down to 25 μm for the focused beam. On the other side, the larger CO_2 spot can drill holes with diameters above 100 μm much faster than the Nd:YAG laser with its small spot. These considerations have led to the dual-laser concept for via drilling in PCBs and flex: the Nd:YAG drills an aperture in the copper layer and the larger CO_2 uses the copper as a conformal mask for drilling through the dielectric down to the underlying copper layer. Typically drilling speeds for commercial systems are of the order of a few hundred vias per second.

In flex circuit applications the lasers are also used for cutting geometries in polyimide (alignment, fixation and fitting holes), excising (cutting out the desired circuitry for use) and skiving (removing the protective layer from a conducting path). Note that excimer lasers still might be used for drilling large arrays of regular high-accuracy holes with mask projection, e.g. in BGA packages. In case of PCB and flex, the excimer ablation technique is too expensive since it is too slow in drilling vias having a random distribution in terms of diameter and position.

3.4.2 Non-ablative applications of excimer lasers

As already stated above for via-drilling, the range of micromachining applications where excimer lasers are the most cost-effective laser tool is reduced during the last years. Successful development of 3ω and 4ω Nd:YAG into reliable, inexpensive, low-maintenance but powerful UV sources has led to the gradual replacement of excimer lasers where mask imaging capabilities are of minor importance.

Although some important examples of commercial excimer laser-processing have

---

[7] Diode Pumped Solid State.

[8] In laser systems working with CO_2 only, ablation of copper is accomplished by an oxidation process prior to laser drilling. The oxide layer enhances the initial copper absorption. Once the copper starts ablating and the oxide is evaporated, coupling of the laser power into the bare copper remains high due to thermal effects [10].

been discussed above, the major applications for these lasers are not based on laser ablation and are situated elsewhere:

- Excimer lasers are currently used in state-of-the-art microlithography equipment at the KrF and ArF wavelengths (down to 0.09 μm line width) and F$_2$ (0.07 μm and below) in the near future [1].

- Another important market for excimer lasers is flat panel display manufacturing, where Active Matrix Liquid Crystal Displays (AMLCDs) are by far the most important segment at this moment. These displays feature pixels with a thin film transistor (TFT) in their corner that switches and holds the state of polarization for light that is transmitted through the liquid crystals. Obviously, fast switching and sufficient holding times of the TFTs assume a high mobility and low leakage-current of the silicon. The silicon films that are deposited by plasma-enhanced and low-pressure chemical vapor deposition are of the amorphous silicon or a-Si type with a low channel mobility of 1 cm^2/Vs and lower [11]. Melting and subsequent crystallization transforms the film into polycyrstalline silicon or poly-Si. The required temperature for this local crystallization process is of the order of 700 °C. Convential heating in an oven will inevitably damage the borosilicate glass substrates. Although high-temperature compatible glasses as quartz could be used, this would be very expensive and become unacceptable for typical display sizes. Instead excimer lasers are employed to locally heat the a-Si to the desired temperature. With cylindrical optics the laser beam is converted into a line-shaped spot that scans the entire display area. This beam geometry is obtained by high compression in one direction and is needed to achieve a sufficient fluence.

- In the field of optical telecommunication excimers are the preferential laser sources for writing Bragg gratings in fibers. Although an interferometric set-up would be able to do the same job, usually a phase mask is used for splitting the laser beam into two wavefronts that mutually interfere. When a fiber is positioned right below the phase mask, the periodic pattern of extremely high and low laser irradiance is transferred into a refractive index modulation in the photosensitive fiber core.

3.5 Key properties of polymer ablation with excimer lasers

In the previous chapter the processes involved in polymer material ablation were discussed in detail. In this section we consider the ablation process again. Not the underlying processes but its suitability for polymer micromachining will be investigated this time.

Although some of the findings here presented can also be encountered in literature, the information is spread over numerous publications and is usually limited to one particular material and a fixed laser set-up (single wavelength, single pulse frequency, etc.). The most important contribution of this section is twofold. Firstly

we have systematically investigated the ablative properties of the commercial polymers PC, PET, PI, PMMA and PS at 193 and 248 nm over a broad fluence range. All results are supported with extensive experimental data. Secondly the properties relevant to micromachining are examined rather than the single-pulse ablation behavior which can be found in many ablation modeling papers and which is of little importance in typical laser machining conditions.

3.5.1 Ablation rates in polymers

Each excimer pulse removes a thin layer with thickness d if the pulse fluence exceeds a certain threshold value F_{th}. This threshold will in general show only a slight dependence on the number of pulses in case of a highly absorbing polymer. Via a fit of the experimental data to a logarithmic curve, d is calculated by

$$d = \frac{1}{\alpha} ln \left(\frac{F}{F_{th}} \right) \qquad (3.4)$$

for $F > F_{th}$. α is the effective absorption coefficient and F the applied laser fluence (mJ/cm^2). The ablation rates of some important commercial polymers have been calculated by measuring the depths of cavities ablated with 20 pulses at different fluences. The ablation rate is then defined by the total cavity depth divided by the number of pulses. Measurement of the fluence was performed offline using a Molectron M500 energy meter coupled to a J9 pyroelectric detector.
During the experiments the fluence is set by tuning the attenuator. Therefore, slight differences in etch depth should be interpreted with caution as the attenuator might be subject to backlash, leading to uncertainties about the exact transmission. Note also that the fluence of successive pulses on the part is subject to noise (up to 10 % for ArF) due to the statistical nature of the excimer discharge, mirror heating, beam absorption by air, etc. For this reason single pulse results should also be read with caution.

The exact data measured for some of the polymers can be found in the previous chapter. In figure 3.32 an overview is given of the fits according to (3.4) at both ArF and KrF wavelengths. Some typical ablation rates of these materials have been summarized in table 3.14 and 3.15. From these data it can be concluded that materials with relatively low absorption coefficicients tend to ablate faster at fluences sufficiently high above their threshold. Etch rates beyond 1 μm for PMMA at 248 nm with 1 J/cm^2 pulses are possible. As the absorption is lower, the etch rate at high fluences will also increase at longer wavelengths. As the maximum output power of excimer lasers at long wavelengths (XeF, XeCl) is in general lower than for KrF operation, the highest ablation rates will often still be obtained for KrF.

The lower absorption of PMMA means that the laser pulse can penetrate deeper into the material beyond the ablated volume. This often leads to ablated cavities with an inferior edge and bottom definition. In figure 3.33 these findings are illustrated by comparing the craters in PC and PMMA ablated at 248 nm (640 mJ/cm^2): the sidewalls have an irregular texture in case of PMMA, while
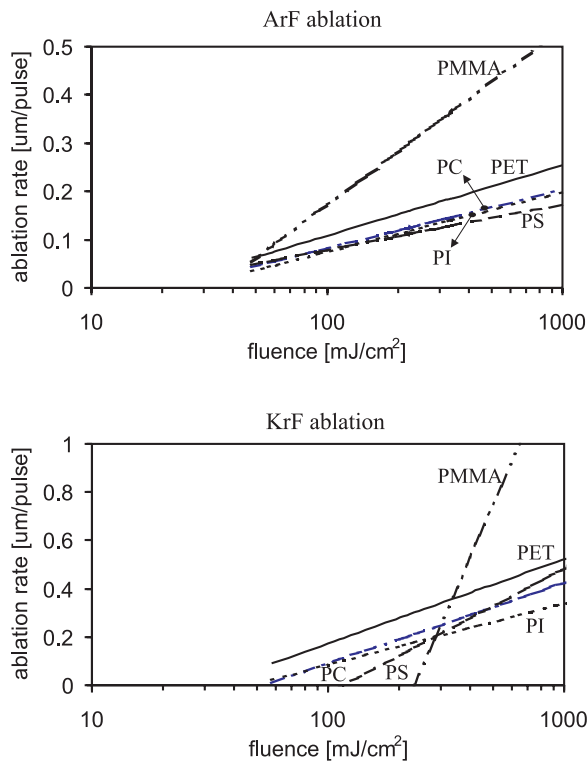
Figure 3.32: Approximated ablation rates versus pulse fluence for commercial polymers.

rather smooth edges are observed for PC. A look at the cavity bottom in PMMA reveals the presence of very small craters due to explosions of microscopic gas bubbles during ablation.

3.5.2 Single and multiple pulse behavior

Microstructures will typically feature a non-uniform surface depth over their entire area, including smooth transitions (lenses, ramps) and step profiles (the edge of a groove). Considering that ablation is an erosive process removing a certain layer of material pulse per pulse, there are two options to vary the local ablation depth: adjust the pulse fluence or select a suitable number of pulses. The first option can be useful but is generally rather impractical since it requires accurate control of the beam fluence during ablation, knowledge of the ablation rate as a function of fluence and can become very complex for complicated structures. A more practical approach is controlling the number of pulses. When the pulse repetition rate is kept constant during operation, the number of pulses that hit a surface is proportional to the exposure time. As the ablation rates in the previous section were experi-

99
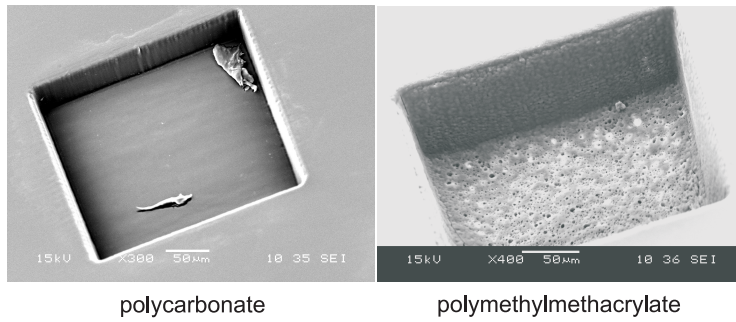
Figure 3.33: Multipulse cavity definition in PC and PMMA due to 50 pulses from a KrF laser at 642 mJ/cm^2.
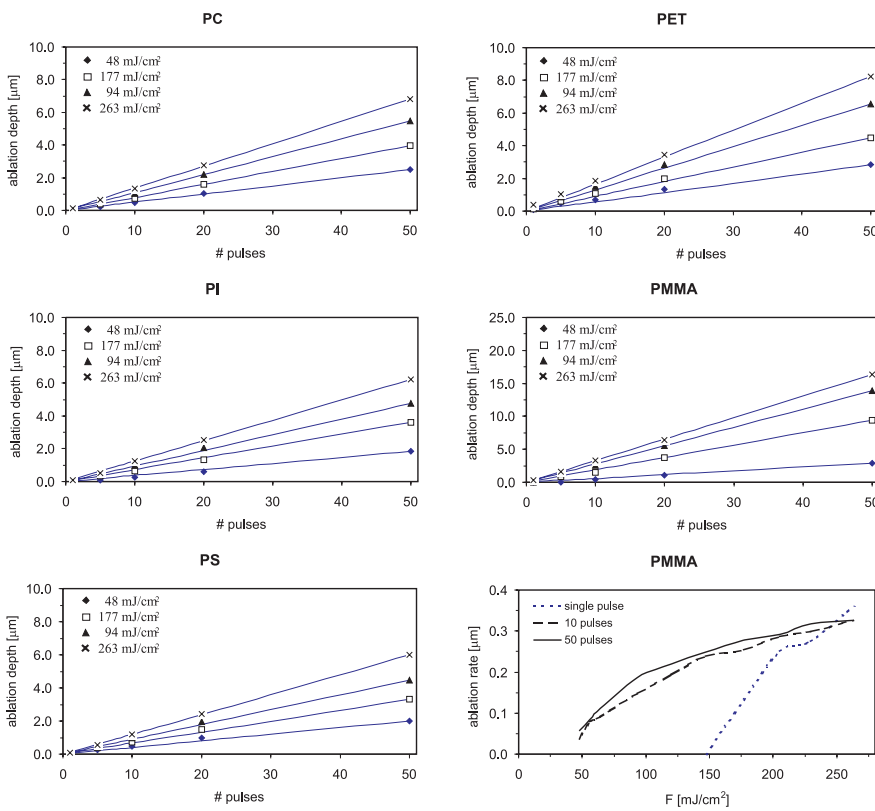

Figure 3.34: Ablation depth for different pulse train lengths at 193 nm (20 Hz operation). Lower right graph: influence of incubation on the ablation rate of PMMA.
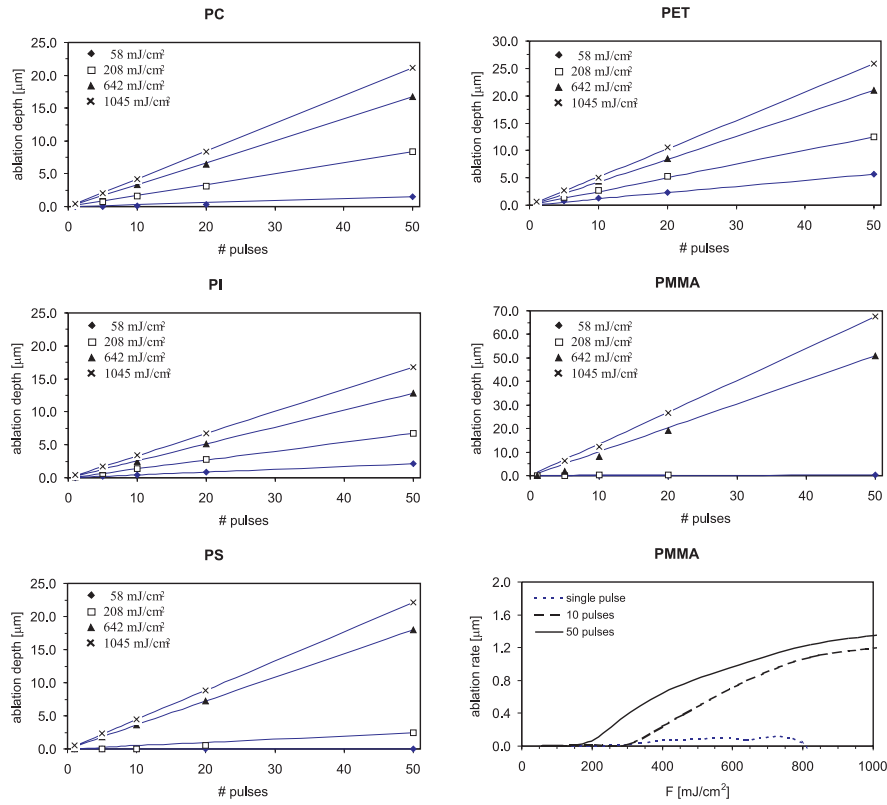
Figure 3.35: Ablation depth for different pulse train lengths at 248_nm (20 Hz operation). Lower right graph: influence of incubation on the ablation rate of PMMA.

polymer	F_{th} [mJ/cm^2]	α [μm^{-1}]	ablation rates [μm/pulse]		
			100 mJ/cm^2	300 mJ/cm^2	1 J/cm^2*
PC	21	18.9	0.078	0.145	0.204
PET	18	15.6	0.104	0.184	0.254
PI	25	18.6	0.075	0.135	0.197
PMMA	34	6.3	0.182	0.342	0.536
PS	15	24.1	0.074	0.126	0.173
* Rates for this fluence are based on literature.					

Table 3.14: Typical ablation rates at 193 nm (ArF ablation) measured at a pulse rate of 20 Hz and averaged over 20 pulses. F_{th} is calculated from a least-square fit to a logarithmic function.

polymer	F_{th} [mJ/cm^2]	α [μm^{-1}]	ablation rates [μm/pulse]		
			100 mJ/cm^2	300 mJ/cm^2	1 J/cm^2
PC	63	6.9	0.073	0.232	0.406
PET	37	6.6	0.168	0.308	0.511
PI	55	9.0	0.086	0.183	0.331
PMMA	272	1.0	-	0.042	1.268
PS	136	4.4	-	0.177	0.438

Table 3.15: Typical ablation rates at 248 nm (KrF ablation) measured at a pulse rate of 20 Hz and averaged over 20 pulses. F_{th} is calculated from a least-square fit to a logarithmic function.

mentally determined from the ablation depths for a train of 20 pulses, a relevant question concerns the validity of the etch rates for different pulse train lengths. Therefore, the polymers were each ablated with a series of pulse trains (1, 5, 10, 20 and 50 successive pulses) at a repetition rate of 20 Hz. Measurement of the cavity depths with a Wyko profilometer supplies the mean etch rate for these pulse bursts. In figure 3.34 and 3.35 the ablation depth versus pulse count is depicted for several fluences at respectively 193 nm and 248 nm, together with the linear fits. Some important conclusions can be drawn from these graphs: PMMA gives rather unpredictable etch rates for different pulse counts. This behavior can be observed in more detail when the average PMMA etch rate is calculated versus fluence and this for different pulse trains (right lower graph). Certainly at KrF incubation effects inside the material strongly affect the etch rate during the first pulses and make accurate micromachining complicated as they create an ambiguity between the pulse count and the total ablation depth. This is especially problematic when undeep features need to be fabricated with high accuracy. More detailed information on this behavior can be found in the previous chapter.

PET, PI and PS seem to perform much better although the etch depth due to the first pulse can still deviate significantly from the average value. Incubation does not play a role in these polymers, but beam fluence fluctuations will remain a source of small deviations in ablation depth. From all polymers, PC showed the
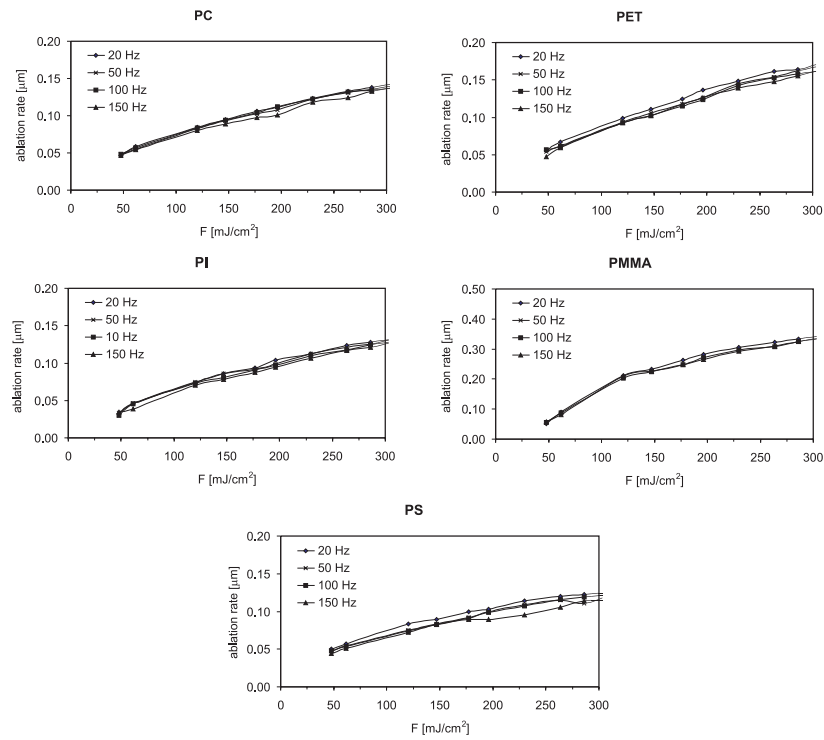
Figure 3.36: Ablation rates for different pulse frequencies at 193 nm (averaged over 100 pulses).

most consistent etch rate values.

3.5.3 Pulse repetition rate

One laser parameter has not been discussed yet: the repetition rate or pulse frequency. Once a suitable fluence, wavelength and polymer is chosen, the fabrication time for a given structure can be reduced by operating the excimer laser at a higher pulse frequency[9]. Although this consideration might be of little use for prototyping applications, it is of major importance for determining the throughput in a production environment. For this purpose the influence of the pulse frequency on the etch rate was investigated: cavities were ablated with 100 pulses fired at a repetition rate f of 20, 50, 100 and 150 Hz. The results are displayed in figure 3.36 and 3.37. No noticeable change in etch rate is observed for pulse repetition rates up to 150 Hz for all polymers except PMMA at 248 nm. For this material the ablation rate increases by more than 30 % if the pulse frequency is changed from 20 Hz to 150 Hz at the KrF wavelength. This can be attributed to the presence of a thermal

---

[9]For scanning ablation, a larger aperture size will also speed up the process.
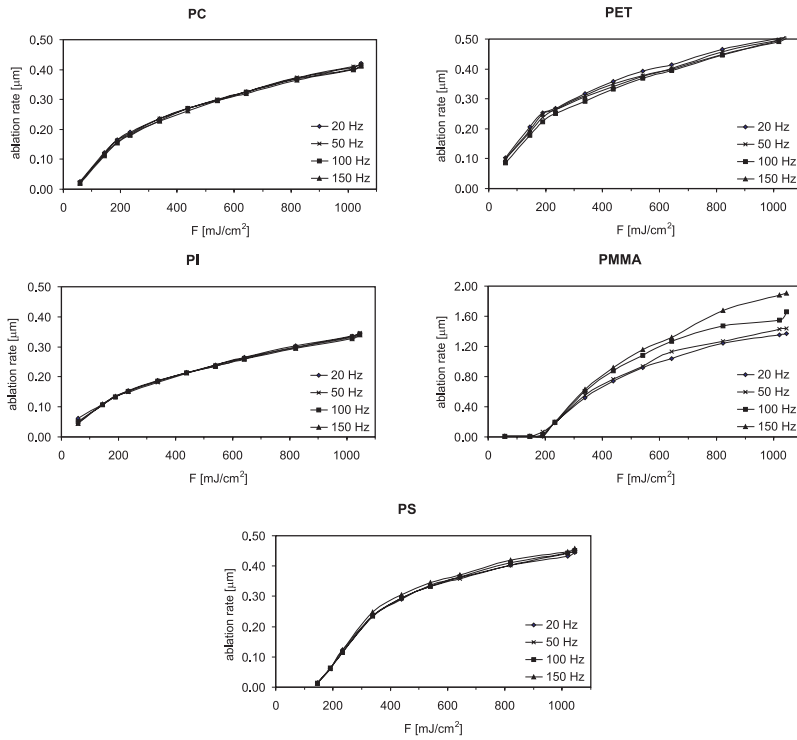
Figure 3.37: Ablation rates for different pulse frequencies at 248 nm (averaged over 100 pulses).

component in the ablation process. Apparently, a repetition rate between 50 and 100 Hz is needed to benefit substantially from the increased etch rate.

In [12, 13] it is suggested that thermal coupling effects require the pulse repetition rate to satisfy

$$f_{min} \simeq 0.1 D \alpha^2 / N$$

with N the total pulse count. This expression takes into account cumulative heating effects due to successive pulses. With $\alpha = 10^3$ cm^{-1} (linear absorption coefficient[10] of PMMA) this implies $f_{min} = 5$ Hz for 100 pulses, which is clearly an order of magnitude lower than experimentally observed. If we use the effective absorption[11] coefficient instead, then the estimated $f_{min} = 50$ Hz turns out to be a very good approximation of the experimental value.

Heating in the material is rather limited in time as only 100 pulses are fired. However, at high repetition rates and high pulse count it is possible that the heating

---

[10] The linear absorption coefficient is measured for very low intensities, much below the ablation threshold.

[11] The effective absorption coefficient is determined from a logarithmic fit of the ablation curve to the predicted etch rate according to the Beer model.
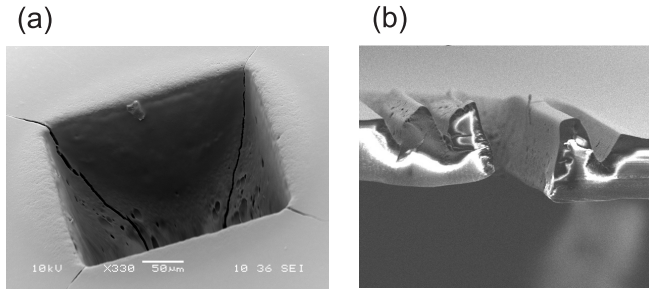
(a)   (b)

Figure 3.38: Damage of the surrounding material due to thermal and shock wave effects during ablation: crack formation (a) and deformation of the cavity (b).

actually compromises the structural integrity of the material. In figure 3.38 examples are given where PMMA is ablated at 248 nm at high repetition rates. Crack formation in the surrounding material matrix and melting effects can be observed. Note that shock waves can also be responsible for the build-up of stress in the material and might contribute to crack initiation.

3.5.4 Heating of the polymer

When the excimer laser pulse is absorbed in the polymer, thermal and non-thermal processes are initiated. In [14, 15] the threshold surface temperature for ablation of PI and PMMA is estimated to be respectively at around 1500 K and 600 K. Usually the damage to the surrounding area is quite low as the major part of the incident energy leaves the substrate along with the ejected material. The heat affected zone −commonly referred to as HAZ in literature− is the area enclosing the ablated crater that is exposed to high temperatures (figure 3.39). The exact temperature levels achieved during ablation depend on the amount of thermal heating and thus on laser and material properties. Assuming that the heat exchange between the decomposing material and the surrounding material is of the order of the pulse duration τ[12], the lateral width of the HAZ can be estimated at a multiple of the thermal diffusion length $L_{th} = \sqrt{D\tau}$ with D the thermal diffusity (expressed in $\text{cm}^{-2}\text{s}^{-1}$). At a distance $4L_{th}$, heat diffusion from the irradiated area will hardly affect the substrate temperature. For polymers ablated with excimer pulses L_{th} does not exceed 0.1 μm and thus remains extremely small. In the vertical direction, direct laser heating should be considered. The laser pulse will likely penetrate a thin layer of the remaining material and inject extra heat that has to be dissipated. The thermal energy deposited in this layer is $Q = CF_{th}$ [14, 17] with C a material dependent constant and F_{th} the threshold fluence for ablation. This energy can

---

[12]Laser heating of the material can only take place during the pulse and substantial ejection of the irradiated material starts on the same time scale as the laser pulse [16]. It is therefore appropriate to estimate the interaction time between the irradiated area and the surroundings at the order of the pulse length.
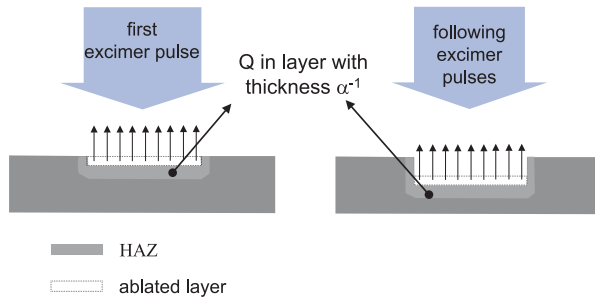
Figure 3.39: Development of the Heat Affected Zone.
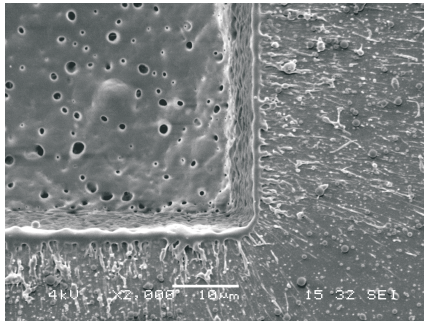
Figure 3.40: Part of the ablation cavity in PMMA (1 J/cm^2, 20 pulses at 248 nm) is depicted in the left upper corner. Solidified bubbles can be seen in the bottom due to excessive heating of the underlying material layer. Melt splashes can be observed around the crater.

be considered confined in a volume with a surface area equaling the beam area and a depth $\simeq 1/\alpha$. Consequently, low absorption coefficients accompanied by high ablation thresholds can considerably heat up the remaining material. In figure 3.40 evidence can be found for the strong heating of PMMA right below the ablated crater. Note that L_{th} and α^{-1} are comparable for high-absorption polymers.

3.5.5 Cavity profile

When a material is mechanically machined as in drilling and milling, the sculpted pattern will feature sidewalls that can be vertical or slanted as desired. The range of wall angles that can be achieved is rather limited unless the incident angle of the beam can be varied. These restrictions result from the limited depth of focus (DOF) of the beam delivery system, the ablation properties of the material and

Figure 3.41: Cavity wall angle versus fluence for PC and PMMA: curves represent calculated values based on (3.5) and markers are experimental values. The walls were measured by examining the cross-section of craters with a nominal depth of 50 μm and ablated at KrF (20 Hz rep rate).

the laser fluence.

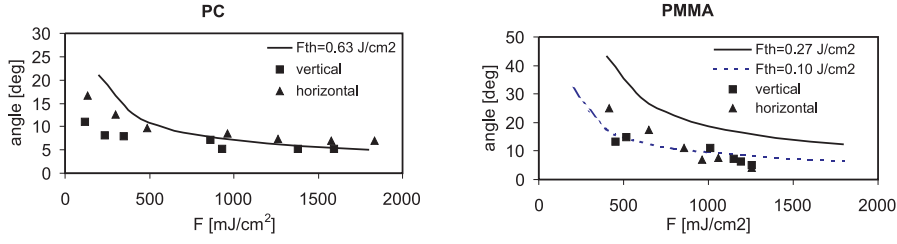Beyond DOF the angular and spatial distribution of the laser rays will differ considerably from that in the image plane and this will obviously have a serious impact on the crater walls. In [18] a numerical model is described which predicts the cavity profile taking the exposure system into account.
Within DOF the irradiance on the cavity bottom will approximate the ray distribution in the image plane and the wall angle ϕ can be calculated by considering a modified fluence $F' = (1 - R(\phi))F$. This fluence takes angle-dependent reflectivity into account. The wall angle will then satisfy the relationship

$$(1 - R(\frac{\pi}{2} - \phi))F = (1 - R(0))F_{thres} \tag{3.5}$$

that essentially expresses the critical surface angle for ablation. Note that ϕ is measured with respect to the vertical plane.

The wall angles obtained with this expression are compared to measured values in case of PMMA and PC in figure 3.41. As the laser beam features a different divergence in horizontal and vertical direction, cross-sections according to both directions were examined. For PC the measured wall angles correspond rather well to the calculated values. For PMMA the calculated angles greatly exceed the measured values if we use the ablation threshold from equation 3.15. This departure can be explained by the dependence of the ablation threshold on the pulse count and fluence for PMMA. If a lower F_{th} (100 mJ/cm^2) is chosen, a much better resemblance is obtained. In both cases taper angles of 4-5° are measured for fluences above 1 J/cm^2.

3.5.6 Dynamic ablation

As mentioned in 3.5.2 ablation depth can be controlled by the local number of pulses. For static ablation the crater depth is obviously equal to the number of
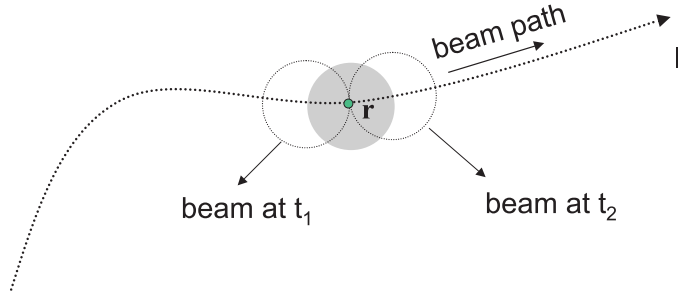
Figure 3.42: Scanning ablation.

pulses fired by the laser, multiplied by the ablation depth per pulse d. For dynamic ablation the depth at a point $\overrightarrow{r}$ can be calculated as:

$$depth(\overrightarrow{r}) = d \int_{l_1(t_2)}^{l_2(t_1)} \frac{f(l)dl}{v(l)}$$

with $v(l)$ and $f(l)$ respectively the local beam velocity and pulse repetition rate along the scanning path (figure 3.42). The integral calculates the total number of pulses during the time that the beam overlaps the point $\overrightarrow{r}$, in the figure indicated as the time interval $[t_1, t_2]$. For a rectangular beam spot of length a that moves with a constant velocity v while the laser is firing at a constant repetition rate f, we can calculate the depth of the ablated groove via

$$depth = d\frac{fa}{v} \tag{3.6}$$

If the laser is only fired during beam translation over the substrate, the ablated groove will feature a ramp with an angle $\theta_{ramp} = atan(\frac{depth}{a})$ at the start and the end. In essence this ramp has a stairway shape with step width v/f and step height d. As the step width drops below the optical resolution of the ablation optics, successive steps will not be resolved any more and the ramp will feature a smooth surface. Since the beam delivery optics of the Micromaster feature a resolution of $\sim$1.5 μm (15 to 90 % transition of fluence at beam edge), this would imply that the scanning speed (in μm/s) should equal the pulse repetition rate (in Hz) to achieve a step width $\simeq 1$ μm and thus a smooth surface. From 3.6 we can deduce that the minimal depth for a smooth groove would be $d \times a$. In practice this value will turn out to be lower as the limited focus depth of the beam will worsen the resolution. This is especially the case when deep trenches are ablated.

During ablation the surface below the laser beam ('surface ablation front' in figure 3.43) has the same inclination θ_{ramp}. If deep trenches are to be fabricated, it is generally a good idea to choose a large aperture in the scan direction. This does not only improve the ablation speed (more material is being removed per pulse) but will also limit θ_{ramp}. In [19] it is suggested that enhanced debris deposition
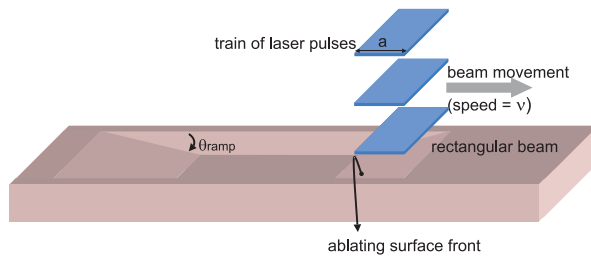
Figure 3.43: Trench fabrication with scanning ablation.
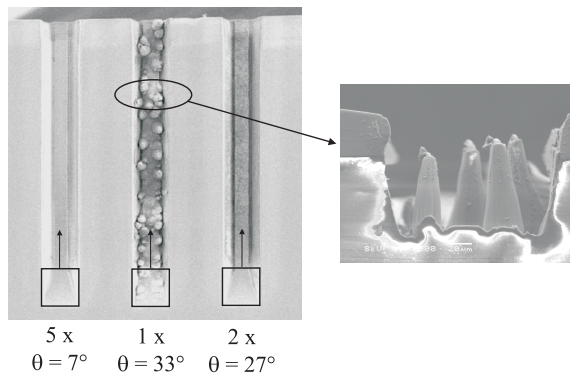
Figure 3.44: Groove fabrication in PC with ArF laser using a square aperture of 164 μm (on-target size). The grooves are all nominally 100 μm deep and the number of passes for each groove are indicated. The central groove shows excessive deformation due to debris obstructing ablation of the underlying polycarbonate.

occurs in the groove as the ejected fragments from the ablating surface front are launched towards the groove and debris deposition can be considered as a sort of self-PLD (Pulsed Laser Deposition). For PET the critical angle was experimentally verified to be 11°.

An alternative is to ablate the grooves gradually by scanning several times over the same surface. Even for a small aperture, the ablating surface angle can be kept low by choosing a desired number of passes. In figure 3.44 grooves are depicted that are ablated with a small aperture. The corresponding number of passes and ablating surface angles are given for each groove. Best surface quality was obtained for the smallest θ_{ramp} (7°). For single pass ablation, the bottom of the groove was entirely covered with conical structures and the depth of the groove could not be measured any more.

3.5.7 Minimum feature size and machining resolution

These quantities are usually a source of confusion and unrealistic expectations concerning the capabilities of a micromachining workstation to produce small features in the part surface. Machining resolution concerns the required distance over which a noticeable change in depth occurs at the edge of an ablated crater. It depends on the mechanical, optical and thermal properties of the material, the depth of the ablated crater and the nature of the underlying laser-matter interaction processes. For this reason it is much more practical to talk about the resolution of the optical system in the workstation. In this context resolution is defined as the distance over which a substantial variation in laser fluence occurs (10-90 % or 20-80 % transition) and is determined by the properties of the optical system: wavelength, NA and aberrations. The resolution can be expressed as $k_1\lambda/NA$ (k_1 is a constant depending on the optical system) and this shows that optics with a higher NA can enhance the resolution. As this can only be achieved with a larger diameter of the optics and/or smaller focal lengths, it usually introduces more aberrations in the system. In turn these aberrations will likely offset the effect of a larger NA. In figure 3.45 the edge response[13] of the projection lens in Optec's Micromaster is given.

The minimum feature size is in direct proportion to the resolution, but will depend on the desired machining pattern. For circular holes the minimum diameter will be of the same order as the system resolution, but the minimum size of e.g. a readible 'a' ablated in a surface (as in marking applications) can be easily ten times larger. In case of polymer machining, the true patterning definition will be of the same order as the optical resolution. For metals, thermal effects will likely detoriate the achievable edge definition.

Another related quantity is the depth of focus (DOF), expressed as $k_2 2\lambda/NA^2$. It determines the distance over which no considerable loss of resolution takes place. Just as in focal point writing, the DOF prescribes the tolerance on the longitudinal position of the part surface. With the part in focus, DOF will obviously also influence the maximum ablation depth, but ablation remains possible beyond the focus depth. As the diffracting beam is highly confined by the side walls of the ablated structure, high etch rates can be maintained.

3.5.8 Machining depth limitations

From 3.5.5 we learn that lower fluences result in higher tapering, lower aspect ratio and thus a more limited machining depth. The maximum depth of a hole can then be assumed to equal $\frac{a}{2}tan\theta$, with a the width of the hole at the surface. For 100 μm holes this amounts up to 600 μm in PC at 1 J/cm^2 since the wall steepness is 85°. This depth is usually quite larger than what would be expected based on the focus depth of the mask projection optics. Higher fluences will result in even deeper holes with higher aspect ratios.

---

[13]In the object (mask) plane, the edge of a rectangular aperture is put on the optical axis. The irradiance profile in the image plane along the direction perpendicular to the edge, is called the edge response of the lens. This response shows resemblance to the step response of a linear system.
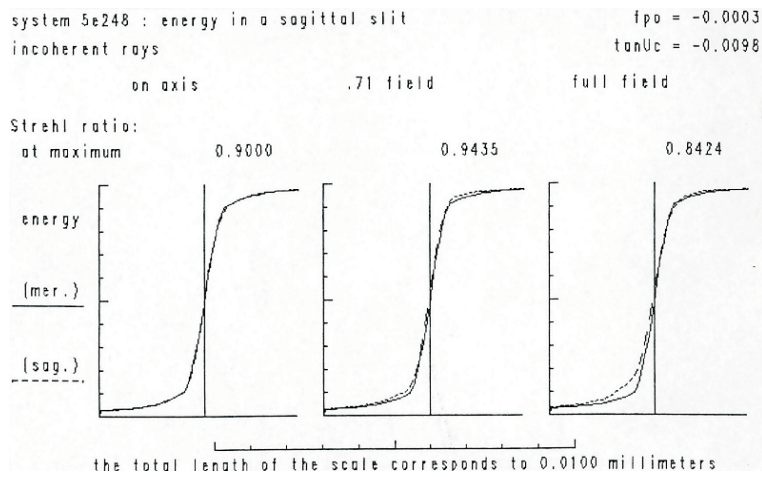
Figure 3.45: Performance of excimer projection lens of Micromaster (courtesy of OPTEC, Belgium).
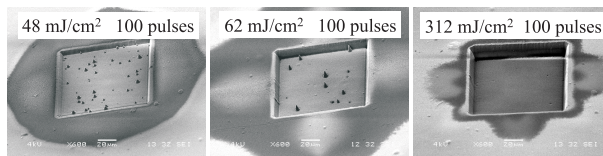
Figure 3.46: ArF ablation of Kapton at different fluence levels and with different pulse counts.

From experimental observations and literature, some other phenomena that further limit machining depth for particular polymers have been described. In polyimide excimer ablation at KrF and ArF with a low fluence favors the formation of a carbon layer [14]. [20] concluded that below a certain threshold ($\simeq$260 mJ/cm^2 for KrF ablation), the layer roughness gradually increases with each pulse until ablation stops: the high roughness and higher threshold of the carbon film prevents further ablation. At higher fluences, the carbon layer does not develop and a smooth ablated surface is created. Using the Kapton film of Goodfellow, we investigated the presence of such a layer during ArF ablation at different fluence levels. SEM images of the ablated cavities (figure 3.46) do reveal the presence of particles that inhibit ablation locally: cones that are randomly spread over the cavity bottom when a fluence of 48 and 62 mJ/cm^2 was applied. Choosing a higher fluence decreases their presence and eventually results in a clear and smooth surface: at 312 mJ/cm^2 no cones can be observed any more. The development of a full carbon layer did not occur in our experiments.

	PC	PET	PI	PMMA	PS
ArF					
depth [μm]	13.3	16.1	12.3	32.2	12.0
roughness [μm]	0.132	0.168	0.125	0.206[1]	0.119
KrF					
depth [μm]	42.0	50.7	34.4	137.0	44.6
roughnes [μm]	0.219	0.421	0.212	1.029[2]	0.296
[1] For a depth of 16.3 μm, 0.166 μm roughness was measured.					
[2] For a depth of 36.1 μm, 0.544 μm roughness was measured.					

Table 3.16: Absolute rms roughness values for craters ablated with ArF (263 mJ/cm^2, 100 pulses) and KrF (1.045 J/cm^2, 100 pulses). In order to make direct comparison with the other polymers possible, the roughness for PMMA is also given for a small cavity depth (obtained with 50 pulses of 263 mJ/cm^2 at ArF and with 50 pulses of 438 mJ/cm^2 for KrF).

3.5.9 Machining roughness

When a cavity is ablated in the polymer, it will usually show a very smooth bottom except for some particular materials such as PET and PMMA. PET features a corrugated surface (figure 3.47) at both 193 nm and 248 nm, and PMMA usually exhibits a melted surface layer with evidence of bursted gas bubbles at the KrF wavelength. We refer to figure 3.40 for a detailed view of the crater ablated at 248 nm.

The surface roughness has been measured in case of PC, PET, PI, PMMA and PS for both wavelengths and the results are depicted in figures 3.48 and 3.49. The roughness was determined in the central part of the cavity (covering about 80 % of the total surface) to exclude etch depth variations at the edges due to diffraction effects. 'Slow' surface deviations (curvature of the bottom) were filtered out. The measurements have been performed by using a white light interferometer (Wyko) sampling the surface at 0.89 μm.
For most micromachining purposes, the relative rms roughness (with respect to the cavity depth) is of much more importance than its absolute value. E.g. an rms roughness of 0.5 μm will probably have little impact on a 100 μm deep groove while it can be a critical issue for a 1 μm shallow trench.
From these graphs we can conclude that as the cavity is ablated deeper, the absolute roughness increases gradually but certainly not linear with the ablation depth. An asymptotic behavior is observed for every polymer: a relative roughness as low as 0.5 % of the full cavity depth is measured for PC at 248 nm.

The values for 193 nm have only been measured up to 340 mJ/cm^2, but it is to be expected that for comparable etch depths the roughness will be of the same order. Note that the graphs only give information on the relative roughness. Absolute surface roughness values can be found in table 3.16 and are important for some dedicated applications as microlens fabrication (scattering losses highly depend on the rms surface roughness).
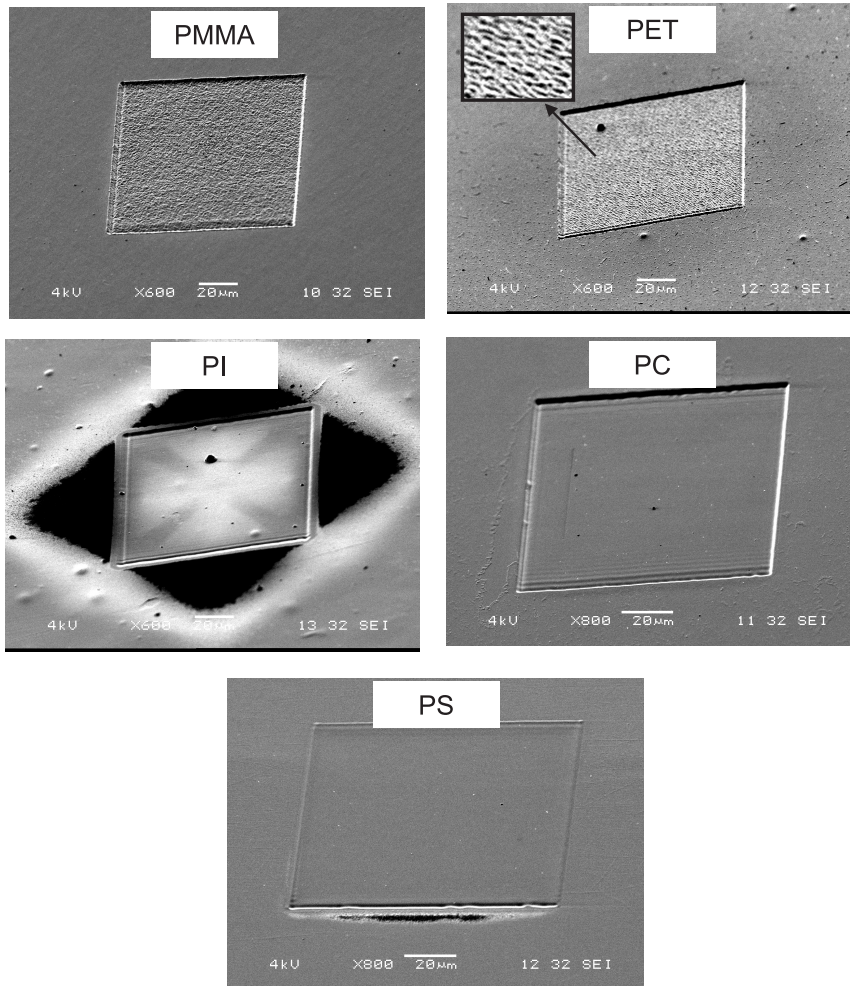
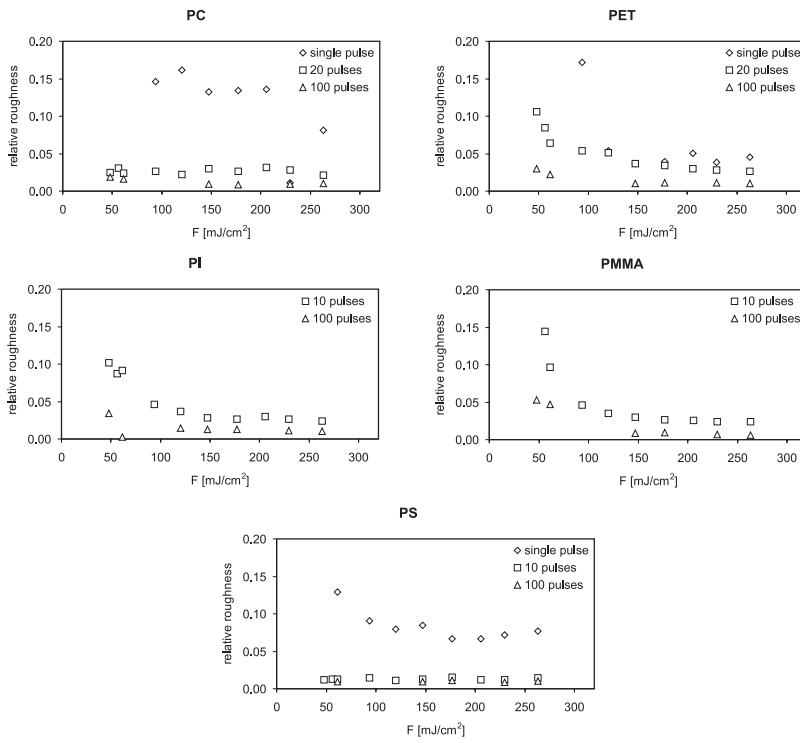Figure 3.47: SEM images of ablated cavity bottoms (KrF ablation).

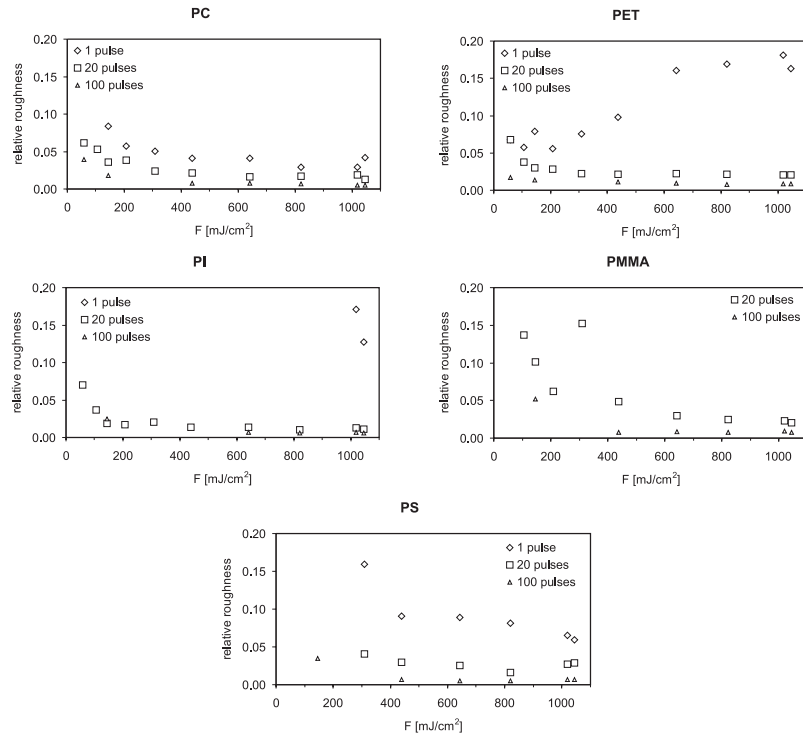Figure 3.48: Relative rms surface roughness of the cavity bottom at 193 nm.

Figure 3.49: Relative rms surface roughness of the cavity bottom at 248 nm.

The curve for PMMA appears to match the other polymers at high fluences, contrary to what would be expected from the surface view in figure 3.47. However, the roughness of PMMA exceeds those measured for the other polymers if cavities of equal depth are considered (see table).

In conclusion, the cavities in the polymers PC, PI and PS feature roughnesses of approximately the same order while PMMA (and to a lesser extent PET) shows a less smooth crater bottom. There is little difference between both wavelengths, except for PMMA that exhibits a more corrugated surface at KrF.

3.5.10   Debris

The laser ablation phenomenon covers a whole series of processes taking place in the material in a very short time: photon absorption, electronic excitation, bond-breaking, heat diffusion, melting, evaporation and ejection of a layer of material in the form of a plume. Depending on the exact nature of the laser pulse (wavelength, pulse duration and fluence) and the material, the thermal or direct bond-breaking nature of the erosion process will be favored. In any case the ejected layer is not always fully decomposed into gaseous constituents: the plume will also contain macroscopic solid particles with a high-molecular content. These particles will usually drop back on the substrate in or close to the ablated area shortly after ejection. They are commonly referred to as 'debris' (figure 3.50). The exact spread of debris is determined by the plume expansion dynamics and depends on the beam shape and size, the fluence and ablated depth. Simple fume extraction techniques do not remove or avoid debris in a satisfactory fashion. There are several ways to counter debris deposition and they can be roughly divided into two categories: either deposition of the particles is prevented during processing or they are removed after finishing the structure.

Development of prevention techniques are based on the observation that the rate of soot formation strongly depends on composition and pressure of the ambient atmosphere and can be surpressed by using He or H_2 as ambient medium. These gases with low atom or molecular weight ($m_{He} = 4$, $m_{H_2} = 2$) allow a faster expansion of the ablation plume and thus decrease the interactions between the ejected fragments. This leads to much less particle formation and recondensation. These observations justify the employment of a sealed flow chamber as sample housing during ablation of structures where debris deposition is not acceptable. For applications where such chambers are too bulky or not practical, a vacuum nozzle with an assisting He flow can be considered. An implementation of the latter is given in figure 3.51.

For post-ablation debris removal, a multitude of techniques are recommended with some being more successful than others: laser cleaning at fluences below ablation threshold, oxygen plasma cleaning, gas jet techniques, liquid wash, removal with ultrasonic waves in a fluid and brushing. However, the bonds between debris and the part surface can have a chemical, fluidic and even an atomic nature. In many cases it will simply not be possible any more to fully remove the particles without damaging the surface. If a sealed chamber or nozzle is not an option and presence of debris in unacceptable, one can consider the use of a sacrificial layer on the part
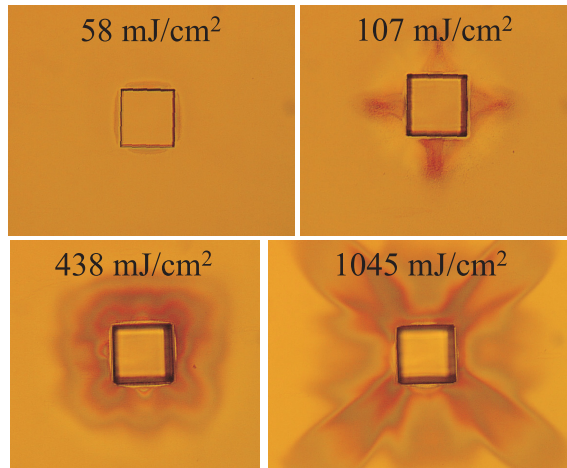
Figure 3.50: Debris pattern around an ablated square hole of 100×100 μm^2 in PI. The hole was created using 100 pulses from a KrF laser operating at 20 Hz in air.

surface. This layer should be thin, ablate very well and adhere sufficiently to the part in order not to interfere with the laser machining process. After ablation the layer should permit easy removal via rinsing in a solution, stripping or other techniques. In this way all debris that was deposited on the layer will be removed as well.

For reducing debris contamination of the machined surface in the Micromaster, a steel flow chamber was built (figure 3.52). A small sample holder in the center is capable of clamping parts with an area up to 3×3 cm^2 and a maximum height of a few mm. Right above the holder, a circular hole is cut out of the steel frame and sealed with a UV window made of Suprasil 1. This material is transparent for the excimer wavelengths 193 and 248 nm. Access to the part is realized by opening the beam window. Although [21] mentions that ambient pressure is of less importance[14] and a gas flow above the ablated area is not needed for clean ablation, it is generally a good idea to connect one side of the chamber to a vacuum pump and the other to a helium bottle. With this set-up, the pressure inside the chamber is reduced to some 100 mBar and a continuous stream of helium is obtained above the sample surface. The combination of both allows efficient extraction of the fumes while debris deposition is largely reduced. Without the He flow, window contamination is inevitable and severely reduces its lifetime. Note that the beam window is not AR-coated: the quartz-air interface introduces an extra 7 % loss in beam fluence.

---

[14]Kuper and Brannon state that the main requirement for debris-free ablation is a He or H$_2$ atmosphere. Up to 1 atm of He, debris formation was almost absent during ablation of polyimide in their experiments. From this observation they concluded that the ambient pressure is of little importance.
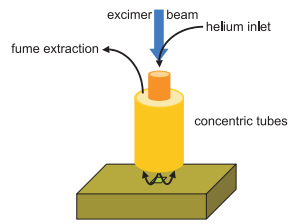
Figure 3.51: Vacuum nozzle with assisting He$_2$ flow for debris removal.
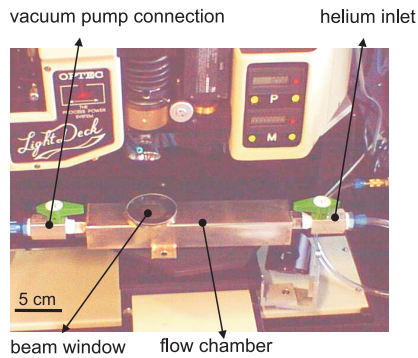
Figure 3.52: Flow chamber mounted onto the translation stage of Micromaster for reduced debris deposition.

The effect of the chamber can be observed in figure 3.53: a circular trench is ablated in PC using the KrF laser. The experiment is repeated twice: once with the sample in air and once in the flow chamber. No appreciable debris was observed in the last case.

As structures are drilled deeper into the sample, it becomes more difficult to avoid debris inside the ablated area: the plume has first to leave the crater before it can expand. In this way the ejected fragments have more time to interact with each other.

3.5.11 Conclusions on micromachining with excimer laser ablation

The observations made in the previous sections can be summarized as follows:

- Polymers are excellent materials for ablation with UV excimer lasers, achieving patterning resolutions of tens of nanometer in the vertical direction (determined by the pulse fluence) and about 1-2 μm laterally (determined by

(a)   (b)
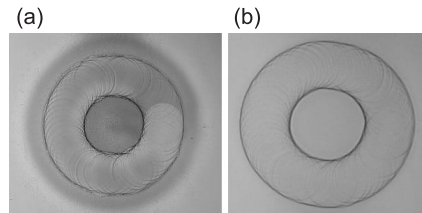
Figure 3.53: Cavity in polycarbonate, ablated with a KrF laser in air (a) and in the flow chamber (b).

the optical resolution). Typical laser fluences for microfabrication are of the order of 0.1-1 J/cm^2. Laser-ablated structures feature tapered side walls, forming an angle of 80-85° with the horizontal. For the applied fluences accurate ablation up to several hundreds of μm deep is possible, depending on the transversal dimensions of the structure.

- After ablation some polymers show a particular surface structure that is not caused by the exposure system. E.g. the corrugated bottom of ablated PET, melted pool with bursted bubbles in PMMA.

- For a given polymer and desired depth resolution, a suitable fluence can be chosen. High speed ablation can be achieved with low absorption polymers as PMMA at 248 nm, but this reduces the depth resolution (= depth per pulse) severely. More accurate patterning can be obtained with PC, PET, PI and PS.

- The definition of a specific pattern in a polymer surface can be achieved by either projection of the corresponding mask (with the same pattern, but enlarged) or by scanning with another, more simplified mask over the substrate.

- In case of scanning ablation a sufficient large aperture in the scanning direction is preferred as this speeds up the ablation process and gives the smoothest results.

- Depth variations in the ablated area can be achieved by controlling the number of pulses that locally overlap. This is a much more feasible solution than pulse repetition and fluence adjustment during scanning.

- Thermal damage around the ablated structures is very limited for the highly absorbing polymers PC, PET, PI and PS. At 248 nm PMMA tends to heat up considerably, leaving behind a melted surface after ablation.

- Debris is deposited in and around the ablated structure during ablation. The use of a flow-chamber or vacuum nozzle can reduce the amount of deposition considerably and is preferred to a debris-removal technique as the particles tend to stick strongly to the surface.

3.6   Prototype ablation of microstructures

In this section an overview is given of prototype components that have been fabricated with excimer laser ablation within the context of this thesis. The flexible machining properties and mask imaging capabilities make excimer laser micromachining very suitable for prototyping fabrication. They have even led to the development of related fabrication technologies as laser-LIGA[15]. In the classical LIGA approach, X-ray lithography is employed to pattern a polymer resist layer on a conducting substrate. The short wavelength of the synchrotron radiation (a few Angstrom) allows accurate fabrication of deep structures with high aspect ratios. After removal of the unexposed polymer, the structure is copied into a nickel master using electroplating. In a final step the master is replicated via injection molding or embossing. One of the alternatives for the high-cost X-ray lithography is direct micromachining of the polymer with an excimer laser. This approach will result in a lower resolution patterning, but cheaper master fabrication.

Excimer lasers can be considered an excellent laser source for general purpose micromachining on prototyping level or fabrication in small quantities. Due to their short wavelength they can be used for virtually any material. Mask projection can either serve for ablating complex patterns or for emulating focal spot writing by using a simple aperture in the mask plane and a high demagnification. Typical penetration depths for a single pulse can be as low as a few tens of nanometer and define the depth resolution. The optical resolution of the projection optics is of the order of 1 μm and determines the lateral resolution.

Various structures have been made with the micromachining set-up at the department of Information Technology and are briefly described below. Some of these components have been extensively investigated for fiber-alignment and fiber-coupling. They are discussed in more detail in the following chapters.

Cloverleaf patterning of a GaN film on a sapphire substrate

A cloverleaf shape in GaN was electrically isolated from the remaining film by scanning laser ablation of the GaN layer with a small square aperture (figure 3.54). The sapphire was left unaffected as it had a much higher ablation threshold. This cloverleaf shape was required for performing Hall measurements on the GaN.

Chip alignment structure

A mastertool (figure 3.55) in polycarbonate consisting of an island of 50 μm high is created by ablation of the surrounding area using excimer laser ablation (KrF at 180 mJ/cm^2). On the 2×1.5 mm^2 island, a vacuum chuck opening, two alignment holes for MT ferrule pins and small alignment features were inserted with the same laser, but with different aperture sizes. The final structure has been successfully used to align the VCSEL chip by matching the alignment crosses on the chip with

---

[15]LIGA is a German acronym for Lithograpfie, Galvanoformung (electroplating) und Abformung (moulding).
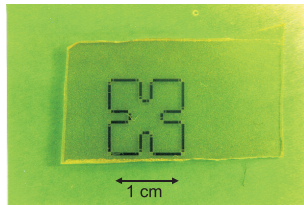
Figure 3.54: Laser-patterned cloverleaf in GaN on sapphire substrate.
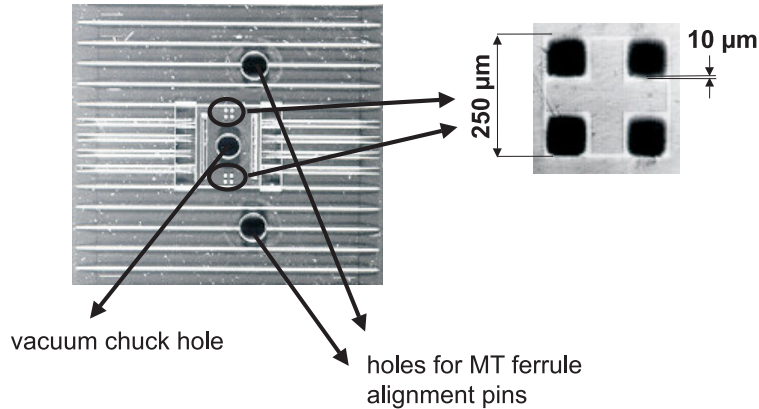
Figure 3.55: Mastertool in polycarbonate for aligning a VCSEL chip with an array of multimode fibers.

the squares on the mastertool [22]. Fixing the chip was achieved with the vacuum chuck. Next, the MT connector with the multimode fiber array is automatically aligned with the VCSELs when its pins are inserted in the alignment holes of the mastertool. Although fabrication time would be considerably reduced to the order of seconds by design and employment of a suitable mask, this was not required as only a single component needed to be fabricated.

Fiber alignment structures

This structure features an array of 8 grooves separated by a pitch of 250 μm. The groove cross-section is optimized for easy insertion and accurate positioning of plastic optical fibers (figure 3.56). Once the fibers are glued in the grooves, several plates can be stacked on top of each other to get a 2D-array of fibers with a fixed pitch [23, 24, 25]. Although such 2D connectors are not yet commercially available, these components will enjoy a growing interest as increasing bandwidth requirements push short-distance interconnect technology towards the implementation of 2D arrays of optical channels.
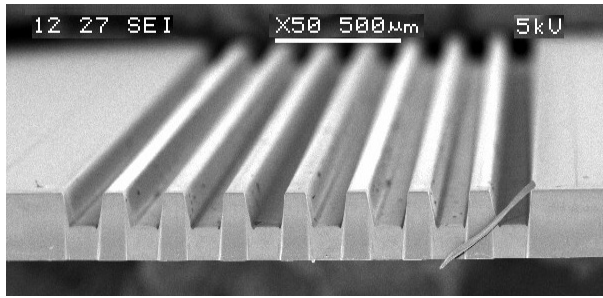
Figure 3.56: Plastic fiber array alignment plate in polymethylmethacrylate with U-shaped grooves.
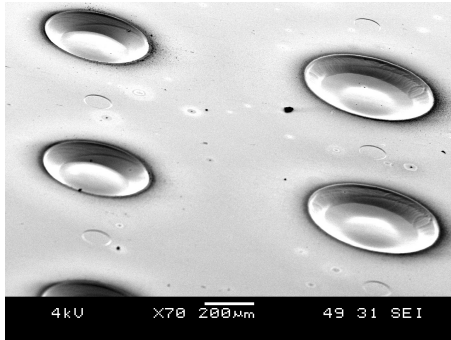
Figure 3.57: Microlenses fabricated in polycarbonate with scanning contour ablation.

Microlens fabrication

Using excimer laser ablation, it is possible to define structures of optical quality in polymer materials. This means that the surface roughness of the machined areas should be well below the wavelength and assumes accurate control of the local ablation depth. Several spherical lenses (figure 3.57) have been made using a technique called scanning contour ablation [26, 27, 28] as elaborately discussed in chapter 4.

Laser patterning of thin polymer films

After sputtering a 100 nm Au layer onto a GaAs substrate, a segmented polyurethane resist is spin-coated onto the gold. Using mask projection well-defined areas of polyurethane are ablated. In a next step the subtrate is immersed in a solution containing an alkanethiol with a suitable endgroup. The alkanethiol is capable of spontaneous chemisorption on the exposed Au areas, forming self-assembled monolayers. The endgroup can have a reactive chemical functionality, enabling the layer
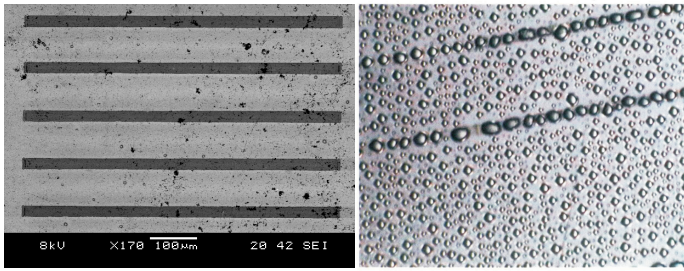
Figure 3.58: Patterning of thin polymer films on Au coated substrates. Note the large vapor droplets on the grooves.

to bind biomolecules covalently. In the experiments a methylendgroup was chosen, making the surface hydrophobic. Finally, the polymer film is stripped off and the entire structure is again immersed in a solution with an alkanethiol. This time an endgroup was chosen that makes the surface hydrophilic. The clear difference in surface behavior in the presence of water is illustrated in figure 3.58.

The patterning and chemisorption process can be repeated multiple times at different locations on the substrate. Every time a different endgroup with another chemical functionality can be chosen. Obviously, this technique has potential for sensor applications and bioanalysis [29, 30, 31].

Optical fiber cleavage

Glass fibers for optical transmission are made of fused silica. This material is highly transparent down to wavelengths as low as 200 nm. This property makes laser machining with KrF and ArF extremely difficult. However, due to its small cross-section the fiber is prone to breakage when exposed to high intensity ArF or KrF pulses. It is believed that thermal shock and crack propagation are the main cleaving mechanisms. Although this assumption is still unproven, it might be possible to 'direct' the breakage in such a way that the resulting fiber facet matches the optical quality of a successful mechanical fiber cleave. Engineered stress patterns created in the fiber cross-section by mechanical or thermal means, are the obvious approaches for controlled laser cleavage [32]. An example of a laser-cleaved fiber can be found in figure 3.59 where the facet orientation corresponds to the beam slit axis. At this moment (June 2003) the facet quality is still inferior to mechanical cleaving. Note that the successful implementation of a laser cleaving system can have a substantial impact on the cleaving and splicing yield since tool wear and operator-dependency of mechanical splicing are excluded.

A second laser-assisted approach aims for the creation of a surface scratch only. This scratch can subsequently serve as fracture initiator when the fiber is put under stress. Positioning of the scratch with a laser is much more precisely than with a classic diamond tool. The scratch is created by projection of a slit aperture
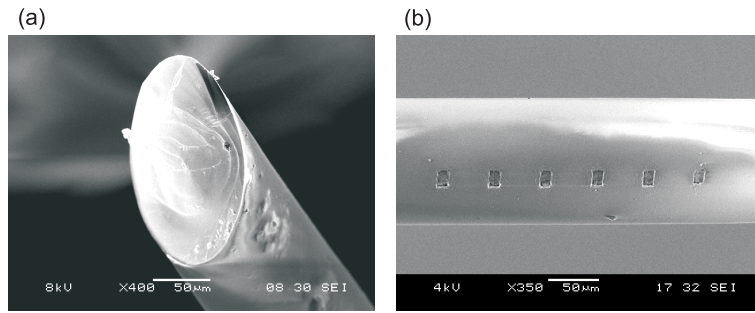
Figure 3.59: A tilted Laser-cleaved fiber facet (a). Optical fiber scribing with an excimer laser for cleaving purposes (b).

onto the fiber surface with a fluence of about 1.5 J/cm^2 at 193 nm. The circular geometry of the fiber acts as a lens for the laser beam and focuses the incident light somewhere underneath the fiber. As a result, the laser spot size is highly concentrated on the lower fiber surface and initiates the ablation of a small cavity with rectangular shape (figure 3.59).

Cutting and excising

By inserting a slit aperture, the excimer laser can be used for clean cutting of polymer and other materials. E.g. the cross-section of the groove array in figure 3.56 was achieved by laser cutting. Another practical example is given in figure 3.60. It depicts a low-cost opto-electronic transceiver module using a FR4 or alumina substrate on which two silicon chips, a CMOS detector and a VCSEL on carrier, are fixed with a conductive epoxy adhesive. Using a high-precision placement tool, the chips are positioned in such a way that both receiver and transmitter are aligned with the fibers from the MT-RJ ferrule. As the prototype detector chips turned out to be larger than expected, the connector alignment holes were partially covered with the chip. Using laser ablation, the obstructing part of the chip was removed without damaging the active chip area [33]. Note that quite some debris is produced during ablation of silicon.

Figure 3.61 illustrates how scanning excimer laser ablation can be used for cutting out arbitrary geometries from a substrate (polyimide in this case).

3.7 Conclusions

The working principle and the specifications of the excimer laser have been explained, revealing that they are capable of delivering large beams with high pulse energies. The employment of these pulsed UV sources for polymer ablation is justified by the excellent cavity definitions that can be achieved in this class of materials. Some typical machining set-ups have been discussed. The first one is

chip area obstructing access to
the alignment hole
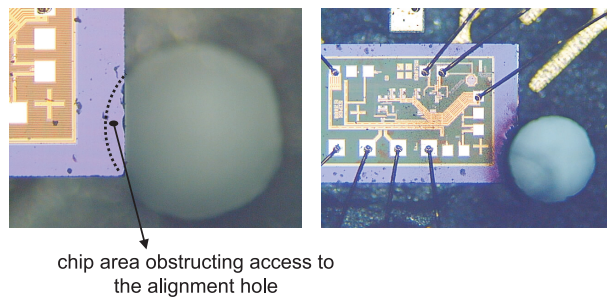
Figure 3.60: Ablation of the chip edge to obtain access to the pin alignment holes.

700 µm
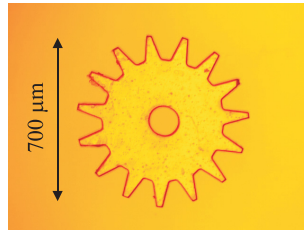
Figure 3.61: Laser cutting of a microscopic gear.

focal-point machining and uses a focused laser beam to scan the sample surface
and to ablate an arbitrary pattern. The other technique is based on projecting
an entire mask pattern onto the substrate with a laser beam. This mask imaging
technique combines speed and flexibility and is very suitable in combination with
an excimer laser.

It has been shown that excimer laser ablation can be successfully employed for
defining microstructures in polymer materials. Several micromachining issues are
treated: cavity definition, surface roughness, depth control, resolution, tapering,
material impact, scanning ablation and debris. These features have revealed both
the capabilities and limitations of the laser fabrication technique.

A brief overview of the diverse components and structures that have been made
within the context of this thesis and some commercial applications further under-
line the potential of excimer laser ablation.

Appendix A   Laser processing overview

When considering material-processing in a broader sense than microfabrication, the list of commercially employed lasers for this purpose is more extensive than given in table. 3.8. Next to pulsed lasers, high average-power lasers operating in cw mode are used as well. Typical high-power laser types are

CO_2 gas laser that is offered in several configurations: sealed, waveguide, slow and fast axial flow, transverse flow and transverse excitation. The excitation can be either DC or RF. Output powers up to 50 kW are possible.

Nd:YAG   solid state laser that is pumped by a flashlamp, arc lamp or diode bar and emits up to 5 kW of output power.

Diode bar consists of an array of semiconductor lasers featuring a high wall plug efficiency but a poor beam quality. For large arrays the total output power can run up to 1 kW.

Excimer   pulsed UV laser source with output powers up to some hundreds of Watts.

The maximum powers are based on the many specifications that can be found in commercial brochures and rather reflect an order of magnitude than an exact value. An important commercial aspect is the relative cost for insertion of the laser into a production process. Some lasers really feature smooth high-power operation during their entire lifetime without substantial maintenance cost (sealed CO_2), while others demand regular maintenance and expensive gas refills (excimer lasers) or need a lot of electrical energy for emitting only low-energy pulses (ultrafast lasers[16]).

---

[16]One should clearly distinguish peak and average power. For ultrafast lasers emitting fs pulses, the peak power can reach a staggering 10^{11} W. But due to the very short pulse duration, the average power is rather poor (< 1 watt). This observation is also reflected in the machining speed: ultashort pulse lasers are perfectly able to smoothly ablate metals (with spot fluences exceeding 10^{18} W/cm^2) like no other laser can, but the removal rate (depth$\times$area) per time unit remains small.

sub-melting	melting	evaporation
annealing	cladding	cutting
hardening	alloying	scribing
	skin melting	trimming
	welding	stripping
	soldering	drilling
	grain-refining	marking
	cutting	shock hardening

Figure 3.62: Typical laser processing applications.
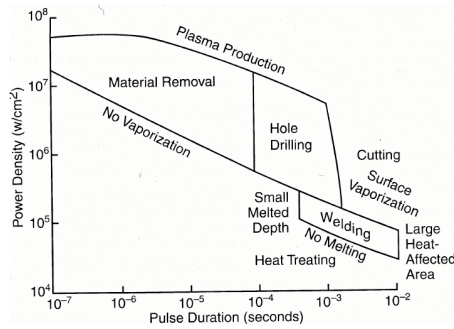
Figure 3.63: Typical fluence requirements for material processing.

Typical laser-based material processing techniques are given in table 3.62 with the corresponding optical power requirements in figure 3.63. In this diagram one emerging application is missing: refractive index patterning in glass with ultrafast lasers. The extremely high photon intensities that can be obtained in the focus of a Ti:Sapphire laser beam are capable of permanently changing the refractive index of some glass blends via a multi-photon process ($\Delta n \simeq 10^{-3}$-10^{-2}).

These high intensities can only be achieved by focusing the beam with a high NA lens and by compressing the pulses down to a duration as short as a few tens of fs (1 fs = 10^{-15} s). Due to the very limited focus depth, the refractive index is only changed in a very small volume in the order of a few μm^3 and smaller. At lower intensities (away from the focal area) the material remains transparent for the beam and this makes true 3-dimensional refractive index patterning possible. It is obvious that the technique is extremely attractive for direct-writing of optical waveguides in bulk material once the process is fully controlled and optimized.

Bibliography

[1] P. Das and R. Sandstrom, "Advances in excimer laser technology for sub-0.25-μm lithography", Proc. IEEE **90**, 1637 (2002).

[2] D. Sabbert, J. Landsiedel, H.D. Bauer and W. Ehrfeld, "ArF-excimer laser ablation experiments on Cycloolefin Copolymer (COC)", Appl. Surf. Sc. **150**, 185 (1999).

[3] G-S Plastic Optics. Data available at http://www.gsoptics.com/custom_optics/charts.html.

[4] HP inkjet technology reports, available at http://www.hp.com/oeminkjet/learn/techreports.html.

[5] M. Roberts, J. Rossier, P. Bercier and H. Girault, "UV laser machined polymer substrates for the development of microdiagnostic systems", Anal. Chem. **69**, 2035 (1997).

[6] F. Wagner and P. Hoffmann, "Electroosmotic flow control in micro channels produced by scanning excimer laser ablation", in Second International Symposium on Laser Precision Microfabrication, Omiya, Japan, Proc. SPIE **4088**, 337 (2000).

[7] S. Broude and G. Ogura, "The use of laser-stripped and metallized fibers for hermetic packaging applications", in IEEE/LEOS Annual Meeting, Glasgow, Scotland, Proc., 548 (2002).

[8] W. Shen and H. Kwok, "Crystalline phases of II-VI compound semiconductors grown by pulsed laser deposition", Appl. Phys. Lett. **63**, 1 (1993).

[9] F. Bachman, "Excimer lasers in a fabrication line for a highly integrated printed circuit board', Chemtronics **4**, 149 (1989).

[10] J. Miller, "Optical properties of liquid metals at high temperatures", Phil. Magaz., 1115 (1969).

[11] M. Gower. "Industrial applications of pulsed lasers to material processing", in Symposium on High Power Laser Ablation, Santa Fe, USA, Proc. SPIE **3343**, 171 (1998).

[12] F. Burns and S. Cain, "The effect of pulse repetition rate on laser ablation of polyimide and polymethylmethacrylate-based polymers", J. Phys. D **29**, 1349 (1996).

[13] Z. Liu, Y. Feng and X. Yi, "Coupling effects of the number of pulses, pulse repetition rate and fluence during laser ablation of PMMA", Appl. Surf. Sc. **165**, 303 (2000).

[14] P. Dyer and J. Sidhu, "Excimer laser ablation and thermal coupling efficiency to polymer films", J. Appl. Phys. **57**, 1420 (1985).

[15] D. Brunco and M. Thompson, "Temperature measurements of polyimide during KrF excimer laser ablation", J. Appl. Phys. **72**, 4344 (1992).

[16] R. Srinivisan, "Ablation of polymethyl methacrylate films by pulsed (ns) ultraviolet and infrared (9.17 μm) lasers: a comparative study by ultrafast imaging", J. Appl. Phys. **73**, 2743 (1993).

[17] G. Mahan, "Theory of polymer ablation", Appl. Phys. Lett. **53**, 2377 (1988).

[18] C. Paterson, A. Holmes and R. Smith, "Excimer laser ablation of microstructures: a numerical model", J. Appl. Phys. **86**, 6538 (1999).

[19] F. Wagner and P. Hoffmann, "Structure formation in excimer laser ablation of stretched poly(ethylene therephthalate) (PET): the influence of scanning ablation", Appl. Phys. A **69**, 841 (1999).

[20] Z. Ball, T. Feurer, D. Callahan and R. Sauerbrey, "Thermal and mechanical coupling between successive pulses in KrF-excimer-laser ablation of polyimide", Appl. Phys. A **62**, 203 (1996).

[21] S. Kuper and J. Brannon, "Ambient gas effects on debris formed during KrF laser ablation of polyimide", Appl. Phys. Lett. **60**, 1633 (1992).

[22] A. Van Hove, J. Haes, K. Naessens, B. Dhoedt, R. Baets and P. Van Daele, "MT compatible red VCSEL module for parallel optical interconnections", in Optoelectronic Interconnects VII; Photonics Packaging and Integration II, San Jose, USA, Proc. SPIE **3952**, 134 (2000).

[23] K. Naessens, A. Van Hove, T. Coosemans, S. Verstuyft, H, Ottevaere, L. Vanwassenhove, R. Baets and P. Van Daele, "Fabrication of microgrooves with excimer laser ablation techniques for optical fibre array alignment purposes", in Laser Applications in Microelectronic and Optoelectronic Manufacturing V, San Jose, USA, Proc. SPIE **3933**, 309 (2000).

[24] T. Coosemans, A. Van Hove, K. Naessens, L. Vanwassenhove, P. Van Daele and R. Baets, "Fabrication of a 2D connector for coupling a 4x8 array of small diameter plastic optical fiber (117/125 um) to MCLED or VCSEL arrays", in 50th Electronic Components & Technology Conference, Las Vegas, USA, Proc., 1236 (2000).

130

[25] K. Naessens, A. Van Hove, T. Coosemans, S. Verstuyft, P. Van Daele and R. Baets, "Microgroove fabrication with excimer laser ablation techniques for optical fiber array alignment purposes", in First International Symposium on Laser Precision Microfabrication, Omiya, Japan, Proc. SPIE **4088**, 327 (2000).

[26] K. Naessens, P. Van Daele and R. Baets, "Laser-ablation-based technique for flexible fabrication of microlenses in polymer materials", in Second International Symposium on Laser Precision Microfabrication, Singapore, Proc. SPIE **4426**, 124 (2001).

[27] K. Naessens, H. Ottevaere, P. Van Daele and R. Baets, "Flexible fabrication of microlenses in polymer layers with excimer laser ablation", Appl. Surf. Sc. **208**, 159 (2002).

[28] K. Naessens, H. Ottevaere, R. Baets, P. Van Daele and H. Thienpont, "Direct-writing of microlenses in polycarbonate with excimer laser ablation", Appl. Opt. **42**, 6349 (2003).

[29] Y. Martele, K. Callewaert, I. Swennen, K. Naessens, R. Baets, V. Van Speybroeck, M. Waroquier, H. Van Aert, P. Dierickx and E. Schacht, "Micropatterning of polyurethanes with lasers", Polym. Int. **51**, 1172 (2002).

[30] K. Callewaert, Y. Martele, L. Breban, K. Naessens, P. Van Daele, R. Baets, H. Geuskens and E. Schacht, "Excimer laser induced patterning of polymeric surfaces", Appl. Surf. Sc. **208**, 218 (2002).

[31] Y. Martele, K. Callewaert, K. Naessens, P. Van Daele, R. Baets and E. Schacht, "Controlled patterning of biomolecules on solid surfaces", Mat. Sc. & Eng. C **23**, 341 (2003).

[32] Patent application by J. Watte, K. Naessens, R.Baets and P. Van Daele, "Optical fibre cleaving", PCT-GB2003-002671.

[33] R. Bockstaele and P. De Pauw, "Fabrication of a low-cost module for gigabit ethernet tranceivers", in VCSELs and Optical Interconnects, Brugge, Belgium, Proc. SPIE **4942**, 44 (2002).

Chapter 4

Laser ablation of plastic refractive microlenses

4.1 Introduction

It is beyond discussion that data communication and information processing greatly affects our modern society and it is to be expected that their impact will grow steadily. The last decade they have been the main drive for the development of high-speed microelectronics and optoelectronics into mature and reliable technologies. Meeting the demands of higher operation speeds and data throughput while taking into account boundary conditions such as low-cost and reliability, inspires a strong tendency towards extreme miniaturization of opto- and microelectronic components and massive parallelism of data channels. Furthermore it encourages the merger of several technologies as wafer scale integration of optoelectronics with microelectronics: VLSI photonics.

Optical transport of information typically relies on optical fibers, free space propagation and integrated waveguide technology. Establishing a link for information exchange between two opto-electronic devices implies successful coupling of light from the source into the transportation medium and back to the detector. Considering the small fiber and waveguide cores, the shrinking source/detector size and the mode mismatch between optoelectronic components and transportation media, efficient power coupling has become quite a challenging and expensive part in system design.

These obstacles have sped up the research efforts in the field of microoptics. Before, this term referred solely to plain miniaturization of macrooptical components such as lenses, prisms and mirrors. These components were used in applications where they offered a cost-effective alternative for bulky macrooptics. Nowadays microoptics has evolved to a much broader science, backed up by advanced microfabrication technologies and making novel applications possible. It offers added-value to miniaturization in terms of improved performance, reliability and efficiency of the photonic system. Similar obstacles such as the optical coupling problem are met

in other applications as laser printing technology, photocopiers, image projection systems, displays, photolithography and optical sensors to name a few. They all have contributed to the development of microoptics into a high-tech discipline.

One of the important building blocks in microoptical systems are microlenses with typical dimensions of the order of millimeter and lower. The term microlens covers a whole range of optical microcomponents that are able to change a wavefront curvature. This includes diffractive structures (binary, multilevel or blazed), fresnel and refractive lenses. In this chapter we will focus on the latter type: lenses that manipulate an incoming wavefront due to refraction at the curved[1] lens-air interface(s). Contrary to diffractive lenses, refractive lenses show little wavelength dependency.

4.2   Microoptics fabrication techniques

In this section we will briefly discuss some fabrication techniques that are currently commercially employed for refractive microoptics. Typically, these processes are suitable for microlens prototyping or for fabrication in small or moderate quantities. An overview of these techniques is given in subsection 4.2.1. Although many of these techniques allow the fabrication of microlenses in large arrays, true low-cost mass production of these components can only be realized by replication technologies such as embossing, molding and casting. These techniques are described in 4.2.2.

4.2.1   Prototyping and small-scale fabrication

Photothermal technique

These lenses are fabricated by exposing photosensitive glass (FOTOFORM, Corning) to ultraviolet light through a chromium mask [1]. The mask pattern consists of circular metalized areas with a diameter of 20 to 1500 μm which coincide with the lens footprints. Next, thermal treatment causes the exposed areas to undergo crystallization and densification due to the presence of noble metal colloids in the material: the glass locally contracts in three dimensions, forcing the unexposed surface to form into spherical shapes (figure 4.1) at both sides of the substrate[2]. During this process the contracting volume becomes optically opaque and can serve as optical isolation for light travelling through adjacent lenses. The lenses cannot be put arbitrarily close to each other as a minimum interstitial space of 10 μm is needed to induce the lens shaping. For a given glass thickness the focal lengths of the lenses are controlled by the exact glass composition. Lenses with an NA up to 0.4 possible are possible.

---

[1]Next to surface profile lenses with curved interfaces, another type of refractive lenses uses a variable refractive index throughout a volume to deflect an incident wavefront (GRIN lenses). This type of lenses, which have in general a flat lens-air interface, will not be discussed here.

[2]Corning speficies that this technique allows the fabrication of bi-convex and plano-convex lenses. Suppression of material contraction at the bottom of the substrate is realized by limiting the UV intensity.
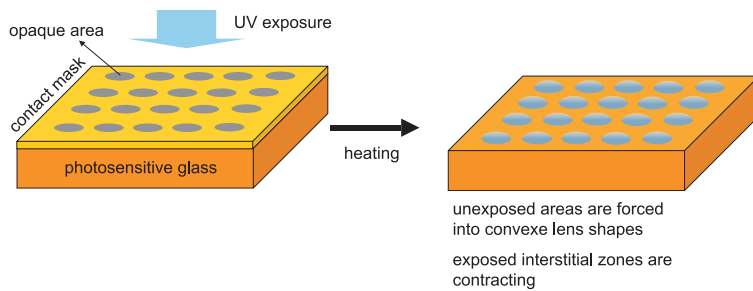
Figure 4.1: Photothermal microlens fabrication process.

Thermal reflow technique

A glass substrate is coated with a photoresist which is subsequently exposed through a chromium mask consisting of circular metalized areas. After development of the resist, the mask pattern is transferred into the resist as a series of cylindrical islands. In a next step the substrate is heated until the resist starts melting and surface tension draws the islands into lens shapes [2]. The lensed pattern can be transferred from the resist into the substrate by reactive ion etching.
Two important limitations can be identified:

1. For very low NA (or equivalent: low resist height) the resist profile does not change into a spherical shape. Instead, the center of the island remains flat and the edges round (fig 4.2), inducing severe aberrations.

2. Assuming the resist volume remains identical before and after the lens formation and assuming that the final shape is perfectly spherical, the required resist thickness can be easily calculated for a given (paraxial) focal length FL. Table 4.1 shows that for small FL the resist thickness can be significantly higher than commonly encountered in microlithography. As the resist layer becomes thicker, spinning a perfectly flat and uniform coating faces quite some technological challenges.

It is appropriate to conclude that for a given lens diameter, only lenses with a certain focal length will show a profile that is nearly perfectly spherical.

The reflow technique uses fixed chromium masks for realizing a binary resist pattern on the substrate. Binary means that the resist exposure is locally either 0 or 100 %. However, it is possible to adjust the local remaining resist thickness after development by carefully controlling the resist exposure dose. This observation forms the basis for the use of grayscale or halftone masks [3]. The halftone effect is realized by patterning the mask substrate with very fine metal features (lines or dots) which cannot be individually resolved by the lithographic system any more. As a result, the corresponding resist area receives an averaged exposure dose. If we define the fill factor as the local ratio between the metalized surface (sum of the

focal length [μm]	resist thickness [μm]
100	14.7
200	5.5
400	2.6

Table 4.1: Required resist ($n = 1.6$) thickness for lenses with a diameter of 100 μm.
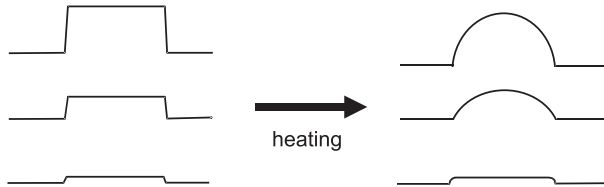

Figure 4.2: Resist profile before and after heating for several resist thicknesses.

dot or line areas) and the mask area, then it is clear that this dose is determined by the local fill factor. Next to halftone masks it is sometimes possible to achieve the same resist sculpture by translating a certain binary mask pattern during exposure. The scan velocity −which can be variable during exposure− will then determine the local dose. It is obvious that design of the mask pattern needs to take the exact intensity response of the resist into account in order to reproduce the desired dose distribution in the resist. Note that thermal reflow is not needed any more when mask dragging and/or halftone masks are used for sculpting the resist.

Direct[3] laser-writing

This technique is based on the use of a HeCd laser ($\lambda = 442$ nm) for sculpting the resist layer [4]. The full area is raster-scanned by a focused beam approximately 1-10 μm in diameter. The scanning speed and intensity can be modulated. It is the local exposure dose that unambiguously determines the developed relief height. For many applications rotationally symmetric lenses are needed. Therefore raster-scanning is often replaced by contouring the laser spot around a central position, gradually changing the radius of the scanned circle. After finishing the laser-writing, the resist still requires development.

This technique is essentially a serial writing technique, meaning that only one single lens can be written at the time. The writing time for a microoptical structure of 1 cm^2 typically takes up to a few hours and certainly does not favor a short experimental cycle. The true advantage of this process is the ability to accurately

---

[3]The terminology 'direct-write' commonly refers to either the absence of a mask pattern and/or the absence of an intermediate resist layer for pattern transfer into the substrate. In the current context, direct-write refers to the maskless nature of the process only. This means that a focused beam is used instead.
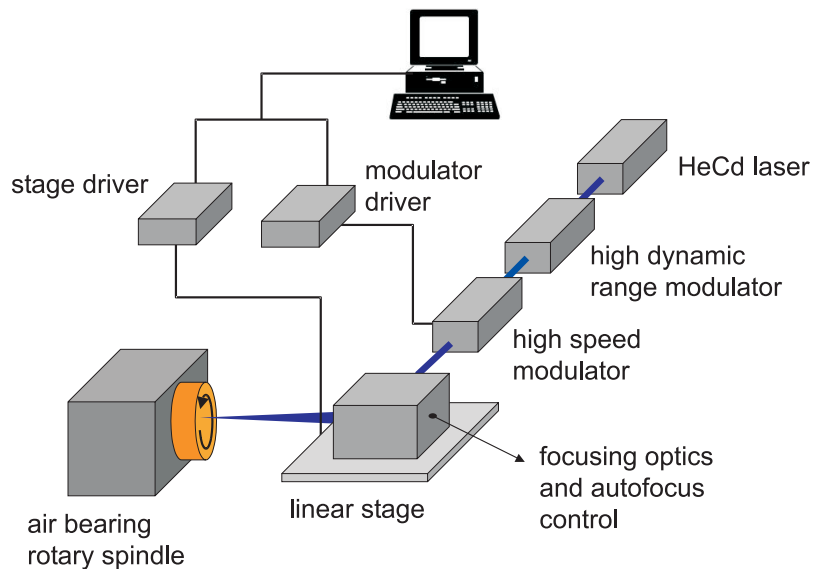
Figure 4.3: Laser-writing system with rotational scanning stage (courtesy of Rochester Photonics Corporation, USA).

produce microoptical structures of arbitrary shape[4], which is not possible with e.g. a photothermal or reflow process.

A variant on this technique is the use of an e-beam [5] or a focused ion beam [6]. The latter has sufficient energy to directly mill away materials as quartz or glass, making a resist spinning and development process redundant.

Microjet printing

In microjet printing [7] a single droplet[5] of a liquid optical material is ejected from a print head every time its piezoelectric actuator is pulsed. These droplets show high uniformity in volume. With this technique microlenses can be made using a print head with an orifice of 30 to 60 μm. This microchannel is directed towards a remote target substrate at 1 mm and ejects heated droplets. The substrate is kept at a lower temperature than the droplets, but still above room temperature.

For a given substrate type, droplet material and orifice size, the diameter and focal length of the printed lenses show a logarithmic dependence on the number of locally deposited droplets. In addition, these lens characteristics also depend on the substrate material, its surface state and the droplet viscosity. In turn, the viscosity is determined by the operating temperatures. The exact lens shape will be the result of a delicate balance between the droplet viscosity and surface tension. Suitable

---

[4]This does not only include aspherical lens shapes but also microlenses that consist of diffractive structures superimposed on a refractive surface.

[5]The property of ejecting individual liquid drops from the printhead is called 'drop-on-demand'.
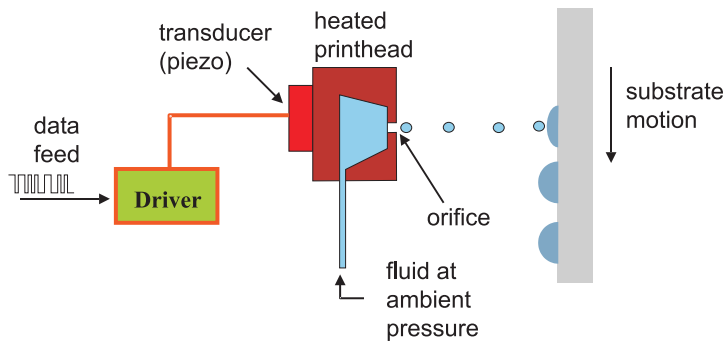
Figure 4.4: Microjet microlens printing principle (courtesy of Microfab, USA).

materials for the droplets are UV curing optical epoxies rather than acrylics and photoresists because of their better thermal and chemical stability.

Deep lithography with protons

When a highly energetic proton beam penetrates a substrate made of linear high-molecular-weight PMMA, the protons will split the long polymer chains [8]. The irradiated volume has a surface area equaling the proton beam size and a length determined by the penetration depth. The latter depends on the incident beam energy and can run up to several mm for energies above 15 MeV. The irradiated material has a lower molecular weight, exhibits free radicals and will as a consequence show a different behavior than the bulk material. This is expressed in two important observations for the irradiated area:

- increased solubility

- higher diffusion velocity for small molecules

The first property allows selective etching of the irradiation areas with specific solvents. The second offers the possibility to induce a swelling mechanism in those areas by local diffusion of a monomer vapor in a controlled environment. The use of Styrene and MMA as monomer vapor is reported in respectively [9] and [10]. A typical lens fabrication scheme can be summarized as follows:

1. Irradiation of the areas in the PMMA substrate that will be the footprints of the lenses. Although the irradiation itself is very short in time, the full time span for this process including the sample preparation and time to obtain vacuum chamber conditions, can run up to several hours.

2. Annealing of the substrate to relax internal stresses and to help avoid cracks (1 hour - 90°C).

138

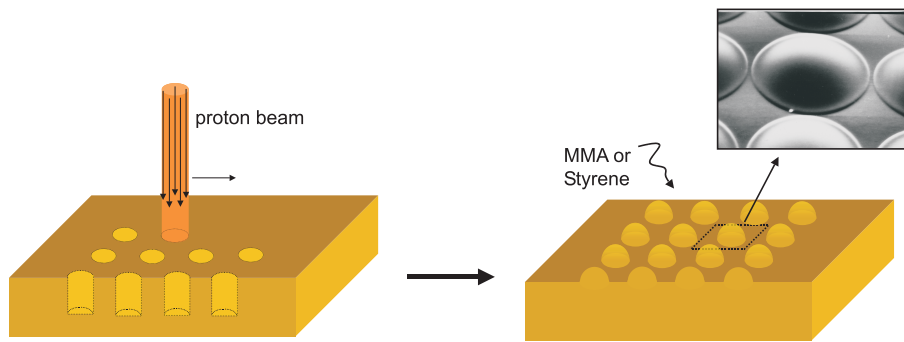Figure 4.5: Microlens fabrication with deep proton lithography and monomer diffusion (SEM close-up on the microlenses is courtesy of Korea Institute of Geology).

3. Styrene or MMA vapor diffusion (1 hour - 90°C).

4. Stabilization of the swollen lenses. This can either be accomplished by UV exposure for 1/2 hour or via a thermal procedure taking 4 hours at 70°C.

The stabilization procedure is necessary to prevent out-diffusion of the monomer, which would detoriate the lens shape stability.

Laser ablation

Laser ablation is a technique which is more recently introduced as a feasible microoptics fabrication technology. It should be stressed that although laser ablation shows some resemblance to laser-writing, it differs significantly from the latter. The laser-writing process involves a focused HeCd laser operating in continuous wave and is used to supply a resist with a spatially non-uniform exposure dose. After development a continuous surface relief is obtained in the resist. This profile is limited in depth up to a few microns.

On the other side, CO_2 or excimer laser ablation involves a beam size which is much larger than the (sub)micron focused spot of the HeCd laser and typically amounts up to several tens of microns or larger. The intensity of the pulsed laser is powerful enough to instantaneously vaporize the material where the beam hits the substrate surface. Every laser pulse thus results in a microscopic hole with lateral dimensions equaling the beam size and a depth determined by the material, laser wavelength and laser fluence (typically between 10 nm and several μm). In other words, no development process is needed. Although the depth per pulse is limited, it is possible to fire several pulses in succession and the maximum obtainable depth of the ablated structure extends far beyond the few microns for the HeCd laser-writing technique. Another important advantage of laser ablation is the whole range of materials that can be structured with ablation. Although plastics are one of the more interesting material systems for photonic applications, laser ablation is not limited to this type of materials and can be applied to structure polymers,

139

semiconductors, quartz, glass, composites, etc. It should be noted that for every laser ablation source, the range of machinable materials might be more restricted. Laser ablation for micromachining purposes is elaborately discussed in chapter 3.

A few microoptics fabrication techniques using laser ablation can be found in literature and an overview is given in 4.3.1. A new technique which is fully based on excimer laser ablation and offers great flexibility in terms of lens shapes, is developed in the framework of this doctoral research work [11, 12]. In a nutshell, the fabrication process is based on successive ablation of well-chosen circular trenches using a pulsed excimer beam with a typical size of some 100 μm. The fabrication time is of the order of minutes and no other processes than pure laser ablation are involved. Although the experimental results have up till now been limited to fabrication of lenses in polycarbonate, the technique can be extended to any material that can be laser-machined with a surface finish that equals optical quality.

Combined techniques

To complete the overview, a few lens fabrication processes need to be added which are related to combinations of the techniques above.

One method is based on the ablation of islands in a doped teflon resist, spin-coated on a silica or silicon substrate [13]. Amorphous teflon was chosen for its excellent transmission from the deep UV to the IR (190 nm $-$ 2 μm) and doping is needed to increase the absorption at 193 nm (ArF laser line). Thicknesses as high as 100 μm were achieved for the spin-coated layer. After ablation of the cylindrical islands, the remaining dopant concentration was out-diffused by thermal annealing. In a final step the samples were heated up to the melting temperature of the amorphous teflon (300°C) for half an hour to obtain a melting effect similar to thermal reflow of resist.

A second technique shows quite some similarities with the irradiation and swelling process in Deep Proton Lithography. But in this case both processes occur simultaneously [14]. PMMA doped with 0.25 wt % diphenyltriazene (DPT) is irradiated with a single pulse from an excimer XeCl laser (308 nm) at 3 J/cm^2. This fluence is well below the single-pulse threshold for ablation which can be estimated at 5 J/cm^2. Under these conditions a balanced combination of thermal softening of the polymer matrix with material expansion due to nitrogen release from the irradiated DPT is achieved. This results in a rotationally symmetric parabolic lens shape. The simplicity of the set-up has also some important drawbacks: the diameter of the fabricated lenses was limited to a mere 15 μm and it was experimentally observed that larger beam sizes result in doughnut-like profiles[6]. For the given fluence the swelling height is limited to 1.5 μm. Above 3 J/cm^2 bubble formation in the material is favored and these fluences should therefore be avoided.

Finally, in [15] a process is described for fabrication of microlenses by UV excimer irradiation of PMMA followed by styrene diffusion. A PMMA substrate is irradiated at sub-ablative fluence with KrF laser pulses of 10 mJ/cm^2. The number of pulses determines the sag of the lenses and typically varied between 8,000 and

---

[6]The maximum diameter is not given explicitly in the paper, but it should be below 100 μm.

30,000 pulses for lens heights up to 30 μm. The lenses had diameters between 200 μm and 1 mm.

Summary

All lens fabrication technologies show excellent results in terms of either optical quality, flexibility in lens profile, ease of fabrication, prototyping speed or compatibility with heterogeneous integration, etc. A brief summary of the advantages and disadvantages of each fabrication process might be able to give a better idea on how it performs with regard to competing techniques. We therefore introduce some benchmarks:

1. Fabrication parameters: process cycle time, material choice, repeatibility and compatibility with monolithic integration and the assembly process. Although all techniques are able to fabricate lenses, these processes take place on a very different time scale. We make a distinction between two durations for the cycle time: "long" indicating several hours and "short" for a fabrication time in the range of minutes. Note that this parameter applies to the full time span of the fabrication scheme, including the possibly slow diffusion and annealing processes. Obviously, this parameter gains importance when the fabrication technique is applied for fast prototyping.

Other important properties are the choice of lens/substrate material, repeatibility, possibility of monolithic integration and compatibility with a (heterogeneous) assembly process. This implies that the opportunity to insert microlenses in a finished or almost finished heterogenous assembly can be considered an added value of a lens fabrication technology. Although all techniques are able to produce stand-alone lenses, they are seldomly suitable for fabricating these structures on an assembled module. This is a natural consequence of the fact that this module usually cannot be exposed to reactive gases, diffusion agents or high temperatures.

The other property, monolithic integration, refers to the integration of multiple microoptical elements on a single carrier: facets or mirror planes, refractive lenses and diffractive structures, all combined on the same polymer.

Repeatibility applies to the ability to fabricate the same lens at different times and the dependence of the lens quality on variable process conditions.

2. Lens parameters: lens diameter, NA, flexibility of lens shapes. Lenses are typically associated with spherical shapes because of technological challenges related to fabrication of non-spherical lenses. This is particularly the case for glass optics. However, some applications require microoptical functionality that cannot be satisfactorily met with spherical lens shapes. The ability to make aspherical lenses can thus be considered an important advantage for a given fabrication technique. This feature is particularly interesting for plastic components as replication techniques do not impose any limitation on the lens shape to be replicated.

141
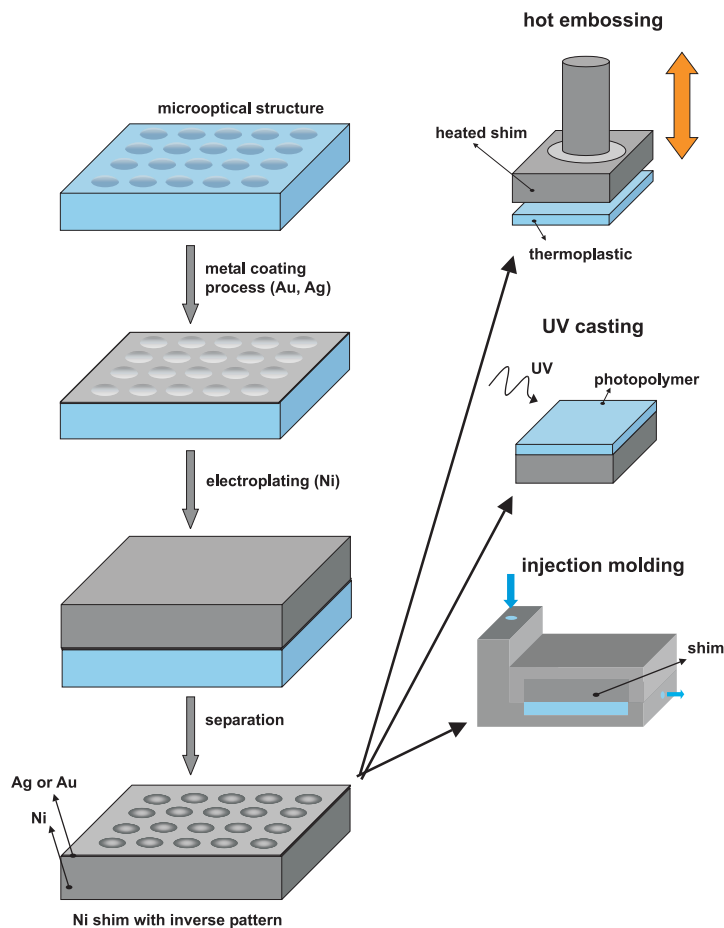
Figure 4.6: Replication scheme for plastic microoptics.

3. Lens array fabrication. Many optical coupling problems that can be met by insertion of microoptics, are not solved with a single lens but rather need arrays of identical lenses. When a technique is capable of making such lens arrays in a substantial shorter time than required by serial writing (i.e. fabricating the lenses one by one), this is considered a plus.

An overview of the discussed lens fabrication techniques is given in table 4.2. Note that these technologies are still maturing, in particular the more recently introduced DLP and contour ablation.

4.2.2 Replication technology

All of the techniques mentioned in 4.2.1 are focused on the fabrication of lenses on a small scale or for prototyping purposes. Mass production of these components

technique	fabrication parameters					lens parameters			array	references
	cycle time	material	repeat.	monolith.	assembly	diameter range	NA range	flexibility		
photothermal	long	Corning Fotoform	+	-	-	20-1500 μm	<0.40	-	+	[16]
thermal reflow	long	resist	+	-	-	10-2000 μm	0.15-0.45	-	+	[17]
reflow + etching	long	resist silica semiconductor	+	-	-	10-2000 μm	0.15-0.45	+/-(1)	+	[17]
laser-writing	long	photoresist	+	+/-	-	<10 mm		+	-	[4]
microjet	short	UV curable epoxy	+	-	+/-(2)	20-5000 μm	0.05-0.33	+(3)	+	[18]
DLP	long	PMMA	+/-	+/-	-	50-2000 μm	0.1-0.7	-	+	[10]
contour ablation	short	Polycarbonate Polystyrene Polyimide	+/-(4)	+/-	+	<1 mm(5)	0.04-0.6	+(6)	+/-(6)	[12, 11]

(1) Etching into substrate is possible by a well-considered choice of etching gases.
(2) Taking into account that the working distance between print head and substrate is very limited and that substrate temperature control is crucial.
(3) Different lens shapes require different operating temperatures, substrate materials and epoxy types.
(4) In this chapter, the influence on the lens quality of most ablation fabrication parameters is discussed.
(5) All experimental results have been limited to 100-200 μm lenses, but there is no physical limitation to smaller lenses. 1 mm is a reasonable upper limit as larger lenses take more time to ablate.
(6) The lenses cannot be put arbitrary close to each other, but should be separated by at least the beam spot size.

Table 4.2: Overview of the fabrication technologies.

143

can be achieved by so-called replication techniques that duplicate the prototype structure in plastic material. Figure 4.6 depicts the replication process steps for a microlens array. First, the prototype microoptical structure is coated with a thin conductive Au or Ag layer through a sputtering or evaporation technique. In a next step the structure is immersed in an electrolyte bath and plated with Ni up to a thickness of 50-100 μm. After electro-plating the Ni shim is separated from the prototype part and is now ready to be used as a master for mass replication. Three commercial techniques can be employed for replication:

- injection molding: the Ni shim is used as part of a mold. Its surface relief is copied into a plastic which is injected in liquid phase under high pressure in the mold. After cooling and solidification the replica can be separated from the mold.

- (UV)-casting: a UV-curable polymer film on a rigid carrier is pressed against the shim and rapidly cured.

- (hot) embossing: the heated shim is pressed in a thermoplastic polymer film, permanently copying its surface pattern into the polymer.

It should be noted that all techniques are able to reproduce micrometer and nanometer features, and the cost of the replica is relatively independent of the complexity of the structure.

4.3 Laser ablation of microoptics

4.3.1 State-of-the-art microoptics fabrication with laser ablation

In literature a few laser-ablation based microlens fabrication techniques can be found. The most promising method is reported in [19]. With an ArF excimer laser ablation system based on mask projection, Fresnel lenses are fabricated in polyimide. The mask consists of a transparent quartz carrier on which several complex metal patterns are lithographically defined. The microlenses are 8-level diffractive structures which are fabricated by selecting in succession 3 appropriate mask patterns via a computer-controlled mask stage. With the number of laser pulses varying from 1 to 4 and a typical mask step and settle time of 600 ms, it takes about 3 to 5 s to complete a single lens. The disadvantage of this technique is that for every lens diameter and focal length, custom mask patterns are required. Although many patterns can be put on a single mask, this approach is probably not cost-effective for fabrication of different prototyping lenses.
Another microlens fabrication process uses a focused CO_2-laser operating at 5 kHz to locally heat a glass substrate [20]. As strong heating can cause cracks in the substrate, heat-resistant and thermal shock-proof glass as Corning 7059 is preferred above common glass types. The laser spot supplies the glass surface with the necessary thermal energy for melting. If a suitable laser fluence and irradiation

time is chosen, the glass will not ablate and will start deforming. In the central region of the laser spot, a spherical-like lens will appear that is surrounded by a circular trench. Although the exact surface deformation mechanism is not well-understood, it is presumably the result of the surface tension distribution in the affected area. The lens diameter can be chosen by selecting an appropriate spot diameter. After solidification, thermal annealing (640°C) ensures that residual stresses in the substrate are removed.

A method for creating structures with a desired wavefront transmission is reported in [21]. A 50 μm UV-curable resin is coated on a glass carrier and covered with a polished quartz plate. After curing with UV irradiation through the quartz, the plate is removed. Next the coated glass is mounted on a translation stage in a laser ablation system. The set-up is designed to micromachine the polymer surface with an ArF excimer laser while an interferometer detects the transmission wavefront. The measured wavefront is compared with the desired one and a computer generates a pulse distribution map to correct the phase error. After completing this ablation process, the wavefront is measured again and a new pulse distribution map is generated. This procedure is repeated until the phase error becomes acceptable.

A last technique is described in [22] and uses grayscale masks for laser-induced dry etching of integrated InP microlenses with a KrF laser. Although dry-etching implies the use of reactive gases and should not be confused with laser ablation, the described mask technique can be readily transferred to a pure ablation process.

4.4 Microlens properties

An extensive analysis of the optical behavior of microlenses is beyond the scope of this thesis. Instead an overview is given of the most important lens parameters, followed by a brief summary of geometric and wave-based lens analysis. For a more detailed theory on lenses we refer to [23].

4.4.1 Definition and terminology in geometrical optics

In figure 4.7 a microlens with refractive index n_L and diameter D forms a window between two media with refractive indices respectively n_1 and n_2. In the first medium an object is located at a distance S_o ('object distance') from the lens; in the second medium the image of the object is formed at a distance S_i ('image distance'). We can now define some lens dimensions and properties:

Optical axis the line which intersects the lens in the center, perpendicular to the local surface profile.

Image reproduction of the object by light rays originating from the object and deflected by the lens.

Primary and secondary lens surface respectively the first and second lens surface that rays from the object encounter. Note that 'front' and 'back' often replace the terms 'primary' and 'secondary'.

Focal point the point where refracted rays that originate from a collimated beam parallel with the optical axis, meet. For a positive lens this point lies at the opposite side of the incident beam. A negative lens will have a focal point lying on the same side as the incident beam. The focal points on the object and image sides are called respectively the front focal point (denoted by f_F) and back focal point (denoted by f_B).

Principal surface the principal surfaces of a lens are the virtual surfaces formed by the intersections of the forward extension of incident rays entering the lens parallel to the optical axis, and the backwards extension of the refracted rays when they leave the opposite lens surface towards the focal point. The primary principal surface is defined by rays entering the lens parallel to the optical axis from the image side (indicated on the figure). The secondary principal surface is defined by the rays entering the lens parallel to the optical axis from the object side. Note that for a infinitely small lens, both surfaces coincide. For real lenses, the positions of both planes depend on the exact lens curvatures and can lie either inside or outside the lens.

Principal points the intersections of the primary and secondary principal surfaces with the optical axis, respectively called the primary and secondary principal points.

Vertex the intersection of a lens surface with the optical axis. The intersection of the primary lens surface is defined as the primary vertex; the intersection with the secondary surface is the secondary vertex.

Effective focal length (EFL) the distance between the primary (secondary) focal point and the primary (secondary) principal point. For a positive lens, this length is positive. For a negative lens, the EFL is negative.

Focal length (FL) the primary (secondary) focal length is the distance between the primary (secondary) vertex and the primary (secondary) focal point. Again, this length can either be positive or negative.

Conjugate ratio the ratio of image distance to object distance along the optical axis of the lens. Both distances are measured from the object (image) to primary (secondary) principal plane.

Numerical aperture (NA) the NA of a lens is the sine of the angle between a marginal ray[7] and the optical axis, multiplied by the refractive index of the medium. The NA can be defined in both the image and object space. If no image or object distances are given, the NA refers to the angle made by a marginal ray originating from the focal point.

F-number (F/#) this is the effective focal length divided by the clear aperture of the lens: $F/\# = \frac{EFL}{D}$. It is also called focal ratio, speed or relative aperture.

The knowledge of these terms is required to understand the paraxial behavior of lenses described in the following section.

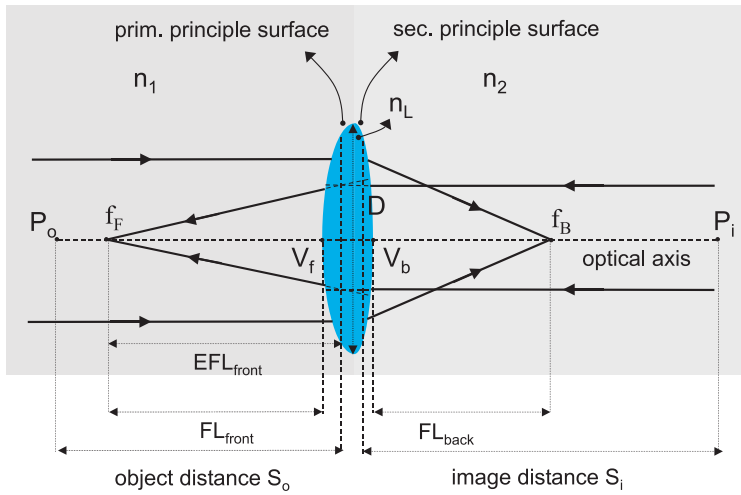[7] A marginal ray is a ray which leaves the lens at its outer edge.

Figure 4.7: Definition of lens properties.

4.4.2 Lens imaging within the paraxial approximation

Light can be depicted as traveling electromagnetic (EM) waves through space. In the approximation that the wavelength of the EM wave is very small compared to spatial variations in the optical structure, the wave can be modeled by rays pointing towards the local direction of propagation. Using the laws of refraction and reflection, these rays can be traced through an optical system via[8]

$$
\begin{array}{ll}
n_1 sin\theta_1 = n_2 sin\theta_2 & \textbf{refraction} \\
\theta_1 = \theta'_1 & \textbf{reflection}
\end{array} \tag{4.1}
$$

which is valid at a well-polished interface between two materials with refractive index n_1 and n_2. θ_1 and θ_2 are the angles between the local surface normal and respectively the incident and refracted ray.

When the geometrical approach is justified, the geometrical wavefront will be a close approximation of the physical one. It can be constructed with the knowledge that it is locally orthogonal to the ray direction and that the optical path lengths for all rays are equal from one wavefront to the other.

Equation (4.1) makes fast calculation of light propagation throughout an optical system possible and forms the base for sophisticated commercial ray trace tools. For centered systems[9] there is a significant simplification of the refraction law that makes an analytic approach of ray propagation more feasible. This simplification is valid for rays propagating close to the optical axis, meaning that these rays will

---

[8]Next to a change in propagation direction, these laws also describe the optical power distribution between the reflected and refracted wave.

[9]Centered optical systems consist of rotationally symmetric refracting and reflecting surfaces which have a common axis, the optical axis.
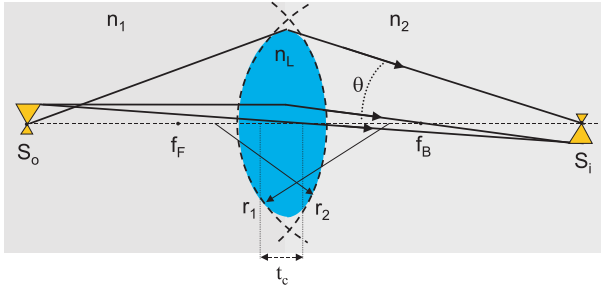
Figure 4.8: Imaging properties of lenses.

always make a small angle of incidence with the normal of the lens surface. In this paraxial case the refraction law is reduced to

$$n_1\theta_1 \simeq n_2\theta_2$$

For angles smaller than 14°, the error due to approximating $sin(\theta)$ by θ is less than 1 %.

Within the paraxial approach, it is possible to summarize the image formation properties of spherical lenses in a few equations. These properties refer to the ability of a lens to capture rays emitted by a single object point and subsequently redirect all those rays to another single point. This occurs independently of the angles and locations of the incident rays on the lens surface and is called stigmatic imaging. In addition, ideal imaging behavior implies two other conditions to be fulfilled. Firstly, the object and image need to be geometrically identical except for a constant scaling factor called the magnification. If this condition is not met, the image is distorted. Secondly, a plane normal to the optical axis in the object space should be imaged onto a plane in the image space. If this is not the case, the image suffers from field curvature.

For a lens with EFLs EFL_F and EFL_B , the following relationship is valid for the object and image distance S_o and S_i:

$$\frac{n_1}{S_o} + \frac{n_2}{S_i} = \frac{n_1}{EFL_F} = \frac{n_2}{EFL_B} \tag{4.2}$$

which is known as the lens formula in Gaussian form. The focal lengths can be calculated from

$$\frac{n_1}{FL_F} = \frac{n_2}{FL_B} = \frac{n_L - n_1}{r_1} + \frac{n_2 - n_L}{r_2} - \frac{t_c(n_L - n_1)(n_2 - n_L)}{n_L r_1 r_2} \tag{4.3}$$

with t_c the thickness of the lens in the center and r_1, r_2 the radii of curvature for both spherical lens surfaces. By convention r$_1$ is positve and r_2 is negative for the lens depicted in the figure. The magnification (ratio of object size to image size) is

$$m = \frac{n_2 S_i}{n_1 S_o} \tag{4.4}$$

and equals the conjugate ratio if the media at both sides of the lens are identical.

Within the paraxial approximation the numerical aperture can be calculated via

$$NA = \frac{nD}{2 \times EFL}$$

with EFL being the front or back effective focal length and n equaling respectively n_1 or n_2.

The F-number is given by

$$F/\# = \frac{n}{2NA}$$

4.4.3 Lens aberrations under monochromatic conditions[10]

Within the paraxial approach a spherical lens profile was suitable for stigmatic imaging. However, experimental verification of the imaging behavior will show that this is only approximately true: a single object point will likely result in a blurred spot in the image plane and the image will not always be geometrically similar to the object. These deviations are called aberrations. To quantify the phenomenon, we can consider single lens imaging in figure 4.9. A single object point P_o and its Gaussian (paraxial) image P_i is given. Both points and the optical axis lie in the same plane, called the meridional plane. At the exit plane of the lens a spherical wavefont ψ_0 is formed which converges towards P_i in case of stigmatic, unaberrated imaging. This ideal wavefront is called the Gaussian reference sphere.

However, a real wavefront deviates from this ideal case and will lead to rays reaching the image plane in different locations around P_i. As we are considering centered systems, it is sufficient to identify the object point with a single coordinate h, corresponding to the distance between the optical axis and P_o. The paraxial image point P_i will be located at a distance mh of the optical axis. If we identify rays at the exit plane with their polar coordinates (r,θ) as in figure 4.10, the wavefront aberration function $\Delta\psi(h, r, \theta)$ (=difference in path length) can be written by definition as:

$$\Delta\psi(h, r, \theta) = \psi(h, r, \theta) - \psi_0(h)$$

ψ_0 coincides with ψ on the optical axis. Although $\Delta\psi$ is defined here in the exit plane of the lens, it is possible to calculate the wave aberrations at any plane between the exit pupil of the optical system and the Gaussian image plane.

The aberration $\Delta\psi(h, r, \theta)$ can be identified with a displacement $\Delta\varepsilon(h, r, \theta)$ between the Gaussian image point P_i and the intersection of the Gaussian image plane with the ray originating from (r, θ) in the pupil plane. $\Delta\varepsilon$ is called the ray aberration.

As the system is rotationally invariant, $\Delta\psi$ will depend on h, r and θ through h^2, r^2 and $\overrightarrow{h} \cdot \overrightarrow{r}$ ($= hr cos\theta$). A power-series expansion will thus be of the form

$$
\begin{aligned}
\Delta\psi(h, r, \theta) &= \sum_{l=0}^{\infty}\sum_{m=0}^{\infty}\sum_{n=0}^{\infty} c_{lmn}(h^2)^l(r^2)^n(hrcos\theta)^m \\
&= \sum_{l=0}^{\infty}\sum_{m=0}^{\infty}\sum_{n=0}^{\infty} c_{lmn}h^{2l+m}r^{2n+m}cos\theta^m
\end{aligned} \tag{4.5}
$$

---

[10]Polychromatic aberrations will not be considered here as they are determined by wavelength dispersion of the lens refractive index, rather than the exact surface shape.
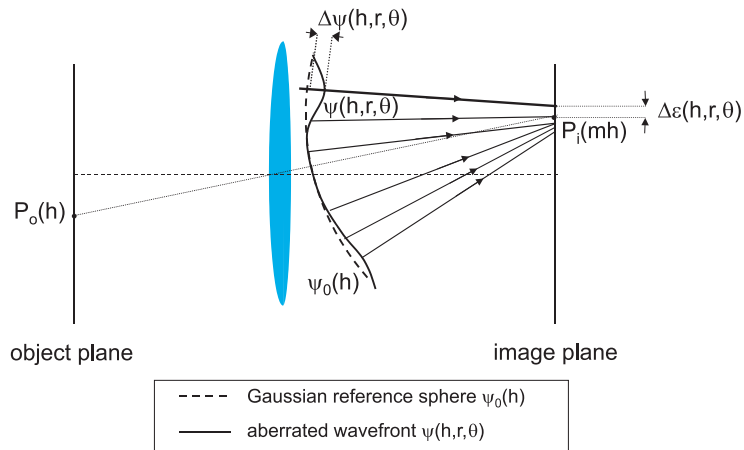
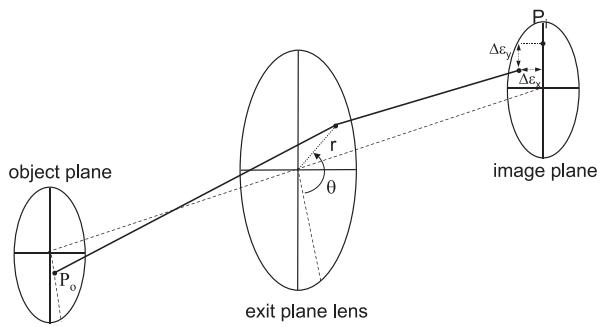Figure 4.9: Wavefront and ray aberrations in an imaging system.

Figure 4.10: Polar coordinate system in the exit plane of the lens.

r^4	spherical aberration
$r^3 h cos\theta$	coma
$h^2 r^2 cos^2\theta$	astigmatism
$h^2 r^2$	curvature of field
$h^3 r cos\theta$	distortion

Table 4.3: The five Seidel aberrations.

The degree of this expansion is $2(l+m+n)$. c_{000} equals 0 if the Gaussian reference sphere is chosen to coincide with the aberrated wavefront on the optical axis. c_{010} and c_{001} can also be ignored as these terms ($\sim r^2$ and $\sim hrcos\theta$, respectively called defocus and tilt) implicate that the reference sphere is not centered around the paraxial image point. The term $c_{100}h^2$ is called 'piston' and generally differs from 0. Since it does not include any r or θ dependence, it does not affect imaging. The lowest order aberration terms of significance will therefore be of the 4th power and are given in table 4.3. In case $\Delta\psi$ can be adequately approximated by these aberrations, we can write:

$$\psi(h,r,\theta) = \frac{1}{8}S_1 r^4 + \frac{1}{2}S_2 hr^3 cos\theta + \frac{1}{2}S_3 r^2 h^2 cos^2\theta + \frac{1}{4}(S_3 + S_4)r^2 h^2 + \frac{1}{2}S_5 rh^3 cos\theta$$

where the coefficients S_i are chosen in accordance with the Seidel notation[11].
Via differentiation, we find for the ray aberrations:

$$\begin{aligned} \Delta\varepsilon_y &= \sigma_1 r^3 cos\theta + \sigma_2 r^2(2+cos2\theta)h + (3\sigma_1 + \sigma_4)rh^2 cos\theta + \sigma_5 h^3 \\ \Delta\varepsilon_x &= \sigma_1 r^3 sin\theta + \sigma_2 r^2 sin2\theta h + (\sigma_3 + \sigma_4)rh^2 sin\theta \end{aligned}$$

In case the object point is located on the optical axis, there will be only one primary aberration present: spherical aberration. In figure 4.11 a cross-section of a planoconvex lens is given and a few rays are traced for the case of an object at infinity. After propagation through the lens, the rays converge, but not all to the same point. In the plane of 'best focus'[12], a small image point surrounded by a broad halo due to spherical aberration can be distinguished (figure 4.12a).
Reducing spherical aberrations is accomplished by a number of ways:

Suitable form factor Aberrations can be considered as a departure from the paraxial approximation. In other words, reducing the angle of incidence on the lens interfaces will decrease aberrations. This is in particular the case for spherical aberration. In this context we can define a form factor for a spherical lens by $q = \frac{r_2 + r_1}{r_2 - r_1}$. For a biconvex and a planoconvex lens, q equals respectively 0 and ± 1 depending on the orientation of the lens. To a certain extent, reduction of the aberrations can be accomplished by a good choice for q.

---

[11]These 4th power aberrations correspond to third order ray aberrations. They are called the primary or Seidel aberrations.

[12]Best focus refers to the location where the blur of the spot is minimal. This spot is also called the 'disc of least confusion'.
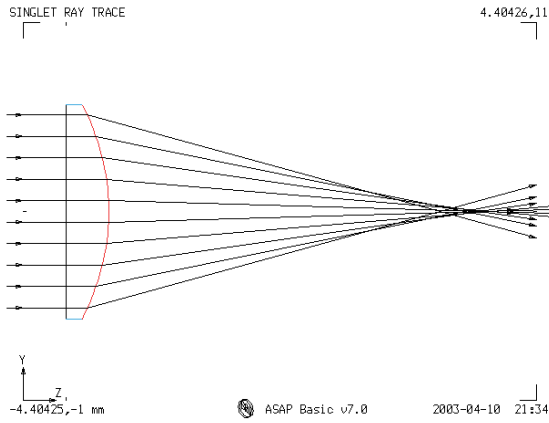
Figure 4.11: Ray propagation through a planoconvex lens.

focal plane spot of planoconvex lens   focal plane spot of lens corrected for spherical aberration
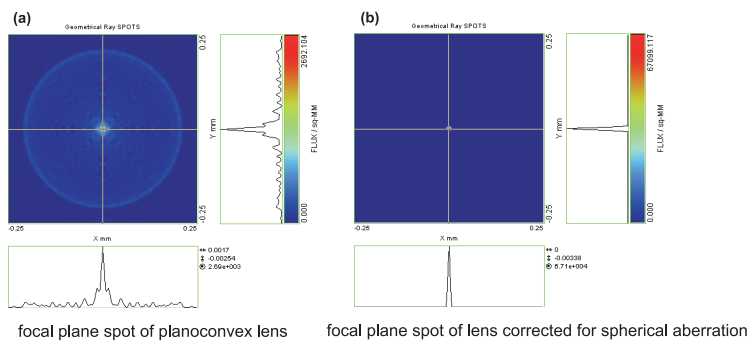
Figure 4.12: Focal spot of a planoconvex lens (a) and a non-spherical lens corrected for third order spherical aberration (b).

Aspherical lens surfaces it is possible to optimize the lens shape for the specific imaging situation. Just like spherical lenses satisfied the paraxial conditions for imaging, other lens shapes as elliptical, parabolic and hyperbolic profiles might succeed in stigmatic imaging in non-paraxial situations (fig 4.12b).

Reduction of lens power it can be shown that $\Delta\varepsilon_x$ and $\Delta\varepsilon_y$ have a cubic dependence on the lens power. In turn, the lens power is inversely proportional to the focal length. As the overall power of a series of successive lens interface is the sum of the individual powers, it is beneficial to replace a single lens with a short focal length by several lenses with longer focal lengths.

If the aberrations are considered in an optical system for a fixed object point, then we can include the object height h into the coefficients of the power series. For an exit pupil with radius a, we can rewrite r as ρa $(0 \leq \rho \leq 1)$. The power expansion

152

becomes

$$\Delta\psi(\rho,\theta) = \sum_{m=0}^{\infty} \sum_{n=0}^{\infty} c'_{nm} \rho^{2n+m} cos^m\theta$$

A similar expansion is possible by using a compete set of Zernike polynoms to represent the aberrated wavefront:

$$\Delta\psi(r,\theta) = A_{00} + \frac{1}{\sqrt{2}} \sum_{n=2}^{\infty} A_{n0} R_n^0(\rho) + \sum_{n=1}^{\infty} \sum_{m=1}^{n} A_{nm} R_n^m(\rho) cosm\theta$$

The radial polynom are given by

$$R_n^m(\rho) = \sum_{s=0}^{\frac{n-m}{2}} (-1)^s \frac{(n-s)!}{s!(\frac{n+m}{2}-s)!(\frac{n-m}{2}-s)!} \rho^{n-2s}$$

and satisfy the orthogonality condition

$$\int_0^1 R_n^l(\rho) R_{n'}^l(\rho)\rho d\rho = \frac{1}{2(n+1)} \delta_{nn'}$$

For a given wavefront aberration, the coefficients A_{nm} $(0 \leq n \leq \infty, 0 \leq m \leq \infty)$ can be calculated via

$$A_{nm} = \sqrt{1+\delta_{m0}} \frac{2(n+1)}{\pi} \int_0^{2\pi} \int_0^1 \Delta\psi(\rho,\theta) R_n^m(\rho) cosm\theta \, \rho d\rho d\theta \qquad (4.6)$$

An interesting feature of the Zernike expansion, is that the coefficients A_{nm} are proportional to the mean-square value of the corresponding aberration:

$$\begin{aligned}
< \left(\frac{1}{\sqrt{1+\delta_{m0}}} A_{nm} R_n^m(\rho) cosm\theta \right)^2 > &= \frac{\int_0^{2\pi} \int_0^1 \left(\frac{1}{\sqrt{1+\delta_{m0}}} A_{nm} R_n^m(\rho) cosm\theta \right)^2 \rho d\rho d\theta}{\int_0^{2\pi} \int_0^1 \rho d\rho d\theta} \\
&= \frac{A_{nm}^2}{2(n+1)(1+\delta_{m0})}
\end{aligned}$$

The mean-square value for the full wave aberration is then

$$< \Delta\psi^2 > = \frac{\int_0^{2\pi} \int_0^1 \Delta\psi(\rho,\theta)^2 \rho d\rho d\theta}{\int_0^{2\pi} \int_0^1 \rho d\rho d\theta} = \sum_{n=0}^{\infty} \sum_{m=0}^{\infty} \frac{A_{nm}^2}{2(n+1)(1+\delta_{m0})}$$

On the other side, the average wavefront aberration is given by

$$\begin{aligned}
< \Delta\psi > &= \frac{\int_0^{2\pi} \int_0^1 \Delta\psi(\rho,\theta)\rho d\rho d\theta}{\int_0^{2\pi} \int_0^1 \rho d\rho d\theta} \\
&= A_{00}
\end{aligned}$$

153

As the standard deviation σ^2 of the wavefront aberration can be calculated using the identity $\sigma^2_{\Delta\psi} = <\Delta\psi^2> - <\Delta\psi>^2$, we can conclude that

$$\sigma^2_{\Delta\psi} = \sum_{n=1}^{\infty} \sum_{m=1}^{\infty} \frac{A^2_{nm}}{2(n+1)(1+\delta_{m0})}$$

The different terms in the Zernike expansion are identified with third-order, fifth-order aberrations, etc. Note that the Zernike coefficients require an evaluation of $\Delta\psi$ over the entire exit pupil of the optical system (4.6), contrary to the Seidel coefficients which follow from paraxial considerations.

4.4.4 Spot size calculation

One of the most appreciated properties of lenses next to imaging, is the opportunity to concentrate light into a small focal spot. The spot is obtained when source rays enter the lens parallel to the optical axis. At the other side of the lens these rays will be collected at the back focal point. Within the geometrical optics approach and paraxial approximation, the minimum spot size is infinitely small due to equation (4.4) which predicts a zero magnification for an object distance equaling infinity. In reality, the non-ideal lens surface profile (aberrations) and the limited size of the lens diameter (diffraction at the pupil) has to be taken into account and will result in blurring of the spot. In the former sections the influence of aberrations on the optical lens behavior has already been discussed. But even in the absence of these surface anomalies, broadening of the focal spot will occur. Blurring is then the result of diffraction and the spot size can be calculated based on wave considerations. In this context we define $P_{ideal}(r, \theta)$ as the pupil function of an ideal, unaberrated lens. This function equals 1 within the diameter of the lens and 0 outside that area.

For a plane wave incident on the lens, the normalized intensity profile at the focal plane follows from a far field calculation through the lens pupil $P_{ideal}(r, \theta)$ (Fraunhofer diffraction pattern):

$$PSF_{dl}(r) = \left| \frac{2J_1 \left(\frac{kDr}{2FL} \right)}{\frac{kDr}{2FL}} \right|^2 \tag{4.7}$$

and is called the Point Spread Function of the diffraction-limited (dl) lens. In this expression, r is the radial coordinate in the focal plane with the focal point as center, k the wave number ($k = 2\pi/\lambda$), D the lens diameter and J_1 the first order Bessel function of the first kind. This function is plotted in figure 4.13. The power within the central spot approximates 83 % of the total transmitted power through the lens and its diameter D_{spot} is given by the location of the first zero crossings of $PSF_{dl}(r)$ around the center[13]:

$$D_{spot} = 2.44\lambda F/\# \tag{4.8}$$

---

[13]In chapter 3 the spot size of a Gaussian beam was calculated as the full $1/e^2$ width of the beam waist and equaled $1.27\lambda F/\#$. Here the spot size due to uniform illumination is defined as the distance between the two central zero crossings.
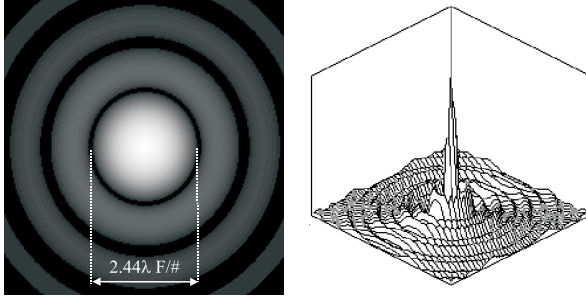
Figure 4.13: Plot of the far field pattern $I(r) = PSF_{dl}(r)$ in the focal plane of a lens illuminated with a plane wave.

Lenses showing a focal spot of this size are considered diffraction-limited. Their performance limitations are dominated by the physical nature of light and not by surface imperfections. More generally it can be shown that the spot in the image plane originating from an object point P_o will show the same intensity profile centered around the Gaussian image point.

In case of an aberrated lens the pupil function can be written as:

$$P_{abe}(x, y) = P_{dl}(x, y)e^{j\Delta\phi(x,y)} = P_{dl}(x, y)e^{jk\Delta\psi(x,y)}$$

whith $\Delta\psi$ the wavefront aberration at the exit pupil of the lens. The (complex) amplitude impulse response $h(x_i, y_i, x_o, y_o)$ is calculated by taking the fourier transform of this pupil function:

$$h(x_i, y_i, x_o, y_o) \sim \int \int P_{abe}(x, y)e^{-j\frac{kx}{d_i}(x_i - Mx_o)}e^{-j\frac{ky}{d_i}(y_i - Mx_o)}dxdy \qquad (4.9)$$

The indices i and o refer to the image and the object plane respectively, R is the radius of the reference sphere and M denotes the magnification. From this amplitude impulse response, a more general expression for the PSF is obtained via

$$PSF_{abe}(x_i, y_i, x_o, y_o) = |h(x_i, y_i, x_o, y_o)|^2$$

Note that in case of aberrated lenses, PSF_{abe} generally becomes dependent on the object position. In the following discussion, we assume that $(x_o, y_o) = (0, 0)$ or PSF_{abe} is calculated for on-axis illumination.

Often, one is only interested in the peak intensity $PSF_{abe,max}$. This point is called the diffraction focus and can be found as the center of the reference sphere that minimizes $\sigma_{\Delta\psi}$. In this context, the Strehl Ratio is defined as

$$SR = \frac{PSF_{abe,max}}{PSF_{dl}(0)} = \frac{1}{\pi^2}\left|\int_0^{2\pi}\int_0^1 e^{jk\Delta\psi(\rho,\theta)}\rho d\rho d\theta\right|^2 \qquad (4.10)$$

155

meaning that it equals the peak intensity of the aberrated spot, normalized by the peak intensity for the diffraction-limited spot. For small aberrations the complex exponential in (4.10) can be expanded into a Taylor series up to the second order term and it can be shown that

$$SR = 1 - (\frac{2\pi}{\lambda})^2 \sigma^2_{\Delta\psi} \tag{4.11}$$

PSF and SR are both valuable lens performance factors in applications aiming at collection and focusing of light. However, they give little information and insight on the general imaging behavior of the lens. From this angle, the Optical Transfer Function (OTF) is much more interesting. The OTF is defined as

$$OTF(f_x, f_y) = \frac{\int\int PSF(x_i, y_i)e^{j2\pi(f_x x_i + f_y y_i)}dx_i dy_i}{\int\int PSF(x_i, y_i)dx_i dy_i} \tag{4.12}$$

and can be considered as a normalized inverse fourier transform of the PSF. Equations (4.12) and (4.9) implicate that an autocorrelationship exists between the OTF and lens pupil function. The optical transfer function is essentially a complex function: the amplitude is called MTF (Modulation Transfer Function) and the phase is named Phase Tranfer Function (PTF). The MTF reflects the reduction in contrast for the object to the image and is dependent on the spatial modulation frequency. The object's intensity profile can be decomposed in its fourier spectrum and all of these spatial frequencies will be found in the image plane. The MTF prescribes then the remaining modulation ratio for each of these frequencies. For a diffraction-limited lens with diameter D, the MTF is

$$MTF_{dl} = \frac{2}{\pi}\left(acos(f/2f_c) - \frac{f}{2f_c}\sqrt{1 - \left(\frac{f}{2f_c}\right)^2}\right)$$

with $f_c = \frac{D}{2\lambda z}$ the cut-off frequency and z the distance to the lens. This MTF is depicted in figure 4.14.

4.4.5 Lens quality criteria

Microlens analysis based on the quantities stated above can be quite complex for evaluation and comparison purposes. In most cases it is extremely useful to have some rules of thumb that allow simple quantification of the lens' performance. In literature two important criteria can be found.

Rayleigh's quarter wavelength rule

This criterion states that a maximum wavefront deviation $\Delta\psi_{max}$ that does not exceed 0.25λ can be tolerated for near diffraction-limited performance. This criterion is based on Rayleigh's findings concerning the wavefront at the exit pupil of a lens suffering from primary spherical aberration: limiting the departure of the wavefront down to $\lambda/4$ with respect to the reference sphere, diminishes the
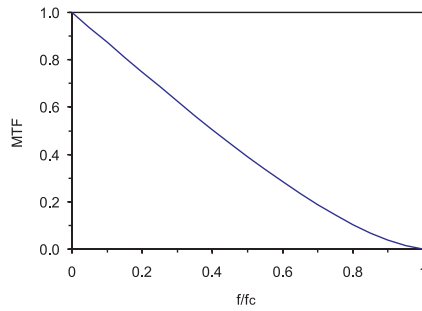
Figure 4.14: MTF of a circular lens.

Gaussian focus intensity by less than 20 %. Obviously, as the peak aberration in a real wavefront is not solely responsible for the true light distribution in the image plane and since the aberration tolerance is very application-dependent, this criterion should be interpreted as a rule of thumb rather than a strict requirement.

Maréchal's criterion

Maréchal formulated a rule that guarantees a minimum diffraction focus intensity (Strehl Ratio), independently of the exact nature of the aberrations in the wavefront. For this purpose he used the relationship (4.11). According to Maréchal, a system is well-corrected if the strehl Ratio is not smaller than 0.8. Using (4.11) this criterion corresponds to a root-mean-square wavefront deviation $\sigma_{\Delta\psi}$ that does not exceed $\lambda/14$.

4.5 Characterization and measurement techniques

Several techniques are described below for measuring lens properties. The instrumentation can be classified according to the quantities they measure: one class is suitable for measuring physical surfaces, more in particular the lens-air interface. The other type is capable of measuring aberrations in wavefronts transmitted through the lens.

4.5.1 Surface measurement

The instruments described in this paragraph can be used for measuring the lens surface, either partly or the entire lens. From these measurements we can readily derive the radius of curvature, the lens height, diameter and surface roughness.

White light interference profilometer

This profilometer uses two-beam interference to measure a local surface height (figure 4.15a). A white light source is collimated and illuminates an aperture which in

157

turn is imaged onto a sample surface through a microscope objective. Part of the beam that leaves the objective in the direction of the measured surface is reflected on the beam splitter and is used as reference beam. The beam reflected from the surface interferes with the reference and a fringe pattern is observed at the CCD camera. This fringe pattern will show maximum contrast when the microscope is focused on the surface height for which the reflected beam shows no optical path difference (OPD) with respect to the reference beam (4.15b). Through calibration this zero OPD is achieved for the surface height which is imaged sharply through the microscope on the CCD. As the OPD increases, the intensity contrast of the fringes will gradually decrease and eventually disappear as soon as the OPD becomes larger than the coherence length of the source light. This coherence length is determined by a spectral filter which is inserted in the beam path. It typically features a spectral bandwidth of 40 nm centered around 650 nm, corresponding to a coherence length of about 8 μm.

Measurement of the surface profile is accomplished by a piezo-driven translation of the objective and reference surface in the vertical direction while the CCD captures images at well-determined intervals (e.g. every 100 nm translation). Data manipulation produces the fringe intensity envelope and the location of maximum contrast. This procedure is performed for a matrix of sample points on the surface simultaneously.

As the interferometer is only capable of measuring part of the sample surface at the same time[14], fast image capture and data processing are essential for making this set-up a successful surface characterization tool. Contrary to phase-shifting interferometry, this profilometer does not suffer from the limitation on the maximum height difference between neighboring samples points ($\lambda/4$ limit).

In our experiments we used a Wyko NT2000, installed at the Department of Applied Physics and Photonics of the Vrije Universiteit Brussel. The profilometer is capable of measuring areas up to $1.9{\times}2.5$ mm^2 depending on the lateral sampling. The vertical resolution is in the nm range. In figure 4.16 the measurement results are displayed for a cone-shaped surface. Inside the "intensity" window, a typical fringe pattern can be observed.

As the sample is measured optically through an objective with a limited NA, the measurable range of surface inclinations is limited. The maximum allowable tilt for a surface —located on the optical axis of the profilometer— in order to reflect light within the NA of the objective, is estimated by

$$\alpha_{max} = \frac{asin(NA)}{2}$$

Confocal microscopy

Another profilometer is based on the principle of confocal microscopy, explained in figure 4.17a. A point source is imaged through an objective on a sample. The

---

[14]Contrary to phase-shift interferometry where 3 or more fringe patterns are sufficient for measuring a full sample area, this profilometer only measures the sample area where the fringes are visible at that time. In addition, the measured surface height is independent of the reflection phase at the surface.
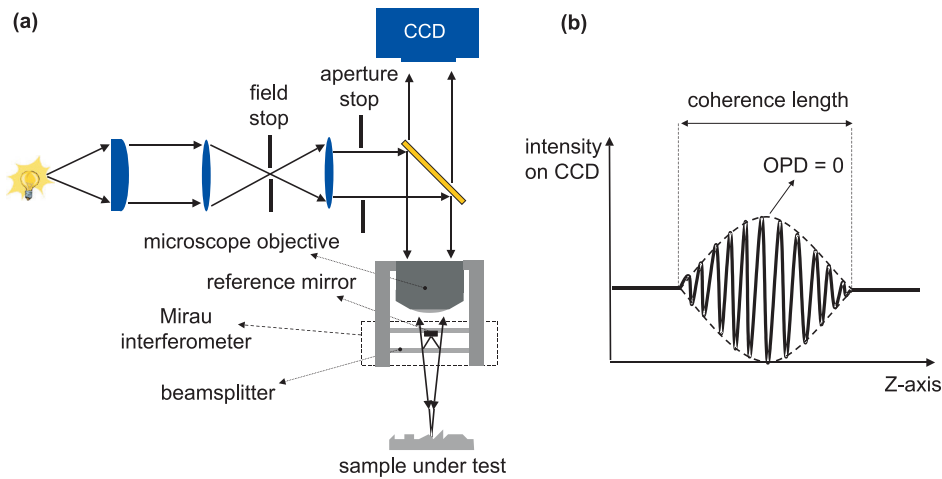
Figure 4.15: Wyko optical profilometer set-up (a). Fringe intensity envelope during scanning (b).
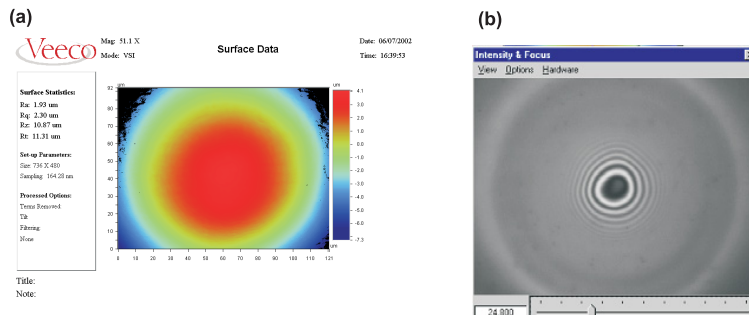

Figure 4.16: Typical representation of the measured surface (a). Captured image of the fringe pattern when microscope is focused on the central part of the surface (b).
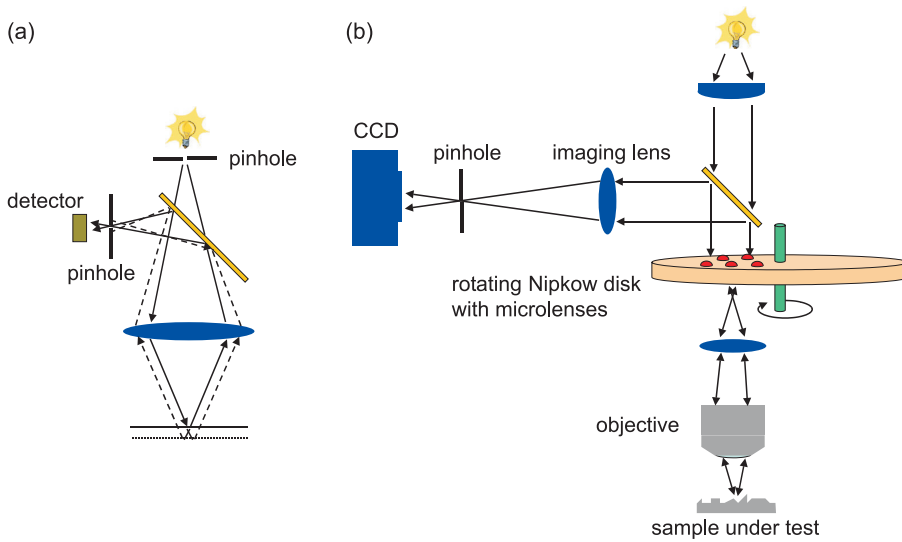
Figure 4.17: Principle of focal microscopy (a). Confocal microscopy set-up for surface measurement (b).

reflected light is focused back onto a point-detector. The measured power will show a maximum when the illuminated surface is at the image plane of the point source. Any shift in the vertical direction will lead to a decrease in that detector signal as the light of the point source is distributed over an area centered around the pinhole. A practical implementation for profilometry is given in figure 4.17b. The detector is replaced by a CCD and the point sources are realized by microlenses mounted on a disk. Each CCD pixel corresponds to a very small area[15] on the sample. To prevent cross-talk between the different point-sources (a microlens can capture reflected ligh that was emitted by a neighboring lens), the lens spacing is taken quite large. By well-considered positioning of those lenses, it is possible to scan the full sample area when the disk has rotated 360°. Again, the signal on a CCD pixel will peak if the corresponding sample height is at the image plane of the corresponding point source.

Some surface profiles of ablated structures have been obtained using this technique. The confocal microscopy was put at our disposal by Thermo Scientific at Breda, the Netherlands.

SEM

Scanning Electron Microscopy offers the opportunity to visually examine a sample surface with nanometer accuracy. Instead of the optical microscopes explained

---

[15]This area is determined by the magnification of the microscope objective: S_{ccd}/M^2 with M the magnification and S_{ccd} the area of a CCD pixel.

above, this device uses a focused electron beam which continuously scans the sample. The interactions between beam and atoms of the specimen produce a lot of information. For topographic purposes, the observation of secondary electron generation is the most interesting. This process only occurs in a very thin layer below the surface and the number of secondary electrons strongly depends on the incident angle of the beam. Although the high-resolution images give a good impression of the surface quality, SEM is not suitable for surface profilometry.

4.5.2 Wavefront measurement

The interferometer described in this paragraph can be used for evaluating the optical performance of lenses in terms of wavefront aberrations. As mentioned in 4.4.5, knowledge of these wavefront anomalies gives an indication of the expected imaging qualities by comparing them to the Maréchal and Rayleigh criterion. In addition, the Strehl ratio of the lens can be estimated by calculating the standard deviation of the aberrations. This ratio is of overriding importance in situations where the lens needs to collect light and direct it into a small area.

Mach-Zehnder interferometer

The Mach-Zehnder interferometer set-up is illustrated in figure 4.18. The polarized beam of a HeNe laser ($\lambda = 633$ nm) is split in two linear polarized plane waves of which one will act as a reference beam and the other will be transmitted through the microlens under test. Polarization maintaining fibers are used to transport the beams towards the microscope. The illumination objective is a high NA objective that is able to transform the incoming plane wave into a nearly perfect spherical wavefront. In turn, the microlens converts this wavefront back into a wave which shows resemblance to a plane wave.
Due to lens imperfections the transmitted wavefront will deviate from a perfect plane wave. By observing the interference pattern of the aberrated and reference wave on the CCD, a quantitive measurement of the microlens aberrations can be accomplished[16]. Note that the aberrations introduced by the high-quality illuminiation objective are usually negligible compared to the microlens.

After measurement the calculated phase distribution can be used for determining the PSF and MTF. In addition, the instrument's software offers the opportunity to approximate the measured aberrations by a Zernike polynomal expansion (up to 10th order).
The interferometer can also be used for measuring the paraxial focal length of the lens by plane wave illumination of the microlens. This is accomplished by removing the illumination objective from the beam path and thus illuminating the microlens with a plane wave. Making abstraction of lens aberrations, the wavefront at the exit pupil of the lens can be written as

$$\psi(x,y) = Ce^{jk\frac{x^2+y^2}{2FL}}$$

---

[16]The phase of the aberrated wave can be fully determined by 5 measurements, each with another reference wave phase.
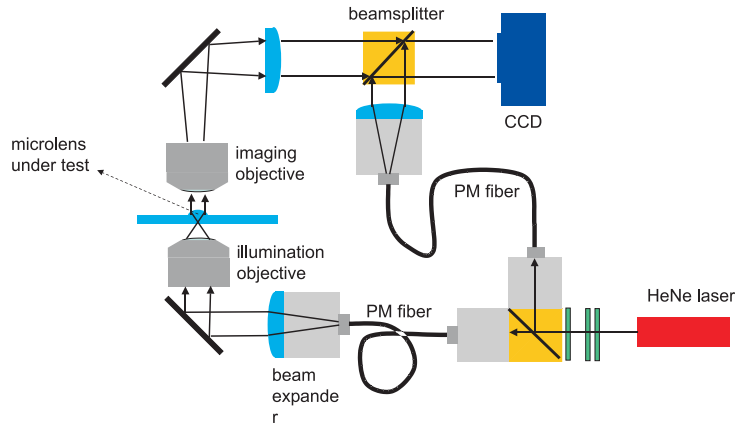
Figure 4.18: Mach-Zehnder interferometer for wavefront aberration measurement.

with C a complex constant. For a lens with a diameter D, the maximum phase deviation between the center and the rim of the lens at the exit pupil is

$$\Delta = \frac{k(D/2)^2}{2FL}$$

The observed fringe pattern at the CCD will show multiple concentric rings within the area of the lens. As one fringe period equals a phase difference of 2π, the total phase deviation between the center and the rim of the lens can also be written as

$$\Delta = n2\pi$$

with n the number of fringes. From both expressions FL can be calculated via

$$\frac{1}{FL} = \frac{2n\lambda}{(D/2)^2}$$

The Mach-Zehnder interferometer that we used for characterizing our lenses is installed at the Department of Applied Physics and Photonics of the Vrije Universiteit Brussel.

4.6 Laser ablation of rotationally symmetric microlenses

4.6.1 Process overview

The process discussed in this section is a newly developed microlens fabrication technique called scanning contour ablation. A circular excimer laser beam is used

a. scanning contour ablation

excimer beam

polymer sample

translation stage

b. lens surface smoothing

(large) excimer beam

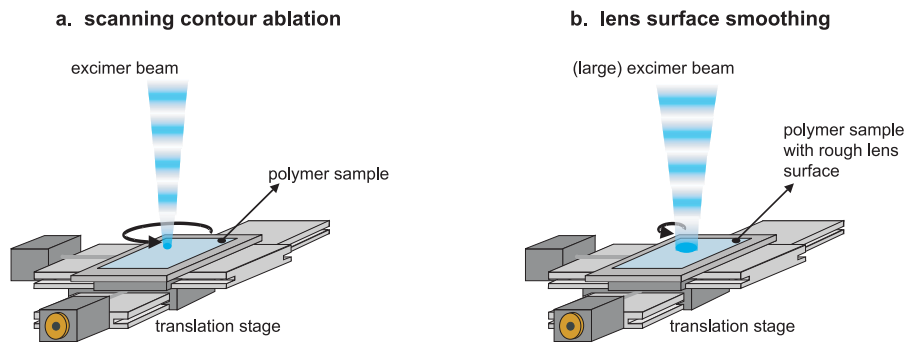polymer sample
with rough lens
surface

translation stage

Figure 4.19: Lens fabrication based on scanning contour ablation: process steps.

for firing pulses on a polymer substrate at a constant pulse rate and with a pulse fluence high enough to induce ablation. During that pulsed laser operation the stage makes successive circular, concentric moves with well-chosen diameters and at well-chosen contour velocities. The result is a pattern of circular chains of overlapping pulse craters. Depending on the contour diameter and velocities, the amount of removed material changes from the center of the contours towards the edge. In case of a cw laser, the structure would be highly smooth and fully rotationally-symmetric. Due to the discrete character of pulsed operation, the surface structure will deviate from the ideal shape and will need additional processing for obtaining a smooth structure. This is achieved by using a large beam covering the full lens area and by drilling the full structure deeper into the material. As ablation is accompanied by a limited amount of thermal heating, this process improves the surface quality to a large extent. It is shown that these improvements can even lead to a surface finish of optical quality[17]. Successful machining of lenses requires

- A high-accuracy sample stage which is able to make smooth contour moves.

- An excimer laser with a stable output power and operating at a constant pulse repetition rate.

- A circular beam aperture without burring for contour ablation and a large aperture for surface smoothing. For microlenses with a diameter of 200 μm, typical aperture dimensions are 100 μm for scanning contour ablation and some 250 μm or larger for the smoothing process.

- A projection system that images the laser illuminated aperture onto the polymer surface.

---

[17]Optical quality is obtained when scattering losses become negligible. As scattering is proportional to$(\delta/\lambda)^2$ with δ the rms surface roughness, a surface can already be considered of optical quality when $\delta < \lambda/10$.
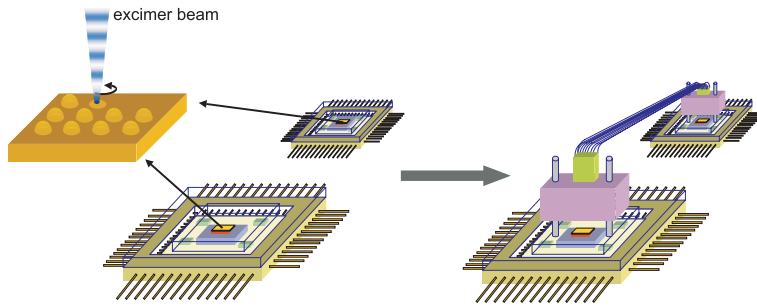
Figure 4.20: Microlens insertion on a heterogeneous opto-electronic assembly.

4.6.2 Motivation for microlens fabrication with contour ablation

The contour ablation technique makes it possible to fabricate microlenses in a quick and flexible way. Compared to the techniques described in 4.2.1, it offers some unequaled advantages as listed below.

As the technique is based on laser ablation, it shares key benefits as direct-write and contactless surface sculpting capability. There are no stringent process requirements like high temperature operation, high vacuum or clean-room environment, etc. The technique can also be applied to several polymer materials.

An important consequence is the opportunity to use laser ablation for integrating microoptical functionality in a late phase of heteregeneous assembly. This is illustrated in figure 4.20, where two chips communicate optically instead of electronically to ensure a sufficiently large bandwidth. The optical link consists of several channels in parallel. In turn, each channel features an optical pathway consisting of air gaps between the opto-electronic chip (receiver and transmitter) and connector, and a length of plastic optical fiber (POF). The gaps ensure the integrity of the opto-electronics and a minimum value of several tens of μm is needed for that purpose. Depending on the air gap and the size and NA of respectively the emitters/receivers and POF, only a part of the optical power can be coupled successfully in and out of the corresponding fiber. The resulting optical power and throughput penalty can be reduced by insertion of microlenses on top of the emitters and receivers. These optics with diameters up to the fiber pitch in the connector, will serve as light guiding and collecting structures in the air gaps.

One obvious approach is the alignment of a suitable lens array with the receiver array and the subsequent fixation. This manual operation can be quite time-consuming, expensive and not without risk for the opto-electronic components. A more attractive method is based on the contactless fabrication of the lenses in a polymer layer which has been spin-coated on the chip surface during the semiconductor processing. Laser ablation is one of the rare techniques which make this approach feasible. In addition, visual alignment verification is possible through the laser beam optics with on-axis camera systems.

Another advantage concerns the exact lens profile: the contour ablation technique

is not limited to spherical lens profiles. Although it is common knowledge that a spherical geometry is generally not ideal for stigmatic imaging, the expense for fabricating aspherics has inhibited their use, at least in glass materials. With the introduction of plastic replication techniques, the manufacturing cost has become independent of the exact surface profile to be reproduced. To take advantage of this flexibility, a prototyping technique is required that is capable of making these surfaces. Contrary to other technologies which commonly rely on swelling or thermal reflow, contour ablation allows the fabrication of microlenses of arbitrary shape. In addition, an extension of the contour technique to non-rotationally symmetric microlenses can be found in 4.7.

Some of the prototyping techniques allow parallel processing, meaning that lens arrays can be fabricated at the same time. This feature is of importance for microlens applications where (large) arrays of optical beams are involved, in particular optical interconnects. The contour ablation technique as described below uses a single circular aperture for writing a single lens. With a mask pattern consisting of an array of identical circular apertures, it is possible to ablate an entire array of microlenses at the same time. The maximum number of lenses that can be fabricated simultaneously is limited by the excimer beam size and the field of the beam projection optics.

4.6.3 Theoretical analysis of circular contour ablation

In essence the proposed technique is based on ablating several concentric circular trenches with scanning ablation[18]. Each trench is realized by moving the sample along a circular path while the excimer laser is firing pulses at a constant pulse frequency and fluence (figure 4.21). Whenever a trench is finished, the laser stops and the stage moves to a new starting position for ablating the next trench. During the contouring of the stage, every point on the sample makes a circular movement with the same diameter but with a different center. The laser beam remains on a fixed position during the process.
For a given beam diameter, each trench is determined by its depth which is proportional to the number of overlapping pulses, and contour diameter that fixes the exact profile of the trench. In order to derive an analytic expression for the trench depth, we will first consider cw operation of the laser.

Trench profile calculation for a CW laser

We assume that the laser fluence is homogeneous over the entire beam area. Consequently the ablated crater has a uniform depth, proportional to the exposure time. This means that we neglect the presence of depth variations close to the edge of the crater due to diffraction effects that are typically limited to a few μm from the edges.
Given the diameter of the beam (ϕ) and of the contour (D), the contour velocity

---

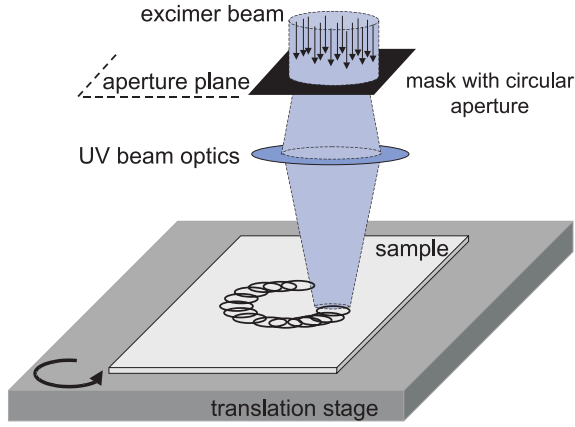[18]Scanning implies the ablation of a series of holes in the sample which is moved in between the pulses.

Figure 4.21: Principle of scanning contour ablation.

of the stage (v) and the ablation depth per unit of time (k), the profile of a single trench can be written as

$$y(r) = ap(r)$$

in which

$$
\begin{aligned}
a &= \frac{\pi D k}{v} \\
p(r) &= \begin{cases} \frac{1}{\pi} acos \left(\frac{D^2+4r^2-\phi^2}{4rD} \right) & \text{if} & \frac{D-\phi}{2} < r < \frac{D+\phi}{2} \\ 1 & \text{if} & r < \frac{\phi-D}{2} \\ 0 & \text{if} & r < \frac{D-\phi}{2}, r > \frac{D+\phi}{2} \end{cases}
\end{aligned}
\qquad (4.13)
$$

In these expressions r is the radial coordinate with the origin being the center of the trench (c_0 in figure 4.22a) and p can be interpreted as the relative exposure time of a point with coordinate r. 'Relative' means here with respect to the full contour scan time. In the area scanned by the beam during one contour, the material has either been ablated continuously —these locations were always within the beam during the full contour scan— or only during a limited amount of time. In the first case, $p(r)$ is 1.0 and in the second case it is assigned a value which is proportional to the time required for the beam to pass over the spot. This value can be calculated by determining the arc length of a circle with radius r within the beam area as illustrated in figure 4.22a for $r = r_1$. The factor a represents the full ablation depth for locations with $p = 1.0$, and is proportional to the full contour scan time.

For a typical beam diameter of 100 μm, an ablation rate of 5.0 μm/s and a contour velocity of 10 μm/s, the resulting profiles for D values of 50, 100 and 200 μm (respectively $D < \phi$, $D = \phi$ and $D > \phi$) are illustrated in figure 4.22b. From these curves it can be seen that $y(0)$ features a different limit value for $D \to \phi$ from below or from above. For a contour diameter smaller than the beam diameter, a flat central part in the trench can be observed. This property will be of particular interest for smoothing purposes as described in the following sections.
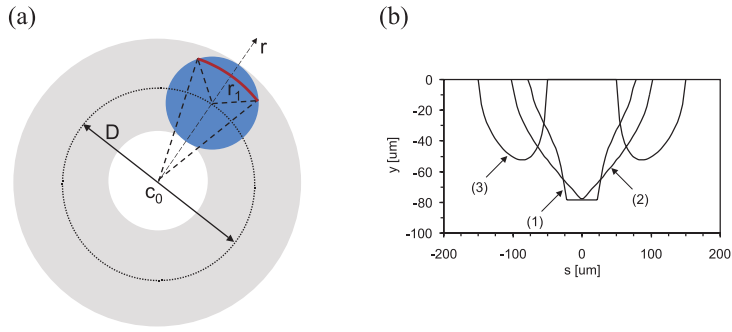
Figure 4.22: Trench fabrication with scanning contour ablation. (a) Shows the relevant parameters for calculating the trench profile. (b) Gives the trench cross-section for $\phi = 100 \; \mu m$, $k = 5.0 \; \mu m/s$, $v = 10 \; \mu m/s$ and $D = 50 \; \mu m$ (1), $100 \; \mu m$ (2) and $200 \; \mu m$ (3).

Pulsed laser operation

In case a pulsed laser is employed, the ablation depth per unit of time should be replaced by $k = df$ in which d is the ablation depth per pulse and f is the pulse repetition rate. As a result of the discrete character of the pulsed laser ablation process, the exact trench pattern will deviate from the calculated profile obtained with a cw laser.

A quantitative analysis is performed on the three basic trench shapes: trenches were ablated using the contour scanning technique under the conditions in table 4.4.

Although the experiment was solely performed using the KrF excimer laser, similar results are to be expected for ArF irradiation. A possible solution to improve the surface quality and thus mask the discrete nature of the ablation process, is drilling the structure deeper into the material by ablation with a large aperture covering the full trench area. Within this ablated area surface ripples with high spatial frequency content ablate faster than flat surface parts and thus the entire area becomes smoother. To verify this statement experimentally, trench shape profiles were measured that had either undergone contour ablation only, contour ablation followed by drilling 5 μm deeper ('1× smoothing') and contour ablation followed by drilling 10 μm deeper ('2× smoothing') into the substrate. In figure 4.23 trench profiles measured with a confocal microscope are compared with the theoretical curves for values of D equaling 40, 100 and 200 μm. It can be seen that the contour-ablated profiles practically equal the theoretical curves, except for a few irregularities that are probably due to the discrete ablation process (e.g. the indicated area for $D = 200 \; \mu m$). The smoothing process successfully removes these anomalies. Another observation is that smoothing also rounds sharp edges and corners. This effect is the most pronounced in the close-up of the trench with $D = 40 \; \mu m$.

The contour-ablated profile for $D = 100 \; \mu m$ illustrates some of the limitations of

167

contour velocity	20 μm/s
pulse frequency	20 Hz
pulse energy	450 mJ
fluence	100 mJ/cm^2
aperture	100 μm
material	polycarbonate
ambient medium	air

Table 4.4: Ablation conditions for fabrication of the trenches in figure 4.23.

the laser ablation technique. The theoretical curve can only be achieved if D and ρ both equal *exactly* 100 μm. In practice this can only be reached within ± 1 μm due to the stage resolution. As a result the cross-section of the ablated part will show either a dip or a bump in the center. By drilling the structure sufficiently deeper, these bumps/dips can also be smoothened.

Optimization of the contour set

We now assume that when successive concentric trenches are ablated on top of each other with a pulsed laser, the resulting surface relief can be written as the sum of the individual trench profiles. A plain verification of this statement is given in figure 4.24: a structure consisting of two overlapping trenches with different contour diameters is ablated with an excimer laser. The cross-section is compared to the expected profile from adding up the individual trenches. Very good agreement between both theoretical and experimental values can be observed except for the steep walls around the central part. At those edges, a slight deviation due to rounding of the sharp corners by the ablation process −during the second contour with $D = 40$ μm− can be seen. A full 3D view of these structures is given in figure 4.25. The validity of the CW approach for pulsed operation will be further discussed in a next paragraph on lens surface roughness.

 A next assumption is that superposition of well-chosen concentric trenches with profiles as described in the previous paragraph, can result in an arbitrary rotationally symmetric surface shape, for example a microlens. Therefore, optimization of the contour diameters and velocities is necessary. These diameters determine the overlap between the neighboring trenches and can be chosen to achieve a smooth surface in accordance with the intended microlens shape (mathematically described by $Y(r)$), while the scan velocities determine the overlap of the successive pulses in a trench and consequently also its depth. This optimum set of contours minimizes

$$\varepsilon = \int_0^{\Phi/2} \left| Y(r) - \sum y_i(r) \right|^n 2\pi r dr \qquad (4.14)$$

where y_i is the trench profile for the i-th trench with diameter D_i and velocity v_i and n is an integer ($n = 1, 2, \ldots$). The integral is evaluated over the one-dimensional lens cross-section (Φ is the lens diameter). In some applications the central part of the lens can be more important than the rim (e.g. for Gaussian
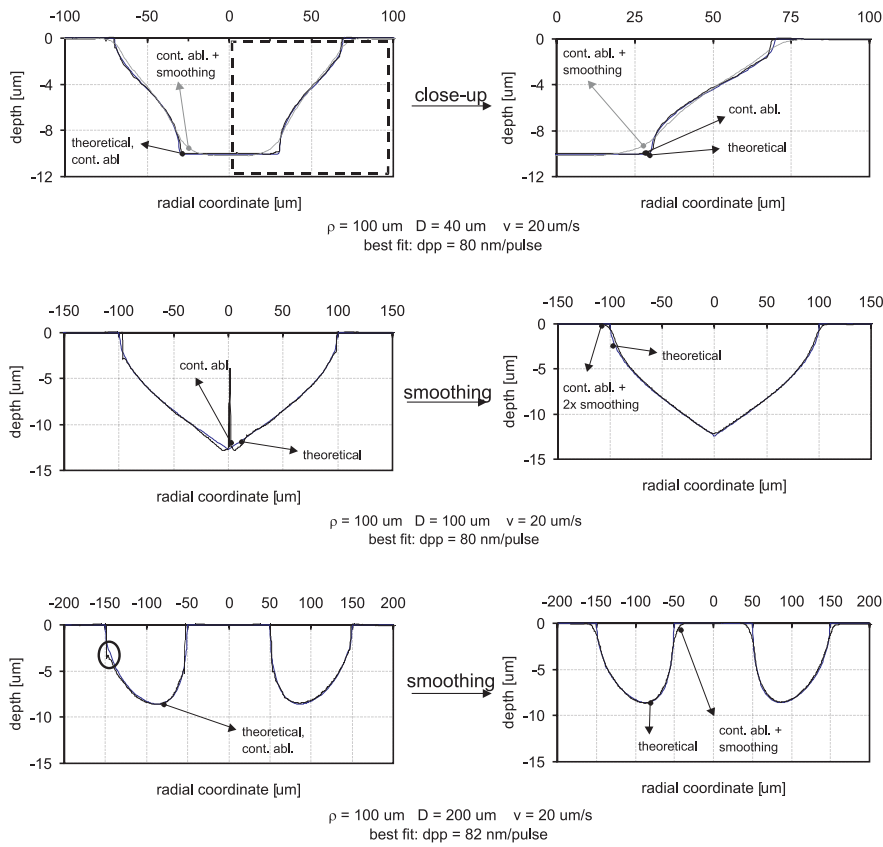
168

Figure 4.23: Comparison between theoretical and measured cross-section of ablated trenches for different values of D (exact ablation conditions are given in table 4.4).
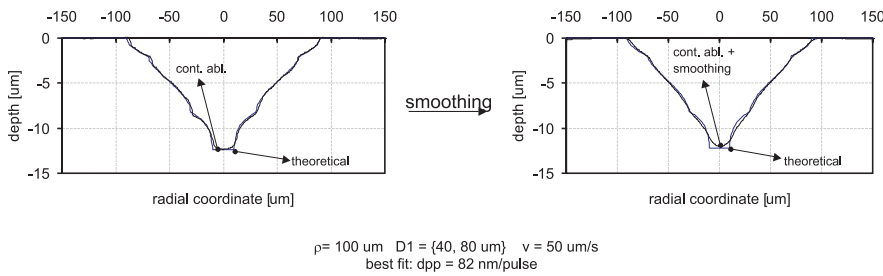

Figure 4.24: Comparison between the calculated and measured cross-section of a structure consisting of two ablated trenches with $D = 40$ and 80 μm. Ablation conditions are as indicated in table 4.4 except for the contour velocity which has been chosen at 50 μm/s.
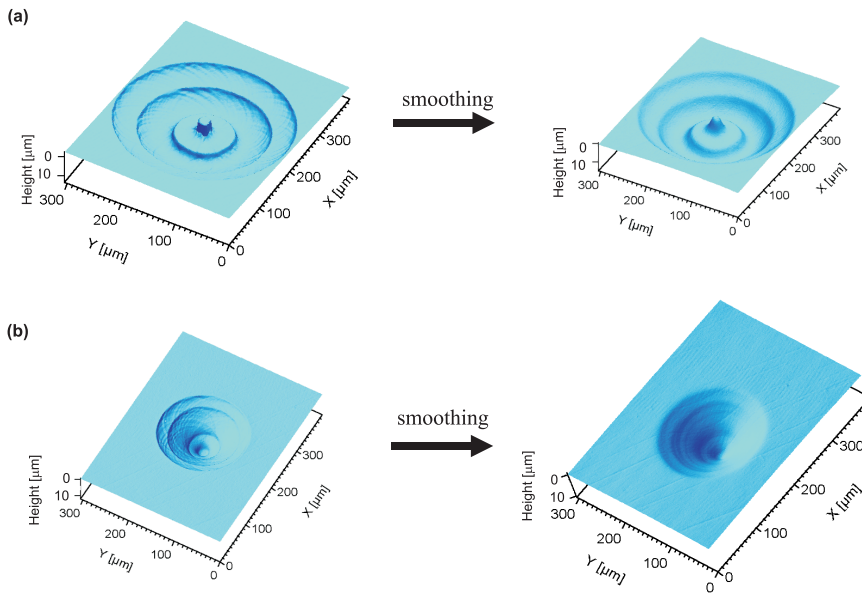
169

Figure 4.25: 3D image of ablated structures consisting of two trenches, respectively $D = 60$ and 100 μm (a) and $D = 40$ and 80 μm (b).

beams). In this case advantage can be taken of introducing weighing factors in the integral.

Equation (4.14) will generally feature many solutions. For example a single trench from one solution can always be replaced by two trenches with the same diameter but ablated at twice the contour velocity.

A range of valid diameters and velocities is determined as follows: contour diameters larger than $(\Phi + \phi)/2$ are ignored since they do not overlap any more with the lens area and diameter smaller than D_{min} are disregarded as well. This minimum has been introduced to avoid that the sample would be forced to make small contours at elevated speeds, which could cause the stage to stall. For the experimental part we chose $D_{min} = (2/5)\phi$ or 40 μm for a 100 μm beam size. Larger D_{min} values produced inferior approximations in the central lens area with our optimization algorithm.

Concerning the contour velocities: a minimum speed was applied to ensure that a reasonable number of contours are involved. At low speeds, deep and steep trenches are etched and large amounts of polymer material are removed. Intuitively it can be expected that getting a smooth transition with neighboring, overlapping trenches can be difficult since the ablation process acts differently on sharp edges than on flat surfaces. In addition, part of the ablated material is dropped back onto the nearby polymer surface (debris), potentially blocking future pulses of ablating the covered surface. This effect increases with the amount of material taken away per trench. For a typical beam diameter of 100 μm and ablation rates up to 0.1 μm/pulse, a
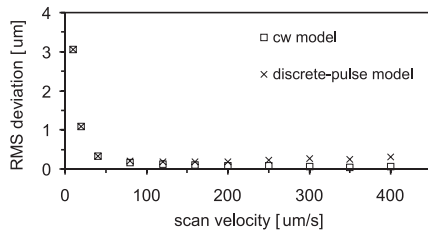
Figure 4.26: Calculated RMS deviation of the approximating surface according to the cw model used in the optimization algorithm and according to the discrete-pulse approach for several maximum scan velocities. Calculations are valid for a 200 μm lens with $R = 250$ μm and an on-target beam size of 100 μm.

minimum scan velocity of 40 μm/s proved to give satisfactory results.

The choice for the maximum scanning speed value should be based on the following considerations: if the trench profiles can be accurately described by (4.13), higher values allow better approximation of the desired profile (lower ε) since the minimum trench depth is lower. In the cw approach the effect of this parameter can be determined by searching for optimum contour sets with different maximum scan velocities and calculate the root-mean-square (rms) deviation between the computed approximation and the desired lens profile. This is illustrated in figure 4.26 for a particular lens shape with radius of curvature $R = 250$ μm and lens diameter $\Phi = 200$ μm. The deviation between the ideal spherical lens shape and the cw approximation decreases substantially as higher scan speeds are allowed. Other lenses will provide analogous results.

A second consideration takes the discrete character of pulsed laser ablation into account: as the scan velocity is increased (while other laser parameters remain constant), fewer pulses will be fired onto the substrate in a single contour movement and the ablated trench pattern will show substantial deviation from the ideal profile as in figure 4.22. The effect of discrete pulse operation on the resulting lens shape can be calculated numerically, based on the geometry of the ablated cavity due to a single-pulse laser shot. The cavity was modeled as a perfectly circular hole with diameter ϕ, vertical side walls and a homogeneous depth d. The positions of the ablated pits were calculated based on the contour diameter, contour velocity and pulse frequency. In figure 4.26 the results of these calculations are shown for the same lens as mentioned above. Yet this time, the true trench pattern was taken into account in order to compute the ablated surface. We will refer to this approach as the 'discrete-pulse model' in the figure. We clearly observe that the approximation tends to worsen when contour speeds above 150 μm/s are present, contrary to what the cw model predicts. Although a simple model for the single-pulse cavity was used, this behavior was qualitatively observed in our experiments. The main result from the discussion above is that beyond a certain maximum speed, further increasing the contour velocities to obtain a more accurate approximation does not make sense any more. Strictly speaking, the optimum contour speed limit is only valid for the particular lens and for every other lens the rms calculations should be

171

repeated.

An algorithm based on simulated annealing was developed to minimize expression (4.14). In our implementation we chose $n = 2$ as in this case the algorithm minimizes the rms (root mean square) deviation between the desired lens shape and the calculated approximation. Simulated annealing was preferred since it is capable of finding a global optimum and can be easily implemented. It starts with a given set of contours and calculates ε via (4.14) where the integral was replaced by a discrete sum taken in sample points along the desired cross-section. In a next step a new solution is proposed which corresponds to the former set, but a limited number of randomly selected contours have slightly −and again randomly− changed velocities and/or diameters. A new ε' is calculated for this modified set and compared with the former value. For ε'$<\varepsilon$ the proposed solution is accepted while in the case ε'$>\varepsilon$ acceptance only occurs with a certain probability. This probability decreases with time, eventually terminating the optimization process. Although the user proposes the initial number of contours, the algorithm can freely change this by suggesting velocities and/or diameters outside the valid range. In this case the parameter will be given a value just outside its range so the contour can always be recalled by only a slight adjustment of one of its parameters. It should be noted that the desired lens is not limited to spherical surfaces only for the scanning contour technique. In essence it can be any arbitrary rotationally symmetric form including parabolic, elliptical and linear profiles.

An example of a structure approximated by an optimum set is given in figure 4.27: a conical structure with its top buried 5 μm below the polycarbonate surface. An aperture of 100 μm was used and 19 contours were needed to ablate the full structure. The laser was operated at 20 Hz, taking away a layer of 70 nm per pulse. The time required to ablate the cone was slightly more than 3 minutes. The measured 3D surface and cross-section are obtained with confocal microscopy. Observation of the profile revealed a wall angle of 9.5°, very close to the design value of 10°. A 3D impression of the structure based on the discrete-pulse model is included for comparison.

As $Y(r)$ is approximated by addition of grooves and since the latter satisfy $p^\alpha(\alpha r) = \alpha p(r)$ with $p^\alpha(r)$ the groove profile for a beam size of $\alpha\phi$ and a lens diameter of αD, this scalability is also valid for the final lens shape. For a spherical convex lens shape for example, this means that the optimum set for a radius of curvature R and diameter Φ can also be used for a lens with diameter $\alpha\Phi$ and curvature αR by multiplying all contour diameters by α.

Fabrication tolerances

In the preceeding analysis a number of laser related quantities were assumed to be well-known and well-controllable. In this paragraph we will discuss the influence of some parameters on the resulting lens shape. The latter is based on a contour set obtained by the optimization algorithm, taking a nominal aperture of 100 μm and a nominal etch rate of 70 nm/pulse into account. The shape is then calculated as $\sum y_i(r)$. In this summation taken over all contours, the etch rate and aperture size
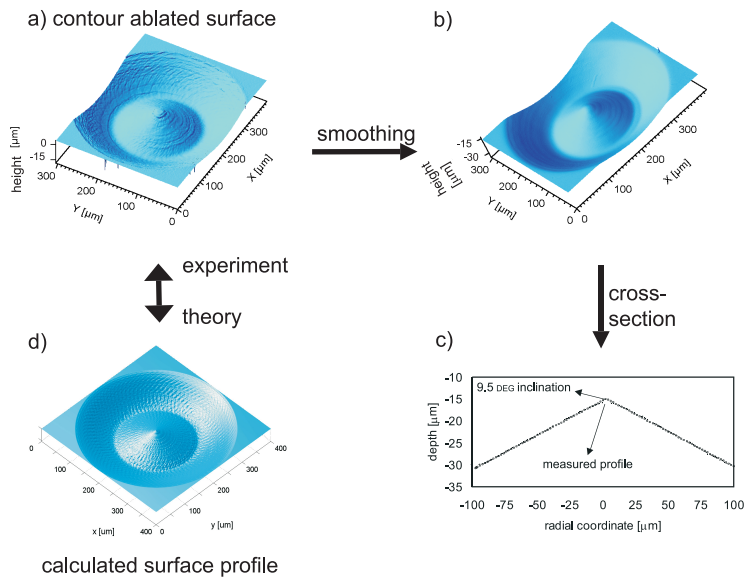
Figure 4.27: Measured (a) and calculated (d) 3D image of a conic structure. The same structure after laser smooting is given in (b) and the measured cross-section in (c). Contour velocity and diameter ranges were 40-150 μm/s and 25-150 μm respectively. After fabrication the cone was driven approximately 11 μm deeper in the surface to obtain optical surface quality.
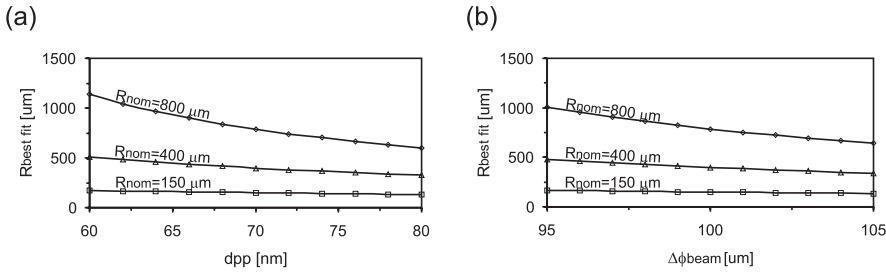
Figure 4.28: Influence of etch rate deviation (a) and beam spot size (b) on ablated lens shape.

have one by one been varied within a given range. The analysis is performed on three spherical lenses (R_{nom} = 150, 400 and 800 μm), all with a diameter of 200 μm. The contour velocity range was limited to values between 50 and 250 μm/s.

- Average pulse fluence (etch rate)

Selecting a laser fluence is usually accomplished by using a variable attenuator consisting of one or more quartz plates through which the beam passes. Rotation of the plates changes the incident angle of the beam and due to Fresnel reflections, the power in the transmitted beam can be controlled. Although there is an unambiguous relationship between incident angle and transmitted power, mechanical restrictions (backlash) and coating detoriation limit the accuracy of beam transmission control. Next to mechanical issues, heating of the mirrors can also influence the reflection magnitude of the HR[19] coating. It is therefore interesting to observe what happens to the theoretical lens profile when the average fluence only approximately equals the nominal value for which the contour calculations were performed. The obtained lens profiles are fitted to spherical shapes to verify the change in radius of curvature and to measure the RMS surface deviation. This gives an idea of the sphericity of the fabricated lens (figure 4.28). From these simulation results we can conclude that a tolerance of $\pm$2 nm (3 %) in etch rate corresponds to a variation in curvature radius of $\simeq$6% for R_{nom} = 800 μm and <3 % for R_{nom} = 150 μm.

- Aperture size

As will be explained in the following sections, the typical fabrication procedure for lenses is based on calculation of the contours for a chosen beam spot diameter. Before laser ablation of the lenses, this beam diameter is set to the desired value by choosing a suitable beam aperture and demagnification. Verification of the beam size is accomplished by visual inspection via the camera on the micromachining
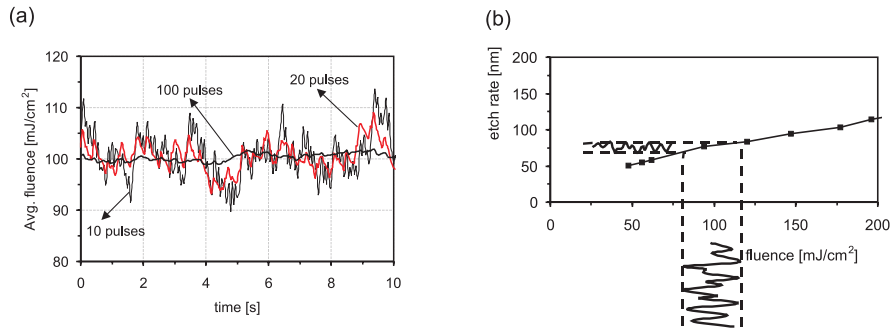
---

[19]High Reflection.

Figure 4.29: Measured pulse fluence variations in the sample plane (a). Etch rate fluctuations due to fluence variations (b).

system (image magnification on the camera is 50× for a beam demagnification of 5×). Obviously, small deviations in beam size (<1-2 μm) are difficult to detect. In figure 4.28b the influence of small aperture size deviations on the lens shapes is depicted. A tolerance of ±1 μm on the spot size corresponds to a variation in radius of curvature < 5% for $R_{nom} = 800$ μm and < 3% for $R_{nom} = 150$ μm.

- Pulse-to-pulse fluence stability

The deviations in pulse energy discussed above are constant or only slowly varying on time scales much larger than the fabrication time for a single lens. Other variations can take place on a much smaller time scale: fluctuations in the pulse energy inherent to the excimer laser operation. A typical measurement of the pulse fluence at the sample plane is displayed in figure 4.29. The curves represent the moving average over the indicated number of pulses. Expressing the subsequent variation in ablation depth implies knowledge of the material's ablative behavior. In the figure we added a graph of the measured ablation depth versus pulse fluence for polycarbonate at 193 nm. For a given nominal pulse fluence, the local slope of the curve will determine the fluctuation of etch depth for any fluence variation. E.g. at a fluence of 100 mJ/cm^2, the nominal ablation rate is 77 nm/pulse. Variations of 5 and 10 % in fluence will cause the etch depth to vary respectively 3 and 6 %.

4.6.4 Experimental fabrication of spherical lenses

Fabrication set-up

The set-up for lens fabrication consists of an ArF laser (Lumonics PulseMaster 848), combined with beam handling equipment for micromachining (Optec Micromaster) as depicted in figure 4.30. The sample is put in a flow chamber mounted on top of the translation stage. The ambient pressure is below 100 mbar inside the chamber. A small flow of helium above the sample removes the ablation fumes so they cannot
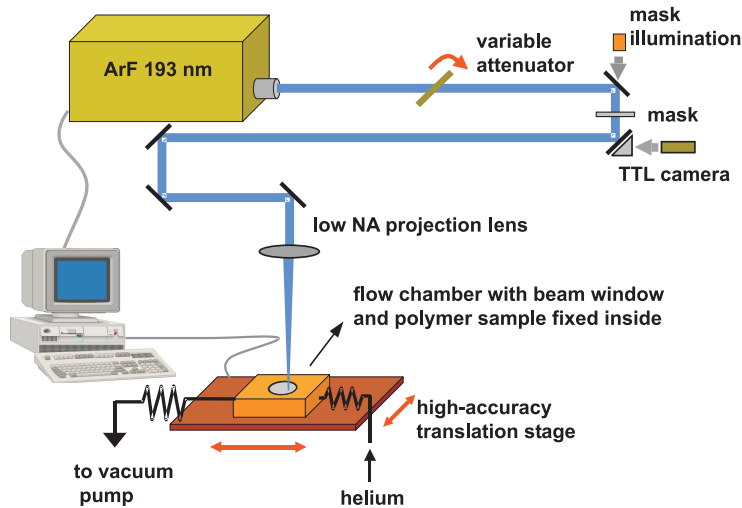
175

Figure 4.30: Excimer laser ablation set-up for microlens fabrication.

contaminate the UV-window, which may lead to damage by laser heating. The low ambient pressure reduces debris deposition around the ablated area considerably [24]. In order to select a homogeneous part of the laser beam, a 2 μm thick film of BCB[20] on a Si substrate is ablated with multiple pulses. A suitable, homogeneous part of the beam is selected when the film is etched away simultaneously over the entire aperture area since the spin-coated film is highly uniform.

A number of optically transparent and high quality commercial polymers can be used for microoptics fabrication: polycarbonate, polyimide (Kapton), PMMA and PET. These polymers were tested on their suitability for micromaching with excimer lasers (figure 4.31). PMMA was found to show incubation effects [25]: ablation only starts after a few pulses at low fluences, meaning that the ablated depth is not unambiguously determined by the pulse count. In addition the machined surface looks rather rough. PET develops a corrugated surface on the cavity bottom [26] which makes it unsuitable for optics. Polyimide (Kapton) produces a lot of debris during ablation and its yellow color makes it less attractive for optical purposes. Polycarbonate does not show any incubation, even at fluences close to the threshold. The ablated surface is very flat and smooth: multi-pulse ablation indicates that the rms surface roughness approaches values below 0.5 % of the ablated depth for static ablation with an ArF laser. Since no homogenizer is available in our set-up, it is to be expected that this value decreases substantially for scanning ablation. Next to its ablative qualities and low water absorption, the optical (little haze, high transmission, spectral passing band 360 to 1600 nm) and thermal properties (mainly a high upper working temperature of 115-130°C) of polycarbon-

---

[20]Benzo-Cyclo Buthene. Dow Chemical's CYCLOTENE is a high-purity resin that has been derived from BCB and has applications in microelectronics.
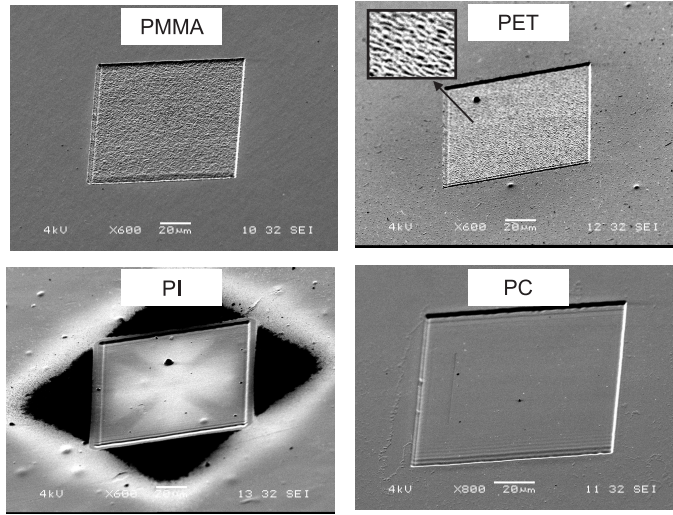
Figure 4.31: Ablation tests on commercial polymers: cavities due to 20 pulses at 47 mJ/cm^2 with an ArF laser.

ate make it a very suitable candidate as substrate material for microoptics. The polycarbonate samples are films with a thickness of 500 μm and were delivered by Goodfellow Inc.

The ArF wavelength was preferred above KrF as the absorption of PC is larger at 193 nm than at 248 nm and higher absorption means better depth control per pulse.

Contour set calculation

Using the technique described in 4.6.3 we calculated contour sets for spherical lenses with different focal lengths. In this case the desired lens shape can be defined as

$$Y(r) = - \left(offset + R - \sqrt{R^2 - r^2} \right) \tag{4.15}$$

in which the minus-sign clearly indicates that lenses will be buried below the sample surface and $offset$ equals the depth of the lens center. For every R the optimization procedure is reiterated 20 times and the best approximation (minimum ε) is selected for fabrication.

Table 4.5 summarizes the main results for 200 μm diameter lenses with R between 125 and 1500 μm, to be fabricated with an aperture of 100 μm. The optimization proceeds in two steps: first the contour velocity is kept fixed at 100 μm/s while the diameters are optimized. In a second phase both parameters are allowed to vary. This time the starting temperature of the simulated annealing procedure is chosen considerably lower than in the first step and the contour set is fine-tuned.

177

R_{target} [μm]	sag [μm]	# contours	deviation[1] [μm]
125	50	37	0.129
150	38	30	0.130
175	31	25	0.131
200	27	22	0.120
250	21	20	0.118
300	17	19	0.096
400	13	15	0.110
600	8	13	0.113
800	6	12	0.105
1000	5	10	0.101
1500	3	9	0.101
[1]Rms values calculated according to the cw model.			

Table 4.5: Calculated lens characteristics for a υ range of 40-150 μm/s, $f = 20$ Hz, $\phi = 100$ μm and $d = 0.07$ μm. The lens diameter and offset are respectively 200 μm and 5 μm.

This approach produced very reasonable results in practice, with typical calculation times of the order of a few minutes per iteration.

Direct-writing of the microlenses

The calculated sets were used for making lenses in polycarbonate with a pulsed ArF excimer laser operating at 193 nm. Although the optimization procedure was based on a range of contour velocities between 40 and 150 μm/s, this range can be scaled according to the true ablation depth per pulse and desired pulse frequency. This is very useful as only one optimization needs to be performed to fabricate a lens at any laser fluence.

During initial experiments every trench was started at the same angular position. The result was a lens with a clear imprint of these starting positions next to each other, mainly due to the lack of an electronic shutter. For that reason we have chosen to start every trench at a random position around the lens center. In addition every contour is scanned two times by the laser at twice the prescribed contour speed. This approach helped to spatially average out the effects of fluence fluctuations due to discontinuous laser operation. For clarity reasons, scanning speed values mentioned in the text will always refer to the single-contour speeds (including the results in figure 4.26).
The successive contours were ablated starting with the largest diameter and gradually decreasing the contour size. This sequence was preferred above the reverse since the final lens surface proved to be smoother as experimentally verified.

The fabrication process is performed in two phases: in a first stage the sample surface is ablated via the scanning contour method based on the optimum contour sets as described in the previous subsection. The result is a surface with a lot of
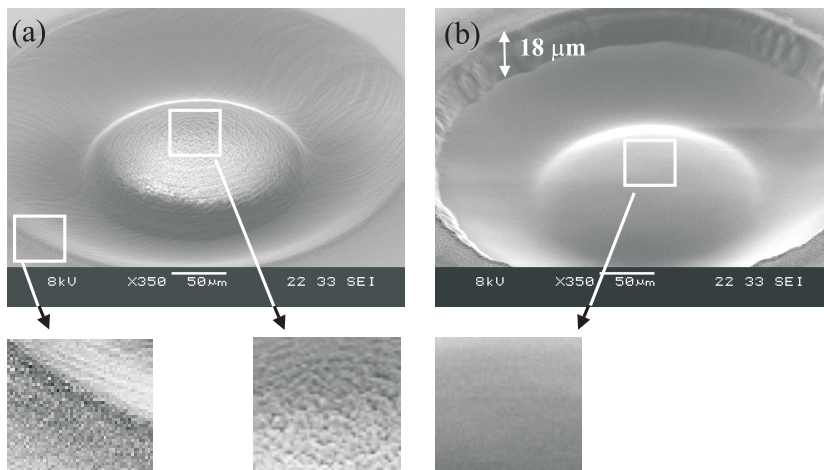
Figure 4.32: Microlens with $R = 800$ μm in polycarbonate: surface after scanning contour ablation (a) and after laser smoothing (b).

debris and with a texture in which the individual pulses can be distinguished. In a second phase optical finish of the lens surface is achieved by ablation of the entire lens area with a large beam aperture. During this process the sample is contouring with a small diameter (typically 20 to 30 μm). In this way a structure similar to case (1) in figure 4.22b is ablated on top of the lens with the flat central part at least equaling the lens area. Three distinct effects are achieved. Firstly, debris is ejected from the surface, forced to leave the lens area and deposited near the ablated zone. Secondly, as spatially rapidly varying features ablate faster than flat areas, the surface gradually becomes smoother. The presence of a thermal component in the photoablation process is believed to be responsible for this. Thirdly, as during the surface smoothing a layer of polycarbonate is physically removed, it is important that the large laser beam is as homogeneous as possible in order not to deform the lens shape. Since our set-up lacks a beam homogenizer, the contouring of the smoothing beam ensures that the laser fluence is spatially averaged over the lens area.

During this process we used a laser fluence of 140 mJ/cm^2, taking away a layer of approximately 18 μm (200 shots). It has been experimentally observed that fewer shots still leave the discrete pulse pattern in the lens surface. Figure 4.32 illustrates the effect of this 'laser cleaning' procedure: a smooth surface buried in the polymer surface and surrounded by steep walls is accomplished after smoothing the surface. Debris is deposited close to the smooth area.

Surface characterization of the lenses

Some lenses have been measured with the Wyko profilometer and one of the results is depicted in figure 4.33. Cross-sections of these surfaces can be fit to a spherical
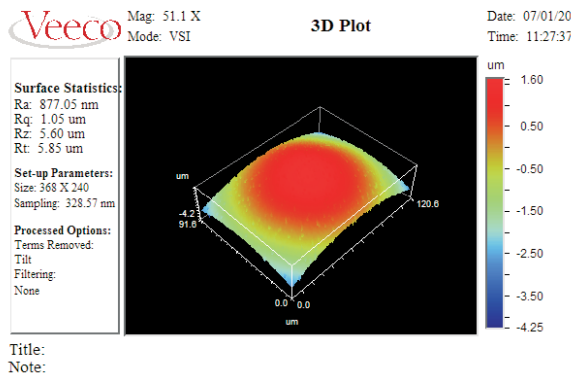
Figure 4.33: Wyko measurement of a contour-ablated lens with $R = 600$ μm.

shape to get an idea of the sphericity of the lenses (figure 4.34). Not all lens surfaces could be measured with the profilometer due to increased surface roughness and the limited numerical aperture of the Wyko objective. For moderate values of R (between 250 and 300 μm), only the central part was visible on the profilometer; for slower lenses the entire lens area has been scanned successfully. As can be seen from the graphs, the spherical fits and the Wyko measurements nearly coincide for all lenses except for the faster lenses. On the average there is only 3 % deviation between the target and measured R. Note that the artefacts observed for these lenses can also be attributed to insufficient caption of the reflected light. Finally the surface roughness was determined within a region of 50×50 μm^2 for two representative series of lenses. The results are given in figure 4.35. For lenses with a focal length > 1 mm (F-number > 5) the rms surface roughness remains well below 40 nm.

Optical characterization of the lenses

Table 4.6 summarizes the main properties of the ablated lenses, including the focal lengths (FL) and fabrication times for the different lenses. The focal lengths of the slow lenses were measured with the interferometer using a fringe count on the lens surface under plane wave illumination. An optical microscope was employed to determine the focal spot position of the fast lenses under illumination with a white collimated beam. Note that FL is defined here as the distance between the lens top and the plane where the whole bundle of rays has the smallest diameter (circle of least confusion). Given these focal lengths, a commercial raytrace tool (ASAP, Breault) was used for back-calculation of the effective radius of curvature (R_{calc}).

Excellent agreement between target and calculated R values can be observed for $R_{target} > 250$ μm, proving the accuracy of the fabrication process within the given range of focal numbers. For the fastest lenses the calculated R can be considerably larger than the target value. A gradual deviation can be observed from
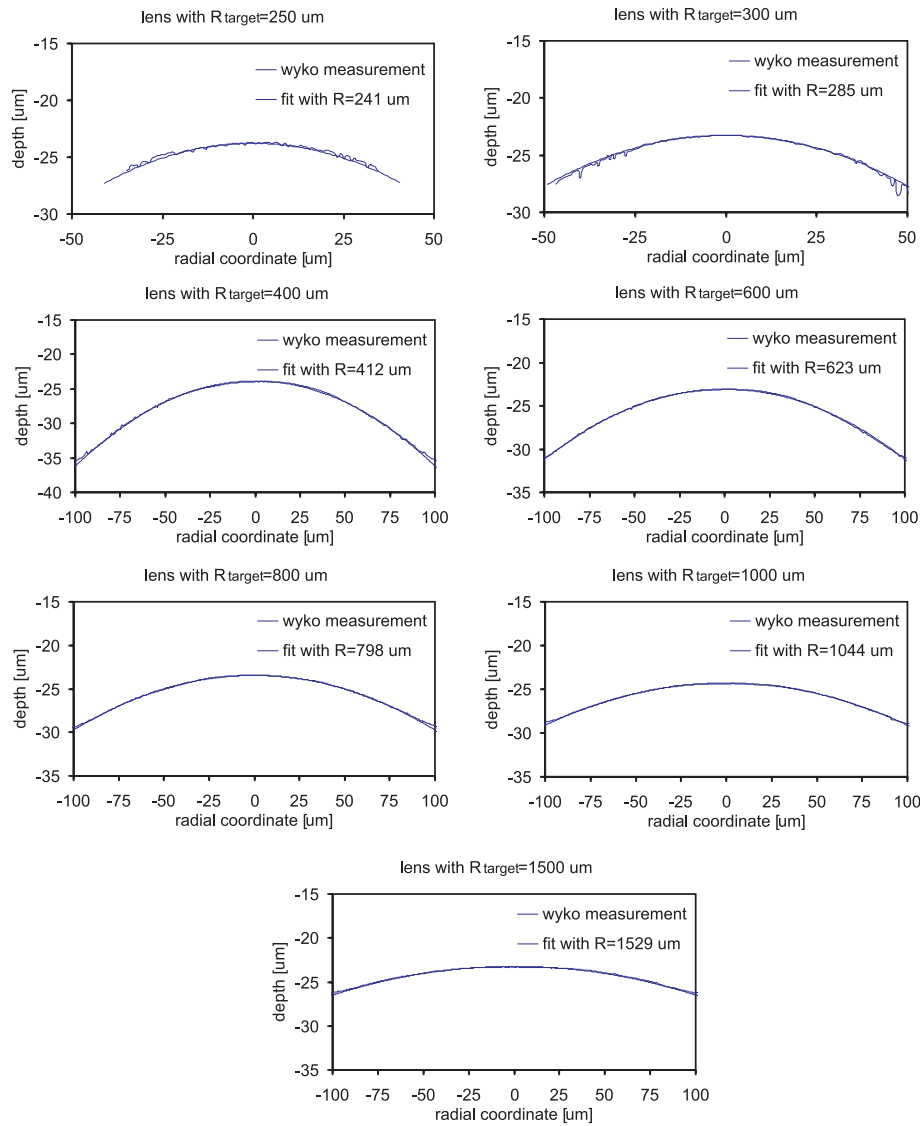
Figure 4.34: Lens profiles with their corresponding spherical fits. Lenses are made at an ablation rate of 59 nm/pulse, 20 Hz pulse repetition rate and a 100 μm beam aperture.
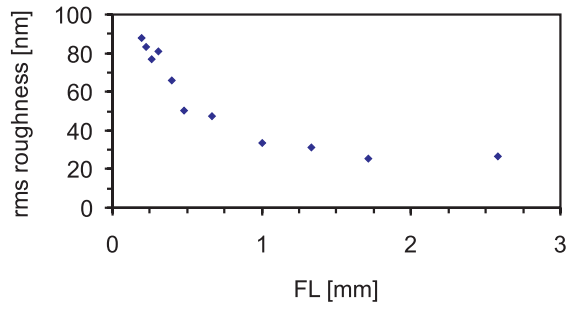
Figure 4.35: Surface roughness of the lenses versus focal length.

| R_{target} [μm]	FL[1] [μm]	R_{calc}	F-number[1]	fab. time[2]
125	151±14	154	0.8	06m 03s
150	189±13	167	1.0	04m 35s
175	244±6	189	1.3	03m 55s
200	309±6	218	1.7	03m 19s
250	399±9	263	2.1	02m 44s
300	480±9	305	2.6	02m 37s
400	666±11	407	3.6	01m 57s
600	1000±14	595	5.4	01m 38s
800	1333±38	786	7.2	01m 24s
1000	1717±53	1007	9.3	01m 13s
1500	2580±55	1507	13.9	00m 59s
[1]Values averaged over lenses made with 4 different laser fluence levels (62, 101, 134 and 177 mJ/cm^2), respectively removing 59, 78, 89 and 103 nm/pulse. [2]Measured for a fluence = 177 mJ/cm^2, $f = 20$ Hz.				

Table 4.6: Microlens fabrication parameters.
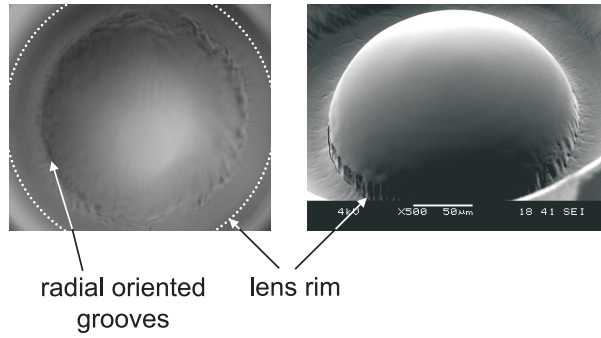
Figure 4.36: Photograph of the lens surface for $R = 125$ μm, showing the radial groove pattern and the rippled rim area (a). SEM image of another ablated lens (200 μm diameter), evidencing more clearly the irregular structure at the lens rim (b).

F/2 to F/0.8, indicating that these high F-numbers might be more problematic for the scanning contour technique. By contrast, contact profilometry of the lens with $R_{target} = 125$ μm revealed a radius of curvature that nearly matched the target shape over practically the entire lens area except at the rim (where rounding was observed). Determining the exact cause of the deviation for R requires more extensive surface profilometry and will be part of future research.

The lenses were visually inspected with an optical microscope. All lenses had a smooth surface except the fastest lens with a $R_{target} = 125$ μm. It featured an irregular structure at the rim and the imprint of small, radially oriented grooves between the center and the rim (figure 4.36). Although the exact nature of both observations is not entirely clear to us, it is expected that the irregularities at the lens rim are caused by ablation at the edge of the beam spot on a steep surface. A SEM image in figure 4.36b of another lens seems to affirm this observation.
The grooves are likely due to beam reflection at the crater walls outside the lens area during laser cleaning. As the surface becomes smoother when the lens is driven deeper into the surface, the reflection will increase substantially. For higher R_{target} the wall angle is not suited any more for deflecting the laser beam towards the lens surface.

In order to characterize the lenses optically we used Mach-Zehnder interferometry for wavefront aberration measurement and SEM for analysis of the surface profile. As the microlens is buried in a polymer film, the measured wavefront aberrations account for the planoconvex lens with the flat polycarbonate interface at one side and the curved microlens surface at the other. The wavefront was evaluated at the exit pupil of the lens for a spherical incident wavefront from the flat interface side. For a 'perfect' lens this wavefront would be a plane wave if the incident wavefront originates from the focal point of the plano-convex lens.

All measurements have been limited to the central 90 % of the lens (diameter of
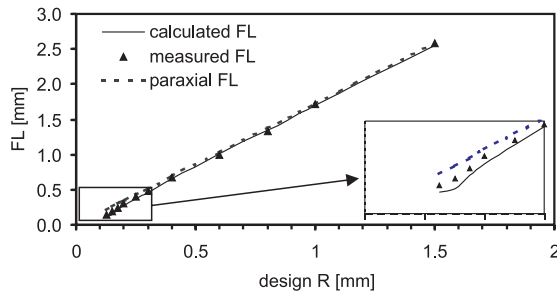
Figure 4.37: Measured, calculated and paraxial focal lengths. Values are averaged over all etch rates.

190 μm) as this allowed a more relaxed alignment of the interferometer with the microlens. After the measurement the wavefront is fitted to a Zernike polynom -10th degree to ensure a sufficient fit— in order to quantify the wavefront aberrations $\Delta\Psi$ with respect to a plane wave. One of the most important values in these calculations, the root-mean-square or rms wavefront aberration, is used throughout this section. As the interferometer uses a helium-neon laser with $\lambda = 632.8$ nm, all aberration values are expressed in this wavelength.

Before summarizing the main results of the MZ interferometric measurements we would like to emphasize that a number of technological issues also influence the lens quality and thus the aberration measurements. These are accuracy of the translation stage (backlash), finite resolution and vibrations due to resonance effects, pulse-to-pulse fluence variations resulting in ditto etch depth spread, timing-jitter between the stage movement and the laser firing which leads to non-equidistant pulses on the sample and non-uniformity of the beam. These issues cause a noticeable spread on the aberration measurement results.

The results of the measurements are summarized below and used for discussion of some important parameters in scanning contour ablation. The experiments have been limited to single aperture and lens diameter values. All lenses had a diameter of 200 μm, a size which is compatible with standard pitches of 250 μm in VCSEL or LED arrays for telecom purposes. The beam aperture was chosen 100 μm, ensuring fast fabrication. Typical measurement results as produced by the MZ interferometer are given in figure 4.38. In one case (FL=1.33 mm, F/#=7), the aberrations are very low and the lens can be considered diffraction-limited according to Maréchal. The lens with the small FL=0.264 mm (F/#=1.39) features much higher aberrations and does not fulfill the Maréchal or Rayleigh criterion anymore. From the wavefront aberrations the MTF can be derived via the point-spread function (Fourier Transform). For both lenses the modulation transfer function has been added in figure 4.38.

Focal length

Figure 4.39 illustrates the measured rms wavefront aberrations and the correspond-

(a)   lens with FL = 0.264 mm (R_{target}=0.175 mm)

unwrapped phase [lambda]

Mean -0.1368
RMS   0.3152
P-V   1.7776
Max   0.4226
Min   -1.3549

0.000

-0.500

-1.000

(b)   lens with FL = 1.330 mm (R_{target}=0.8 mm)

unwrapped phase [lambda]

Mean   0.0000
RMS   0.0528
P-V   0.4129
Max   0.1855
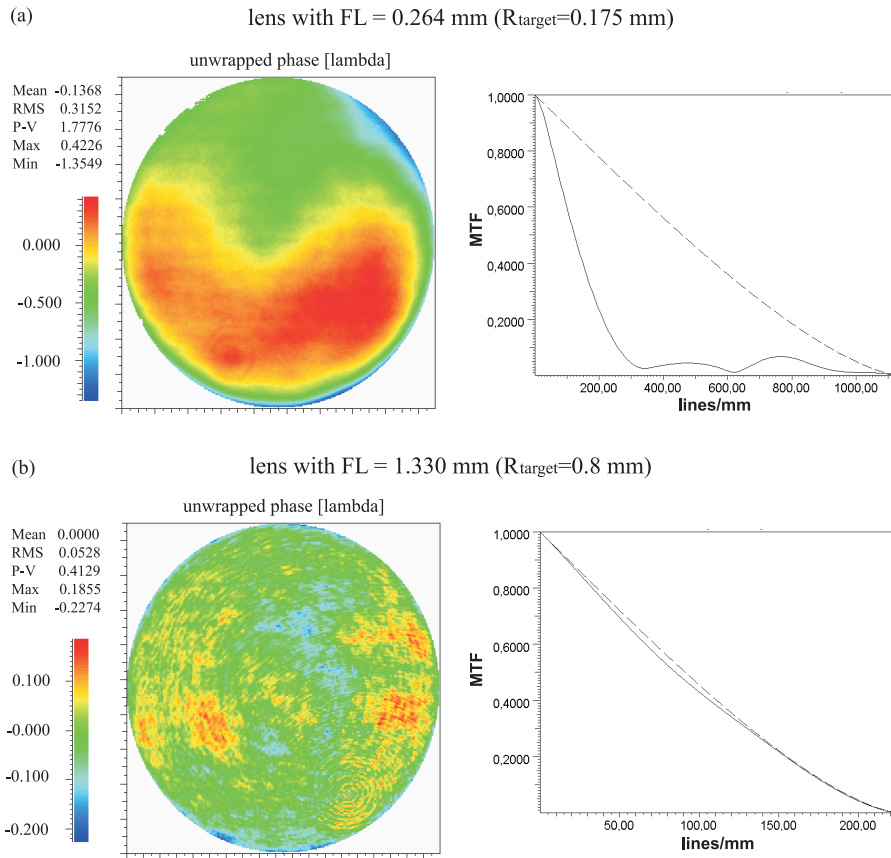Min   -0.2274

0.100

-0.000

-0.100

-0.200

Figure 4.38: Typical phase distribution of a wavefront and corresponding MTF, measured right above the lens for an incident spherical wavefront coming from the focal plane. (a) FL = 0.264 mm and (b) FL = 1.329 mm. Diffraction-limited performance according to the Maréchal criterion is obtained for rms wavefront aberration $\sigma_{\Delta\psi} < 0.07\lambda$.
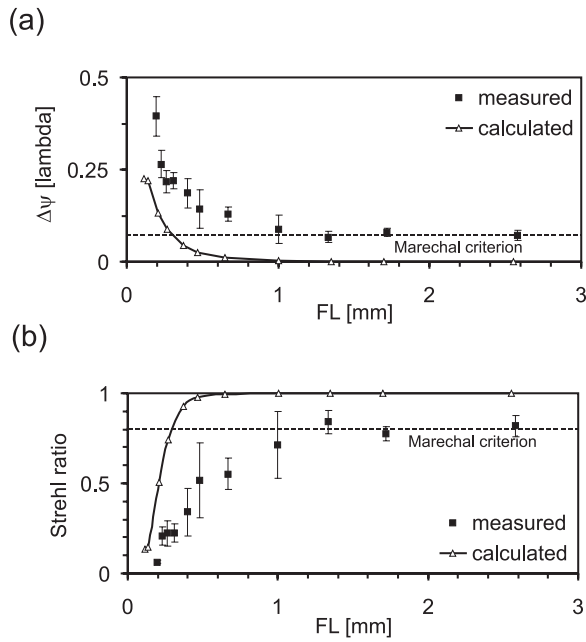
(a)

(b)

Figure 4.39: Rms values of wavefront aberrations $\Delta\Psi$ of the ablated lenses (a) and their corresponding strehl ratios (b) for different focal lengths. The aberrations have been measured within the central diameter $= 190$ μm for all lenses (total lens diameter $= 200$ μm). The corresponding focal numbers can be obtained from table 4.6.

ing strehl ratios of the ablated microlenses averaged over several etch rates. They are compared to values calculated by ASAP for perfectly shaped spherical lenses. High strehl ratios are achieved for slow lenses and peak values up to 0.93 corresponding to rms aberrations below 0.05 λ, are measured for the etch rate of 59 nm/pulse.

Analysis of the wavefront aberrations in case of the fast lenses indicates that the optical thickness at the rim is too large with respect to the central lens area. One likely cause for this phenomenon is the smoothing process that probably ablates less deep at the slanted rim than at the flat center. These aberrations could be reduced by deliberately fabricating an adjusted lens shape, correcting for non-homogeneous ablation during smoothing.

Etch rate

Within the laser fluence measurement range (60-180 mJ/cm^2, limited by the attenuator range for a demagnification of 5×) we were able to obtain etch rates between 59 and 103 nm/pulse.

In figure 4.40 the results are summarized, averaged over all lenses and lenses with focal numbers of F/5.0 or higher respectively. The latter shows that the aberra-
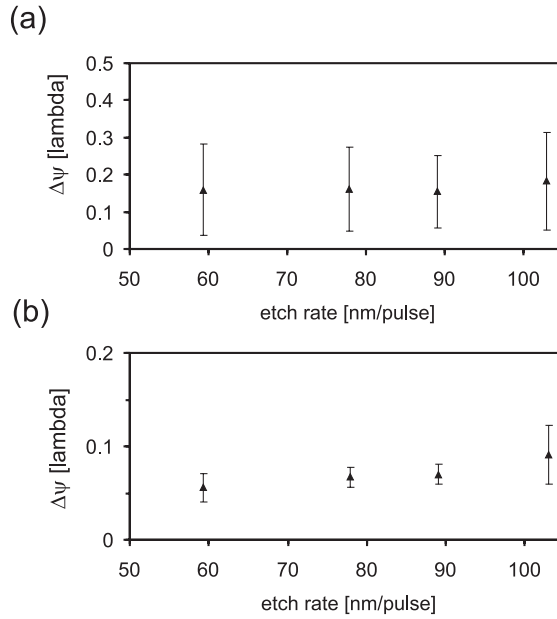
(a)

(b)

Figure 4.40: Rms wavefront aberrations for different etch rates averaged over all lenses (a) and lenses with F-numbers of F/5.0 or higher (b). Note the high spread due to large aberrations present in the fast lenses in graph (a).

tions (and their spread) tend to increase as the etch rate is enhanced. This can be intuitively understood as lenses with high F-numbers need little material to be ablated. The optimization algorithm will thus likely select a small number of contours with high corresponding scan velocities. With higher etch rates those velocities will increase even more, resulting in higher surface roughness as previously indicated in figure 4.26. A second effect is that every individual pulse has a larger impact on the overall lens shape as more material is being removed per pulse. Fluence variations and stage positioning errors become more relevant and this will increase the spread on the aberrations.

Pulse frequency

This parameter is particularly interesting since it decreases fabrication time just like the etch rate, but now the pitch between successive pulses remains constant. The pulse frequency does not affect the surface quality noticeably (figure 4.41). For the subset of lenses with F-numbers above F/5.0, the rms aberrations are of the order of 0.05λ with very low spread. Note that within the applied pulse frequency range, no change in etch rate can be detected in accordance with previously reported results for polyimide and PMMA [27].

Velocity range

In order to check the influence of this parameter we calculated optimum sets for
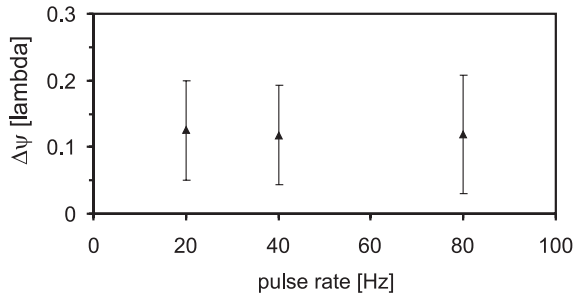
187

Figure 4.41: Rms wavefront aberrations for different pulse rates, averaged over all lenses.
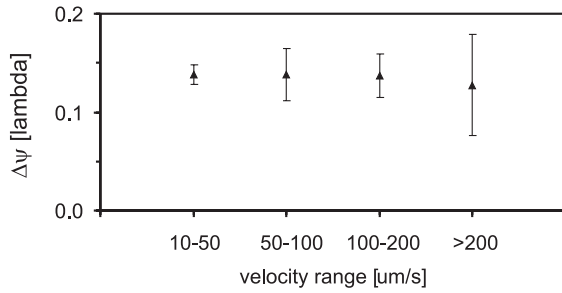

Figure 4.42: RMS wavefront aberrations for different contour velocity ranges.

lenses ($R_{target} = 250$ μm) with single-contour speeds within the following ranges: 10-50, 50-100, 100-200, 200-500 μm/s. The reported results are averaged over 4 identical lenses fabricated under identical conditions (figure 4.42).

Contrary to the case where the etch rate was varied, a different optimum set is calculated for higher scan velocities and the etch rate remains constant at 76 nm/pulse. Wave aberrations do not seem to depend on the chosen scan velocity range, although the spread on the results seems to increase with higher velocities. This can be brought in accordance with the results in figure 4.26: higher scan velocities increase the surface roughness due to the discrete-pulse effect.

4.6.5   Non-spherical lens shapes

As already stated in 4.6.2, aspherical lens shapes are often preferred to spherical lenses because of their superior behavior in particular situations. The contour ablation technique can be applied for non-spherical lens fabrication as the lens profile can be chosen arbitrarily.
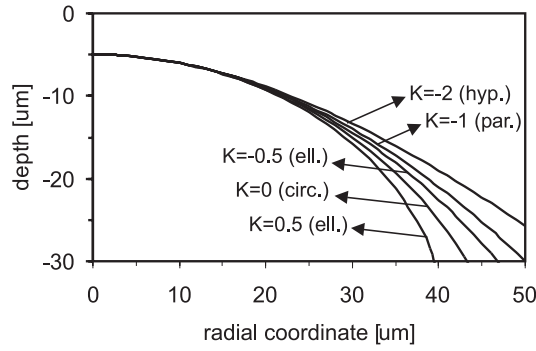
Figure 4.43: Aspherical lens shapes for $R = 50$ μm and $offset = 5$ μm.

The contour calculation is essentially the same as for the case of a spherical lens, but instead of (4.15) another mathematical expression should be used. For parabolic, elliptical and hyperbolic shapes, the profile can be implicitly written as (r is the radial coordinate)

$$r^2 + 2R(Y_{desired} + offset) + (K + 1)(Y_{desired} + offset)^2 = 0$$

with $offset$ indicating the depth down to which the structure is buried.

The nature of this shape changes with K according to

$$
\begin{array}{rcccl}
 & K & < & -1 & hyperboloid \\
 & K & = & -1 & paraboloid \\
-1 & < K & < & 0 & ellipsoid \\
 & K & = & 0 & sphere \\
 & K & > & 0 & ellipsoid
\end{array}
$$

R should be interpreted as the radius of curvature at the vertex of the lens (at $r = 0$). This radius is defined by

$$R = \left. \frac{(1 + y'^2)\sqrt{1 + y'^2}}{y''} \right|_{r=0}$$

The change in surface profile with K is illustrated in figure 4.43 with an example.

Parabolic lenses with 200 μm diameter were fabricated using contour ablation for two values of R. Table 4.7 and figure 4.44 give the contour set details and fabrication parameters. Figure 4.45 compares the measured cross-section with the desired profile.

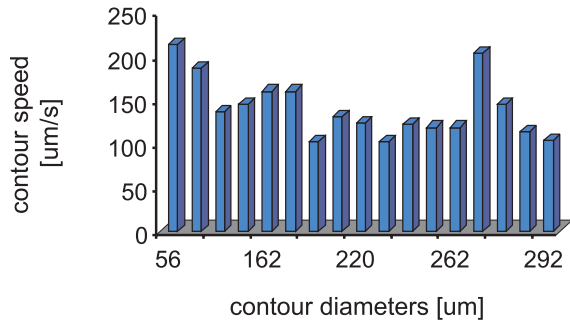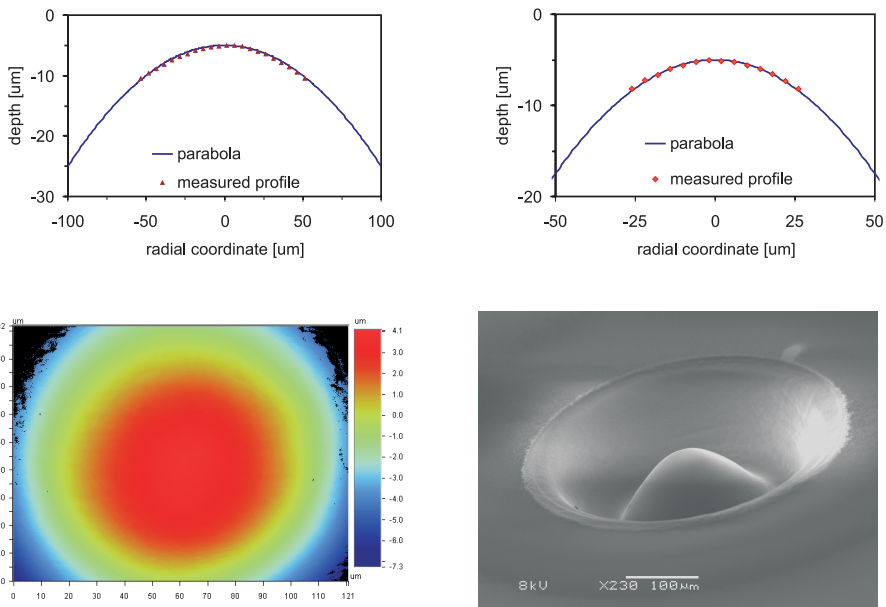Figure 4.44: Contour diameter and velocity distribution for parabolic lens with $R = 250\ \mu$m.

Figure 4.45: Surface measurements of the parabolic lenses. WYKO profilometer cross-sections for $R = 250\ \mu$m (a) and $R = 100\ \mu$m (b). Surface of the lens for $R = 250\ \mu$m with WYKO (c) and SEM (d). Note that only the central part of the lenses is measurable due to the limited numerical aperture of the profilometer.

	1	2
R [μm]	250	100
$offset$ [μm]	5	5
# contours	17	39

Table 4.7: Ablated parabolic lenses: lens and fabrication parameters. Ablation rate is 0.102 μm per pulse and the repetition rate equals 20 Hz. Note that R is here the radius of curvature at the vertex.

4.7 Extension of the technique for non-circular microoptics

All of the lenses discussed in the previous section refer to structures which are rotationally symmetric and feature a circular footprint. Although this type of lens will be satisfactory for numerous applications, for some particular situations its performance might be inadequate. Consider the case of coupling an elliptical beam into a circular waveguide, a situation which is encountered when light is coupled from an edge-emitting laser diode into a SM fiber. As these lasers are frequently used for generating optical signals for telecom purposes and SM fiber is the preferred transmission medium for long haul applications, this particular coupling problem is of great importance. It is obvious that the lack of rotational symmetry in the laser beam suggests that the best solution will not be a lens with rotationally invariant behavior.

One way to break up the rotational symmetry is to use a non-circular aperture with the most obvious choice being an ellipse. However, one of the most powerful features of the contour technique is its flexibility in terms of lens shape. Exactly this property will suffer from the use of an elliptical aperture since the fabrication of circular lenses will become very difficult.

Another approach implies non-circular contours while maintaining the aperture circular[21]. This technique is discussed below.

Trench profile calculation

The basic set of trenches is not longer limited to the three profiles in figure 4.22, as both axes of the elliptical contour can be independently smaller, equal or larger than the aperture diameter. Figure 4.46 illustrates two cases of contour diameter values. An important observation is that the choice of one contour axis length influences the trench profile in the orthogonal direction which will largely complicate the optimization process.

---

[21]A variable contour speed along a circular path would also be able to introduce asymmetric features.
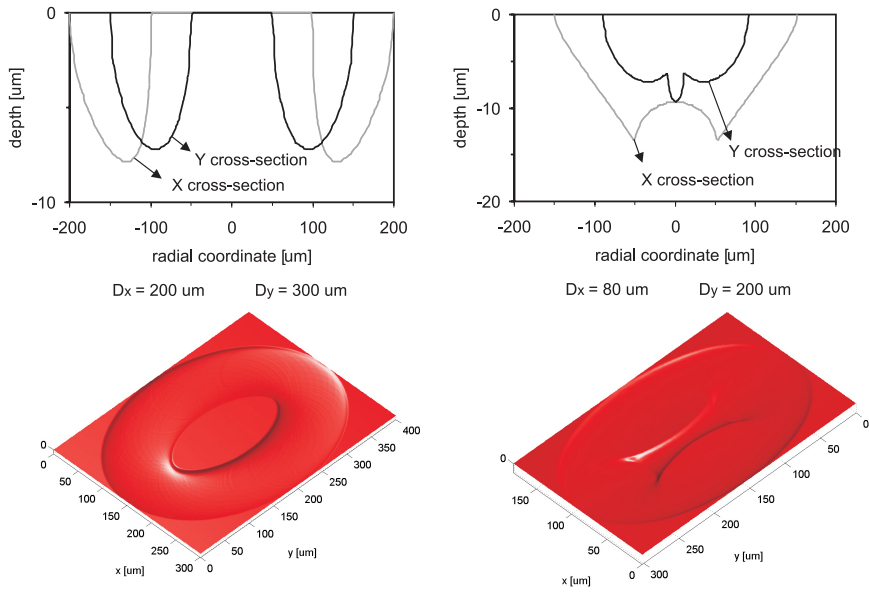
Figure 4.46: Trench profiles for elliptical contour ablation. Aperture diameter = 100 μm, ablation rate = 70 nm/pulse and contour velocity = 20 μm/s. Contour diameters in X and Y direction are indicated.
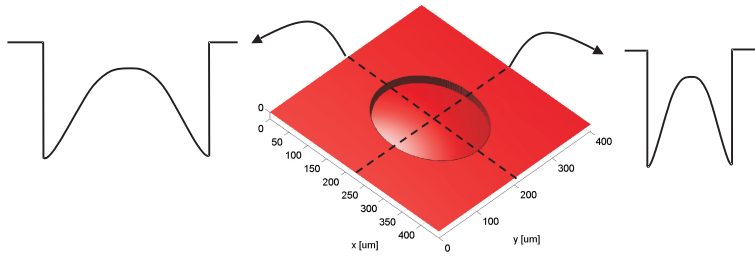
Figure 4.47: Lens surface with a different radius of curvature in x and y direction.

Optimization of the contour set

In figure 4.47 an example of a lens surface with a different curvature for two orthogonal directions is given. The contour lines of equal height in this structure are elliptical with an ellipticity ϵ_{lens}. One can assume that the ablated grooves of which this lens surface will be constructed, need to have the same property. In this case the exact profile should only be matched in one cross-section and would equal the approach as described above for circular trenches. However, it is clear that this requirement cannot be completely met by using a circular aperture.

Therefore the contour set calculation with a circular aperture is performed as follows. The profile of the approximating structure is compared to the ideal shape in two cross-sections (containing the main axes of the lens shape as indicated in figure 4.46) and the simulated annealing algorithm is employed to minimize the profile deviation along *both* axes. The $\epsilon_{contour}$ of the contours is allowed to vary slightly but remains close to ϵ_{lens}. Equal ϵ values for the contours did not result in high-quality approximations, but allowing a tolerance of 20 % seemed to give satisfactory results. Note that due to this tolerance and due to the use of a circular aperture, the contour ablated structure will deviate from the desired one. Even in the case of a perfect match between both cross-sections in both axes planes, the exact surface curves will differ in other planes as the condition for the ellipticity is not satisfied. A contour plot of the ablated lens illustrates this: a truly elliptical lens surface shows contour lines which all have the same ellipticity ϵ. For the ablated approximation this is clearly not the case.

The elliptical contour approach, although attractive since the basic set-up does not change, introduces some technical challenges. Most translation stages are equipped with features to make smooth circular contours[22], but they do not offer these for non-circular motion. Therefore the elliptical contour has to be approximated by successive discrete moves. Instead of using linear translations for this approximation, we chose circular moves for this purpose. The elliptical path is much better

---

[22]Commercial stages offer contouring with circular interpolation: a circular contour move is not approximated by a sucession of discrete translation steps between discrete points, but rather a smooth contour realized by continuously changing velocities for the X and Y stage.
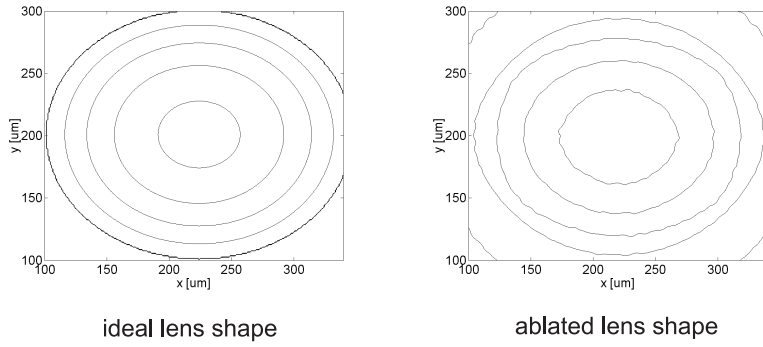
ideal lens shape   ablated lens shape

Figure 4.48: Calculated contour plot of the ideal and ablated lens ($R_x = 600$ μm, $R_y = 400$ μm).

approximated and the transition between the several circular segments is much smoother. The decomposition in circular segments is discussed in the Appendix.

4.8   Lens arrays

The discussion on contour ablation of microlenses has been limited to single lens fabrication: every lens has to be ablated individually and the time necessary to fabricate N lenses equals N times the fabrication time for a single lens.

Using a mask with an array of apertures it is possible to apply the same contour ablation technique for simultaneously ablating several identical lenses. The lens pitch is determined by the aperture pitch on the mask. Figure 4.49 gives a few examples.
An important parameter for lens arrays is the fill factor. This quantity determines the ratio of effective lens area to total array area and is given by

$$FF = \frac{\pi \left(\frac{\Phi}{2}\right)^2}{L^2}$$

with L the size of the unit cell. Using the contour technique a minimum space outside the lens area is needed and corresponds to the beam diameter ϕ as indicated in figure 4.50. This is a consequence of the contour calculation algorithm using contour diameters up to $\phi + \Phi$. The maximum attainable fill factor is then

$$FF = \frac{\pi \left(\frac{L-\phi}{2}\right)^2}{L^2}$$

in which Φ represents the lens diameter and ϕ the beam diameter.
For a given array pitch L of 250 μm, the value of FF is calculated for different
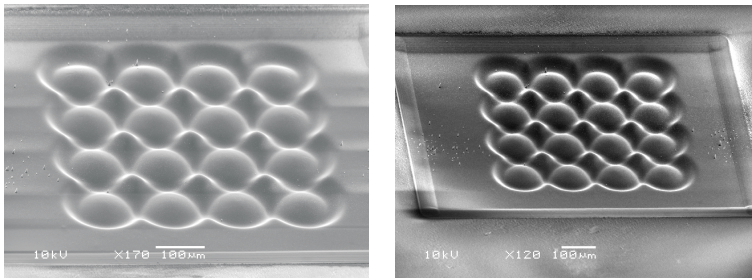
Figure 4.49: Examples of lens arrays fabricated with contour ablation.
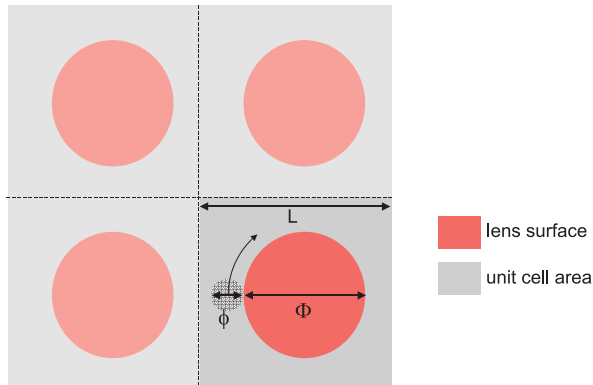
Figure 4.50: Unit cell of an array: definition of several dimensions.

beam sizes (figure 4.51). From this graph we can conclude that for a writing beam size of 100 μm (as the spherical lenses in 4.6.4), the maximum fill factor will equal 28 %. Attempts to increase FF by further limiting the contour diameter range to e.g. Φ, resulted in an inferior and unacceptable lens approximation.

A higher FF can be obtained using a contact mask consisting of holes with an area equal to the lens footprints. The holes feature a pitch twice as large as the lens array's and have a staggered arrangement. The full array fabrication is then accomplished in two steps, with a mask shift over one lens pitch in between. The corresponding FF is also given in figure 4.51.

During fabrication of lens arrays, special attention has to be paid to the uniformity of the lenses. It is to be expected that high uniformity can be obtained for a homogeneous beam. Still, surface and aberration measurements have yet to be performed to quantitatively support this assumption.

195
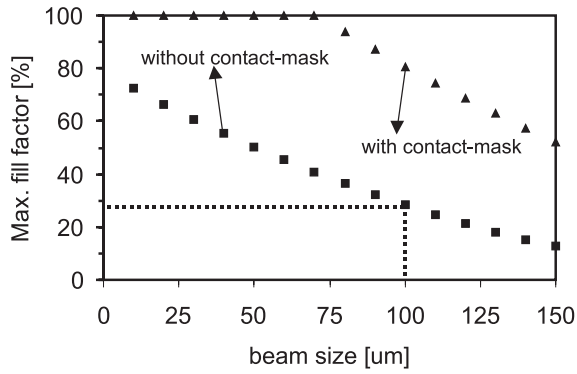
Figure 4.51: Maximum attainable fill factor versus beam diameter for an array with a pitch of 250 μm. The fill factor for a 100 μm beam size is indicated.

4.9 Conclusions

Excimer laser ablation can be used successfully to create a broad range of microlenses. As the microlens shape is determined by the substrate contouring rather than complex mask patterns, one single aperture can be employed for different lenses in terms of focal length, surface profile and diameter. The feasibility of the contour scanning technique has been verified by fabrication of 200 μm spherical microlenses with an etch rate roughly between 60 and 100 nm/pulse. The lenses had an F-number between 0.8 and 14, corresponding to a fabrication time between 6 and 1 minute per lens. Best results in terms of wave aberrations were obtained for low etch rates and contour velocities. The pulse repetition rate did not influence the lens quality noticeably. Nearly diffraction-limited performance has been achieved for lenses with a focal length above 1 mm ($>$F/5).

Finally it is shown that the technique can be easily extended to fabricate lens arrays and lenses with non-circular footprints.

Appendix A Approximation of an ellipse by circular arcs

Commercial translation stage drivers seldom offer elliptical contouring as an operation mode, this contrary to e.g. circular contouring. In this appendix a method is shown for approximating an elliptical path by successive circular arcs.

In the first quadrant of an ellipse with main axes a and b, a set of points P_i ($0 \leq i \leq N$) lying on the perimeter is selected. Instead of choosing them equally spaced, their location is determined by the curvature range in the ellipse. The parametric expression for the ellipse is given by

$$\begin{array}{rcl} x(t) & = & a cos(\theta) \\ y(t) & = & b sin(\theta) \end{array} \qquad (4.16)$$

with $\theta \in [0, 2\pi[$. The curvature for this function is given by

$$K(\theta) = \frac{x'(\theta)y''(\theta) - y'(\theta)x''(\theta)}{\sqrt{((x'(\theta))^2 + (y'(\theta)))^2)^3}} = \frac{ab}{\sqrt{(a^2 sin^2(\theta) + b^2 sin^2(\theta))^3}} \qquad (4.17)$$

Combining both expressions, we find for K:

$$K(x, y) = \frac{ab}{\sqrt{\left(\left(\frac{bx}{a}\right)^2 + \left(\frac{ay}{b}\right)^2\right)^3}} \qquad (4.18)$$

As points on the ellipse should satisfy

$$\left(\frac{x}{a}\right)^2 + \left(\frac{y}{b}\right)^2 = 1 \qquad (4.19)$$

we can calculate the coordinates of a point on the ellipse where the curvature is K by using (4.18) and (4.19):

$$\begin{array}{rcl} x(K) & = & a\sqrt{\left|\frac{\lambda - a^2}{b^2 - a^2}\right|} \\[2mm] y(K) & = & b\sqrt{\left|\frac{\lambda - b^2}{a^2 - b^2}\right|} \end{array} \qquad (4.20)$$

197

with $\lambda = \left(\frac{ab}{K}\right)^{2/3}$.

From (4.18) we learn that the curvature in $(a,0)$ and $(0,b)$ is respectively $K_{a,0} = a/b^2$ and $K_{0,b} = b/a^2$.

The points P_i are now chosen according to the curvatures

$$K_i = (1 - i/N)K_{a,0} + (i/N)K_{0,b} \qquad (4.21)$$

Through these points a number of arcs are constructed. For $1 \leq i \leq N - 2$, these arcs each connect three successive points P_{i-1}, P_i and P_{i+1}. The arc connecting P_0 and P_1 is constructed in such a way that it also contains the reflected point of P_1 through the Y-axis. In a similar way the arc through P_{N-1} and P_N also contains the reflected point of P_{N-1} through the X-axis.

If (x_{i-1}, y_{i-1}), (x_i, y_i) and (x_{i+1}, y_{i+1}) are the coordinates of P_{i-1}, P_i and P_{i+1}, we can calculate the center coordinates of the circle through these points according to

$$\begin{aligned}
x_{c,i} &= \frac{\alpha\beta(y_{i-1} - y_{i+1}) + \beta(x_{i-1} + x_i) - \alpha(x_i + x_{i+1})}{2(\beta - \alpha)} \\
y_{c,i} &= -\frac{1}{\alpha}\left(x_{c,i} - \frac{x_{i-1} + x_i}{2}\right) + \frac{y_{i-1} + y_i}{2}
\end{aligned}$$

where α and β are the slopes of the lines through respectively P_{i-1} and P_i, and P_i and P_{i+1}. The radius is given by the distance between $(x_{c,i}, y_{c,i})$ and one of the P's involved. Note that it is possible that one of the lines is vertical and thus possesses an infinite slope. In this case another line combination through the three points should be chosen.

Bibliography

[1] N. Borelli, D. Morse, R. Bellman and W. Morgan, "Photolytic technique for producing microlenses in photosensitive glass", Appl. Opt. **24**, 2520 (1985).

[2] D. Daly, R. Stevens, M. Hutley and N. Davies, "The manufacture of microlenses by melting photoresist", Meas. Sci. Technol. **1**, 759 (1990).

[3] D. Purdy, "Fabrication of complex micro-optical components using photo-sculpting through halftone transmission masks", Appl. Opt. **3**, 167 (1994).

[4] M. Gale, M. Rossi, J. Pedersen and H. Schutz, "Fabrication of continuous-relief micro-optical elements by direct laser writing in photoresist", Opt. Eng. **33**, 3556 (1994).

[5] S. Aoyama, N. Horie and T. Yamashita, "Micro Fresnel lens fabricated by electron-beam lithography", in Computer and Optically Formed Holographic Optics, Proc. SPIE **1211**, 175 (1990).

[6] P. Kung and L. Song, "Rapid prototyping of multi-level diffractive optical elements", OSA Technical Digest Series: Diffractive Optics **11**, 133 (1994).

[7] D. MacFarlane, V. Narayan, W. Cox, T. Chen and D. Hayes, "Microjet fabrication of microlens arrays", IEEE Phot. Techn. Lett. **6**, 1112 (1994).

[8] M. Kufner, S. Kufner, M. Frank, J. Moisel and M. Testorf, "Microlenses in PMMA with high relative aperture: a parameter study", Pure Appl. Opt. **2**, 9 (1993).

[9] H.-J. Woo, Y.-S. Kim, H.-W. Choi, W. Hong, S. Lee, M. Kufner and S. Kufner, "Optimisation of microlenses fabricated by deep proton irradiation and styrene diffusion", Microelectron Eng. **57-8**, 945 (2001).

[10] H. Ottevaere, B. Volckaerts, V. Baukens, J. Lamprecht, J. Schwider, A. Hermanne, I. Veretennicoff and H. Thienpont, "Uniform 2D plastic microlens arrays made with DLP: a focus on fabrication and characterization issues", in 8th Micro Optics Conference, Osaka, Japan, 316 (2001).

[11] K. Naessens, H. Ottevaere, R. Baets, P. Van Daele and H. Thienpont, "Direct-writing of microlenses in polycarbonate with excimer laser ablation", Appl. Opt. **42**, 6349 (2003).

[12] K. Naessens, H. Ottevaere, P. Van Daele and R. Baets, "Flexible fabrication of microlenses in polymer layers with excimer laser ablation", Appl. Surf. Sc. **208**, 159 (2002).

[13] S. Mihailov and S. Lazare, "Fabrication of refractive microlens arrays by excimer laser ablation of amorphous teflon", Appl. Opt. **32**, 6211 (1993).

[14] F. Beinhorn, J. Ihlemann, K. Luther and J. Troe, "Micro-lens arrays generated by UV laser irradiation of doped PMMA", Appl. Phys. A **68**, 709 (1999).

[15] S. Lazare, J. Lopez, J.-M. Turlet, M. Kufner, S. Kufner and P. Chavel, "Microlenses fabricated by ultraviolet excimer laser irradiation of poly(methyl methacrylate) followed by styrene diffusion, Appl. Opt. **35**, 4471 (1996).

[16] Corning data sheet on SMILE lens arrays. Available at http://www.corning.com/photonicmaterials/pdf/PI104_SMILE.pdf.

[17] M. Kufner and S. Kufner, "Micro-optics and lithography", VUB press, 177 (1997).

[18] W. Cox, T. Chen and D. Hayes, "Micro-optics fabrication by ink-jet printing", Optics and Photonics News, June 2001, 32 (2001).

[19] X. Wang, J. Leger and R. Rediker, "Rapid fabrication of diffractive optical elements by use of image-based excimer laser ablation", Appl. Opt. **36**, 4660 (1997).

[20] M. Wakaki, Y. Komachi and G. Kanai, "Microlenses and microlens arrays formed on a glass plate by use of a CO_2 laser", Appl. Opt. **37**, 627 (1998).

[21] T. Jitsuno, K. Tokumura, N. Nakashima and M. Nakatsuka, "Laser ablative shaping of plastic optical components for phase control", Appl Opt. **38**, 3338 (1999).

[22] R. Matz, H. Weber and G. Weimann, "Laser-induced dry etching of integrated InP microlenses", Appl. Phys. A **65**, 349 (1997).

[23] M. Born and E. Wolf, "Principles of optics", 7th (expanded) edition, Cambridge University Press (1999).

[24] T. Berden, E. Kreutz and R. Poprawe, "Debris-reduced laser machining of polymeric waveguides for optoelectronic applications", in Laser Applications in Microelectronic and Optoelectronic Manufacturing VI, San Jose, USA,Proc. SPIE **4274**, 432 (2001).

[25] R. Srinivasan, B. Braren and K. Casey, "Nature of 'incubation pulses' in the ultraviolet laser ablation of polymethyl methacrylate", J. Appl. Phys. **68**, 1842 (1990).

[26] B. Hopp, M. Csete, K. Revesz, J. Vinko and Z. Bor, "Formation of the surface structure of polyethylene-therephtalate (PET) due to ArF excimer laser ablation", Appl. Surf. Sci. **96-8**, 611 (1996).

[27] F. Burns and S. Cain, "The effect of pulse repetition rate on laser ablation of polyimide and polymethylmethacrylate-based polymers", J. Appl. Phys. **29**, 1349 (1996).

201

Chapter 5

Excimer laser ablation of microalignment structures for photonic applications

This chapter describes our research on two particular microalignment structures that have been fabricated with excimer laser ablation. Both have been employed successfully in parallel optical interconnect demonstrators.

5.1   Introduction

At the Photonics Research Group of Intec excimer laser ablation has been used successfully for the fabrication of microstructures suitable for optical alignment purposes. Two particular applications are discussed in detail in this chapter: the prototype fabrication of a 2D 4×8 plastic optical fiber ferrule and a mastertool for alignment of a VCSEL-chip with a 1×8 MT connector.

Excimer laser ablation is not the only technique that is capable of making these alignment components. An elaborate discussion of feasible microfabrication techniques does not fit in the present work as too many technologies can be employed for this purpose. A brief overview can be found in tables 5.1 and 5.2.
Still, one can argue that laser-beam machining and excimer laser ablation in particular offers quite some advantages compared to other traditional fabrication techniques. Firstly, the absence of chemical substances and physical contact between the machining tool and the part are some of the appreciated properties of laser ablation. Secondly, it allows microstructuring on top of heterogeneous assemblies at any stage of the assembly process. This feature has great potential in heterogeneous opto-electronic modules requiring the insertion of microstructures in a late phase of the assembly. Few other techniques can match these advantages.

203

Machining Method	Material/Application	Typical Min./Max. Size Feature	IC Compatible	Tolerance	Aspect Ratio (Depth/Width)	Important Reference on Technique	Initial Investment Cost/Access
Group: Traditional Techniques (Not Involving Photolithography-Defined Masks)							
Chemical milling (S), (Ba)	Almost all metals	From submillimeters to a few meters (x,y); max thickness (z) ±1 cm	Yes	Lateral tolerance 0.25 to 0.5 mm	±1	Harris[15]	Low/good
Electrochemical machining (S/A), (Ba)	Hard and soft metals, turbine blades, pistons, fuel-injection nozzles	Minimum size devices larger than in chemical milling because of the contacting need	Fair	Lateral tolerance < 10 μm	(S) 100	(A) Romankiw,[37] (S) Phillips[47]	±$400,000/good
Electrodischarge machining (EDM) (S), (Se)	Hard, brittle, conductive materials used for tools and dies	Minimum holes of 0.3 mm in 20-mm thick plate	No	Lateral tolerance, 5–20 μm	100	Kalpajian[51]	High/good: equipment with numerical control is common
Electrodischarge wire cutting (EDWC) (S), (Se)	Hard, brittle materials; many punch-and-die applications	Minimum rods 20 μm in diameter and 3 mm long	No	Lateral tolerance, 1 μm	>100	Saito[53]	High/good: does not require special electrodes
Electron-beam machining (EBM) (S/A), (Se)	Hard-to-machine materials	(S) most suited for large numbers of simple holes (<0.1 mm)	Fair	(S) ~10% of feature size (5 μm on a 50-μm hole)	(S) 10 is typical but 100 is possible	Taniguchi[56]	Very high/fair ±100,000 when using modified SEM
Continuous deposition (A), (C); e.g., doctor's blade technology	With all materials available in inks, e.g., glucose sensors	Most suited for inexpensive disposables, from 100 μm to a few millimeters	No	15 μm	—	Harper[91]	Low/good
Focused ion-beam on a lathe (S/A), (Sc)	Very pure IC materials	From submicrons to millimeters	Yes	(S) 50–100 nm	—	Vasile[88]	High/poor
Hybrid thick film (A), (Ba)	Wide variety of materials available in inks	Minimum feature size 90 μm	Fair	12 μm	—	Harper[91]	±$30,000/good
Laser-beam machining (LBM) (S/A), (Se)	Complex profiles in hard materials	(S) Holes from 10 μm to 1.5 mm at all angles	Fair	1 μm	(S) 50	Helvajian[63]	±$50,000 but up to $400,000 for a five-axis system/good
Plasma-beam machining (PBM) (S/A), (Se/Ba)	Very high temperature materials	(A) only used for thick films > 25 μm; (S) for very thick films > 2.5 mm	No	(A) 20 μm for a 25-μm thick film; (S) typical ±3 mm but 0.8 mm is possible	—	Pfender[92]	±$600,000/fair
Stereo lithography (A), (Se)	Polymeric photosensitive materials	Max. 10 × 10 × 10 mm (x,y,z)	Yes	Minimum solidification unit 5,5,3 μm (x,y,z)	—	Ikuta[93]	Low/good
Ultra-precision mechanical machining (S), (Se)	Form-stable materials	From submillimeters (e.g., 0.2-mm hole) to meters	No	1 nm by the year 2000	—	Boothroyd[4]	$400 k/good
Ultrasonic machining (S), (Se)	Hard and brittle materials	Holes from 50 μm to 75 mm	No	Lateral tolerance 10 μm	2.5 μm for a 250-μm hole	Bellows[82]	$20 k/good

Table 5.1: Traditional microfabrication techniques. Taken from [1].

Machining Method[a]	Material Application	Typical Min./Max. Size Feature	IC Comparable	Tolerances	Important Reference on Technique	Aspect Ratio (Depth/Width)	Shape and Height/Depth	Initial Investment Cost/Access
Group: Nontraditional (Involving Photolithography-Defined Masks)								
Photofabrication (S)	Plastic, glass (ceramic), e.g., fluidic elements	Max. x,y = 40 × 40 cm and max z = 0.6 cm	Yes	Lateral tolerance 20 μm	Trotter[24]	~3 for photoplastics; ~20 for photoglass	x,y is free; z = up to 6 mm	Medium/poor to medium
Photochemical milling (S)	Printed circuit boards, lead frames, shadow masks	Max. 60 × 60 cm, max. thickness < 0.5 mm	Yes	13 μm (printed circuits)	Allen[21]	±1	x,y is free; z = up to 0.5 mm	Medium/good
Wet etching of anisotropic materials (S)	Crystal Si, GaAs, quartz, SiC, InP	Max. wafer size, min. feature a few microns	Fair	1 μm	Kern[94]	100	x,y,z shape locked in by crystallography, z height of the wafer	Low/good
Dry etching (S)	Most solids	Max. wafer size, min. feature submicron	Good	0.1 μm	Manos[95]	10	x,y shape free; z = up to 200 μm	High/good
Polysilicon surface micromachining (S/A)	Poly-Si, Al, Ti, etc.	Max. wafer size, min. feature submicron	Good	0.5 μm	Howe[96]	—	x,y free; z = 0.1 to 10 μm, but preferably 1–2 μm	High/fair
SOI (S)	Crystalline Si	Max. wafer size, min. feature submicron	Good	0.1 μm	Diem et al.[97]	—	x,y free; z height depending on the epilayer, e.g., 100 μm	High/poor
LIGA (S/A)	Ni, PMMA, Au, ceramic, etc.	10 × 10 cm or more, 0.2 μm	Fair	0.3 μm	Ehrfeld[98]	>100	x,y free; z up to several cm	High (>M$35)/ poor
UV transparent resists (S/A)	Polyimide, SU-8, AZ-4000	Max. wafer size	Good	0.5 μm	Ahn et al.[31]	10	x,y free; z up to 100 μm	Medium/fair
Molded polysilicon HEXSIL (Keller) (S/A)	Poly-Si, Ni, etc.		Good	0.5 μm	Keller[99]	10	x,y free; z up to 100 μm	High/poor
Erect polysilicon (Pister) (S/A)	Poly-Si	.	Good	0.5 μm	Pister[97]	10	x,y free; z up to mm	High/poor

Note: S = subtractive, A = additive, Ba = batch, Se = serial, C = continuous.

[a] All batches.

Table 5.2: Non-traditional microfabrication techniques. Taken from [1].

Taking into account that intense excimer laser pulses are capable of smoothly removing polymer layers, we can consider excimer laser ablation as a preferred technique to create structures with microfeatures in polymer materials.

5.2 Prototyping of a 2D Plastic Optical Fiber ferrule for chip-to-chip interconnect

It is beyond doubt that an ever increasing demand for data throughput, module compactness and efficiency drives the development of novel technologies for IC packaging and interconnects. There is broad consensus on the fact that electrical interconnects will not be able to handle the large data streams solely in the near future. One of the technologies that is able to alleviate this expected electrical bottleneck, is (parallel) optical interconnect. This is in particular the case for large datastreams on chip-to-chip and intra-chip level.

In optical interconnect technology optics is used to route modulated light beams, thereby replacing metallic interconnects. There are two distinct approaches for transporting optical signals: guided wave or free space propagation. In the first case waveguides (e.g. optical fibers) are used to transmit the beams. They are similar to the metal paths in case of electrical signals except that they are able to propagate waves in the optical frequency range. The other alternative uses optics to manipulate the wavefront of the beams (e.g. microlenses) to direct the light beam in free space, without the use of an intermediate guiding medium. Each approach has its advantages and disadvantages and the relative merits depend on many factors, in particular interconnect distance. In the following we will focus on the guided wave approach.

Guided wave interconnects require two important components: the interfaces or connectors with the receiver and emitter, and the optical waveguide. Plastic Optical Fiber (POF) is an excellent candidate for short distance interconnect [5]: it is very cheap, a high quality end facet can be easily obtained with a hot knife cut and compact bends are possible due to the high numerical aperture. Commercial availability of 125 μm diameter fibers permits the use of POF in parallel interconnects with a standard pitch of 250 μm. The higher transmission losses compared to glass fiber are irrelevant for interconnect distances of the order of 1 meter or less.

The connector part is another issue. Currently, well-performing connectors for single fiber and fiber arrays (MT) are commercially available. But these multifiber MT connectors, featuring 8 or 12 fibers at a pitch 250 μm, are unable to handle 2D fiber arrays. On the other side typical short-distance interconnect sources such as surface emitting VCSELs and RCLEDs are extremely suitable for creating 2D arrays of emitters. As increasing data transfer rates will soon need optical interconnects to be fully two-dimensional, prototype connectors have to be developed that are capable of handling those 2D data streams.

In this section we will discuss a prototype ferrule that is suitable for coupling a 4×8 array of plastic optical fiber to VCSEL or RCLED arrays. It is capable of holding 32 optical channels with the fibers placed at a pitch of 250 μm. In turn,

the ferrule can be fixed in a larger connector frame containing alignment features like pins or pinholes. The full structure can be used for aligning the fibers with an emitter/receiver array. A more elaborate description of the assembly process and the fiber position measurements[1] can be found in [2]. We will here limit the discussion to the assembly of the ferrule only, with a focus on the laser ablated grooves.

5.2.1 Layout of the ferrule

The basic structure in the ferrule is a polymer plate with a thickness slightly below 250 μm. In this plate an array of 8 grooves is fabricated using excimer laser ablation. These grooves are 10 mm long, 125 μm deep and separated by a pitch of 250 μm. The cross-section of the grooves is optimized for holding a 125 μm plastic optical fiber.

The ferrule assembly process is depicted in figure 5.1. In a first step the POFs are inserted into the grooves. Next the fibers are fixed permanently with a UV curing adhesive. In a final phase, several plates are stacked on top of each other using a method called 'virtual' alignment. Afterwards they are glued together and the ferrule is now ready to be incorporated in a connector package containing the alignment pins.

5.2.2 Fabrication of the groove array

A trench geometry is preferred for holding the fibers in a suitable position. An alternative is a plate with precision holes through which the fibers are positioned, but this solution does not allow an easy insertion of the fibers. A plastic has been chosen as base material. This choice is based on the consideration that injection molding or casting will be used for low-cost mass fabrication or replication of the connector in plastic. The groove geometry and plastic substrate material make excimer laser ablation a well-suited prototype fabrication technique for this structure.

The groove array consists of parallel trenches of 125 μm deep and 10 mm long, spaced by 250 μm. The width of the groove is optimized for carrying a fiber with a diameter of 125 μm, corresponding to the nominal diameter of the POFs. This means that at a depth of 62.5 μm, the groove is exactly 125 μm wide with an accuracy of approximately 1 μm. This accuracy is not determined by the ablation process itself but by the optical microscope used for measuring the groove width and pitch.

As substrate material we used two different commercial polymers: polycarbonate (PC) and polymethylmethacrylate (PMMA). In the following paragraphs we discuss two distinct ways to make the groove array. One method is based on scanning the surface with a simple square beam spot ('scanning aperture') and the other uses

---

[1]The connector assembly process has been developed by T. Coosemans within the framework of the OIIC (Optically Interconnected Integrated Circuits) project. Our contribution, the fabrication of the groove plates, has been an essential part in this assembly.
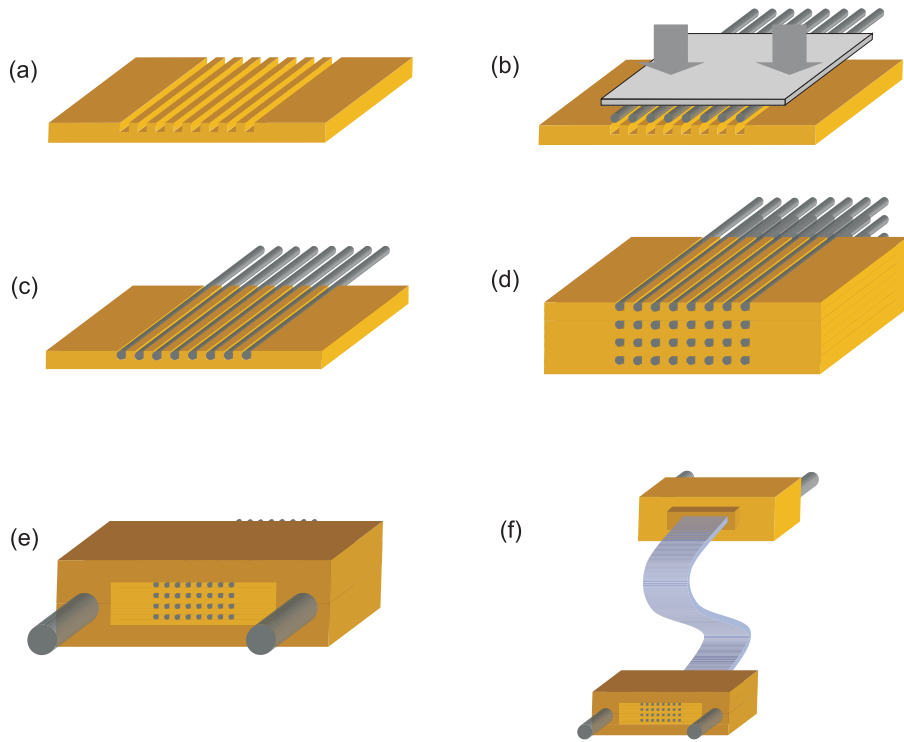
Figure 5.1: Ferrule assembly process (a)→(d). Integration of the ferrule into a connector housing with alignment features is given in (e)→(f) but is not part of this work.
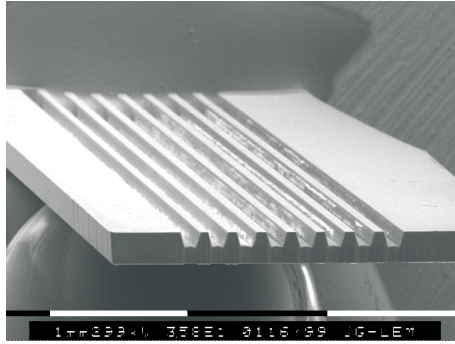
Figure 5.2: Groove array fabricated with KrF at 180 mJ/cm^2 with the scanning aperture technique. The substrate material is PC.

a more sophisticated mask pattern consisting of several rectangular areas ('hybrid mask scanning'). For both methods the influence of some important fabrication parameters is investigated: laser fluence, pulse repetition rate and number of passes that the laser beam makes to obtain the full groove depth. The experiments and the prototype fabrication have all been carried out in air. No flow chamber was used.

Fabrication based on scanning aperture fabrication

This method is an excellent prototyping technique as it requires no custom mask pattern to be inserted in the beam path. By using a simple square aperture, the desired pattern is written into the polymer. The size of this aperture matches the upper groove width.

To illustrate this approach we fabricated a suitable trench array in PC. The grooves have been made with a fluence of 180 mJ/cm^2 at the KrF wavelength, corresponding to an etch depth of approximately 150 nm/pulse. The pulse frequency was chosen at 10 Hz to obtain a smooth processing. At this fluence the wall angle is about 72° (18° with respect to the vertical direction) and an on-target beam aperture of 160 μm is needed to obtain a width of 125 μm at the semi-depth. For a demagnification of 4×, this corresponds to a square aperture at the mask plane of 660 μm. Figure 5.2 depicts the result of this approach. The grooves were not ablated to full depth at one go. The beam passed three times over the same groove until a depth of 125 μm was obtained. Note that the accuracy on the pitch of the grooves is determined by the positioning accuracy of the stage in this direction.

An important disadvantage is the extremely slow fabrication speed: approximately 12 hours of laser operation is required to finish the entire structure.

209

Fabrication based on hybrid mask scanning [3, 4]

In order to reduce the fabrication time to an acceptable level for fast-prototyping, a mask pattern has been designed. Its exact dimensions are given in figure 5.3. A Heraeus Suprasil 1 mask substrate is chosen because of its excellent transmission qualities in the deep UV. The beam mask is realized by lithographic definition of a resist pattern on the substrate and subsequent deposition of a layer Cr (200 nm) and Au (50 nm) with electron beam evaporation. The pattern was restricted to 4 grooves with an on-target length of 500 μm due to the projection optics' limited field of view.

This method was used successfully to fabricate a suitable trench array in PMMA. The grooves have been made with a fluence of 270 mJ/cm^2 at the ArF wavelength, corresponding to an etch depth of approximately 215 nm/pulse. The pulse frequency was chosen 20 Hz to obtain a smooth processing although higher repetition rates up to 50 Hz were also successful. At this fluence the wall angle is about 78° (12° with respect to the vertical direction). The width of the grooves was chosen 155 μm in order to obtain the necessary 125 μm width at the semi-depth. For a demagnification of 5× this corresponds to a rectangular aperture at the mask plane of 760 μm wide per groove. Figure 5.3b depicts the result of this approach. The grooves were not ablated to full depth at one go. The beam passed two times over the same groove until a depth of 125 μm was obtained. The accuracy on the pitch of the grooves is now mainly determined by the acuracy of the mask pattern. Still, the translation stage needs to perform one shift in the direction perpendicular to the grooves in order to obtain 8 parallel grooves.

Compared to the scanning aperture technique, the fabrication time is now reduced to a mere 20 minutes (20 Hz operation) by taking advantage of the increased beam pattern size. Note that if the entire groove structure would fit into the field of the projection lens, scanning would not be needed any more and fabrication would merely take a few seconds.

Discussion

Groove arrays with an acceptable surface quality and suitable cross-section can be obtained within a range of fabrication parameters. The most important ones are discussed below and their impact on the groove quality is experimentally verified. These experiments have focused on the fabrication of grooves with a depth of nominally 100 μm. These grooves have been obtained with aperture and hybrid mask scanning, both in PMMA and PC. For each combination of a base material and fabrication method, the pulse frequency, the fluence and the number of passes to obtain the full groove depth were varied. For each of these grooves the surface roughness was measured with the Wyko profilometer at Vrije Universiteit Brussel and SEM was employed for observation of the cross-sections.

- Wavelength and material

It is known from chapter 3 that PMMA ablates very fast at 248 nm due to its low absorption coefficient at this wavelength. However, the benefits of this higher etch
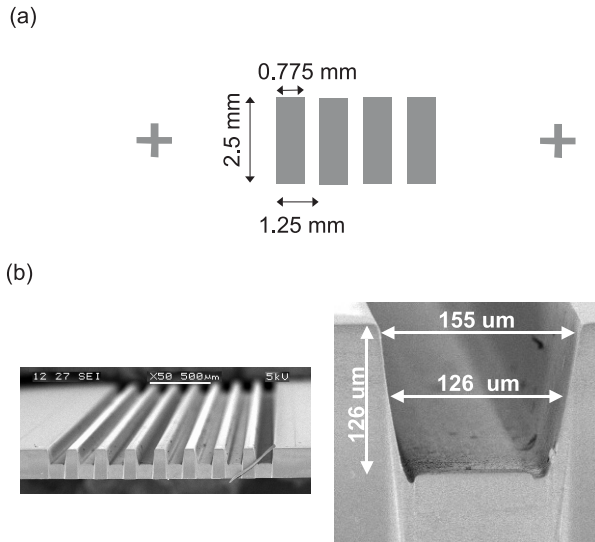
Figure 5.3: Mask layout for 'hybrid mask scanning' (a). Dark areas are transparent. Groove array fabricated with ArF at 270 mJ/cm^2 with hybrid mask scanning (b). The substrate material is PMMA. The dimensions are optimized for a demagnification of 5×.

rate is accompanied by an increased roughness of the surface bottom as illustrated in figure 5.4. ArF ablation gives a much smoother structure than KrF for PMMA.

PC ablation of deep structures at 193 nm usually produces a lot of black soot or debris in and around the ablated area when no flow chamber is employed. The result is that the deposited debris covers the groove surface and inhibits further ablation. The effect on the groove quality is illustrated in figure 5.5. Cone formation occurs at fluences up to 260 mJ/cm^2 (fluence range limited by the attenuator and demagnification). On the other side PC ablates smoothly at 248 nm with no debris redeposition influencing subsequent ablation.

- Pulse frequency and fluence

Increasing the pulse repetition rate obviously speeds up the fabrication process. For both materials a better surface quality was observed if the fluence was considerably higher than the ablation threshold. However, if both parameters are chosen too large, the substrate can be damaged and the groove array might deform. The exact range of fluences and pulse repetition rates that induces such changes in the substrate cannot be derived from our experiments.

An example is given in figure 5.6 for PMMA at 248 nm where the effect was most pronounced. For this reason the pulse repetition and fluence have been limited to respectively 50 Hz and 300 mJ/cm^2 during fabrication.
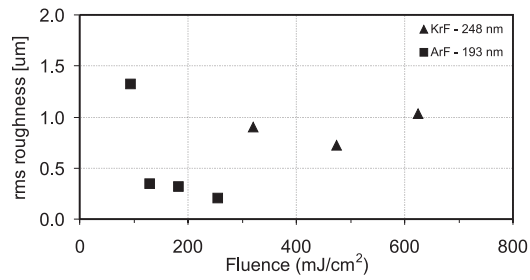
Figure 5.4: Rms surface roughness for grooves ablated in PMMA at both wavelengths. The applied method was hybrid mask scanning.
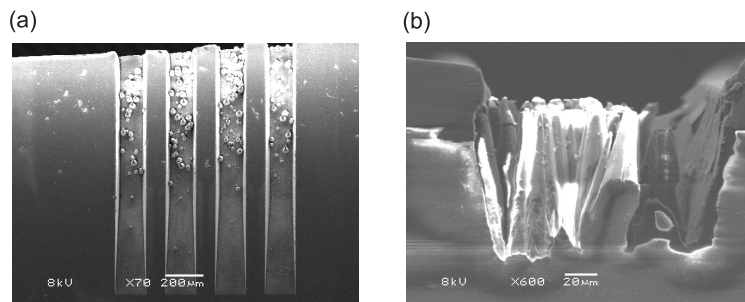

Figure 5.5: SEM image of a groove array ablated in PC at 193 nm: top view (a) and cross-section (b).
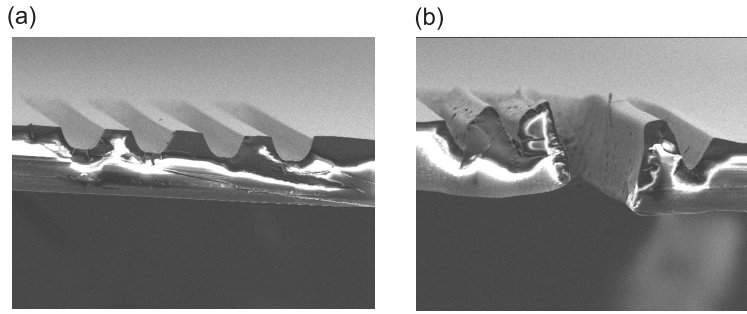
Figure 5.6: PMMA ablated at 248 nm (690 mJ/cm^2) with the hybrid mask scanning method. (a) at 5 Hz and (b) at 100 Hz.
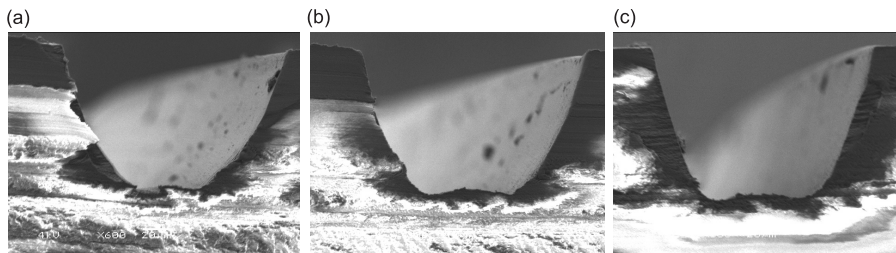

Figure 5.7: Grooves ablated in PMMA at 193 nm with (a) 94 mJ/cm^2, (b) 130 mJ/cm^2, (c) 182 mJ/cm^2.

Note that the fluence level determines the wall angle of the grooves: higher fluences produce steeper walls. This is qualitatively illustrated in figure 5.7.

- Number of passes over a single trench

The number of scan times has been varied while keeping the total number of fired pulses constant. Figure 5.8 summarizes the results: if a single square aperture is used, more passes speed up the ablation process; for the hybrid mask technique, the gain in speed is very little or even absent. This behavior can be explained based on the angle of the material surface that undergoes ablation. This angle equals $atan(d/a)$ with d the depth of the groove obtained in a single scan and a the aperture size. It is obvious that for the scanning aperture technique, this angle is rather large when the grooves are ablated in one scan (38°). This large angle will decrease the fluence on the surface and slow down ablation. When a trench is ablated by scanning the beam several times in succession, the ablating surface will be much more horizontal and the ablation speed will increase. From the graphs depicting the surface roughness, the same conclusions can be drawn: in case of aperture scanning, multiple passes are benefitial. In case of hybrid mask scanning there is little difference.
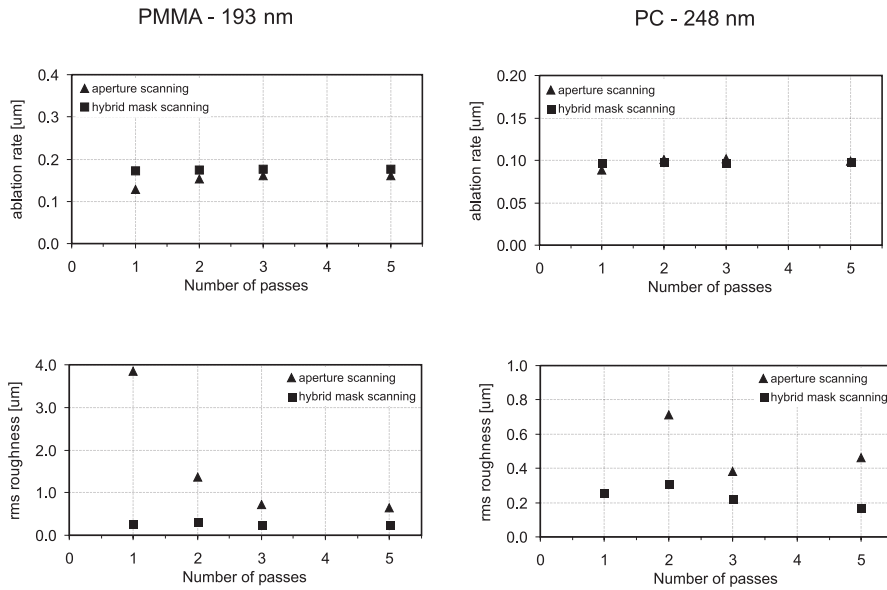
PMMA - 193 nm

PC - 248 nm

Figure 5.8: Ablation rate and rms roughness versus the number of beam passes for PC and PMMA.

We can thus conclude that the most suitable fabrication technique is either ablating PMMA at 193 nm or PC at 248 nm. Due to the higher etch rates of PMMA, this material has been preferred for prototype fabrication of the plates. The hybrid mask scanning technique was applied because it reduces the fabrication time one order of magnitude compared to aperture scanning: only 20 minutes were needed to create the full groove structure. A suitable combination of fluence and pulse frequency prevented the substrate from deformation: 20 Hz pulses at 270 mJ/cm^2. Both can be increased to some extent for even faster operation. The trenches were scanned twice but strictly speaking, this was not required.

After laser ablation of the grooves, the substrates were rinsed with distilled water and dried with nitrogen to remove debris particles as much as possible.

5.2.3 Insertion of the fibers

After laser ablation of the trench arrays, the fibers are inserted in the individual grooves and fixed with UV curing glue. The set-up used for this purpose is given in figure 5.9: it is basically used to guide an array of POFs through 2 standard MT ferrules and stretch them. The fibers are automatically separated by a pitch of roughly 250 μm. Then the groove plate is aligned with the fibers and pushed against them until they fully entered the grooves. Finally, UV curing glue is used to fix the fibers permanently in the grooves. Afterwards a smooth facet is obtained by cutting the whole with a hot knife at 110 °C.
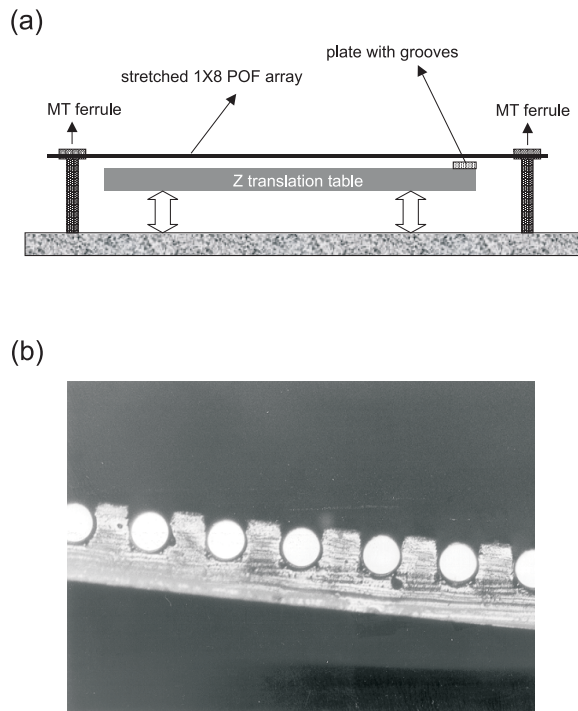
Figure 5.9: Set-up for fixing the fibers into the grooves (a). POFs glued into a plate with a groove array (b).

POF	fiber diameter (min/max)	pitch	Y position
125/63	119 ± 7 (105/135)	249 ± 10	± 10
125/116	125 ± 2 (120/129)	248 ± 6	± 4.8

Table 5.3: Measured POF diameters and positional accuracies of the POFs in a single plate and their standard deviations expressed in μm [2]. Target pitch is 250 μm. Note the high diameter tolerance for the 125/63 Asashi POF.

5.2.4 Stacking of the plates

The following step in the assembly process of the ferrule is stacking the substrates on top of each other. Accurate stacking is obtained by applying a technique called 'virtual' alignment. This method is based on the use of two key instruments: a translation stage with micron precision and two cameras that can move independently. The principle is explained in figure 5.10. The 'virtual' alignment technique is extremely suitable for quick and flexible assembly of prototype devices and avoids the use of mastertools or alignment masks.

5.2.5 Experimental results on the ferrule assembly

Positional accuracy of the POF cores in a single plate

The exact fiber positions are verified by scanning the knife-cut facet of the plate with an RCLED on a high-accuracy translation stage. A detector is attached to the other end of the POFs and measures the transmitted power for every position of the RCLED.

Two different fibers have been used for the experiments, both having a specified nominal outer diameter of 125 μm. One type has a core diameter of 116 μm (Toray) and the other features a smaller core of 63 μm (Asashi). The results are represented in table 5.3 and the measured quantities are indicated in figure 5.11.

The standard deviation on the fiber core position in a single row is quite large but one should consider that non-concentricity of the core and non-uniformity of the cladding diameter contribute significantly to this phenomenon. The positional accuracy in case of the commercial Toray POF (with a more uniform cladding diameter) is much better than for the Asashi type.

Positional accuracy of the POF cores in a stack

The same measurement procedure is repeated for a stack of plates. But this time the pitch in both the X and Y direction is measured. The results are represented in table 5.4 and the measured quantities are indicated in figure 5.12a. A front image of a stack is given in figure 5.12b.
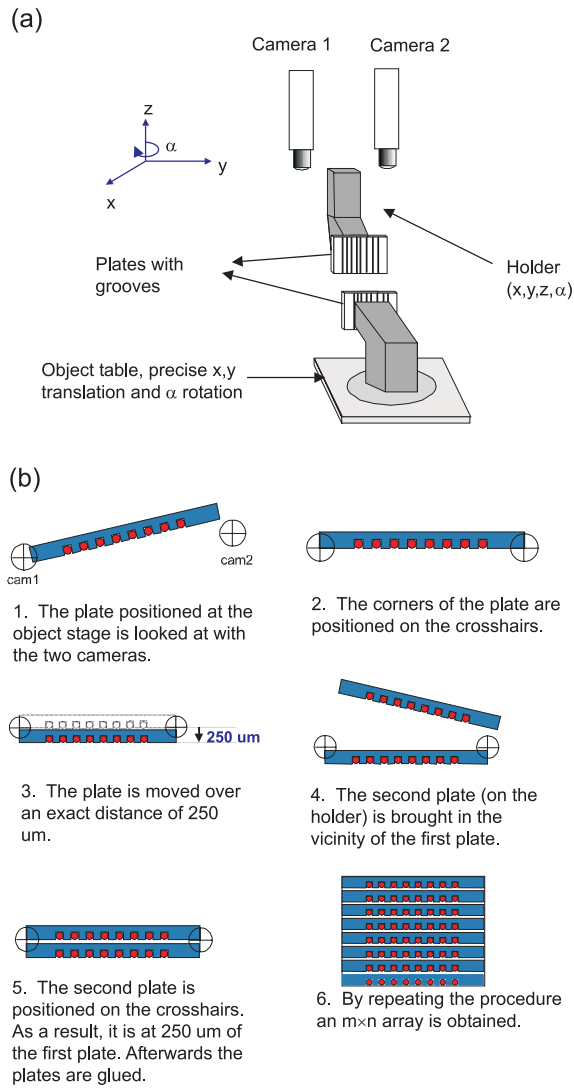
216

(a)

Camera 1   Camera 2

z

α

y

x

Plates with
grooves

Holder
(x,y,z,α)

Object table, precise x,y
translation and α rotation

(b)

cam1   cam2

1. The plate positioned at the
object stage is looked at with
the two cameras.

2. The corners of the plate are
positioned on the crosshairs.

↓ 250 um

3. The plate is moved over
an exact distance of 250
um.

4. The second plate (on the
holder) is brought in the
vicinity of the first plate.

5. The second plate is
positioned on the crosshairs.
As a result, it is at 250 um of
the first plate. Afterwards the
plates are glued.

6. By repeating the procedure
an m×n array is obtained.

Figure 5.10: 'Virtual' alignment set-up [2] (a). Stacking procedure for the fiber
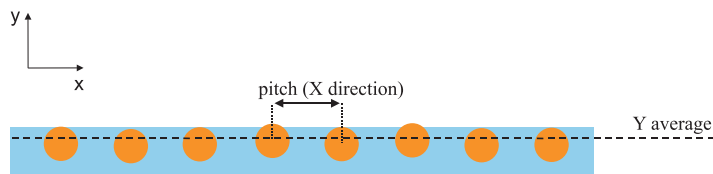arrays with 'virtual' alignment (b).

y

x

pitch (X direction)

Y average

Figure 5.11: Definition of the quantities in table 5.3.

217

		pitch in X direction		pitch in Y direction	
POF	array	target	measured	target	measured
125/63	4×8	250	249 ± 10	250	246 ± 11
125/116	2×8	250	248 ± 6	280	279.5

Table 5.4: Measured positional accuracies of the POFs in a stack of plates and their standard deviations expressed in μm. The pitch in X direction is taken from the previous table. Note that the target pitch in the Y-direction for the Toray POF was 280 μm during the test as no plates of smaller thickness were available at that time.
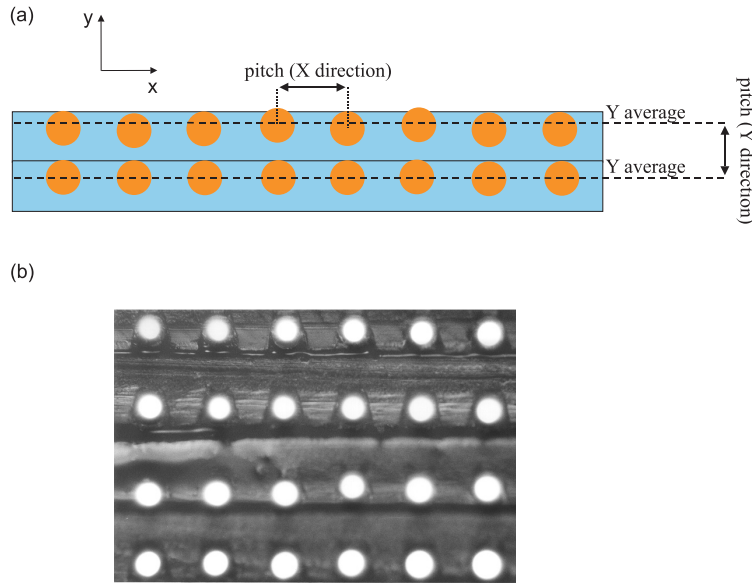

Figure 5.12: Definition of the quantities in table 5.4 (a). Front view on a 4×8 stack (b).

5.3 Fabrication of a mastertool for alignment of a VCSEL chip with an MT connector

As stated before, polymer fibers and surface emitting sources (VCSELs and RC-LEDs) offer quite some potential in cost-effective, short-distance parallel interconnects. Key advantages of these surface emitting devices are: on-wafer testing facilities, reduced packaging costs and availability in 2D arrays. In this section a VCSEL/POF module assembly is described that uses a laser ablated tool for aligning the VCSEL chip with the MT ferrule. A more elaborate description of the
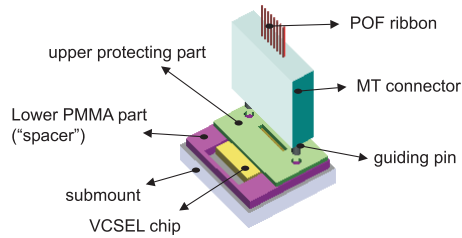
Figure 5.13: Assembly of the VCSEL/POF module.

assembly process and the coupling measurements[2] can be found in [5].

5.3.1 Integration scheme

The fully assembled module is depicted in figure 5.13. An MT connector in which an array of plastic optical fibers (Toray 125/116) is connectorized and terminated, can be plugged in and out of the heterogeneous opto-electronic assembly. The latter consists of a carrier (glass, ceramic) on which a VCSEL chip is mounted. The carrier features a high thermal conductivity, excellent mechanical stability and is suitable for surface patterning with a metal layer (wirebonding). In the carrier two large holes are drilled to receive the alignment pins of the connector through the spacer. Due to the large holes, mounting of the chip only needs little positioning accuracy ($\pm$ 100 μm).

Next, a spacer is fixed on the same mount and encloses the chip. As this part features high-accuracy alignment holes for the MT pins of the connector (700 μm diameter), it is essential for proper operation of the module that this spacer is accurately aligned with the VCSEL-chip. For this purpose a mastertool is applied. This is a component that will not be part of the assembly but will be used as an aid for aligning two or more subparts of the module. In this particular case it needs alignment features that allow an accurate positioning of the spacer with respect to the VCSEL-chip. This is achieved with a high-accuracy translation and rotation stage, equipped with cameras that visualize the relative position of the mastertool and chip.

Finally, an optical window can be put on top of the spacer to protect the VCSEL-chip from damage when the MT connector is not plugged in the module.

5.3.2 Fabrication of the mastertool

The mastertool is essentially a plate in polycarbonate with a nominal thickness of 250 μm, suitable for ablation with an excimer KrF laser [6]. Two important features are laser ablated on the mastertool: two 700 μm holes with a spacing of 4.6 mm

---

[2]The mastertool we fabricated has been applied by A. Van Hove for alignment of the VCSEL chip in a transmitter module for datacom purposes.
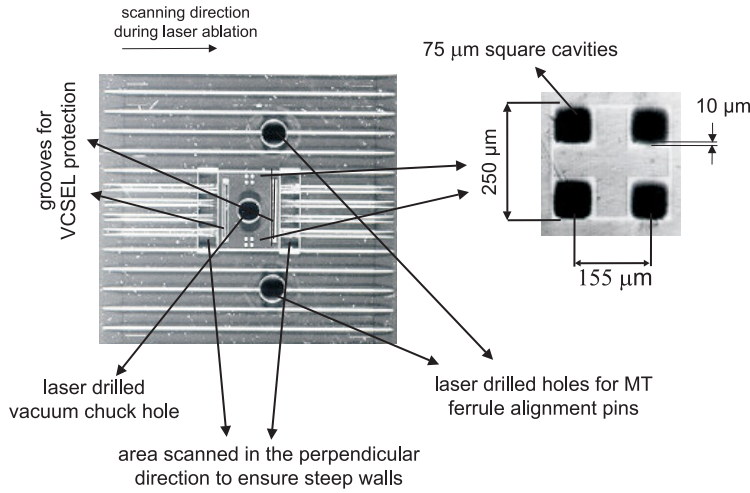
Figure 5.14: Laser ablated mastertool in a PC plate with a thickness of 250 μm (KrF laser, 10 Hz).

for receiving the MT pins of the connector and two features that can be aligned with the metallized alignment crosses on the chip. A suitable pattern consists of 4 squares of 75 μm spaced by 155 μm as depicted in figure 5.14. From the figure it can be seen that the alignment crosses of the chip can be fitted in the squares. The pattern has been created by using a 200 μm aperture (on-target spot of 50 μm for a demagnification of 4$\times$) and scanning ablation down to a few microns deep. The holes for the MT pins have been created by percussion drilling through the entire substrate.

A small difference in height is desired between the top surface of the spacer and the VCSEL-chip in order to avoid damage of the chip by the MT connector. This working distance —it equals the distance between the individual VCSELs and their corresponding fibers— has been chosen 50 μm. This distance complicates accurate alignment of chip and spacer if the mastertool has no surface relief, due to the cameras' limited depth of focus (at a magnification of 300$\times$ for precise alignment). For this reason a central island of 2$\times$2.5 mm^2 was created on the mastertool by laser ablation of the surrounding material to a depth of 50 μm. When the spacer is picked up by the mastertool, it fully fits in the lower area. Once it is brought in the desired position, the chip will make physical contact with the island on the mastertool. As the on-target laser beam is much smaller than the dimensions of the ablated area, scanning was necessary to process the entire surface. A square beam aperture of 2.5 mm —the largest available on the ablation mask at that time— was selected and corresponded to a 620 μm spot on-target for a demagnification of 4$\times$. Between the scanned strips an overlap of 20 μm was chosen to avoid the formation of bumps due to the non-vertical side walls of the grooves. In the center of the island a through-hole is ablated to allow vacuum clamping of the chip. A rectangular cut-out (0.150$\times$2 mm^2) was provided at both sides of the island to

protect the VCSELs areas from damage.

Due to the chosen scanning direction, the side walls at the left and right side of the island feature a very slow ramp ($\theta_{ramp} \sim 5°$ with respect to the horizontal). This can complicate the placement of the spacer around the chip. Therefore both sides of the island have been additionally scanned in the perpendicular direction. This ensures steep walls with an angle slightly smaller than 80°.

After ablation the mastertool has been rinsed with isopropylalcohol and dried with pressurized air in order to remove debris.

5.3.3   Experimental results on assembly and coupling losses

The assembly set-up is able to position the components within an accuracy of 5 to 10 μm. During the tests two different mastertools have been employed. One type is a laser ablated structure and has been described above. The other tool has been obtained by microdrilling and does not feature the central island. The tolerance and edge quality of the alignment features on the laser ablated tool are much better than in the microdrilled component. This is due to the fact that alignment marks are not ablated through the polymer and due to the edges which are less prone to crumbling off.

The VCSELs (lasing threshold 1.5 mA, maximum output power 1 mW) emit in the 650 nm region and POF attenuation in this wavelength range can be estimated at 1.2 dB/m. Typical termination losses in the MT connector are 0.5 dB including 0.3 dB Fresnel losses. Coupling losses for the VCSEL-POF module as low as 1-1.4 dB have been measured for a 20 cm POF link length [5]. Taking the termination losses, POF attenuation (0.33 dB) and NA mismatch[3] (2.13 dB) into account, losses due to misalignment can be neglected. Cross-talk between the channels remained below -45 dB.

5.4   Conclusions

It has been shown that excimer laser ablation is a viable microfabrication technique for components with microalignment features. Two particular applications have been discussed.

The first one concerns a 2D ferrule for POF fibers. This ferrule contains a stack of PMMA plates with microgrooves, ablated with the ArF excimer laser. These grooves have dimensions that correspond to the diameter of the plastic fibers and have been fabricated with micron accuracy. It has been shown that mask projection can considerably speed up the fabrication process. A suitable process window for laser ablation of the grooves was defined and experimentally verified. The grooves have been fabricated with ArF pulses of 270 mJ/cm^2 at 20 Hz, resulting in an etch rate of 215 nm/pulse and a wall angle of 78°. Experimental results show that the accuracy of the fiber positions in the stack is of the order of 1-2 μm within the same plate and 4-5 μm in the vertical direction. These promising average values

---

[3]The spontaneous emission from the VCSEL causes a relatively important amount of light to be emitted outside the NA of the POF.

are accompanied by standard deviations up to 11 μm. They are largely due to the non-uniformity of the plastic fibers as experimentally verified.

The second component is an aid for accurate alignment of a VCSEL-chip with a surrounding spacer. This mastertool in PC is equipped with MT pin holes, alignment features for the chip, a vacuum chuck hole and a central island. It has been fabricated by scanning excimer laser ablation (KrF ablation, 180 mJ/cm^2 at 10 Hz). The obtained tolerances on the alignment components were within 2 μm and largely surpassed the assembly accuracy.

Bibliography

[1] M. Madou, "Fundamentals of microfabrication", ISBN 0849394511, CRC Press, New York, 358-359 (1997).

[2] T. Coosemans, PhD thesis in preparation, INTEC, Ghent University.

[3] K. Naessens, A. Van Hove, T. Coosemans, S. Verstuyft, H, Ottevaere, L. Vanwassenhove, R. Baets and P. Van Daele, "Fabrication of microgrooves with excimer laser ablation techniques for optical fibre array alignment purposes", in Laser Applications in Microelectronic and Optoelectronic Manufacturing V, San Jose, USA, Proc. SPIE **3933**, 309 (2000).

[4] K. Naessens, A. Van Hove, T. Coosemans, S. Verstuyft, P. Van Daele and R. Baets, "Microgroove fabrication with excimer laser ablation techniques for optical fiber array alignment purposes", in First International Symposium on Laser Precision Microfabrication, Omiya, Japan, Proc. SPIE **4088**, 327 (2000).

[5] A. Van Hove, "Termination and interconnection technology for parallel opto-electronic systems", PhD thesis, INTEC, Ghent University (2001).

[6] A. Van Hove, J. Haes, K. Naessens, B. Dhoedt, R. Baets and P. Van Daele, "MT compatible red VCSEL module for parallel optical interconnections", in Optoelectronic Interconnects VII; Photonics Packaging and Integration II, San Jose, USA, Proc. SPIE **3952**, 134 (2000).

Chapter 6

Microlens design and fabrication for single-mode fiber coupling

A comprehensive study of fiber-to-fiber coupling is conducted based on Gaussian beam calculus. The insertion of microlenses in the optical paths is evaluated and it is shown how higher coupling efficiencies and/or relaxed alignment tolerances can be achieved by well-considered lens design. Suitable microlenses have been fabricated with excimer laser ablation as described in chapter 4 and their optical performance is experimentally evaluated.

6.1   Introduction: SM fiber-to-fiber coupling

In chapter 5 the importance of cost-effective and low-loss optical interfacing between chips and/or fibers was emphasized. Although refractive structures might be employed in any of these interfaces, we will focus on one particular application: coupling between single-mode fibers (SMF). Contrary to POF or multimode glass fiber, alignment tolerances are much tighter for SM fibers.

As will be shown, microoptics can considerably enhance this coupling in terms of efficiency and alignment tolerances.

SMF connectors for single fibers are commercially available in multiple standards. They all show excellent insertion losses below 0.2-0.3 dB. In figure 6.1 the most important types are given: ST ("Straight Tip"), SC ("Channel Connector") and FC ("Face Contact"). As optical interconnects are typically used to handle large data streams in parallel, there is a growing interest in multifiber implementations. These interconnects, either in a 1-D (e.g. MT) or 2-D array configuration, suffer from very tight alignment tolerances, high sensitivity to the presence of dust particles and/or lack of commercial availability. The alignment tolerances in case of an MT ferrule do not only apply to the position of the fiber holes −a maximum coupling
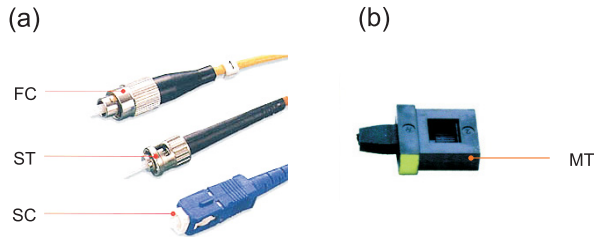
Figure 6.1: Commercial SM connectors for single (a) and multiple fibers (b).

loss of 0.3 dB assumes a maximum hole eccentricity below 0.7 μm$-$ but also to the diameter of the alignment pins and their relative position towards the fibers. As an indication, the required tolerance on the pin diameter can be as low as 0.1 μm and increases the connector manufacturing cost considerably.

Microlenses in the optical pathway can expand and collimate the light beams of the fibers. The larger beam sizes lead to more relaxed transversal and longitudinal alignment tolerances for the relative position of both connector parts and thus to potentially lower assembly costs.

A comprehensive description of the (multiple) SMF-to-SMF coupling problem and a discussion about the advantages of microoptics in the optical path can be found in section 6.3 of this chapter.

6.2 Calculation of coupling efficiency

A critical aspect of the coupling problems mentioned in the previous paragraph is related to the coupling performance of the interface between fibers. Next to long-term stability, sensitivity to thermal variations and mechanical stresses, this performance is mainly determined by the maximum light coupling efficiency between the fiber modes and its sensitivity to alignment errors. In this section we will focus on both parameters. Although only the specific coupling problem of SM fiber-to-fiber is elaborated, we chose to keep the analysis more general. This means that some coupling expressions will feature an arbitrary scalar field next to the fiber mode, making them applicable to fiber-to-chip coupling problems as well.

Within the scalar approximation, the power coupling efficiency between a normalized field ψ_1 and the fiber mode ψ_2 (figure 6.2) can be determined by evaluation of the overlap integral [1]

$$\eta = \left| \int \int_S \psi_1 \psi_2^* dS \right|^2 \tag{6.1}$$

in any plane where both modes are present. In the next sections, expressions for the fiber mode are derived based on the Gaussian beam model.
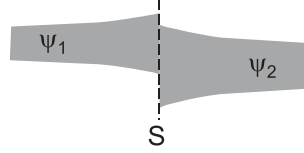
Figure 6.2: Overlap of two optical fields.

6.2.1 Gaussian approximation of the SM fiber modal field

A step-index SM fiber typically has a core diameter D of 9-10 μm and a refractive index contrast Δn of the order of 0.001 and lower. Single-mode operation is achieved when the normalized frequency of the propagating field $V = (D/2)k\sqrt{n_{core}^2 - n_{cladding}^2}$ is below 2.405 and the corresponding mode is denoted HE_{11}. The wavelength at which V equals 2.405 is called the cut-off wavelength.
The distribution of the transversal field component of HE_{11} can be adequately approximated by a Gaussian profile. There are several ways to find a suitable Gaussian fit. In general equating the $1/e$ field width usually leads to a poor approximation and should be avoided. Best results are achieved when the launching power of the Gaussian into HE_{11} is maximized, which is equivalent to maximizing the overlap between the mode and the Gaussian field.
If the normalized fiber mode is denoted $\psi(r, \phi)$, this overlap is determined by

$$\rho = \left| \int \int \psi(r, \varphi) \cdot \sqrt{\frac{2}{\pi w_f^2}} e^{-\frac{r^2}{w_f^2}} r dr d\varphi \right|^2 \tag{6.2}$$

and approaches 1 as the Gaussian fit matches the true fiber mode. w_f is the semi-diameter of the waist or semi-waist of the Gaussian profile. It can be shown that the Gaussian approximation gives rise to $\rho \geq 0.96$ for V between 1.924 and 4.329. In this frequency range w_f can be approximated by [2]

$$\frac{w_f}{D/2} = 0.65 + 1.629V^{-3/2} + 2.879V^{-6}$$

Corning SMF-28 single-mode fiber is considered the standard optical fiber for telephony, cable television, submarine and private network applications in the transmission of data, voice and/or video services. With a core diameter of 8.3 μm, a refractive index difference of 0.36% and a nominal refractive index of 1.468, we can calculate for $\lambda = 1.55$ μm that $V = 2.096$ and $w_f = 5.1$ μm. According to the specifications the semi-diameter of the mode-field indeed equals $5.2 \pm$ 0.4 μm. The true HE_{11} and Gaussian field approximation are given in figure 6.3.

6.2.2 Gaussian beam propagation model

The following sections will discuss the coupling efficiency (CE) and tolerances for misalignments. Analytical expressions for CEs are preferred as they provide a more
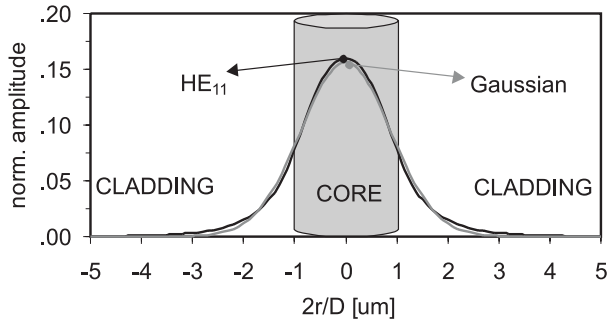
Figure 6.3: HE_{11} and its Gaussian approximation.

clear understanding of how several design parameters (fiber and/or waveguide mode size) and misalignments situations (longitudinal, transversal and angular) impact the CE.

It has already been shown that the transverse electrical field distribution of the SMF mode can be successfully approximated by a Gaussian shape. To evaluate the overlap integral (6.2) at a given plane in an optical system[1] in which a Gaussian beam is launched, we need expressions for the field distributions at that plane. We will now investigate the behavior of Gaussian beams in such systems, starting with the simple case of propagation in a uniform, lossless medium.

An elliptical Gaussian mode in the waist plane ($z = z_0$) is expressed as

$$\psi(x', y') = \sqrt{\frac{2}{\pi w_{ox} w_{oy}}} e^{-\left(\frac{x'^2}{w_{ox}^2} + \frac{y'^2}{w_{oy}^2}\right)}$$

with

$$x' = x - x_0$$
$$y' = y - y_0$$

w_{ox} and w_{oy} are the semi-waist sizes of the beam in respectively the x- and y-direction and the maximum field amplitude is located at (x_0, y_0).

As this mode propagates a distance $z - z_0$ along the z-axis in a uniform lossless medium with refractive index n and wave number $k_0 = 2\pi/\lambda$, the normalized transverse field can be calculated based on the Kirchoff-Huygens diffraction integral (paraxial wave approximation)

$$\psi(x', y', z - z_0) = A e^{-\left[\frac{x'^2}{w_x^2(z-z_0)} + \frac{y'^2}{w_y^2(z-z_0)} + j\frac{nk_0}{2}\left(\frac{x'^2}{R_x(z-z_0)} + \frac{y'^2}{R_y(z-z_0)}\right) + j\phi(z-z_0)\right]} \quad (6.3)$$

---

[1] An 'optical system' can be a simple flat interface between two different optical materials, a layer of an optical material, a lens-shaped interface, but also more complex concatenation(s) of the former.
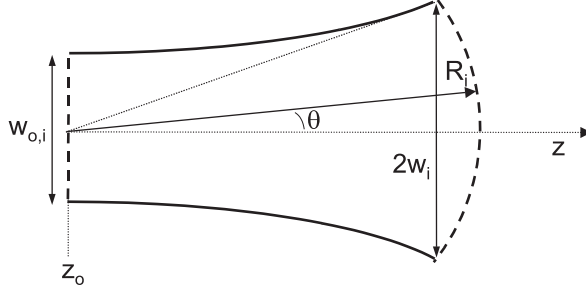
Figure 6.4: w_i and R_i of a Gaussian beam propagating along the z-axis.

$w_{0,i}$ [μm]	θ_i [deg]	$w_i(0)$ [μm]	$w_i(10\ \mu$m) [μm]	$w_i(100\ \mu$m) [μm]
1.0	28.0	1.0	5.0	49.4
2.0	14.1	2.0	3.2	24.8
5.2	5.4	5.2	5.3	10.9

Table 6.1: θ_i, w_i and R_i for some typical beam waist values ($\lambda = 1.55\ \mu$m).

with

$$
\begin{aligned}
A &= \sqrt{\frac{2}{\pi w_x w_y}} \\
\phi(z - z_0) &= \tfrac{1}{2} atan\left(\frac{2(z-z_0)}{k_0 n w_{ox}^2}\right) + \tfrac{1}{2} atan\left(\frac{2(z-z_0)}{k_0 n w_{oy}^2}\right) + n k_0 (z - z_0) \\
w_i(z - z_0) &= w_{0,i}\sqrt{1 + \left(\frac{2(z-z_0)}{k_0 n w_{0.i}^2}\right)^2} \\
R_i(z - z_0) &= (z - z_0)\left(1 + \left(\frac{k_0 n w_{o,i}^2}{2(z-z_0)}\right)^2\right)
\end{aligned}
\tag{6.4}
$$

A is a normalization factor and ϕ consists of a phase term $n k_0 (z - z_0)$ similar to a plane wave phase and a correction for Gaussian beams. w_i and R_i are respectively called semi-width of the beam and wavefront radius of curvature. The index i refers to the direction transverse to the propagation axis, either x or y.

The progress of w_i and R_i during beam propagation is illustrated in figure 6.4. Some numerical examples are given in table 6.1. In the far field approach $z - z_0 \to \infty$, the diffraction angle θ defined as the asymptotic divergence angle of the beam can be calculated from w_i via

$$
\theta_i = \frac{2}{k_0 n w_{0,i}}
$$

This expression indicates that small waists induce highly divergent beams and that the refractive index of the medium will limit the far field divergence with respect to free space. From R_i we can conclude that the beam behaves as a plane wave in the vicinity of the waist $(R \to \infty)$ and develops into a spherical wavefront in the far field.

Although expression (6.3) for the diffracted Gaussian field is very useful for analyzing beam propagation in a single and uniform medium, it becomes less manageable when propagation through successive materials with various refractive indices and non-planar interfaces (lens surfaces) is examined. Therefore we introduce the complex beam parameter q [3]

$$\frac{1}{q_i} = \frac{1}{R_i} - j\frac{2}{k_0 n w_i^2}$$

This beam parameter is easily traced if the optical system can be accurately described by the propagation or ABCD matrix. In this formalism an optical system is mathematically described by a 2×2 matrix which links the position and direction of an outgoing ray[2] with these of an incident ray (figure 6.5):

$$\left[\begin{array}{c} x_2 \\ \alpha_2 \end{array}\right] = \left[\begin{array}{cc} A & B \\ C & D \end{array}\right] \left[\begin{array}{c} x_1 \\ \alpha_1 \end{array}\right]$$

Strictly speaking this formalism is only valid for paraxial rays, i.e. rays that are close to and nearly parallel to the optical axis. Departures from this assumption (aberrations) are neglected.

It can be shown that an optical system with matrix $\left[\begin{array}{cc} A & B \\ C & D \end{array}\right]$ manipulates the incident Gaussian beam with beam parameter q_{in} according to

$$q_{out} = \frac{Aq_{in} + B}{Cq_{in} + D} \tag{6.5}$$

Figure 6.6 shows a few examples of ABCD-matrices of elementary structures that will be used in the coupling analysis below.

As an example, we can apply this technique to the simple case of Gaussian beam propagation through a homogeneous medium of length $z - z_0$. At the beam waist ($z = z_0$) we can write $q_{in,i} = -j\frac{2}{k_0 n w_{oi}^2}$. Using the appropriate ABCD-matrix, $q_{out,i}$ can be calculated via equation (6.5). Separating the imaginary from the real part of $1/q_{out,i}$ provides R_i and w_i equaling (6.4).

If a system consists of n concatenated subparts of which the propagation matrices are known, the overall optical behavior is in the geometrical approach prescribed by the following ABCD matrix (figure 6.7)

$$\left[\begin{array}{cc} A & B \\ C & D \end{array}\right] = \left[\begin{array}{cc} A_n & B_n \\ C_n & D_n \end{array}\right] \cdots \left[\begin{array}{cc} A_2 & B_2 \\ C_2 & D_2 \end{array}\right] \left[\begin{array}{cc} A_1 & B_1 \\ C_1 & D_1 \end{array}\right]$$

---

[2]In the approximation that the wavelength of the EM wave is considered very small compared to spatial variations in the optical structure, this wave can be modeled by rays pointing towards the local direction of propagation. Using the laws of refraction and reflection (geometrical optics theory), these rays can be traced through an optical system. The geometrical wavefront is locally orthogonal to the ray direction and can be constructed by considering sufficient rays through a system. As the geometrical approach is justified, this geometrical wavefront will be a close approximation of the physical one.
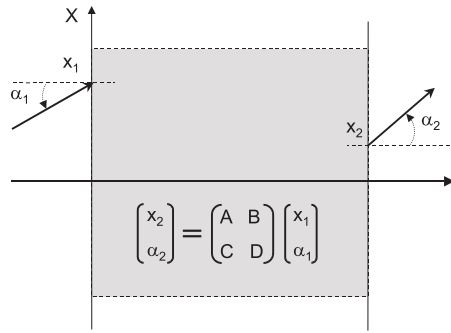
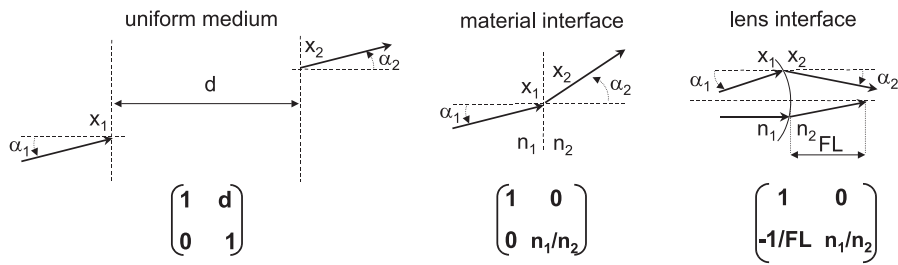Figure 6.5: ABCD-matrix formalism.

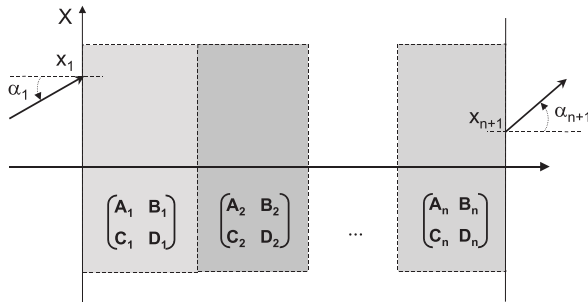Figure 6.6: Some ABCD-matrices of common optical structures.

Figure 6.7: An optical system consisting of several subsystems with known ABCD matrices.
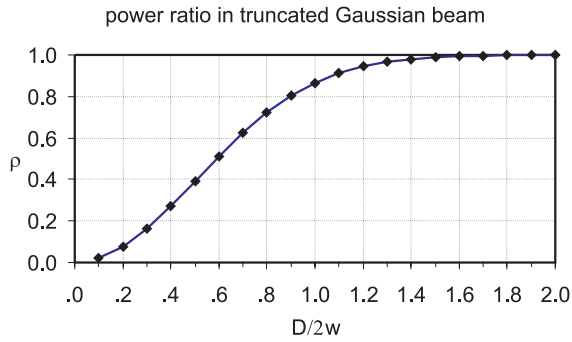
Figure 6.8: Power transmitted by a truncated Gaussian beam as a function of the aperture to beam diameter ratio.

6.2.3 Gaussian beam truncation

An important issue in dimensioning an optical system is truncation or clipping of the Gaussian beam. This can be due to the limited size of an optical component, e.g. the diameter of a lens or aperture. This truncation induces losses in power transfer. If ρ denotes the fractional power of a Gaussian beam contained within an aperture with diameter D, then ρ can be calculated as

$$\rho = \frac{\int_0^{2\pi} \int_0^{D/2} e^{-\frac{2r^2}{w^2}} r dr d\varphi}{\int_0^{2\pi} \int_0^{\infty} e^{-\frac{2r^2}{w^2}} r dr d\varphi} = 1 - e^{-2\frac{(D/2)^2}{w^2}} = 1 - e^{-\frac{D^2}{2w^2}}$$

where w is the semi-width of the Gaussian beam.

Figure 6.8 shows that the transmission equals 99 % for an aperture diameter of $3w$. Next to power loss, beam clipping also changes the propagation characteristics of the beam and thus affects the analysis in the following sections. A detailed study of this problem can be found in [4, 5].

6.2.4 Power coupling efficiency of a Gaussian beam into a SM fiber

In a next section the coupling between two SM fibers is considered. Arguments can be put forward to introduce microoptical functionality in the light path from one waveguide or fiber to the other. A discussion of the benefits of this approach should be based on detection and comprehension of the critical coupling parameters on one side, and a solid optimization procedure for the optics design on the other side. Before looking at microoptics, let us first consider the simple case of coupling an arbitrary Gaussian mode to a fiber without any intermediate optics as depicted in figure 6.9. The Gaussian beam waist and the fiber are separated by a distance Δz. The fiber is oriented along the beam propagation direction except for a small

but arbitrary alignment error. The incident beam can originate from either another fiber or a chip. Using the ABCD-matrix formalism it is possible to find an analytical expression for the overlap between the propagating beam and the fiber mode[3]. The position and orientation of the fiber is described by Δx, Δy, Δz, $\Delta\varphi_x$ and $\Delta\varphi_y$ as shown in the figure. Compared to the situation of a perfectly aligned incident Gaussian beam with the fiber mode ($\Delta x = \Delta y = \Delta z = \Delta\varphi_x = \Delta\varphi_y = 0$), we can interpret Δx and Δy as transversal, $\Delta\varphi_x$ and $\Delta\varphi_y$ as angular and Δz as longitudinal misalignments. In appendix A the overlap integral is explicitly calculated and the coupling efficiency can be expressed as:

$$\eta(\Delta x, \Delta y, \Delta z, \Delta\varphi_x, \Delta\varphi_y) = \eta_0(\Delta z)\eta_x(\Delta x, \Delta z, \Delta\varphi_x)\eta_y(\Delta y, \Delta z, \Delta\varphi_y) \qquad (6.6)$$

with

$$\eta_0 = \frac{4}{\sqrt{(\frac{w_x}{w_0}+\frac{w_0}{w_x})^2+\left(\frac{nkw_xw_0}{2R_x}\right)^2}\sqrt{(\frac{w_y}{w_0}+\frac{w_0}{w_y})^2+\left(\frac{nkw_yw_0}{2R_y}\right)^2}}$$

$$\eta_x = e^{-\left[\frac{2\Delta x^2}{w_0^2}-\frac{2\left(\frac{\Delta x^2}{w_0^4}-(\frac{k\Delta\varphi_x}{2})^2\right)\left(\frac{1}{w_x^2}+\frac{1}{w_0^2}\right)+\frac{n^2k^2\Delta x\Delta\varphi_x}{R_xw_0^2}}{(\frac{1}{w_0}+\frac{1}{w_x})^2+\left(\frac{nk}{2R_x}\right)^2}\right]}$$

$$\eta_y = e^{-\left[\frac{2\Delta y^2}{w_0^2}-\frac{2\left(\frac{\Delta y^2}{w_0^4}-(\frac{k\Delta\varphi_y}{2})^2\right)\left(\frac{1}{w_y^2}+\frac{1}{w_0^2}\right)+\frac{n^2k^2\Delta y\Delta\varphi_y}{R_yw_0^2}}{(\frac{1}{w_0}+\frac{1}{w_y})^2+\left(\frac{nk}{2R_y}\right)^2}\right]}$$

For reasons of clarity, we omitted writing out explicitly the Δz dependence of w_x, w_y, R_x and R_y. They can be calculated via (6.4). η_0 is the coupling efficiency when only longitudinal misalignments are present. η_x and η_y can be interpreted as correction factors for the coupling efficiency when misalignments in respectively the X-Z and Y-Z plane are present.

When fiber-to-fiber coupling problems are considered, all waist sizes reduce to $w_{ox} = w_{oy} = w_0 = 5.1 \ \mu$m. Different waists in the x and y direction can be applied for fiber-to-chip coupling, but this will not be discussed here.

Coupling efficiencies differing from unity give rise to losses in the optical power transfer from one light guiding medium to another. As these are usually measured in dB, we define the optical loss as

$$L = -10\log(\eta) \qquad (6.7)$$

An important advantage of this approach is that the total loss in an optical link can be simply expressed as the sum of the losses in the successive coupling structures and transmission media.

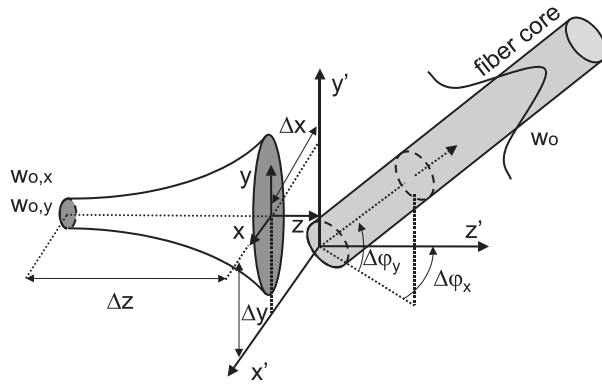[3]Reflection and scattering losses will be ignored throughout this chapter.

Figure 6.9: Coupling of a Gaussian beam into a SMF mode.

6.3 SMF-to-SMF coupling

6.3.1 Performance benchmarks for fiber connectors

In this section different connector layouts −with or without integrated optical functionality− will be analyzed. A clear performance interpretation of and comparison between these connectors implies some measurable quantities, i.e. benchmarks that give a realistic image of the quality. These can be of a various nature and the most important ones are

- mechanical robustness including response to stress (tensile, compressive, torsion, ...), shock and vibrations

- flammability

- corrossive properties

- temperature behavior

- humidity resistance

- ease of handling

- optical coupling efficiency and backreflection

- endurance, measured in times mating/demating before mechanical wear or additional optical losses are introduced

The simplified analysis below is limited to evaluation of the optical properties of the connector and the effects of misalignments between the connector blocks. Quantities that will be used as a benchmark for the connector are

234

- minimum coupling loss L_{min}

- 0.2 dB tolerance for transversal, longitudinal and angular misalignments, equaling a coupling efficiency of 0.96

- 0.3 dB tolerance for transversal, longitudinal and angular misalignments, equaling a coupling efficiency of 0.93

The tolerance values were chosen based on a typical specification sheet for SMF connectors that indicates 0.2 dB as a typical and 0.3 dB as a maximum loss.

6.3.2 Bare fiber-to-fiber coupling

As already mentioned in the introduction, well-performing SMF connectors for single fibers are widely commercially available. However, increasing data transfer and the tendency to parallel handling of large data streams appeal for multi-fiber connector solutions. One commercial connector type is MT which handles 8 or 12 SMFs in a 1-dimensional array design. This type suffers from three important disadvantages:

1. Fixation of the fibers is realized by high-accuracy V-grooves in the ferrule[4]. The manual insertion process should be performed in a controlled environment, making the connector not field-installable. In addition the V-groove approach is incompatible with 2-dimensional fiber arrays as this would require successive stacking of parts with V-grooves. This procedure would inevitably introduce important alignment errors as can be deduced from table 5.4.

2. Imposing the same loss tolerances on MT as on single-fiber ferrules greatly complicates the connector fabrication and fiber insertion process. This implies an increased manufacturing and installation cost.

3. If the connector is opened and closed in an environment where dust particles are present, then it is very well possible that such particles end up between the mating connector parts. Due to this contamination the optical coupling performance can degrade drastically.

4. As the tight tolerances concern in particular the alignment between the two mating connector parts and since the connector coupling has a semi-permanent nature (connectors can be mated and demated several times during their lifetime), the performance of the connector largely depends on the frequency of this operation and the skills of the operator. This is an undesirable property and a well-considered connector design should therefore eliminate this operator-dependency as much as possible.

---

[4]The ferrule is the part of the connector which holds the fibers and alignment pins or holes. It is usually made from precisely shaped ceramics, stainless steel or engineered plastics. Together with the plastic package, the ferrule makes up the connector.
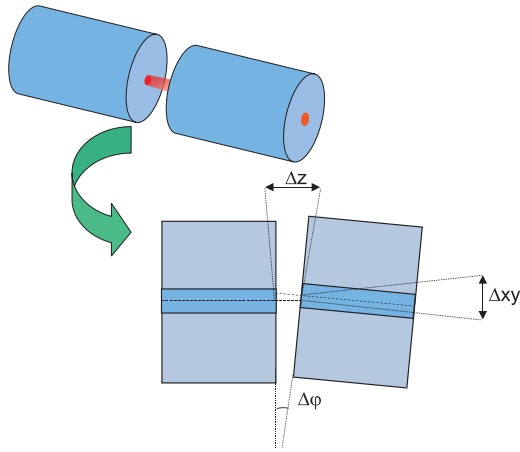
Figure 6.10: Geometry of SMF-to-SMF coupling.

	air		index-matching	
loss tolerance	0.2 dB	0.3 dB	0.2 dB	0.3 dB
Δxy [μm]	± 1.1	± 1.4	± 1.1	± 1.4
Δz [μm]	± 23.8	± 29.3	± 35	± 43
$\Delta\varphi$ [deg]	± 1.2	± 1.4	± 0.8	± 1.0

Table 6.2: Alignment tolerances for SMF-to-SMF coupling. Semi-waist of the fiber mode is 5.1 μm.

In a bare SMF coupling situation two fibers are brought in close proximity and are aligned, i.e. the fiber axes are parallel and the fiber core areas overlap as good as possible (figure 6.10). Still, the power coupling from one fiber to another will differ from 100 % due to alignment errors. Using equation (6.6) and (6.7) and assuming a Gaussian approximation with $w_0 = 5.1$ μm for the fiber mode, the tolerances for the alignment errors can be calculated (table 6.2). As there is no mode mismatch involved in coupling from one SM fiber to another, the maximum coupling efficiency is 100 % excluding reflection losses. Note that these losses can always be minimized by applying suitable AR coatings on the optical interfaces. Unity coupling efficiency can thus be obtained for perfectly aligned butt-coupled fibers. The tolerances have been calculated for either an air gap between the fibers or an index-matching gel. Due to rotational symmetry, Δx and Δy are equal and denoted by Δ_{xy} in the table.

These tolerance values indicate that longitudinal misalignments are of little importance since the acceptable Δz is quite large[5]. The transversal offset or tilt tolerances however, are very stringent as respectively a mere 1.4 μm or 1.4° mis-

---

[5]Most SMF connectors enforce phsyical contact between the facets of the two fibers for proper operation. This avoids reflection losses as the air gap between the fibers is absent. This condition is not considered here.

	air		index-matching	
loss tolerance	0.2 dB	0.3 dB	0.2 dB	0.3 dB
δxy [μm]	± 0.6	± 0.7	± 0.6	± 0.7
δz [μm]	± 11.9	± 14.7	± 17.3	± 21.3
$\delta\varphi$ [μm]	± 0.6	± 0.7	± 0.4	± 0.5

Table 6.3: Fiber position tolerances in each connector part. These tolerances assume that equally large fabrication inaccuracies are present in both connector parts. Air and an index-matching gel are chosen as intermediate medium.

alignment is sufficient to reach the upper limit of acceptable losses. Note that these tolerances are valid if only one alignment error is present at the time. Every combination of misalignments results in even lower tolerances. In figure 6.11 the coupling losses are calculated for different misalignments.

From fabrication point of view, the connector tolerances are even more stringent since fiber-to-fiber coupling requires two identical connector blocks. As a single manufacturing technique is used for both blocks, the average geometrical inaccuracies in the parts are equal. Consequently, the allowable connector fabrication tolerances δz, δxy and $\delta\phi$ for *each* connector block are simply half of the previously calculated values (worst case scenario). Table 6.3 summarizes the results for these tolerances.

Present micromanufacturing and replication techniques allow very precise mass fabrication, compatible with these accuracies and at an acceptable cost. Still, the Δxy tolerance might be problematic for alignment between both connector pieces as this procedure not only depends on the fabrication accuracy but also on the operator skills and the frequency of mating and demating. It is therefore instructive to make a distinction between two sources of fiber misalignment:

1. <u>Fabrication errors</u>: errors in the *individual* fiber position and orientation in each connector block, related to the connector fabrication and installation (fiber insertion) process. The tolerances on the final component are well-known and controllable since they are determined by the fabrication technology. Tolerances for these errors are indicated with δ_i and they are given in table 6.3 for the bare fiber-to-fiber coupling case.

2. <u>Operation errors</u>: errors introduced due to mating and demating of the connector parts. In other words, they relate to misalignment between the connector blocks and thus to *all* fibers. Since this typically takes place in non-controlled environment and since this operation can be repeated any number of times, these misalignments are unknown and rather uncontrollable. Tolerances for these errors concern the alignment between the connector blocks and are indicated by Δ_i. Table 6.2 summarizes these tolerances for the bare fiber-to-fiber coupling case.

It is without discussion that any connector design that reduces the influence of alignment errors due to operation circumstances (i.e. large operation tolerances)
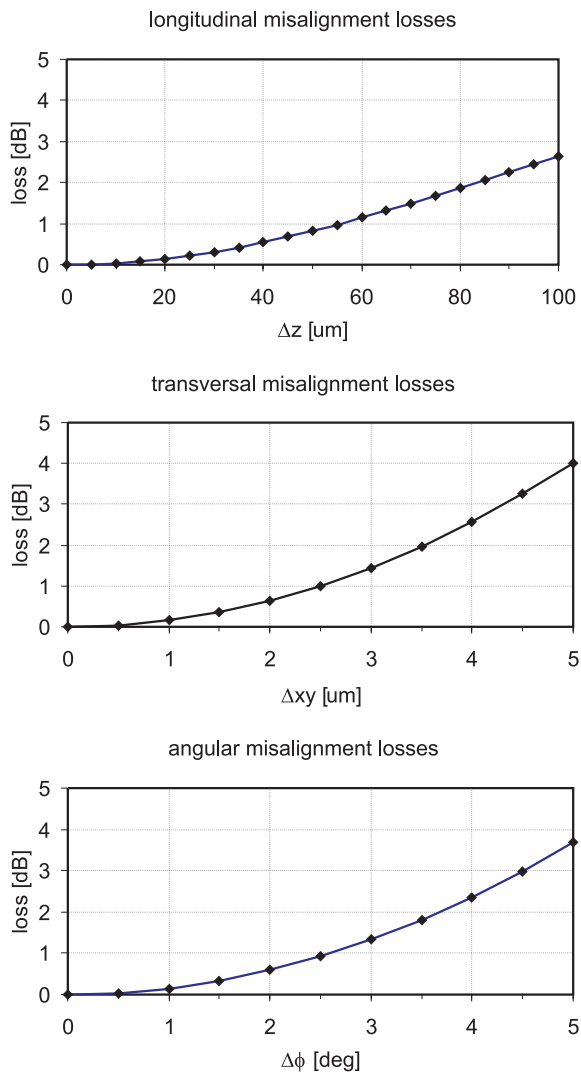
Figure 6.11: Coupling losses due to longitudinal, transversal and angular misalignments for bare SMF-to-SMF coupling.

improves the reliability and thus the performance of the connector. Even if this happens at the expense of more stringent but feasible fabrication tolerances.

6.3.3 Microlens-equipped SMF connectors

In this part we investigate a connector design based on integrated microoptics. Lenses that are inserted in the beam path between the fiber facets basically serve to reconstruct the wavefront from one fiber at the facet of the other. If we denote the q-factor of the Gaussian fiber mode at the facet as q_0, then the ABCD-matrix of the connector should fulfill the condition

$$Cq_0^2 + (D - A)q_0 - B = 0 \qquad (6.8)$$

which results from expression (6.5) with $q_{out} = q_{in} = q_0$.
As the coupling problem is perfectly symmetric and as the connector structure must allow semi-permanent coupling (open and close the light path), the connector should consist of two symmetrical parts that can be attached and detached. To minimize reflection losses, it is desirable to limit the number of interfaces in the connector. Taking the former considerations into account, this minimum is two interfaces per connector part: one facing the fiber, the other facing the mating part. One implementation of such a connector system is given in figure 6.12. Every fiber-to-fiber optical path ('channel') is equipped with dedicated microoptics: two lens surfaces, one for every connector part. Note that symmetry implies that a beam waist should be located centrally between the two lenses.
The connector should be able to handle many fibers in parallel in either a 1-D or 2-D configuration. For this reason the most suitable fiber attaching technique will likely not be a V-groove clamping system due to misalignment errors that would be introduced in stacking of V-grooves. A more convenient design of the connector parts would feature on one side an array of holes with (sub)micron accuracy. In these holes the fibers are inserted and fixed afterwards. At the other side an array of microlenses is fabricated that is perfectly aligned with these holes. The mechanism that is responsible for relaxing the transversal misalignments between the connector blocks can be understood from figure 6.12. Each lens will convert the fiber beam to a larger beam waist $2w_a$ in the center of the optical path between both fibers. These waists coincide right between the connector blocks. As a result, the operation tolerances for transversal misalignment will depend on the overlap of both beam waists instead of the smaller fiber modes. In the following analysis we will concentrate on the light path and the microoptical design, making abstraction of the exact fiber clamping technique.
The exposed lens surfaces are a disadvantage of the design in figure 6.12 as they make the connector vulnerable to damage. A cover plate can be used for optics protection, but these issues will not discussed here.
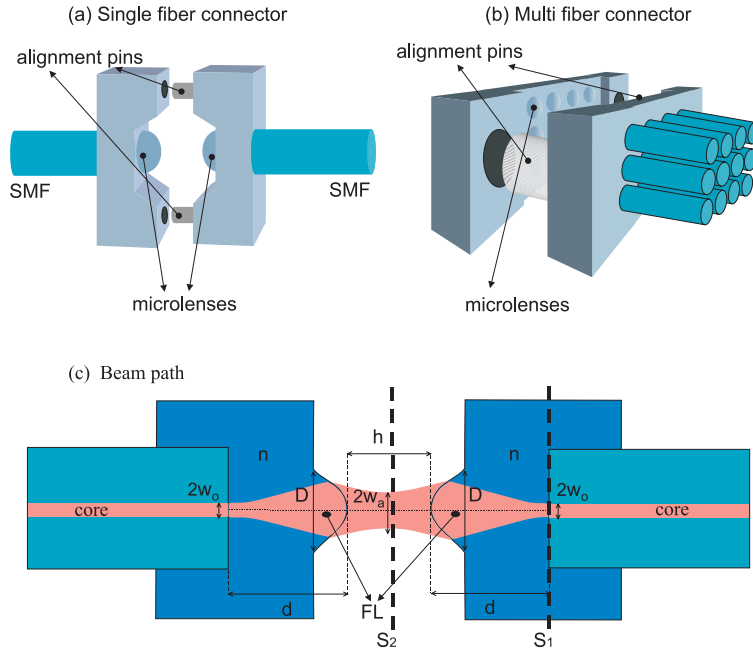
239

(a) Single fiber connector

(b) Multi fiber connector

(c) Beam path

Figure 6.12: SMF-to-SMF coupling with microoptics in the light path.

Paraxial optical analysis

For the microlens-equipped system we can calculate the ABCD-matrix as follows:

$$
M \;=\; \underbrace{\begin{bmatrix} 1 & d \\ 0 & 1 \end{bmatrix}}_{connector} \; \underbrace{\begin{bmatrix} 1 & 0 \\ \frac{-1}{FL} & n \end{bmatrix}}_{lens} \; \underbrace{\begin{bmatrix} 1 & h \\ 0 & 1 \end{bmatrix}}_{air\,gap} \; \underbrace{\begin{bmatrix} 1 & 0 \\ \frac{-1}{nFL} & \frac{1}{n} \end{bmatrix}}_{lens} \; \underbrace{\begin{bmatrix} 1 & d \\ 0 & 1 \end{bmatrix}}_{connector}
$$

The distance between the fiber facet and the lens surface or working distance is denoted with d, equaling an optical distance nd. The separation between the two lenses (air gap) is h, w_a is the semi-waist of the beam in the center and the focal lengths of the lenses are both FL. The connector blocks are made of a material with refractive index n at the wavelength of the fiber mode.

The minimum lens diameter D_{lens} is determined by the beam size at the lens interface and thus depends on d . It is given by

$$
D_{lens} = \rho w_{lens}
$$

with

$$
w_{lens} = w_0 \sqrt{1 + \left(\frac{2d}{knw_0^2} \right)^2}
$$

240

For a power transmission of at least 99 %, ρ should equal 3 or higher. In this case the minimum lens diameter is

$$D_{lens} = 3w_0\sqrt{1 + \left(\frac{2d}{knw_0^2}\right)^2}$$

Together with the focal length FL, d also determines the necessary separation h between both microlenses. This parameter can be calculated by demanding that the Gausian beam exiting the lens surface will converge to a beam waist ($R \to \infty$) at a distance $h/2$ from both lenses

$$h = 2\frac{\alpha_n d\left(\frac{\alpha_n d}{FL} - \alpha_n n\right) + \frac{1}{FL}}{\left(\frac{\alpha_n d}{FL} - \alpha_n n\right)^2 + \frac{1}{FL^2}} \tag{6.9}$$

or in a more conventional form

$$\frac{1}{h/2} = \frac{1}{FL} - \frac{n}{d + \frac{z_r^2}{d - nFL}} \tag{6.10}$$

with

$$\alpha_n = \frac{2}{knw_0^2} = \frac{1}{z_{r,n}}$$

$z_{r,n}$ is called the Rayleigh length[6] of the beam in the connector medium. It can be seen that for $z_{r,n} \to 0$, equation (6.10) reduces to the well known lens formula[7] in geometrical optics. The semi-waist of the image can be verified to equal

$$w_a = \frac{FL}{kw_o}\sqrt{\frac{4}{1 + \alpha_n^2(d - nFL)^2}}$$

Figure 6.13 illustrates the imaging behavior of a lens-shaped interface for several focal lengths.

We can summarize the upper formulae for the connector parameters as

general system

$$\begin{aligned}
h &= 2\frac{\alpha_n d\left(\frac{\alpha_n d}{FL} - \alpha_n n\right) + \frac{1}{FL}}{\left(\frac{\alpha_n d}{FL} - \alpha_n n\right)^2 + \frac{1}{FL^2}} \\[2mm]
D_{lens} &= 3w_0\sqrt{1 + (\alpha_n d)^2} \\[2mm]
w_a &= \frac{FL}{kw_0}\sqrt{\frac{4}{1 + \alpha_n^2(d - nFL)^2}}
\end{aligned} \tag{6.11}$$

The optical system is fully specified if two parameters from the set (FL, d, h) are chosen. In figure 6.13 two particular operation points can be distinguished:

---

[6] The Rayleigh length of a Gaussian beam is the distance over which the beam width increases from its waist size w_o to $\sqrt{2}w_o$. At z_r the wavefront curvature reaches a minimum.

[7] More specifically, this is —confusingly enough— the Gaussian form of the lens formula.
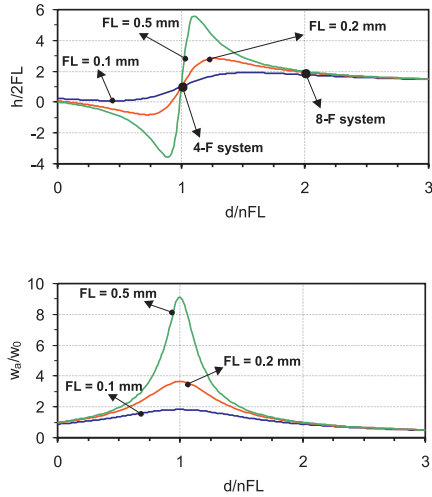
Figure 6.13: SMF waist imaging with a lens.

a) 4-F optical system

In case $d = nFL$ the connector parameters can be verified to be

4 − F system

$$
\begin{aligned}
d &= nFL \\
h &= 2FL \\
D_{lens} &= 3w_0\sqrt{1 + (\alpha_n d)^2} \\
w_a &= \frac{2FL}{kw_0}
\end{aligned}
\tag{6.12}
$$

This configuration is called a 4-F system since the distance between object and image plane equals $4FL$ if the system would consist of two lenses surrounded by air. Note that the choice of one parameter fully determines the 4-F system.

b) 8-F optical system

if $w_a/w_0 = 1$ and assuming that the focal length is large compared to z_r, then the connector parameters can be calculated:

8 − F system

$$
\begin{aligned}
d &= 2nFL \\
h &= 4FL \\
D_{lens} &= 3w_0\sqrt{1 + (\alpha_n d)^2} \\
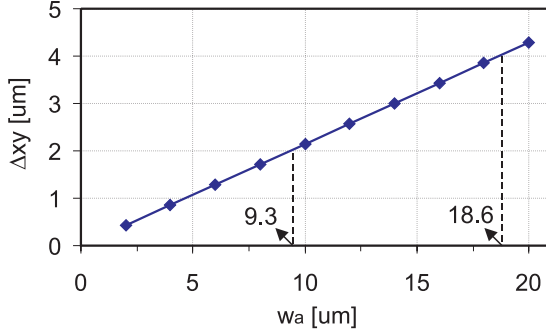w_a &= w_0
\end{aligned}
\tag{6.13}
$$

Figure 6.14: Dependence of the transversal tolerance Δxy on the semi-waist w_a between the connector blocks.

This system consists of successive lenses separated by an air gap of four times their focal length; the object and image are located at a distance $2nFL$ from the lenses. All beam waists that occur in the system equal the fiber mode size.

Note that the focal length, lens separation and working distance are independent of the beam size in case of a 4-F or 8-F system.

Design based on adjusting the transversal tolerance

From table 6.2 we learned that the tolerances for Δxy and $\Delta \varphi$ are respectively 1.1 μm and 1.2°. As the standard pitch for fiber interconnects is 250 μm and the multi-fiber connector will typically handle some 8×8 fibers, the facet dimensions of the ferrule should be at least 2×2 mm^2. If we assume that the fibers and ferrule facet are polished perfectly flat and normal to the fiber axes, then we can verify that the tolerance on tilt between the connector facets $\Delta \phi = 1.2°$ corresponds to a wedge-shaped gap of 42 μm. It is obvious that this tolerance requirement is easily fulfilled by the existing connector fabrication techniques. On the other hand, the accuracy on the transversal position of the fibers ($\Delta xy = 1.1$ μm) is of greater concern since wear of the connector blocks due to mating and demating can compromise the tight tolerance and might drastically decrease the endurance of the connector. It is therefore appropriate to relax that tolerance value to a more comfortable level, even if this implies sacrificing tilt tolerance.

Relaxing the transversal misalignment tolerances between the connector blocks requires a beam waist between the blocks which is larger than the fiber mode. This can be obtained by an optical system as mentioned above. Next to more relaxed transversal alignment tolerances, the larger beam reduces the connector sensitivity to dust particles and thus potentially allows operation of the connector in the field. For a given desired Δxy, a corresponding waist size can be found via equation (6.11). In the particular case of a 4-F optical system, the obtained tolerances for a range of semi-waists w_a are given in figure 6.14. As $w_a = w_0$ for the 8-F system, this optical layout cannot be used for enhancing the transversal tolerances. Before
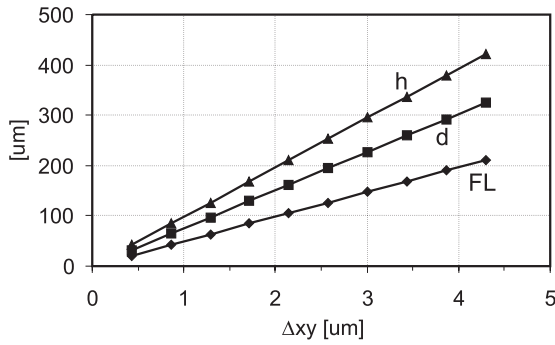
Figure 6.15: 4-F system parameters as function of the required transversal tolerance Δxy.

$\Delta xy_{0.2dB}$ [μm]	w_a [μm]	FL [μm]	d [μm]	h [μm]	D_{lens} [μm]
2	9.3	98.0	150.9	196.0	32.0
4	18.6	196.0	301.9	392.1	57.9

Table 6.4: 4-F system parameters for two values of Δxy.

analyzing the general case we will first consider the feasibility of a 4-F system.

a) 4-F system design

From expression (6.12) we can derive

$$
\begin{aligned}
FL &= \frac{kw_a w_0}{2} \\
d &= \frac{nkw_a w_0}{2} \\
h &= kw_a w_0 \\
D_{lens} &= 3w_0 \sqrt{1 + \left(\frac{w_a}{w_0}\right)^2}
\end{aligned}
\tag{6.14}
$$

for a given w_a. These relationships are depicted in figure 6.15.

In the following we will focus on two particular values for the transversal tolerances as this simplifies the analysis: $\Delta xy = 2$ and 4 μm. Both are feasible from a connector operation point of view, certainly when compared to the marginal 1.1 μm in case of bare fiber-to-fiber coupling. The fully specified 4-F designs that match these Δxy are given in table 6.4.

We performed a tolerance analysis on the connector design for the two systems given in the table. Losses due to connector fabrication and operation errors are treated separately. Losses due to the finite lens aperture are excluded since these lenses can virtually be made arbitrarily large up to the fiber pitch of 250 μm. This size is a multiple of the minimum lens diameter based on the 99 % transmission criterion (table 6.4). Note that δ is used to indicate tolerances related to dimensions
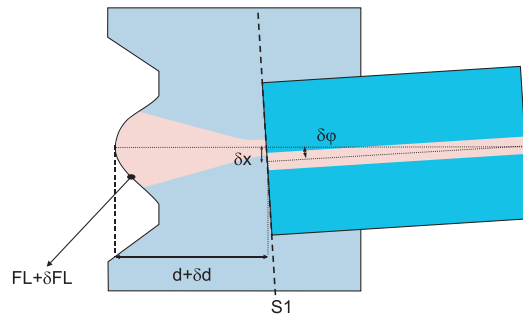
Figure 6.16: Alignment errors in a connector part due to fabrication inaccuracies.
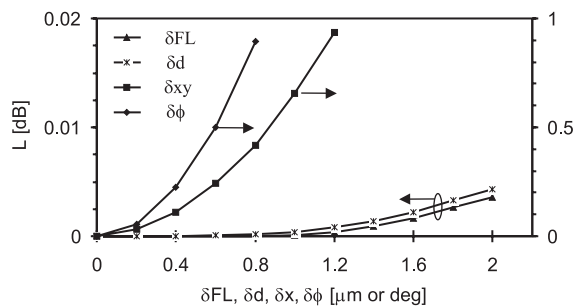

Figure 6.17: Losses due to fabrication errors in the parts.

inside each of the connector parts (fabrication tolerances), while Δ is related to connector part-to-part misalignments (operation tolerances).

- connector fabrication tolerances

In a typical connector manufacturing process a single master component is fabricated and afterwards replicated by e.g. a moulding technique. This means that fabrication errors in the master are copied into the replicas. Therefore it is instructive to consider losses due to fabrication errors that are present in both connector parts. A worst case scenario assumes that these inaccuracies are the same for each part (both in magnitude and sign, e.a. $\delta xy_{part\,1} = \delta xy_{part_2}$, etc.). The geometrical deviations considered in the analysis are depicted in figure 6.16.

The tolerances for such fabrication errors are given in table 6.5 and figure 6.17. They have been calculated using ASAP[8] (see Appendix B). The tolerances for transversal offset and tilt towards the microlenses are identical to the bare fiber-to-fiber coupling case with the connector material as propagation medium. This is

[8]ASAP is a raytracing tool that is capable of handling coherent field propagation and is a product of Breault Inc., Arizona, USA.

	identical errors in both parts			
	$\Delta xy_{0.2dB} = 2$ μm		$\Delta xy_{0.2dB} = 4$ μm	
loss tolerance	0.2 dB	0.3 dB	0.2 dB	0.3 dB
δd [μm]	± 17.5	± 21.6	$-21.1/+15.3$	$-25.4/+19.4$
δFL [μm]	$-14.4/+17.6$	$-16.1/+25.8$	$-10.9/+14.8$	$-14.1/+17.8$
δxy [μm]	± 0.6	± 0.7	± 0.6	± 0.7
$\delta\varphi$ [deg]	± 0.4	± 0.5	± 0.4	± 0.5

Table 6.5: Loss tolerances for fabrication errors in the connector blocks.
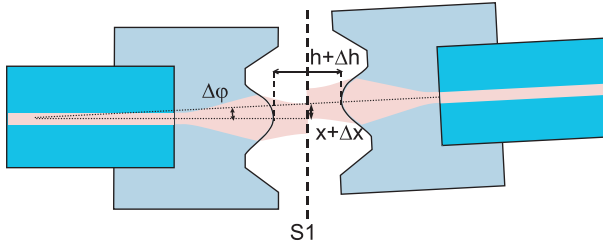

Figure 6.18: Alignment errors between two parts of a connector.

a natural consequence of the fact that the optics reproduce the wavefront coming from one fiber on the facet of the mating fiber.

From the results in the table, it can be concluded that the position and orientation of the fibers with respect to the lenses are very critical due to the small δxy and $\delta\varphi$ tolerances.

- block-to-block alignment (operation) tolerances

Table 6.6 and figure 6.19 summarize the tolerances for misalignments between the connector blocks as defined in figure 6.18. As expected, the transversal tolerances match the prescribed values of 2 and 4 μm. Due to the intermediate large beam waist, the exact distance between the connector facets has become even less important than in the case of bare fiber-to-fiber coupling. Note that these relaxed tolerances have been obtained at the price of a more restricted tilt tolerance between the parts.

b) General system

For a given w_a there is still a degree of freedom left in the design since the expression for w_a in (6.11) allows choosing either a value for d or FL before the system dimensions are fully determined. Figure 6.13 shows that there is a minimum value for FL for a predetermined w_a/w_0:

$$FL_{min} = \frac{kw_0 w_a}{2}$$

	$\Delta xy_{0.2dB} = 2\ \mu m$		$\Delta xy_{0.2dB} = 4\ \mu m$	
loss tolerance	0.2 dB	0.3dB	0.2 dB	0.3 dB
$\Delta h\ [\mu m]$	± 79.4	± 97.8	± 304.5	± 375.1
$\Delta xy\ [\mu m]$	± 2.0	± 2.5	± 4.0	± 4.9
$\Delta \varphi\ [deg]$	± 0.6	± 0.8	± 0.3	± 0.4

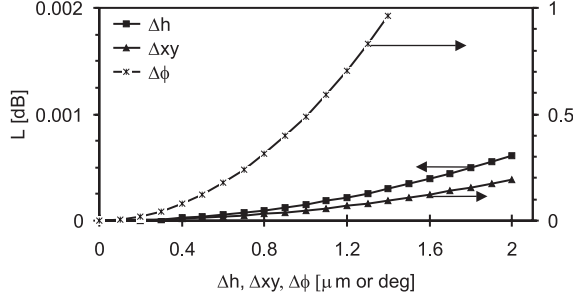Table 6.6: Loss tolerances for misalignment between the connector blocks.

Figure 6.19: Losses due to block-to-block alignment errors.

This value is reached for $d = nFL$, which is the 4-F system. The same graph indicates that for another value of d (and assuming $FL > FL_{min}$), a desired w_a/w_0 can be attained with a positive h. In any case the required focal length, working distance, lens separation and lens diameter will all be larger than in the 4-F case.

Paraxial lens shape calculation

In the previous paragraphs optimum focal lengths for connector lenses were calculated for desired misalignment tolerances. However, these values are insufficient to fully determine the 3-dimensional shape of the microlenses. As the fiber beam is rotationally-symmetric, the microlenses will show a circular footprint. The exact cross-section can be calculated by phase-matching the Gaussian beam coming from the fiber facet with the beam going to the waist w_a. If $\phi(x, y)$ denotes the phase change of the beam by the lens, then the phase match condition demands that (figure 6.20)

$$-\frac{nk(x^2 + y^2)}{2R_1} - \phi(x, y) = \frac{k(x^2 + y^2)}{2R_2}$$

with R_1 the fasefront curvature for the beam coming from the fiber and R_2 the curvature for the beam going to the waist w_a. $\phi(x, y)$ is the phase transformation due to the lens, given by
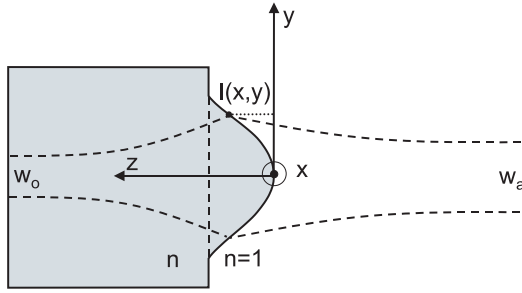
247

Figure 6.20: Phase matching condition at the lens interface.

$$\phi(x,y) = -k(n-1)l(x,y)$$

The lens profile $l(x,y)$ can now be calculated as

$$l(x,y) = \frac{x^2 + y^2}{2(n-1)}\left[\frac{n}{d(1+(\frac{nkw_0^2}{2d})^2)} + \frac{1}{\frac{h}{2}(1+(\frac{kw_a^2}{h})^2)}\right]$$

which is a parabola of the form $l(r) = cr^2$ with $r = \sqrt{x^2 + y^2}$ and c a constant. The radius of curvature R at the vertex is given by $\frac{(1+l'^2(r))\sqrt{1+l'^2(r)}}{l''(r)}$ and equals $1/2c$. The corresponding paraxial focal length is $R/(n-1)$.
In figure 6.21 the lens shape and its spherical approximation are given for the 4-F system with $w_a = 9.3$ μm. Note that the relevant part of the lens has only a diameter of $D_{lens} = 32$ μm (table 6.4).

6.3.4 Lens fabrication with scanning contour ablation

In the following we will discuss how microlenses can be fabricated that are suitable for SM fiber-to-fiber coupling. Although the experiments are limited to single fibers, they give a very good indication of how well microlenses can aid in relaxing alignment tolerances.

Lenses suitable for 4-F imaging of the fiber mode have been fabricated using the scanning contour technique described in chapter 4. In a next section experimental verification of the lens performance is based on measuring the coupling efficiency for a set-up as depicted in figure 6.25: two FC/PC connectorized SM fibers are brought in close approximation and point towards each other. A polymer plate is attached to each fiber facet with a UV curable adhesive and serves as substrate material for the microlens. Fixing the plate perpendicular on the fiber facet is facilitated by the large facet of the FC/PC ferrule. Polycarbonate ($n = 1.54$ at $\lambda = 1.55$ μm) was chosen as base material and is available from Goodfellow Inc. in 250 μm thickness.
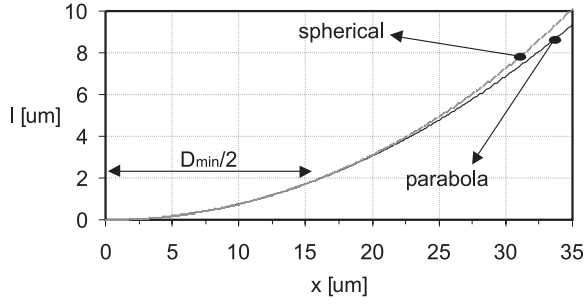
Figure 6.21: Lens cross-section and its spherical approximation for a 4-F system with $w_a = 9.3$ μm, corresponding to a tolerance $\Delta xy = 2$ μm. The radius of curvature at the vertex is 65 μm.

d [μm]	FL [μm]	h [μm]	w_a [μm]	D_{lens} (D_{min}) [μm]
230	149.7	299.3	14.2	70 (45.4)

Table 6.7: Lens parameters for fiber-to-fiber coupling with a 4-F microlens system in a 250 μm thick polycarbonate substrate. The radius of curvature at the vertex is 81 μm.

Taking into account a smoothing depth of 15 μm and a buried depth of 5 μm ($offset$ in equation (4.15)) for the lens, the working distance becomes 230 μm. The other lens parameters can now be calculated via expression (6.14) and are given in table 6.7. The obtained w_a should result in a $\Delta xy_{0.2dB} = 3.1$ μm.

A circular hole of 480 μm in a polyimide film (thickness 50 μm) has been laser-drilled and served as beam aperture. The on-target beam spot was 96 μm at a demagnification of 5×. Calculation of an optimum contour was performed taking this aperture size into account. The target lens shape and its approximation are given in figure 6.22. Only 13 contours were needed to obtain the fit with a calculated rms deviation over the entire surface of 59 nm.
The lens has been fabricated with the ArF excimer laser using a beam fluence of 180 mJ/cm^2, corresponding to an etch rate of 105.4 nm/pulse. For this purpose the MT ferrule is fixed in a holder inside the flow chamber. By coupling light from a red laser diode into the fiber, alignment of the fiber core with the excimer beam is obtained by using the TTL ("Through The Lens") camera on the workstation. As a result, the microlens is positioned right above the fiber core. After contour ablation, the same aperture is applied for smoothing the surface by drilling the lens 15 μm deeper (142 pulses).
Following this procedure, several SM fibers have been equipped with microlenses. Figure 6.23 shows an example.
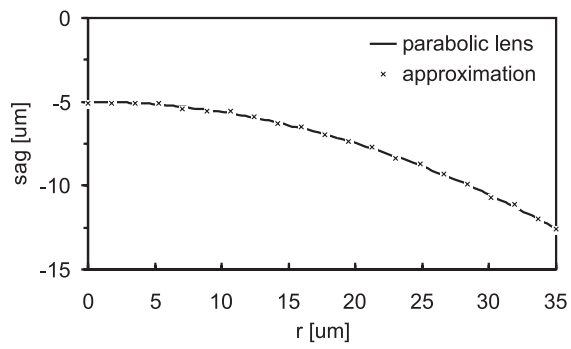
249

Figure 6.22: Semi cross-section of the parabolic lens shape and the calculated fit.

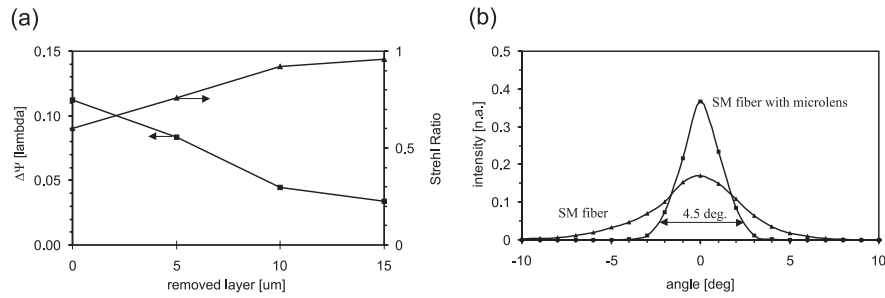Figure 6.23: Microlens equipped SM fiber.

Figure 6.24: Aberrations are measured in the central part (45 μm diameter) of the lens for different values of the removed layer thickness (a). Measured far field of a SM fiber with and without a microlens (b).

6.3.5 Lens performance

The laser ablated lenses have been evaluated in three different ways: measurement of the wavefront aberrations, far field distribution and fiber-to-fiber coupling efficiency.

Mach-Zehnder interferometer measurements

Wavefront aberrations have been measured in the central part of the microlens that transmits 99 % of the fiber beam (diameter = 45 μm). To determine the influence of the smoothing process after contour ablation, these aberrations have been evaluated for different thicknesses of the removed layer. The results are depicted in figure 6.24a: a removed layer of 15 μm (as required for the lens with $FL = 150$ μm) gives a Strehl Ratio of 0.96, corresponding to 0.034λ rms wavefront aberration. The lens can be considered diffraction-limited to both the Maréchal and Rayleigh criterion. Note that these measurements are performed at $\lambda = 633$ nm instead of 1.55 μm.

Far field measurements

In figure 6.24b the far field from a fiber with a microlens on top is compared to the case of a bare fiber without lens. The full angle $(1/e^2)$ is reduced from 10.5 to 4.5 degrees. Indeed, the larger beam waist that is produced behind the lens gives rise to a lower divergence. The measured angle corresponds to a beam waist of 13 μm, very close to the target value of 14 μm.

Coupling experiments

Two lensed fibers are brought in proximity as depicted in figure 6.25 and aligned at a distance of about 300 μm. The transmission losses are measured for the entire
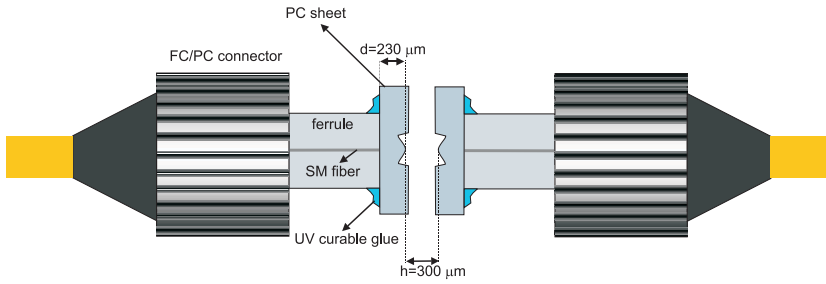
Figure 6.25: Fiber-to-fiber coupling with a 4-F microlens system.

end-to-end loss [dB]	calculated 4-F loss* [dB]	4-F transmission [%]
1.199	0.459	90.0
1.157	0.417	90.8
1.540	0.800	83.2
1.383	0.643	86.2
1.320±0.177	**0.580±0.177**	**87.6±3.5**
*Taking into account a loss per patchcord connector = 0.17 dB and a Fresnel reflection loss of 0.2 dB per lens.		

Table 6.8: Coupling losses for the set-up in figure 6.25 and the estimated losses for the 4-F lens coupling system.

system consisting of two patchcords with the intermediate lens-equipped free-space interconnection. This experiment has been repeated for a series of fibers that have been equipped with microlenses. The results are given in table 6.8. The coupling losses due to the 4-F lens system are estimated by excluding Fresnel reflections from the lens facets and the losses introduced by both fiber patchcords.

The average coupling efficiency of 88 % differs from the maximum value of 100 %, but can still be considered a promising result. It is to be expected that a better positioning accuracy would increase the coupling efficiency significantly: due to misalignments between the fiber core and the microlens, the beam at the exit pupil of the lens tends to become oblique and worsens the coupling.

The sensitivity of the coupling efficiency to transversal misalignments is given in figure 6.26. From the graph $\Delta xy_{0.2dB}$ can be estimated at 3.3 μm, corresponding rather well with the expected tolerance of 3.1 μm.

6.3.6 Conclusions

In this chapter the concept of microlens-equipped 2D connectors for single mode fibers is presented. This connector can potentially feature more relaxed transversal alignment tolerances compared to an ordinary bare fiber facet-to-facet type. For a desired mating tolerance, the lens characteristics and connector dimensions have been calculated.
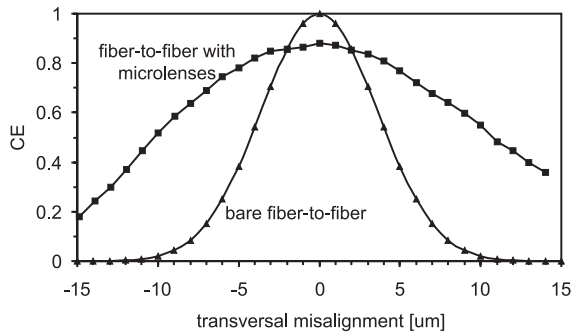
Figure 6.26: Measured coupling efficiency in function of the transversal misalignment between the fibers. For comparison, the calculated results for bare fiber-to-fiber coupling are added.

Scanning contour ablation has been applied to fabricate the desired lens shape in a polymer layer on top of a fiber facet. This lens is ablated in a PC substrate glued onto a FC/PC connector. Given a substrate thickness of 250 μm, a transversal misalignment tolerance of 3.1 μm can be obtained with a 4-F lens system. The ferrule facet allows easy adhesion with a UV curable glue and ensures that the polymer surface is perpendicular onto the fiber axis. Accurate positioning of the lens above the fiber core is obtained by coupling light from a red laser diode into the fiber and localization of the fiber spot.

The lenses have been evaluated in several ways: aberration measurements indicated that the lenses reach a Strehl Ratio of 0.96 and the beam spot size has been derived from far field measurements. Two lensed fibers have been aligned and coupling experiments showed that the average coupling efficiency of the 4-F microlens system can be estimated at 88 %. Although this value still differs significantly from a maximum efficiency of 100 %, it is to be expected that a better positioning of the lens above the fiber would further improve the coupling.

Appendix A Calculation of the overlap integral (6.6)

The field in the X-Y plane of the Gaussian beam entering from the left side in figure 6.9 can be derived from (6.3):

$$\psi(x, y, \Delta z) = Ae^{-\left[\frac{x^2}{w_x^2(\Delta z)} + \frac{y^2}{w_y^2(\Delta z)} + j\frac{nk_0}{2}\left(\frac{x^2}{R_x(\Delta z)} + \frac{y^2}{R_y(\Delta z)}\right) + j\phi(\Delta z)\right]} \tag{6.15}$$

since the mode profile is centered around $(x_0, y_0) = (0, 0)$.
A, ϕ, w_x, w_y, R_x and R_y are given by

$$
\begin{aligned}
A &= \sqrt{\frac{2}{\pi w_x w_y}} \\
\phi(\Delta z) &= \tfrac{1}{2}atan\left(\frac{2\Delta z}{nk_0 w_{ox}^2}\right) + \tfrac{1}{2}atan\left(\frac{2\Delta z}{nk_0 w_{oy}^2}\right) + nk_0(\Delta z) \\
w_i(\Delta z) &= w_{0,i}\sqrt{1 + \left(\frac{2\Delta z}{nk_0 w_{0.i}^2}\right)^2} \\
R_i(\Delta z) &= \Delta z\left(1 + \left(\frac{nk_0 w_{o,i}^2}{\Delta z}\right)^2\right)
\end{aligned}
$$

We now calculate the Gaussian fiber mode profile in the same plane, expressed in the same coordinate system. The Gaussian field *in* the fiber can be written as:

$$\psi_{fiber}(\mathbf{r}, \mathbf{r}_0) = \frac{1}{w_0}\sqrt{\frac{2}{\pi}}e^{-\frac{|\mathbf{r}-\mathbf{r}_0|^2}{w_0^2}}e^{-jn_f\mathbf{k}\cdot\mathbf{r}} \tag{6.16}$$

where $\mathbf{r}$ is the coordinate of a point in the fiber, $\mathbf{r}_0$ the fiber center in the plane containing $\mathbf{r}$ and perpendicular to the fiber axis, n_f the effective index and $\mathbf{k}$ the propagation vector of the fiber mode (oriented along the fiber axis).
$\mathbf{k} \cdot \mathbf{r}$ in the phase term can be expressed as ($X'Y'Z'$ coordinate system):

$$
\begin{aligned}
\mathbf{k} \cdot \mathbf{r} &= k(cos(\Delta\varphi_y)sin(\Delta\varphi_x), sin(\Delta\varphi_y), cos(\Delta\varphi_x)cos(\Delta\varphi_y)) \cdot (x', y', z') \\
&= -k(cos(\Delta\varphi_y)sin(\Delta\varphi_x)x' + sin(\Delta\varphi_y)y' + cos(\Delta\varphi_x)cos(\Delta\varphi_y)z')
\end{aligned}
\tag{6.17}
$$

From the figure it can be seen that

$$
\begin{aligned}
x' &= x + \Delta x \\
y' &= y + \Delta y \\
z' &= z + \Delta z
\end{aligned}
\tag{6.18}
$$

So (6.17) becomes

$$
\mathbf{k} \cdot \mathbf{r} = k(cos(\Delta\varphi_y)sin(\Delta\varphi_x)(x + \Delta x) + sin(\Delta\varphi_y)(y + \Delta y) + cos(\Delta\varphi_x)cos(\Delta\varphi_y)z)
$$

Right outside the fiber facet, the complete phase term can be written as:

$$
-jnk(cos(\Delta\varphi_y)sin(\Delta\varphi_x)(x + \Delta x) + sin(\Delta\varphi_y)(y + \Delta y) + cos(\Delta\varphi_x)cos(\Delta\varphi_y)z)
\tag{6.19}
$$

Note that n is the refractive index of the medium *outside* the fiber and should not be confused with the refractive index of the fiber.

The exponential in (6.16) can be calculated using the following expression for $|\mathbf{r} - \mathbf{r}_0|$ in the plane of the fiber facet:

$$
\begin{aligned}
|\mathbf{r} - \mathbf{r}_0|^2 &= (x' + y' + z')^2 \\
&= \frac{cos^2(\Delta\varphi_y)x'^2 + (1 - cos^2(\Delta\varphi_y)sin^2(\Delta\varphi_x))y'^2 + sin(\Delta\varphi_x)sin(2\Delta\varphi_y)x'y'}{cos^2(\Delta\varphi_x)cos^2(\Delta\varphi_y)}
\end{aligned}
\tag{6.20}
$$

where we used

$$
z' = \frac{cos(\Delta\varphi_y)sin(\Delta\varphi_x)x' + sin(\Delta\varphi_y)y'}{cos(\Delta\varphi_x)cos(\Delta\varphi_y)}
$$

which expresses that $\mathbf{r}$ lies within the plane of the fiber facet. Using (6.18) we obtain an expression for $|\mathbf{r} - \mathbf{r}_0|^2$ in the XYZ coordinate system.

In general the misalignments are quite small, therefore we will simplify (6.19) and (6.20):

$$
\begin{aligned}
e^{-\frac{|\mathbf{r} - \mathbf{r}_0|^2}{w_0^2}} &\approx e^{-\frac{(x + \Delta x)^2 + (y + \Delta y)^2}{w_0^2}} \\
e^{-jn\mathbf{k}\cdot\mathbf{r}} &\approx e^{-jnk(\Delta\varphi_x(x + \Delta x) + \Delta\varphi_y(y + \Delta y) + z)}
\end{aligned}
\tag{6.21}
$$

For the calculation of the overlap integral (6.1), these simplified expressions allow a separate integration for x and y:

$$
\begin{aligned}
\eta &= \frac{2}{\pi w_x w_0} \left| \int_{-\infty}^{+\infty} e^{-\left[x^2(\frac{1}{w_x^2} + \frac{1}{w_0^2} + \frac{jnk}{2R_x}) + x(\frac{2\Delta x}{w_0^2} + jnk\Delta\varphi_x) + \frac{\Delta x^2}{w_0^2} \right]} dx \right|^2 \cdot \\
&\quad \frac{2}{\pi w_y w_0} \left| \int_{-\infty}^{+\infty} e^{-\left[y^2(\frac{1}{w_y^2} + \frac{1}{w_0^2} + \frac{jnk}{2R_y}) + y(\frac{2\Delta y}{w_0^2} + jnk\Delta\varphi_y) + \frac{\Delta y^2}{w_0^2} \right]} dy \right|^2
\end{aligned}
\tag{6.22}
$$

256

where we omitted phase terms that are independent of x and/or y since they do not contribute to η.

Before performing the integration, we note that

$$
\begin{aligned}
e^{-(ax^2+2bx+c)}dx &= \int e^{-a((x+\frac{b}{a})^2+\frac{c}{a}-(\frac{b}{a})^2)} \\
&= \sqrt{\frac{\pi}{a}}e^{-(c-\frac{b^2}{a})}
\end{aligned}
\tag{6.23}
$$

where we used the identity $erf(\infty) = 1$ in which $erf(x)$ is the Error function given by

$$
erf(x) = \frac{2}{\sqrt{\pi}} \int_0^x e^{-\xi^2}d\xi
$$

By using (6.23), we find an expression for η [6]:

$$
\eta = \eta_0 \eta_x \eta_y
\tag{6.24}
$$

with

$$
\begin{aligned}
\eta_0 &= \frac{4}{\sqrt{(\frac{w_x}{w_0}+\frac{w_0}{w_x})^2+\left(\frac{nkw_xw_0}{2R_x}\right)^2}\sqrt{(\frac{w_y}{w_0}+\frac{w_0}{w_y})^2+\left(\frac{nkw_yw_0}{2R_y}\right)^2}} \\
\eta_x &= e^{-\left[\frac{2\Delta x^2}{w_0^2}-\frac{2\left(\frac{\Delta x^2}{w_0^4}-(\frac{k\Delta\varphi_x}{2})^2\right)\left(\frac{1}{w_x^2}+\frac{1}{w_0^2}\right)+\frac{n^2k^2\Delta x\Delta\varphi_x}{R_xw_0^2}}{(\frac{1}{w_0}+\frac{1}{w_x})^2+\left(\frac{nk}{2R_x}\right)^2}\right]} \\
\eta_y &= e^{-\left[\frac{2\Delta y^2}{w_0^2}-\frac{2\left(\frac{\Delta y^2}{w_0^4}-(\frac{k\Delta\varphi_y}{2})^2\right)\left(\frac{1}{w_y^2}+\frac{1}{w_0^2}\right)+\frac{n^2k^2\Delta y\Delta\varphi_y}{R_yw_0^2}}{(\frac{1}{w_0}+\frac{1}{w_y})^2+\left(\frac{nk}{2R_y}\right)^2}\right]}
\end{aligned}
$$

η_0 is the coupling efficiency when neither transversal nor angular misalignments are present. η_x and η_y can be interpreted as correction factors for the coupling efficiency when the misalignments in respectively the X-Z and Y-Z plane are non-zero.

Appendix B Advanced Systems Analysis Program (ASAP)

Some of the connector tolerances have been calculated using a ray tracer rather than via an analytic approach. In the latter case a 2×2 ABCD-matrix was identified with each optical element in the beam path. By matrix multiplication it was possible to calculate the propagation of a Gaussian beam centered around the optical axis throughout the optical system. In some cases, offsets and angular misalignments of the beam with respect to the optical axis of the lenses needed to be incorporated. These calculations have been performed by a commercial ray trace software package.

ASAP is a non-sequential ray tracing CAD tool developed by Breault Research Organization, Tucson, Arizona. It is capable of predicting the propagation of incoherent and coherent fields through a multitude of lenses, apertures and geometrical structures. In the incoherent mode, ASAP simply traces rays through the system by taking the laws of refraction and reflection into account. A flux is attributed to each ray and optical analysis of the system uses the calculated ray distribution in user-defined planes.

Contrary to most other ray tracing tools, ASAP can also handle coherent fields and is thus able to simulate phenomena as diffraction and interference. This coherent field modeling is based on Gaussian Beam Decomposition (GBD). Just like other coherent modeling techniques (e.g. the angular spectrum method), GBD is based on scalar diffraction theory. The basic idea is to decompose a field distribution at an aperture into a set of spatially confined "fundamental beams" as depicted in figure 6.27. These beams are traced —including self-diffraction effects— towards the target surface where they are superposed. A suitable fundamental beam type is an astigmatic Gaussian TEM_{00} beam which is a solution of

$$\frac{\partial^2}{\partial x^2}E + \frac{\partial^2}{\partial y^2}E - 2jk\frac{\partial}{\partial z}E = 0$$

known as the paraxial Helmholtz equation[9]. E is the field amplitude with a slow z-dependence compared to the transverse variations. The beauty of GBD lies in

---

[9]Z is the coordinate along the propagation axis.

the fact that propagation of a single Gaussian beam can be modeled by ordinary ray tracing [7] of 5 rays (figure 6.28). This reduces the problem to a non-coherent situation. One ray is the base ray and gives the location and direction of the Gaussian beam. This base ray is accompanied by 2 additional rays known as the parabasal[10] rays. They define the width and divergence of the Gaussian beam and are traced just like the base ray. As their size and divergences change, so does the size and divergence of the beam. In the plane orthogonal to the basic parabasal rays, two additional parabasal rays are traced to allow astigmatic Gaussian beams. As shown below, the mathematical relationships that exist between the locations and directions of the base and parabasal rays are sufficient to reconstruct the beam at any point. Even if those rays are completely intertwined.

Once all the Gaussian beams have been traced through the system, they are again superposed at the desired plane to reproduce the full field. Depending on the coherence of the source field, this superposition either corresponds to summing the amplitudes or the intensities of the individual Gaussian beams.

In [8] Gaussian beam propagation through an orthogonal[11] optical structure is analyzed. It is shown that tracing a pair of rays in two orthogonal planes containing the propagation axis is sufficient to determine the beam propagation. These two rays are characterized by 4 parameters (2 directions and 2 positions) in both the entrance and exit plane of the structure. Let us assume that these rays have been traced successfully and that the structure can be described by a 2×2 ABCD-matrix (first order theory). Then we have 4 equations that relate the rays at the exit plane with those at the entrance plane, sufficient to calculate the 4 ABCD matrix elements. The obtained values give the Gaussian beam at the exit plane via

$$q_{out} = \frac{Aq_{in} + B}{Cq_{in} + D} \tag{6.25}$$

Analytic expressions for the beam parameters are considerably reduced in complexity if the entrance plane is chosen at the incident beam waist and if the waist ray and divergence ray are chosen as entrance rays. We denote the entrance position coordinate by x and the direction tangent by α. At the exit plane these are respectively x' and α'. The waist and divergence ray are characterized by $(x_w = w_0, \alpha_w = 0)$ and $(x_d = 0, \alpha_d = \lambda/\pi w_0)$. In this case the exit beam parameters are [8]

$$
\begin{aligned}
w' &= \sqrt{x_w'^2 + x_d'^2} \\
z_0' &= (x_d'\alpha_d' + x_w'\alpha_w')/(\alpha_w'^2 + \alpha_d'^2) \\
w_0' &= (x_w'\alpha_d' - x_d'\alpha_w')/\sqrt{\alpha_w'^2 + \alpha_d'^2}
\end{aligned}
\tag{6.26}
$$

w' is the beam semi-width at the exit plane, w_0 the semi-width at the waist plane and z_0' the distance of that plane with respect to the exit plane.

The theory of [8] can now be expanded to general refractive structures for which a single ABCD-matrix is not sufficient to describe the optical behavior. Using

---

[10]Parabasal means that the ray is paraxial to the base ray.

[11]A 2D orthogonal optical system features no cross-terms in its generalized ABCD matrix (containing 16 elements). This means that the system is equivalent to two one-dimensional systems within the paraxial or first-order approximation.
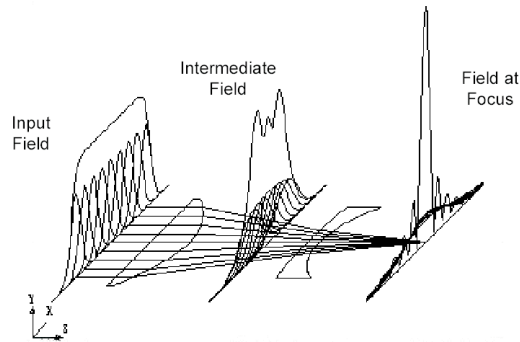
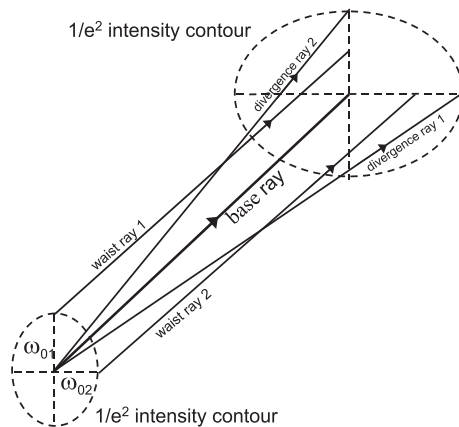Figure 6.27: Principle of Gaussian Beam Decomposition.

Figure 6.28: Definition of the base and parabasal rays.

Gaussian Beam Decomposition the field can be decomposed in multiple, smaller beams before entering the structure. For each base ray it is assumed that first-order theory can be employed. This means that for each base ray a local ABCD matrix can be derived from parabasal ray-tracing. The exit beams are calculated by (6.26). ASAP checks the validity of the paraxial assumption during ray-tracing. If it becomes violated, the user can intervene by increasing the number of beams that are used for decomposition.

Bibliography

[1] H. Kogelnik, "Coupling and conversion coefficients for optical modes in quasi-optics", Microwave Research Institute Symposia Series **14**, Polytechnic Press, New York, 333 (1964).

[2] D. Marcuse, "Loss analysis of single-mode fiber splices", Bell Syst. Tech. J. **56**, 703 (1977).

[3] H. Kogelnik, "On the propagation of Gaussian beams of light through lens-like media including those with a loss or gain variation", Appl. Opt. **4**, 1562 (1965).

[4] P. Belland and J.P. Crenn, "Changes in the characteristics of a Gaussian beam weakly diffracted by a circular aperture", Appl. Opt. **21**, 522 (1982).

[5] K. Lee, "Focusing characteristics of a truncated and aberrated Gaussian beam through a hemispherical microlens", Appl. Opt. **25**, 3671 (1986).

[6] J. Sakai and T. Kimura, "Design of a miniature lens for semiconductor laser to Single-Mode fiber coupling", J. Quant. Electron. **16**, 1059 (1980).

[7] A. Greynolds, "Propagation of general astigmatic Gaussian beams along skew ray paths", in Diffractive Phenomena in Optical Engineering Applications, Proc. SPIE **560**, 33 (1985).

[8] R. Herloski, S. Marshall and R. Antos, "Gaussian beam ray-equivalent modeling and optical design", Appl. Opt. **22**, 1168 (1983).

Chapter 7

Conclusions and perspectives

7.1 Summary and conclusions

The present work had three main objectives: what is excimer laser ablation about, how can it be used for micromachining purposes and which optical applications benefit from laser ablated components.

We extensively discussed the physical processes involved in excimer laser ablation of polymers and described how intense laser pulses can locally remove surface material. In particular we explained the modeling of thermal and non-thermal removal processes and showed how they can lead to well-defined laser ablated cavities in polymer materials. Based on this knowledge, excimer laser ablation technology has been reviewed and the micromachining qualities of laser ablation have been examined in detail. The most important contribution of this part is twofold. Firstly, we have systematically investigated the ablative properties of the commercial polymers PC, PET, PI, PMMA and PS at both 193 and 248 nm over a broad fluence range. All results have been supported with extensive experimental data. Secondly, the properties relevant to micromachining are examined rather than the single-pulse ablation behavior which can be found in many ablation modeling papers and which is of little importance in typical laser machining conditions.

A second part of this thesis dealt with some dedicated applications: the (sub)-micron accuracy of laser ablation has been applied to fabricate microalignment and microoptical components. In particular the latter application, microlens fabrication, has been quite a challenge as the final surface roughness needs to be significantly lower than the wavelength at which the component will be used. In the framework of this doctoral research work, a novel technique called scanning contour ablation has been developed. Contrary to competing lens fabrication techniques, it is capable of fabricating refractive lenses with an arbitrary cross-section in polymer substrates at an acceptable speed. Due to the contactless and direct-write nature of the process, excimer laser ablation can be used at any phase of a heterogeneous opto-electronic assembly.

All these advantages make our microlens fabrication technique extremely attractive

at a prototyping level. Still, one should also take its limitations into account: except for slow lenses, it has not been possible to obtain diffraction limited performance. It is our belief that the limited accuracy of the translation stage and pulse-to-pulse beam fluence variations have contributed significantly to this shortcoming.

7.2 Remaining challenges and perspectives

The experimental work on microlenses in this thesis has been limited to lenses with a circular footprint. Still, in chapter 4 it has been briefly suggested that elliptical footprints −more in particular elliptical types− can also be obtained with scanning excimer laser ablation. A logical extension of the present work would thus involve the investigation of these lenses which have quite some potential in e.g. optical coupling from an edge-emitting laser diode to SM fiber. Another lens type that has not be considered in this work are diffractive lenses. The direct-milling aspect of excimer laser ablation is extremely useful when binary or multi-level diffractive lenses are fabricated with mask projection and has already drawn the attention of other research groups [1].

In a more general context it is fair to say that excimer lasers experience a growing competition from ultrafast lasers for micromachining purposes. These lasers emit pulses as short as a few tens of femtoseconds. Where best results in terms of accurate machining with nanosecond excimer lasers are obtained for polymer materials, ultrafast lasers can treat any material with submicron accuracy due to the lack of thermal processes during material removal. It has been shown that the extreme fluences obtained at the focal beam spot are suitable for locally changing the refractive properties in certain glasses in a permanent way [2]. In addition, the technology has also been used successfully for true 3D microfabrication via photopolymerization [3] with feature sizes below 120 nm. In summary, these lasers offer quite some perspectives for microstructures and microoptics in particular. They will likely gain attention as femtosecond micromachining technology matures, a process which will require a lot of research efforts in the coming years. Especially in the fascinating field of microoptics and nanooptics...

266

Bibliography

[1] X. Wang, J. Leger and R. Rediker, "Rapid fabrication of diffractive optical elements by use of image-based excimer laser ablation", Appl. Opt. **36**, 4660 (1997).

[2] J. Chan, T. Huser, S. Risbud, J. Hayden and D. Krol, "Waveguide fabrication in phosphate glasses using femtosecond laser pulses", Appl. Phys. Lett. **82**, 2371 (2003).

[3] S. Kawata, H. Sun, T. Tanaka and K Takada, "Finer features for functional microdevices", Nature **412**, 697 (2001).